The Geological Society of America
Memoir 222

Structural Analysis and Chronologic Constraints on Progressive Deformation within the Rincon Mountains, Arizona: Implications for Development of Metamorphic Core Complexes

George H. Davis
Eytan Bos Orent
Christopher Clinkscales
University of Arizona, Department of Geosciences, 1040 E. 4th Street, Tucson, Arizona 85721, USA

Felipe R. Ferroni
University of Arizona, Department of Geosciences, 1040 E. 4th Street, Tucson, Arizona 85721, USA, and
Petrobras/E&P-EXP, Av. Henrique Valadares 28, Rio de Janeiro, CEP 20231-030, Brazil

George E. Gehrels
University of Arizona, Department of Geosciences, 1040 E. 4th Street, Tucson, Arizona 85721, USA

Sarah W.M. George
University of Arizona, Department of Geosciences, 1040 E. 4th Street, Tucson, Arizona 85721, USA, and
School of Geosciences, University of Oklahoma, Norman, Oklahoma 73069, USA

Katherine A. Guns
University of California at San Diego, Scripps Institution of Oceanography, Institute of Geophysics and Planetary Physics, 9500 Gilman Drive, MC 0225, La Jolla, California 92093, USA

Catherine E. Hanagan
Amanda Hughes
University of Arizona, Department of Geosciences, 1040 E. 4th Street, Tucson, Arizona 85721, USA

Alexander Iriondo
Universidad Nacional Autónoma de México, Centro de Geociencias, Campus Juriquilla, Querétaro 76230, Mexico, and
University of Arizona, Department of Geosciences, 1040 E. 4th Street, Tucson, Arizona 85721, USA

Gilby Jepson
University of Arizona, Department of Geosciences, 1040 E. 4th Street, Tucson, Arizona 85721, USA, and
School of Geology and Geophysics, University of Oklahoma, Norman, Oklahoma 73069, USA

Clay Kelty
Earth Consultants International, Inc., 1642, E. 4th Street, Santa Ana, California 92701, USA

Davis, G.H., Bos Orent, E., Clinkscales, C., Ferroni, F.R., Gehrels, G.E., George, S.W.M., Guns, K.A., Hanagan, C.E., Hughes, A., Iriondo, A., Jepson, G., Kelty, C., Krantz, R.W., Levenstein, B.M., Lingrey, S.H., Miggins, D.P., Moore, T., Portnoy, S.E., Reeher, L.J., and Wang, J.W., 2023, Structural Analysis and Chronologic Constraints on Progressive Deformation within the Rincon Mountains, Arizona: Implications for Development of Metamorphic Core Complexes: Geological Society of America Memoir 222, p. 1–125, https://doi.org/10.1130/2023.1222(01). © 2023 The Geological Society of America. All rights reserved. For permission to copy, contact editing@geosociety.org.

Robert W. Krantz
Department of Geosciences, Fort Lewis College, 1000 Rim Drive, Durango, Colorado 81301, USA, and
University of Arizona, Department of Geosciences, 1040 E. 4th Street, Tucson, Arizona 85721, USA

Brandon M. Levenstein
Steve H. Lingrey
University of Arizona, Department of Geosciences, 1040 E. 4th Street, Tucson, Arizona 85721, USA

Daniel P. Miggins
$^{40}Ar/^{39}Ar$ Geochronology Laboratory, College of Earth, Ocean, and Atmospheric Sciences, Oregon State University, 104 Administration Building, Corvallis, Oregon 97331-5503, USA

Timothy Moore
University of Arizona, Department of Geosciences, 1040 E. 4th Street, Tucson, Arizona 85721, USA

Samantha E. Portnoy
National Cooperative Geologic Mapping Program, U.S. Geological Survey, 12201 Sunrise Valley Drive, Mail Stop 908, Reston, Virginia 20192, USA

Lauren J. Reeher
University of Arizona, Department of Geosciences, 1040 E. 4th Street, Tucson, Arizona 85721, USA, and
Utah Geological Survey, 1594 W. North Temple Street, Salt Lake City, Utah 84116, USA

Jordan W. Wang
University of Arizona, Department of Geosciences, 1040 E. 4th Street, Tucson, Arizona 85721, USA

ABSTRACT

Investigation of exhumed and well-exposed crustal-scale fault zones provides a rare window into the mechanics and timing of a broad range of deformation mechanisms, strain localization, and fault zone behavior. Here, we apply and integrate geo- and thermochronology analytics to carefully described brittle-ductile structural characteristics of the Catalina detachment zone as exposed in the Rincon Mountains domain of the Catalina-Rincon metamorphic core complex. This core complex is an exhumed extensional, broad-scale-normal-slip shear zone near Tucson, Arizona, USA. The Catalina detachment zone, as formulated here, is partitioned into a brittle-ductile fault-rock stratigraphy that evolved through progressive deformation. The Catalina-Rincon Mountains metamorphic core complex is one of the original type localities of Cordilleran metamorphic core complexes in western North America and has a long history of scientific study to document its structural characteristics and decipher its evolution in the context of Mid-Cenozoic extension. In this Memoir, we seek to provide a thorough accounting of the evolution of this shear zone, through integrating and synthesizing decades of previous research with new mapping, structural data, and geochronological analyses.

The Catalina detachment zone stratigraphy is made up of the Catalina detachment fault, cataclasite, chloritic protocataclasite (referred to in most core-complex literature as "chlorite breccia"), subdetachment faults, and mylonites. When it was active, this zone accommodated a minimum of ~36 km of top-to-the-SW displacement. Characterizing the progressive evolution of this metamorphic core complex fault-rock stratigraphy requires a detailed accounting of the kinematic and temporal history of the detachment zone. Consequently, we first characterize and describe each

structural unit and feature of this crustal-scale fault and shear zone network through the combination of previously published mapping, structural and microfabric analyses and newly collected structural data, thin-section analysis, large-scale mapping, and reinterpretation of stratigraphic and structural relations in the adjacent Tucson Basin. To improve our broad-scale mapping efforts, we employ multispectral analysis, successfully delineating specific fault-rock stratigraphic units at the core-complex scale. We then establish kinematic and absolute timing constraints by integrating results from well-log and seismic reflection data and with new and previously published zircon U-Pb, $^{40}Ar/^{39}Ar$, $^{40}K/^{40}Ar$ geochronological, (U/Th)/He, $^{4}He/^{3}He$, and apatite fission track thermochronological analyses. These temporal constraints indicate a deformation sequence that progressed through mylonitization, cataclasis, minidetachment faulting, subdetachment faulting, and detachment faulting.

This multidisciplinary investigation reveals that mylonitization occurred in late Oligocene time (ca. 26–22 Ma), coeval with rapid exhumation of the lower plate, and that slip on the Catalina detachment fault ceased by early Miocene, ca. 17 Ma. This temporal framework is consistent with results of our subsurface analysis of stratigraphic and structural relations in the Tucson Basin. Onset of metamorphic core complex deformation in southern Arizona slightly preceded that in central and western Arizona and southeasternmost California.

Our compiled data sets suggest a shear-zone evolution model that places special emphasis on the transformation of mylonite to chloritic protocataclasite, and strain localization onto subdetachment, minidetachment, and detachment faults over time. Our model envisions mylonites drawn upward through a fluids-sourced brittle-ductile transition zone marked by elevated fluid pressures. This emphasis draws upon seminal work by Jane Selverstone and Gary Axen in analyzing structural-mechanical evolution in the Whipple Mountains metamorphic core complex. Progressive embrittlement and strength-hardening of the lower-plate rocks are manifest in intensive fracturing and minidetachment faulting, favored by the change in rheology produced by alteration-mineral products. Subdetachment faults, localized by earlier-formed ultramylonite and calc-silicate tectonite, coalesce to produce a proto-detachment fault, which marks the interface between mylonite and chlorite protocataclasite. Linking and smoothing of minidetachment faults within chloritic protocataclasite led to emergence of the Catalina detachment fault proper. All of this, from mylonite formation to final slippage on the detachment fault, kinematically conforms to top-to-the-SW shear. The macro-form of the antiformal-synformal corrugations of the Rincon Mountains began developing while mylonites were forming, continuing to amplify during proto-detachment faulting and detachment faulting.

We emphasize and describe with examples how the timing and tectonic significance of mylonitization, cataclasis, and detachment faulting within the Catalina-Rincon metamorphic core complex continues to be hotly debated. Disagreements center today, as they have in the past, on the degree to which the structures and fabrics in the Rincons are Laramide products, mid-Cenozoic products, or some combination of both. In addressing tectonic heritage with respect to the Catalina detachment zone, it is hoped that the proposed model of progressive evolution of the Catalina detachment-zone shear zone will inform other studies of active and ancient metamorphic core complexes around the globe. In this regard, some new transferable emphases and methodologies emerged from this work, above and beyond what are now standard operating procedures for understanding crustal shear zones in general, and metamorphic core complexes particularly. For example, remote multispectral image analysis combined with ground-truth field analysis permitted mapping the full extent of chloritic protocataclasite, one of the best exposures of same globally, which is perhaps the most strategic fault rock in exploring the brittle-ductile transition. The added value of complete map control for chloritic protocataclasite is exploring, at its base in other metamorphic core complexes, for the presence of subdetachment faulting, i.e., proto-detachment

faulting that influenced localization of detachment zones proper. Another example is the importance of continuously searching for certain mylonite protolith that yields opportunities for closely constraining timing of mylonitization. In our case, it is the Loma Alta mylonite that, more than any other protolith unit in the Rincon Mountains, permitted 'locking' the age of mylonitization as late Oligocene.

We hope that insights from this detailed study will inform analyses of similar crustal-scale fault zones, both ancient and modern. Given its ready accessibility compared to most metamorphic core complexes, the Rincon Mountains present opportunities for others to use this contribution as part of the basis for exploiting this natural laboratory in research, teaching, and public science.

CHAPTER 1

Purpose, context, and organization

ADVANCING UNDERSTANDING OF FAULT ZONE BEHAVIOR

Deciphering the evolution of crustal-scale fault zones is a major goal for researchers in the fields of structural geology and tectonics. Characterization of fault-zone processes such as slip and strain localization along faults and shear zones within the lithosphere poses significant community challenges (Huntington and Klepeis, 2018; Roberts et al., 2002), but their investigation leads to a better fundamental understanding of the ways in which faults work and evolve. With a more comprehensive view of fault systems over multiple spatial and temporal scales, we can both better understand the evolution of plate boundaries and intraplate deformation and also better understand the mechanical processes controlling slip, with implications for regional hazards. Here, we turn our attention toward extensional fault systems, with focus on the Catalina-Rincon metamorphic core complex extensional shear zone system in Tucson, Arizona. We document our investigation and interpretations to characterize this crustal-scale, partially exhumed, brittle-ductile fault and shear zone network, where our main objectives were (1) to interpret how it kinematically and mechanically evolved updip and downdip across a range of spatial scales, and (2) to quantify the timing of activity over its life span.

As the primary fault surface of the Catalina-Rincon metamorphic core complex, the Catalina detachment fault and its underlying lower-plate structures and fabrics are central features to this work. The Catalina detachment fault was first identified and mapped as the "Catalina fault" by Pashley (1966) along the southern margin of the Catalina Mountains and the western and southern margins of the Rincon Mountains for a distance of ~85 km (Fig. 1-1)[1]. In a manner typical of metamorphic core complex detachment faults, the Catalina detachment fault is laterally continuous along its entire 85 km fault trace and separates nonmylonitic rocks (including synextensional sedimentary rocks) in the upper plate (hanging wall) from mylonitic rocks in the lower plate (footwall). It does not tip out; instead, the Catalina detachment fault is truncated and offset by high-angle normal faults, namely, the Pirate fault to the northwest and the Martinez Ranch fault to the southeast (Fig. 1-1). East of the Martinez Ranch fault, in the eastern Rincon and Catalina Mountains, short segments of what is likely the faulted continuation of the Catalina detachment fault surface are locally preserved (Spencer et al., 2019, their fig. 3, p. 5). This area is known as the eastern subregion of the San Pedro detachment fault, which lies to the east of the Catalina-Rincon Mountains on the western edge of the San Pedro Mountains (Fig. 1-1). Spencer et al. (2019) preferred the name "San Pedro detachment fault" to "Catalina detachment fault" and applied it to the entire Catalina-Rincon Mountains metamorphic core complex.

Beneath the Catalina detachment fault surface, there is a sequence of lower-plate brittle-ductile fault rocks with a coherent pseudostratigraphy, which we call the "Catalina detachment zone." It comprises the detachment fault and a downward succession of fault rocks and structures that include ultracataclasite and cataclasite, chloritic protocataclasite, a subdetachment fault zone, and uppermost mylonite (Fig. 1-2). Taken together, ultracataclasite and cataclasite are up to ~15 m thick, whereas chloritic protocataclasite is generally up to ~150 m thick. Exposed mylonites are generally up to ~300 m thick in the Rincon Mountains domain of the Catalina-Rincon metamorphic core complex (Spencer et al., 2022), though we studied only the upper ~100 m interval, i.e., those that immediately underlie the cataclastic and protocataclastic fault rocks. This exhumed and preserved brittle-ductile detachment zone, preserved in the lower plate, affords a rare and detailed look at the processes that created these features.

Two primary synergistic goals motivated this interrogation of the Catalina detachment zone. The first was to develop a structural-kinematic-mechanical model describing the progressive evolution of the Catalina detachment zone in relation to the Catalina-Rincon metamorphic core complex as a whole. Pursuing this goal, we combined detailed structural geologic mapping, outcrop-scale structural analyses, and examination of fabrics, microstructures, and deformation mechanisms. The second goal was to embed the structure-evolution model into a temporal framework based on new geochronologic and thermochronologic analytical work as well as a reassessment of Tucson Basin subsurface faulting data and Oligocene–Miocene basin stratigraphy. The conclusions reached through this work are directly applicable to the structure and tectonics of metamorphic core complexes globally and contribute to an improved understanding of the evolution of crustal-scale shear zones.

[1]In Chapter 1 and throughout this volume, figure numbers and table numbers include chapter number followed by figure number, e.g., Figure 1-5 (Fig. 5 of Chapter 1), Table 3-1 (Table 1 of Chapter 3). Figures and tables in the Supplemental Material begin with the corresponding appendix letter (e.g., Table F-1).

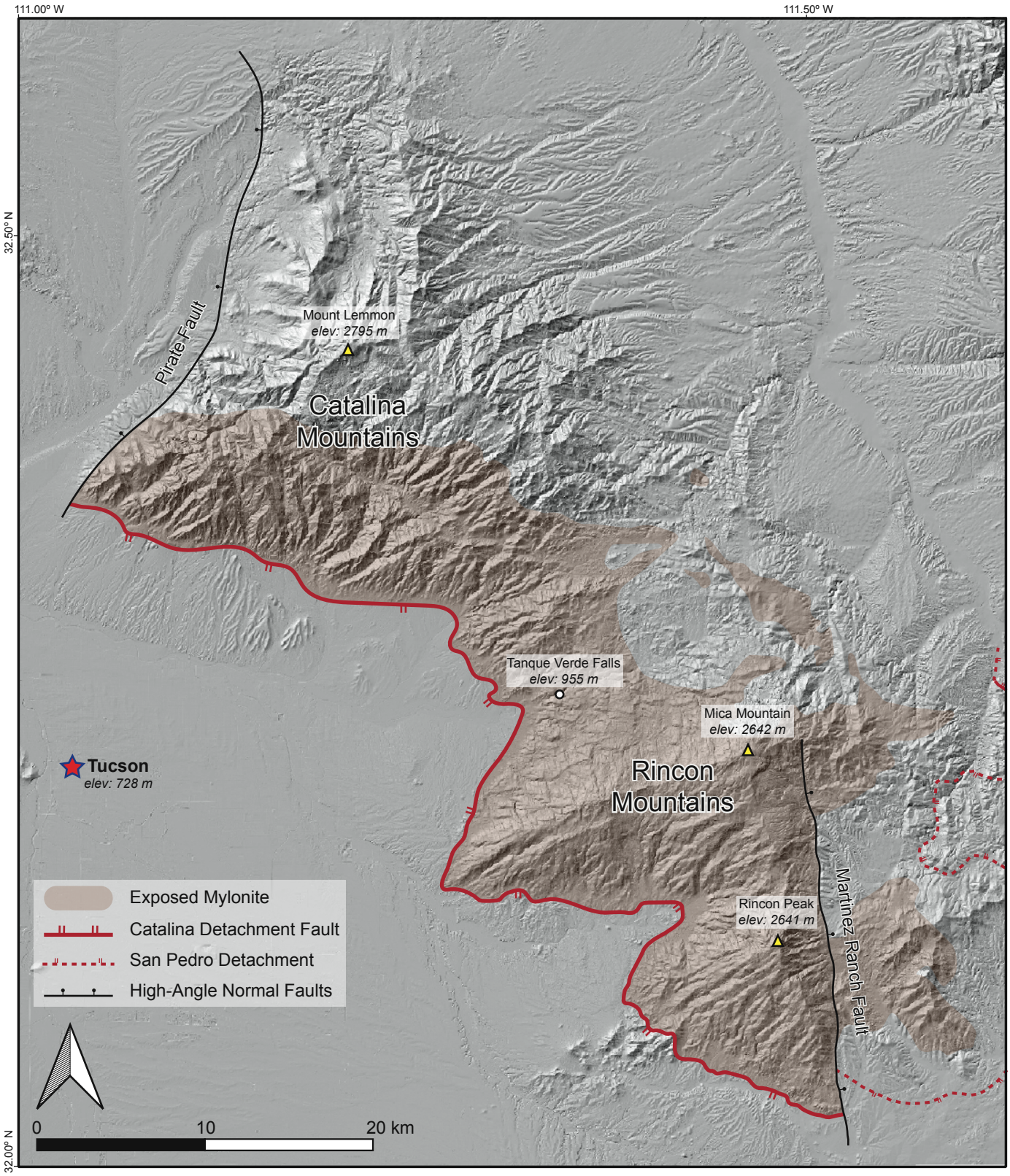


Figure 1-1. Mapped trace of the Catalina detachment fault (red) along the sinuous margins of the Catalina and Rincon Mountains, Tucson, Arizona. Trace of the San Pedro detachment fault (dashed red) is also shown, directly east of the Rincon Mountains. Lower-plate (footwall) mylonites are shown in brown hue. Note that the Pirate and Martinez Ranch faults (high-angle normal faults) are the "end points" for the 85 km continuous, unsegmented trace of the Catalina detachment fault. Spot elevations underscore the considerable topographic relief of the Rincon Mountains as well as elevation of the Tucson Basin.

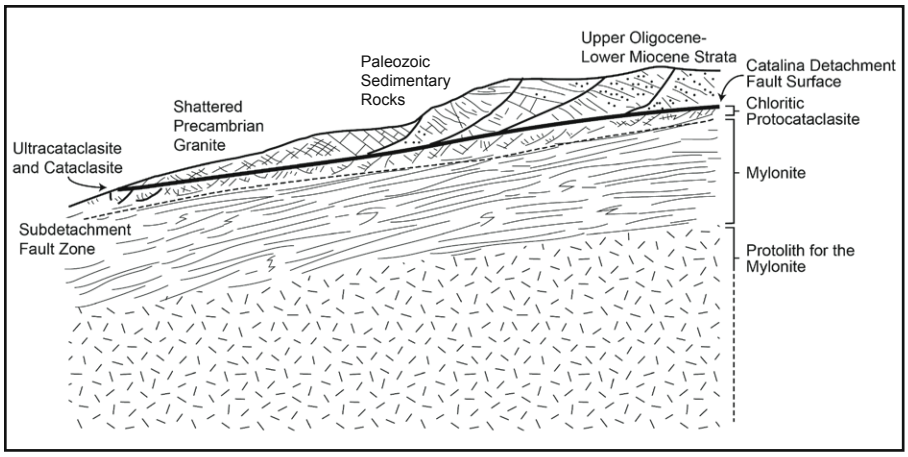


Figure 1-2. Schematic cross-sectional representation of metamorphic core complexes, modified and updated in taxonomy from Davis (1980b, fig. 3-2, p. 123). The fault-rock and structural components of a Cordilleran metamorphic core complex are shown and labeled, with emphasis on the lower plate.

ORIGINAL CHARACTERIZATION OF METAMORPHIC CORE COMPLEXES

The term "metamorphic core complexes" was coined by Peter Coney (1973) in reference to the Shuswap metamorphic complex and its relation to the Canadian Rocky Mountain foreland thrust belt, and then later to metamorphic terranes and related features found discontinuously southward in the North American Cordillera. Between 1974 and 1976, Peter Coney and George Davis, starting with the Snake Range (1974) and the Rincon Mountains (1975), identified about 25 metamorphic core complex candidates in the Western Cordillera, with locations ranging from Alaska to northern Sonora, Mexico. Figure 1-3 includes the subset of those metamorphic core complexes originally identified south of the Snake River Plain (Davis and Coney, 1979) and adds those that have been discovered since that time. For purposes of comparing and contrasting the structural, tectonic, and temporal data across these enigmatic tectonic systems, a 1977 Geological Society of America (GSA) Penrose Conference on "Tectonic Significance of Cordilleran Metamorphic Core Complexes" was held at a conference site located on the trace of the Catalina detachment fault. Seventy-two geoscientists participated, and GSA Memoir 153, titled *Cordilleran Metamorphic Core Complexes* (Crittenden et al., 1980), is a product of this conference. One of the most significant revelations was the striking similarity between a subset of metamorphic core complexes in eastern Nevada and those within a belt extending from southeastern California to northern Sonora (Fig. 1-3). These Cordilleran metamorphic core complexes emerged individually and collectively as type examples of metamorphic core complexes globally.

The basic signatures of metamorphic core complexes identified in advance of the 1977 Penrose Conference, and confirmed through additional investigation, included topographically prominent foliation domes and arches; low-angle extensional detachment faults separating nonmylonitic, faulted, upper-plate rocks from lower-plate cataclastic and mylonitic rocks; expansive exposures of mylonites marked by penetrative low-dipping foliations and shallowly plunging mineral lineations with uniform trends; submylonite granitoid protoliths transformed in part into mylonites; Oligocene–early Miocene cooling ages reflective of rapid exhumation of the lower-plate mylonites; tilted syntectonic Oligocene–early Miocene sedimentary and volcanic rocks cut and offset along detachment faults; Oligocene–early Miocene ignimbrites commonly in immediately adjacent ranges; and tectonic-transport magnitudes in the range of 20–60 km. Crittenden et al. (1980, p. 485) emphasized: "Clearly the most important conclusion regarding these complexes … is that they are startlingly young and … show consistent evidence of horizontal extension and vertical attenuation."

BELT OF CALIFORNIA-ARIZONA-SONORA METAMORPHIC CORE COMPLEXES

A particularly germane feature to this study, especially in relation to kinematic-temporal comparisons, is the corridor of metamorphic core complexes that tracks along an ~130° trend from southeastern California to southern Arizona (near Tucson), and from there along an ~160° trend into Sonora, Mexico, ending at Sierra Mazatán (Fig. 1-3). Spencer (2006) referred to this corridor as the "Southwest North America core-complex belt." As has been known for some time (Davis, 1981; Wust, 1986), there is a tight regional kinematic coordination of the sense and direction of upper-plate tectonic transport and the direction and sense of shear deduced from fabrics in subjacent mylonites (Fig. 1-4; Table 1-1).

Viewed as a whole, the lower-plate, largely mylonitic surface exposures in the California-Arizona belt of metamorphic core complexes constitute a gross area of 2,000,000 km^2 (Fig. 1-4). The Catalina-Rincon metamorphic core complex is notable in its size and location because it is one of the largest (Fig. 1-4). The regional position of the Catalina-Rincon metamorphic core complex marks the southeastern terminus of the California-Arizona section of the Southwest North America core-complex belt and the northern terminus of the part of it that runs south to Sierra Mazatán (Fig. 1-3). The bend in the Southwest North America core-complex belt from southeast to south coincides with an anomalously broad, NE-trending swath of three metamorphic

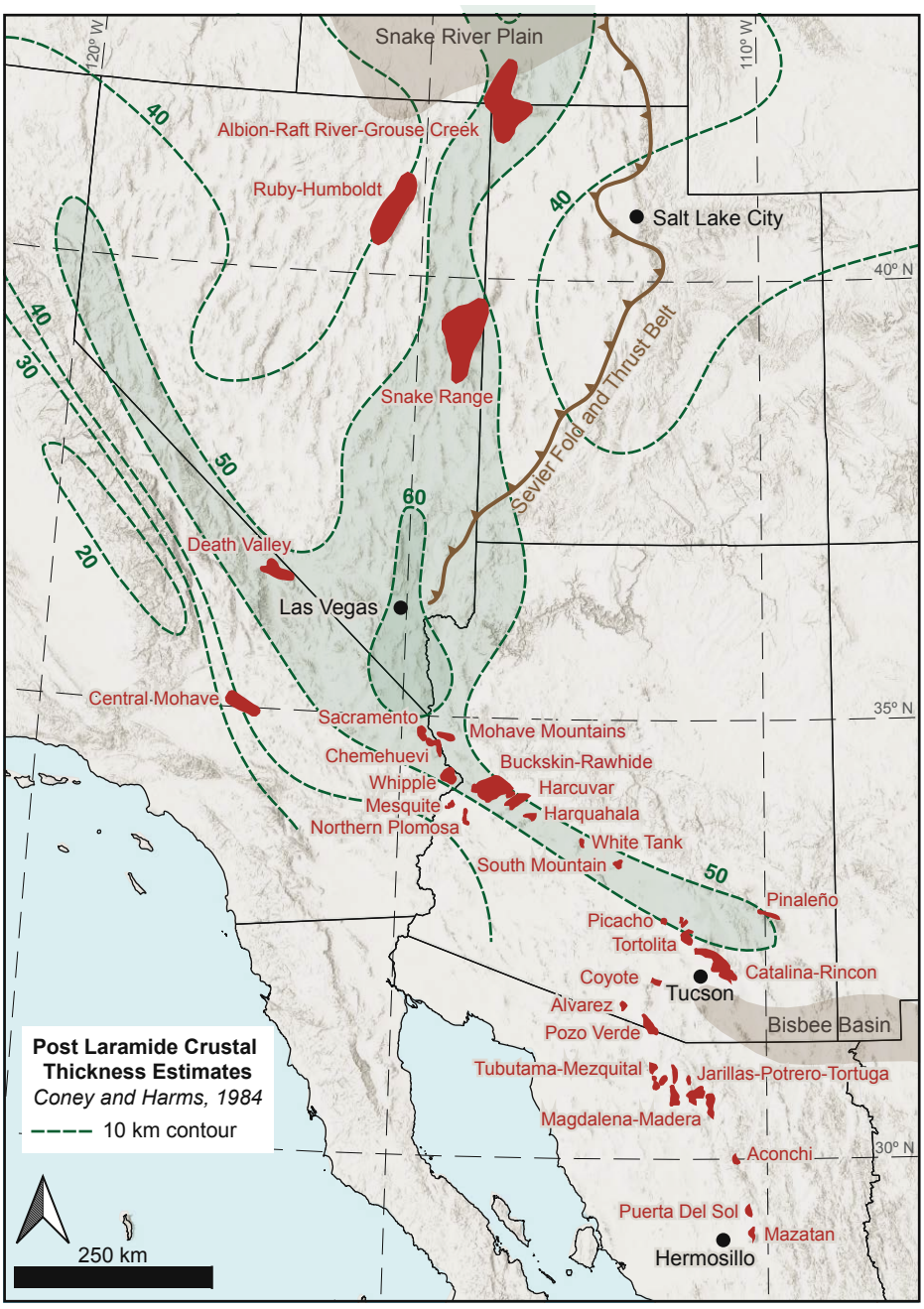


Figure 1-3. Map of Cordilleran metamorphic core complexes in the western North American Cordillera, as adapted from Davis and Coney (1979, fig. 1, p. 121). Isopach contours are estimated crustal thicknesses following compressional shortening due to Sevier/Laramide orogeny deformation, as adapted from Coney and Harms (1984, fig. 2, p. 551).

core complexes, which from SW to NE, are the Coyote, Catalina-Rincon, and Pinaleño (Fig. 1-4).

The southwestern North America belt of metamorphic core complexes possesses several distinct kinematic domains based on the sense of tectonic-transport direction. From the Sacramento Mountains metamorphic core complex (SE California) to the South Mountain metamorphic core complex (Phoenix, Arizona) (Fig. 1-4), the sense-of-transport (detachment faulting) and sense-of-shear (mylonitization) direction is top-to-the-NE. Just south of Phoenix, Arizona, from the Picacho Mountains to the Rincon Mountains, the sense-of-transport and sense-of-shear direction changes to top-to-the-SW. With just a few exceptions (the Sierra Aconchi, Pinaleño, and Coyote metamorphic core complexes), this top-to-the-SW detachment faulting and mylonitic sense of shear continue from southernmost Arizona into Sonora (Fig. 1-4). In the broad NE-trending expanse of metamorphic core complexes centered on Tucson, the dominant regionally coherent top-to-the-SW sense of shear for the Catalina-Rincon metamorphic core complex contrasts with the top-to-the-NE sense of shear in the Pinaleño Mountains metamorphic core complex and top-to-the-N sense of shear in the Coyote Mountains metamorphic core complex (Davis, 1980a) (Fig. 1-3).

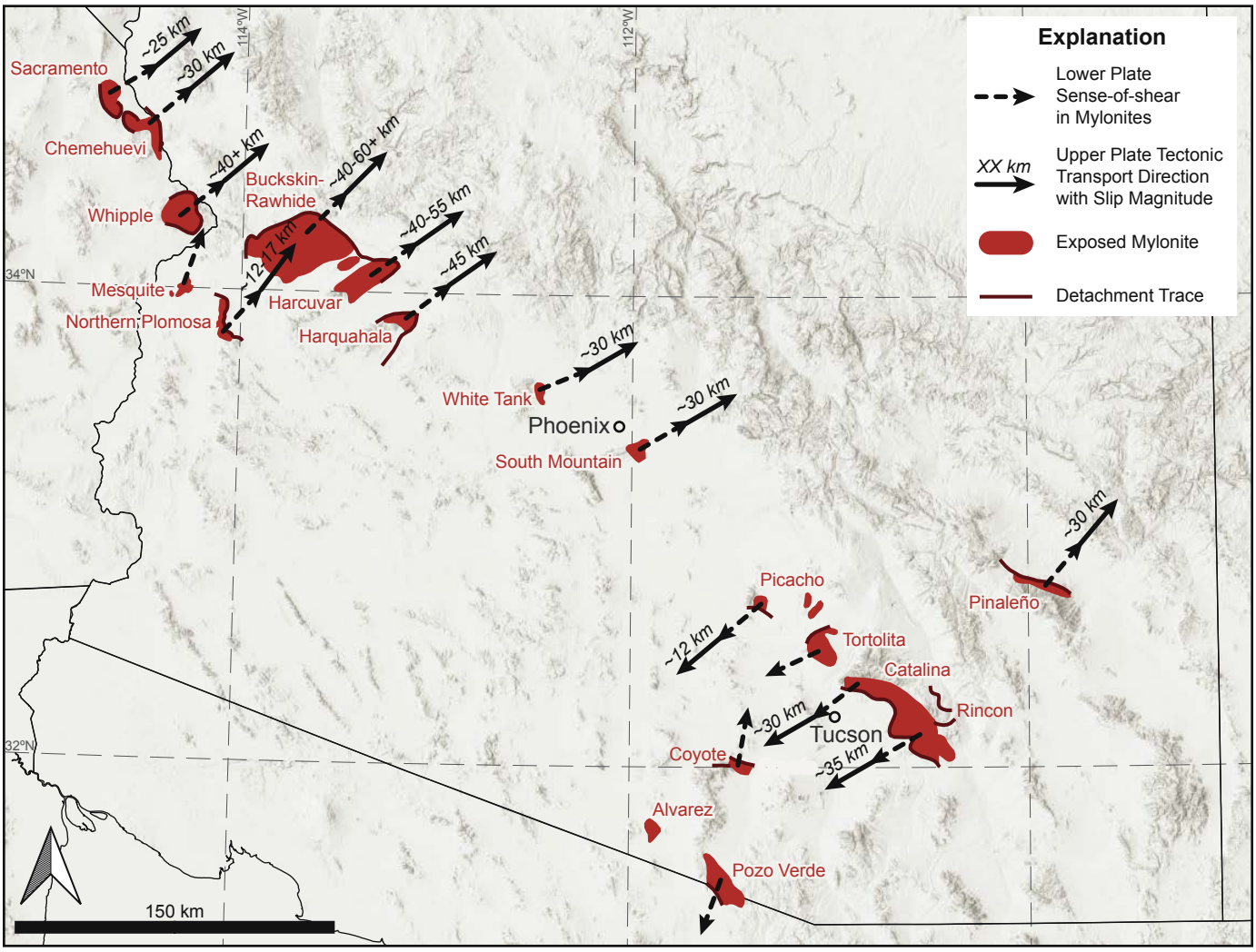


Figure 1-4. Metamorphic core complexes (lower-plate rocks in red) within 305°/125°-trending corridor running from SE California to SE Arizona. Spencer (2006) referred to this belt as the "Southwest North America core-complex belt." Direction and sense of shear in mylonites as well as direction, sense, and magnitude of tectonic transport of upper-plate rocks are shown. Note the high degree of regional coherence between direction and sense of shear in mylonites and direction and sense of tectonic transport of upper-plate rocks.

STRUCTURAL-GEOLOGIC ESSENCE OF METAMORPHIC CORE COMPLEXES

Metamorphic core complexes are common features in orogenic systems formed by high-magnitude extension and redistribution of crust following protracted shortening and crustal thickening. In the process of their formation, these extensional systems progressively expose midcrustal rocks that serve as windows into the mechanical evolution of large-displacement fault systems (Wernicke, 1981). Platt et al. (2015, p. 9), in their global review of metamorphic core complexes, emphasized their essence as "normal-fault displacements sufficient to exhume rocks from below the brittle-ductile transition." Metamorphic core complexes are commonly expressions of brittle-ductile shear zones marked by cataclasites and protocataclasites beneath a detachment fault and mylonites and ultramylonites beneath the protocataclasites.

The lower-plate rocks of metamorphic core complexes preserve the very fabrics and structures that form at depth during core complex extension. These preserved features underscore the inestimable structural-geologic value of metamorphic core complexes and detachment fault zones. Progressive normal-shear structural evolution is such that the entire suite of core complex–related fault rocks and fabrics becomes fashioned into a discrete fault-rock stratigraphy, which Platt et al. (2015) referred to as a distinctive "zonation" of fault rocks. The preservation of fabric sequencing in metamorphic core complexes has long been appreciated (e.g., Davis, 1980a, 1983), but Platt et al. (2015, p. 20) captured the development through a particular mechanical/rheological insight, the essence of which we paraphrase and

TABLE 1-1. COMPARATIVE KINEMATIC INFORMATION, CALIFORNIA-ARIZONA CORRIDOR OF METAMORPHIC CORE COMPLEXES

Name of metamorphic core complex	Approximate mylonitic core area (km^2)	Mylonite lineation		Detachment fault slip		References	
		Direction (±~5°)	Sense	Direction (±~5°)	Sense	Magnitude (km)	
Sacramento	240	~240°/060°	Top-to-the-NE	~230°/050°	Top-to-the-NE	~25	McClelland (1982), Simpson et al. (1991), Spencer (1985)
Chemehuevi	200	~230°/050°	Top-to-the-NE	~230°/050°	Top-to-the-NE	~50	John (1982, 1987)
Whipple	200	~232°/052	Top-to-the-NE	~230°/050°	Top-to-the-NE	~40+	G.A. Davis et al. (1980, 1986), Dickey et al. (1980), Frost (1981), Davis et al. (1982), Davis and Anderson (1991), Lister and Davis (1989), Singleton et al. (2019), Spencer and Reynolds (1991)
Mesquite	35	~198°/018°	Top-to-the-NE				Knapp (2018)
Northern Plomosa	60	~220°/040°	Top-to-the-NE	~215°/35°	Top-to-the-NE	~12–17	Strickland et al. (2018), Spencer et al. (2018b)
Buckskin-Rawhide	650	~225°/045°	Top-to-the-NE	~225°/045°	Top-to-the-NE	~40–60+	Bryant and Wooden (2008), G.A. Davis et al. (1980), Singleton et al. (2014), Singleton (2015), Singleton and Mosher (2012), Spencer and Reynolds (1989a, 1989b)
Harcuvar	250	~235°/055°	Top-to-the-NE	~235°/055°	Top-to-the-NE	~40–55	Bryant (1995), Singleton et al. (2019)
Harquahala	30	~233°/053°	Top-to-the-NE	~235°/055°	Top-to-the-NE	~45	Richard et al. (1990), Prior et al. (2016), Singleton et al. (2019)
White Tank	30	~248°/068°	Top-to-the-NE	~240°/060°	Top-to-the-NE	~30	Reynolds et al. (2002), Singleton et al. (2019); distance of transport estimate, Reynolds (2021, personal commun.)
South Mountain	70	~240°/060°	Top-to-the-NE	~240°/060°	Top-to-the-NE	~30	Reynolds (1985); distance of transport estimate, Reynolds (2021, personal commun.)
Picacho	30	~230°/050°	Top-to-the-SW	~230°/050°	Top-to-the-NE	~12	Davis (1980a, 1980b), Richard et al. (1999), Spencer et al. (2012)
Tortolita	250	~245°/065°	Top-to-the-SW				Davis (1980a, 1980b), Ferguson et al. (2003)
Catalina	400	~220°–245°/ ~040°–065	Top-to-the-SW	~240°/060°	Top-to-the-SW	~40–60	Spencer (2006), Spencer et al. (2022)
Rincon	400	~240°/060°	Top-to-the-SW	~240°/060°	Top-to-the-SW	~40–60	Davis (1980a, 1980b, 2013), Davis et al. (2019), Spencer et al. (2019, 2022)
Pinaleño	50	~220°/040°	Top-to-the-NE	~220°/040°	Top-to-the-NE	~30	Davis (1980a, 1980b), Davis and Hardy (1981)
Coyote	200	~190°/010°	Top-to-the-NE	?	?	?	Davis (1980a, 1980b)
Pozo Verde	200	~200°/020°	Top-to-the-SW	?	?	?	Davis (1980a, 1980b)

Note: NA—not applicable.

elaborate upon in the following way: During footwall ascent, the stress required for footwall deformation increases near the brittle-ductile transition. This induces a localization of strain and displacement. Because of this upward shift from broadly distributed (penetrative) shear to strain-localized shear and slip, exhumation exposes volumes of rock within which earlier-formed fabrics and structures are preserved. These earlier fabrics and structures survive because brittle fabric overprints were localized, and the progressive ascent of footwall rocks toward Earth's surface minimized the possibility of destruction or masking of most or all of the early structures and fabrics by subsequent metamorphism.

Given this straightforward way of thinking about metamorphic core complexes, there may be bewilderment regarding why it took so long to first recognize and then embrace them as such. Partly, it was the tendency to interpret any low-angle fault as a thrust fault. Partly, it was because fundamental breakthrough research on shear zones, microstructures, and deformation mechanisms was late in arriving (see overviews by Snoke et al., 1998, and Davis, 2008). Partly, it was because geochronologic tools of the time were not up to the task. An ongoing challenge derives from the fact that exhumation not only exposes deep rocks, fabrics, and structures that formed during core complex extensional tectonics, but also pre–core complex fabrics and structures. Thus, in all metamorphic core complexes, it becomes essential to distinguish fabrics and structures that were formed syntectonically with core complex deformation from those that were formed prior to the metamorphic core complex, fashioned under entirely different and earlier tectonic and pressure-temperature loading conditions. Addressing this distinction was one of the several major dilemmas that prompted the 1977 GSA Penrose Conference on metamorphic core complexes. It will always be challenging to evaluate the partitioning between pre–core complex and syn–core complex fabrics and structures.

SPECIAL SCIENTIFIC AND ACCESS OPPORTUNITIES AFFORDED BY THE RINCON MOUNTAINS

The geology of the Rincon Mountains is readily accessible in comparison to many of the Cordilleran metamorphic core complexes. The Rincon Mountains fault-network exposures occupy public lands and reside just beyond the edge of Tucson, Arizona. Public lands include a national park (Saguaro National Park, Rincon Mountain District), a wilderness area (Rincon Mountain Wilderness, Coronado National Forest), a county system of distributed land stewardship (Pima County Parks and Recreation Lands), and trust lands (State of Arizona State Trust Lands). Access is good. For example, the eastern stretch of the Cactus Forest ["Loop"] Drive through Saguaro National Park (Rincon Mountain District) follows the trace of the Catalina detachment zone. Moreover, the park's picnic area is nestled among mylonites. Though permits must be obtained for access onto the public lands, the government agencies responsible for granting access have, to date, looked quite positively upon engagement in research, teaching, and public service.

Detailed descriptive and location data contained in this contribution are intended to enable other investigators in the future to study the Catalina detachment zone as expressed in the Rincon Mountains even more fully and with the aid of new and emerging technologies. We hope that interpretations from this work gain traction and hold up, but at the same time, we remain aware that the enigmatic nature of metamorphic core complexes will create perpetual needs to reexamine and reassess. It is with this longer view in mind that we present this documentation of the lower- and upper-plate rocks within the Catalina detachment zone.

The continuity of fault-rock stratigraphy of the Catalina-Rincon metamorphic core complex offers unique insights into the ways in which various fault rocks develop in relation to one another. As in all metamorphic core complexes, the map expressions of fault-rock units and fabrics in the Rincon Mountains are laid out in what amounts to a down-plunge view in the direction of tectonic transport. However, the Rincon Mountains domain of the Catalina-Rincon metamorphic core complex is unusual in the quality and, especially, the continuity of exposure of subdetachment cataclastic and protocataclastic rocks. Why is this important? The cataclastic and protocataclastic fault-rock regimes, sandwiched between the Catalina detachment fault and the uppermost lower-plate core complex mylonites, are a record of kinematic, temporal, and rheological linkage. They reflect transitions in deformation mechanisms: from crystal-plastic deformation of mylonites to fluid-enhanced embrittlement of protocataclastic rocks, to multicycle seismogenic development of cataclasites, to elastic-frictional slip on detachment faults, and to brecciation and pulverization and formation of noncohesive breccias and gouge above the seismogenic zone. Our research products include a complete spatial mapping of cataclastic and protocataclastic rocks that reside between upper-plate rocks and lower-plate mylonites. This detailed mapping is, perhaps, to be expected, but in truth, it is rather special. Though there are important exceptions, such as the Whipple Mountains (G.A. Davis et al., 1980, 1986), South Mountain (Reynolds, 1985), and the Clara Peak area (Singleton, 2013b), the array of published geologic maps of Cordilleran metamorphic core complexes does not typically distinguish the protocataclastic rocks at all, for they are too thin and discontinuous to render. Where mapped, the distributions are typically spotty because these fault rocks are not well exposed or continuously exposed along strike. Thus, core complex maps typically show detachment faults (and overlying upper-plate rocks) in direct contact with underlying mylonite(s), absent the fault-rock unit(s) that are a potential source for leveraging insight regarding the evolution of crustal-scale fault networks, namely, ultracataclasites, cataclasites, and protocataclasites.

ORGANIZATION

Our approach to documenting the geometry and character of the Catalina detachment zone and interpreting its significance

builds upon the observations and interpretations emerging from more than four decades of geologic mapping and detailed structural analysis in the Catalina-Rincon metamorphic core complex. Substantive new structural geologic mapping was added in this investigation, along with a new multispectral remote-sensing analysis of the Catalina detachment zone. Fundamental geologic features and relationships observed at the surface were placed into a model that integrates this surface geology with subsurface relationships in the adjacent Tucson Basin. Moreover, multimethod geochronology and thermochronology were used to constrain the timing and rates of progressive stages of structural evolution, encompassing mylonitization, cataclasis, slip, and exhumation.

We describe here the organizational flow of this GSA Memoir, so that its progression becomes evident and readers can more readily identify parts of particular interest. This starts by introducing the broad-scale geologic features of the region as seen at the surface and in the subsurface. Chapter 2, "Catalina Detachment Zone in Geologic Context," introduces the detailed fault-rock stratigraphy of the Catalina detachment zone and describes this zone in relation to the overall geologic map and multispectral expression of the Rincon Mountains, with ties to the subsurface and overall extended three-dimensional (3-D) geometry.

We then present geological and structural relations in greater detail. Chapter 3, "Expression of the Catalina Detachment Zone in Five Key Subareas," presents descriptions of the detachment zone geology where most fully and best exposed along the margin of the Rincon Mountains. An overview of the detachment zone positioning and properties in each of these subareas is presented, supported by some panoramic photographs that help to capture the expression of the Catalina detachment zone in the landscape. Most data bearing on the structural geology, geochronology, and thermochronology in this GSA Memoir were drawn from these subareas.

This is followed by a shift from subarea geology to the structural details of each of the components of the Catalina detachment zone. In particular, Chapters 4–6 explore, from top to base (i.e., from most brittle to most ductile), the physical, geometric, and kinematic properties of fault rocks and associated structures and fabrics within each element of the Catalina detachment zone. These include "Catalina Detachment Fault and Subjacent Cataclasite" (Chapter 4), "Chloritic Protocataclasite and Minidetachment Faults" (Chapter 5), and "Subdetachment Faults, Ultramylonite, Calc-Tectonite, and Mylonite" (Chapter 6).

After this presentation of collected evidence, we consider the entire evolution of the Catalina detachment zone and the Catalina-Rincon metamorphic core complex. Chapter 7, "Progressive Structural Evolution of the Catalina Detachment Zone," draws upon the substance of Chapters 4–6 and builds an interpretation regarding how and why, during lower-plate ascent through the brittle-ductile transition, mylonitization gave way to protocataclasis, subdetachment faulting, minidetachment faulting, and finally to ultracataclasis and detachment-fault slip. Chapter 8, "Geochronology- and Thermochronology-Based Temporal Framework," presents new geochronology and thermochronology analyses that permit the progressive-evolution model to be embedded into a temporal context. This timing is then compared with temporal constraints extracted from the Oligocene–Miocene sedimentary-basin record.

Chapter 9, "Discussion," places timing of the evolution of the Catalina-Rincon Mountains metamorphic core complex in the comparative context of the southwest North America belt. This final chapter also addresses tectonic heritage, especially Laramide heritage, exploring the degree to which the progressive evolution was influenced by, or can be confused with, earlier tectonic structures and fabrics. We end with 3-D models that capture the geometric and structural essence of the Catalina detachment zone. Following Chapter 9 is "Conclusions," a set of reflections on the overall results.

The inclusion of Supplemental Material[2] leads with Appendix A, and within it, Figure A-1 identifies the locations of rock samples referenced in this contribution, including the approximate depth of each rock sample beneath the Catalina detachment fault. Table A-1 lists the samples, rock types, coordinates, and application(s) in this study. The Supplemental Material concludes with a postscript, which adds context to the initiation and execution of this research.

SUMMARY

This paper is about understanding extensional fault-zone behavior, with special emphasis on the structural, kinematic, and mechanical evolution and timing of strain localization on detachment fault systems. The means is through analysis of the Catalina detachment zone, a progressive-deformation product of crustal-scale shearing manifest in the Catalina-Rincon metamorphic core complex. Regional and local geological context is followed by detailed descriptive and kinematic analysis of the several fault-rock components of the Catalina detachment zone. A structural-evolution model is presented with temporal elements of the model constrained from new geochronology and thermochronology analyses and from structure-stratigraphic relations in the Tucson Basin. Discussion and conclusions consider 3-D modeling and attention to tectonic heritage. Figures, especially maps and photographs, are intended, in part, to convey and support opportunities for future work by others. The Rincon Mountains offer superb accessibility to illuminate structures and fault-rock fabrics and continue to be a natural laboratory for refining understanding of progressive deformation accomplished through ductile to brittle evolution.

[2]Supplemental Material. (A) Rock samples referenced in volume, (B) Multispectral analysis workflow, (C) Zircon U-Pb geochronology, (D) $^{40}Ar/^{39}Ar$ geochronology methods, (E) ^{40}K-^{40}Ar dating of fault gouge, (F) Zircon and apatite U-Th-(Sm)/He thermochronology, and (G) Apatite U-Pb and fission-track thermochronology. Please visit https://doi.org/10.1130/MWR.S.23264675 to access the supplemental material, and contact editing@geosociety.org with any questions.

CHAPTER 2

Catalina detachment zone in geologic context

INTRODUCTION

This chapter presents the general fault-rock and structural stratigraphy of the Catalina detachment zone. Following an overview of the components of the Catalina detachment zone, the geology of the Rincon Mountains is presented. We include subsurface relations in the Tucson Basin as essential features for geologic context. Additionally, multispectral analysis proved to be a perfect complement to geologic mapping in tracing the expression of the Catalina detachment fault, chloritic protocataclasite, and the subdetachment fault zone along the lower margin of the entire mountain range.

DETACHMENT ZONE

Detachment faults, which are a showpiece of Cordilleran metamorphic core complexes, were originally described as "décollement" (Misch, 1960; Davis and Coney, 1979), "denudational faults" (Armstrong, 1972), and "dislocation surfaces" (Rehrig and Reynolds, 1980). Davis et al. (1980) introduced "detachment fault" into the core complex lexicon. This proved to be a prescient choice because, in the Southwest North America core-complex belt (Fig. 1-4), it differentiates Oligocene–Miocene extensional deformation from late Mesozoic to early Cenozoic thrust-related deformation. Nearly from the time of discovery, it was clear that such detachment faults are almost always associated with subjacent, voluminous fault-zone damage in the form of "chlorite breccia" (Crittenden et al., 1980). Chlorite breccia is labeled "chloritic protocataclasite" in Figure 1-2, because this is the rock name we apply to this type of rock in this work (see "Note on Chloritic Protocataclasite" below). Beneath the chloritic protocataclasite, there reside characteristic L-S crystal-plastic mylonites (Fig. 1-2).

The expression "detachment zone" (distinct from "detachment fault") is introduced here to describe the fault-rock stratigraphy and structures within the ductile-brittle shear zone that marks the margin of the Catalina-Rincon metamorphic core complex (Fig. 2-1). Excellent exposures of the Catalina detachment zone are available to be studied and mapped along the margin of the Rincon Mountains, where the trace length of the Catalina detachment fault is ~50 km. The Catalina detachment zone consists of five integral, stacked components: (1) the detachment fault surface proper, including (at the base of the upper plate) loci of noncohesive gouge and/or breccia smeared or plated onto its upper surface; (2) very fine-grained cohesive cataclasite and ultracataclasite; (3) chloritic protocataclasite; (4) subdetachment faults (or fault zones) positioned at or near the base of chloritic protocataclasite; and (5) crystal-plastic mylonites as well as lesser ultramylonite and calc-silicate tectonites. The fabrics and structures of these components resulted from rheological behavior that ranged from elastic-frictional (detachment surface) to quasi-plastic (mylonites) (Sibson, 1977). The microfabric images accompanying Figure 2-1 are intended to underscore contrasts between microstructures and damage in the various "tiers" of the Catalina detachment zone.

NOTE ON CHLORITIC PROTOCATACLASITE

The presence of "chlorite breccia" was integral to the recognition of Cordilleran metamorphic core complexes (Davis and Coney, 1979; Crittenden et al., 1978, 1980; Coney, 1980a, 1980b; G.A. Davis et al., 1980; Rehrig and Reynolds, 1980; Reynolds and Rehrig, 1980). From a practical standpoint during early geologic mapping, outcrops of "chlorite breccia" helped geologists grasp structural positioning even in subareas where a detachment fault surface proper was not exposed. Most "chlorite breccias" are cataclastically overprinted mylonites, although more rarely, the overprinted rock can be nonmylonitic granitoids, such as in places in the Pinaleño Mountains metamorphic core complex (Davis and Hardy, 1981) and South Mountains metamorphic core complex (Reynolds, 1985).

"Chlorite breccia" in the Rincon Mountains domain of the Catalina-Rincon metamorphic core complex, and likely in most such complexes, is not a true breccia. Breccia and cohesive-breccia classifications emphasize percentages of "visible discrete fragments" entrained in fine-grained matrix material (e.g., Robertson, 1999; Woodcock and Mort, 2008). The "chlorite breccia" observed in this and likely other metamorphic core complexes does not meet this definition. Although comminution fabrics produced by cataclastic processes during faulting and shearing are evident in outcrops and thin sections of "chlorite breccia," the overprint is not nearly complete. The most appropriate fault-rock term is "protocataclasite," i.e., a cohesive cataclastic rock distinguished by 10%–50% matrix. We thus substitute "chloritic protocataclasite" for "chlorite breccia" throughout this manuscript. "CPC" is a preferred abbreviation for this mouthful. Two other workers in the Rincon Mountains previously substituted alternative language for "chlorite

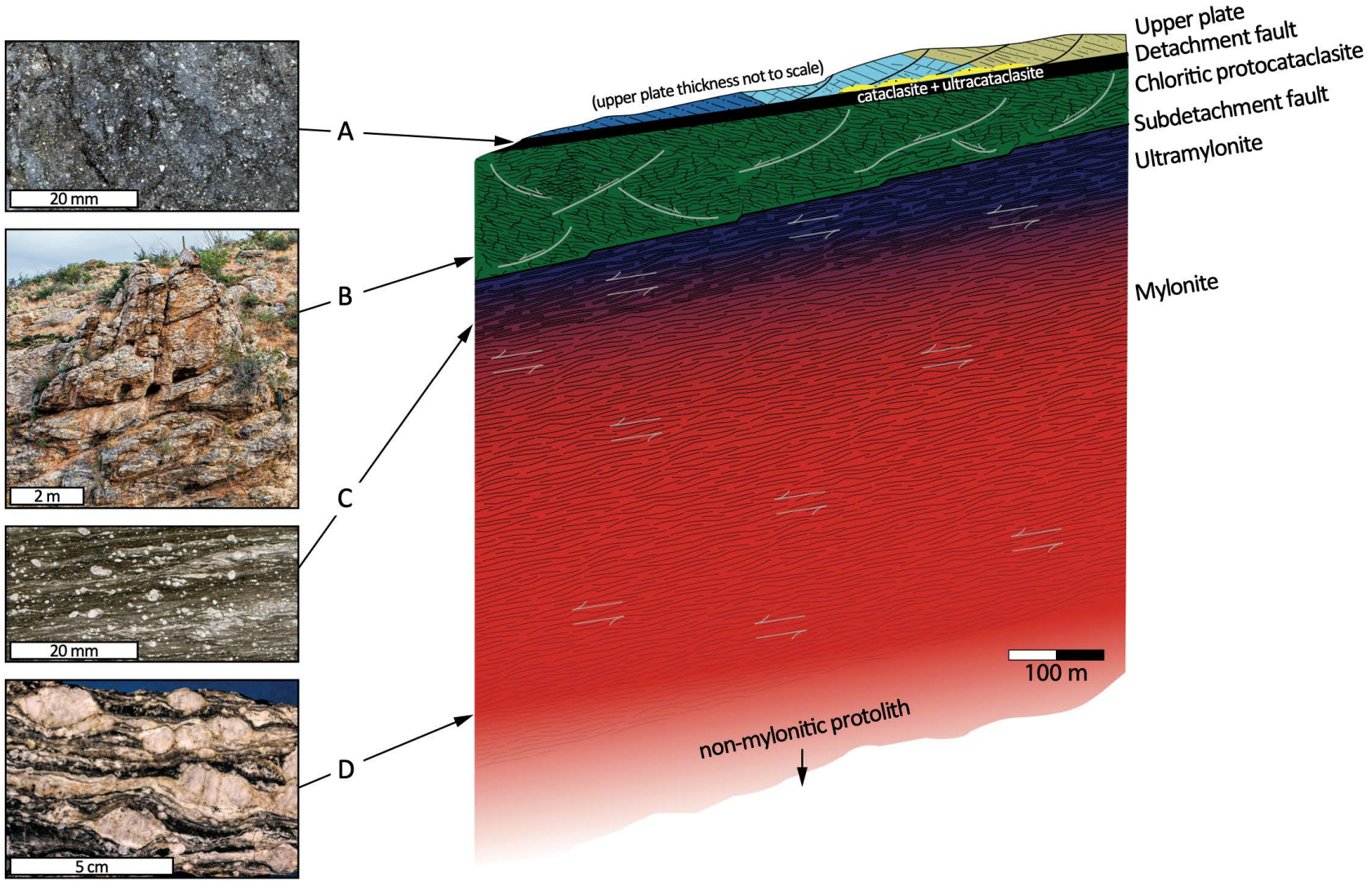


Figure 2-1. Schematic portrayal of the Catalina detachment zone. Upper-plate strata are shown tilted against the Catalina fault. Top of the Catalina detachment zone is the detachment fault surface. Beneath the Catalina detachment zone, there is a thin (up to 7 m) fault-rock unit of cataclasite and ultracataclasite. This ultrafine-grained rock is formed at the expense of underlying CPC, the protolith of which mylonite. A subdetachment fault or fault zone separates CPC from underlying ultramylonite and mylonite. In some metamorphic core complexes, the transition between mylonite and subjacent protolith is exposed but not in the Rincon Mountains. On the left margin, from top to bottom: (A) photomicrograph of ultracataclasite; (B) outcrop photo of CPC showing shallowly dipping minidetachment faults; (C) photomicrograph of ultramylonite derived from Paleocene–Eocene Wilderness Suite Granites; and (D) photomicrograph of mylonite derived from Mesoproterozoic Oracle Granite protolith.

breccia," applying the same basic arguments used here. DiTullio (1983) mapped "chlorite breccia" as "brecciated gneiss," and Force (2002) mapped it as "semi-breccia."

The combination of cataclasis, fracturing, faulting, and shattering in an environment of abundant hydrothermal fluids imparted pervasive chlorite-epidote retrograde alteration. Structural geologic mapping, e.g., by Davis (1987b) and by Lister and Davis (1989), revealed that the contact between CPC and underlying mylonites is generally quite sharp, recognizable in some locales as discrete faults. Davis (1987b, 2013) named these "subdetachment faults." Lister and Davis (1989) emphasized some of these features as products of incisement.

FAULT-ROCK STRATIGRAPHY

The Catalina detachment fault proper (Fig. 2-1) is typically smooth but rarely polished and is normally devoid of slickenlines. The fault surface is commonly rusted in appearance due to Fe- and Mn-oxide coatings on the detachment surface. Gouge formed at the expense of upper-plate rocks immediately above the detachment surface (Fig. 2-1), though exposures of gouge are rare because of its vulnerability to erosion and concealment.

The uppermost lower-plate rock is marked by a discrete resistant ledge of cataclasite, typically 4 m thick or less (Fig. 2-1). Unlike gouge, the cataclasite is a hard, cohesive fault rock. Medium to dark gray, the cataclasite displays a random fabric composed of very small (less than 5 mm) fragments of cataclastically overprinted mylonite set in an extremely fine-grained matrix. During the period in which Cordilleran metamorphic core complexes were being discovered and described, the term "microbreccia" (following Sibson, 1977) was applied to this distinctive ledge of cataclasite. However, "microbreccia" has fallen out of favor in fault-rock classifications.

Locations where the discrete ledge of cataclasite is absent are rare, and in its place is a hard, dense, aphanitic black ultracataclasite (Fig. 2-1), which locally weathers to beige. The black obsidian-like matrix, which dominates the ultracataclasite, carries very tiny but visible cataclasite fragments and white frosted streaks of what appear to be ghosts of cataclasite that survived complete obliteration. Moreover, there are very thin (up to 3 mm) black seams (micro–shear zones) that are integral to the fabric of this rock. Individual seams can be traced no farther than one or two meters.

CPC underlies the cataclasite and ultracataclasite (Fig. 2-1). The contact between the cataclasite/ultracataclasite and CPC is quite sharp but typically presents no expression of a discrete fault or fracture zone. Like the cataclasite and ultracataclasite, CPC is inherently a cohesive fault rock. However, it is much less resistant to overall weathering and erosion than cataclasite and ultracataclasite because it is splintered by very closely spaced fracture surfaces (spacing less than 10 cm), and it is marked by extensive alteration. The alteration is profound, producing its namesake chlorite, but also epidote, titanite, calcite, and iron- and manganese oxides.

The base of the CPC is a discrete subdetachment fault (or fault zone) that tends to be subparallel to the Catalina detachment fault surface (Fig. 2-1). In places, there is clear physical expression of the subdetachment fault, recognizable as a Fe- and Mn-stained planar surface that is marked by abundant, closely spaced joints and microfaults. Almost always, the subdetachment fault zone coincides closely with the immediately underlying subparallel layers of ultramylonite or, more rarely, lenticular pods and lenses of calc-tectonite. Mylonite then crops out beneath the subdetachment fault or fault zone. Deeper yet, country rock is untouched by core complex–related mylonitization (Fig. 2-1).

OVERALL GEOLOGY OF THE RINCON MOUNTAINS

Introduction

Geologic maps cover the overall geology of the Rincon Mountains, thanks to work conducted by the U.S. Geological Survey (e.g., Drewes, 1974, 1977), the Arizona Geological Survey (e.g., Spencer et al., 2001, 2018a; Richard et al., 2005), and Dickinson's (1991, 1992) 1:125,000 map of the Catalina-Rincon metamorphic core complex. Dickinson's geologic map (1992) (Fig. 2-2) was based on a compilation of more than 80 geologic maps prepared by more than 60 previous workers, and on new mapping he himself carried out. Figure 2-2 includes a delineation of subareas with complete exposures of the Catalina detachment zone. These are Saguaro Loop, Loma Alta, X9 Ranch, Posta Quemada–Hidden Spring, and Martinez-Salcido Ranch, which are each explored in more detail in Chapter 3.

Below the Primary Detachment Zone: Lower-Plate Geology

The form of the Rincon Mountains is controlled by the sinuous trace of the Catalina detachment fault (Fig. 2-2; also Fig. 1-1). Within the lower plate, and thus beneath the Catalina detachment fault, Dickinson (1991, 1992) distinguished two dominant mylonitic granitoid suites. The contacts between these two mylonitic suites coincide exactly with contacts between two granitoid bodies mapped by Drewes (1974, 1977). Drewes named one of these "Continental Granodiorite," a Mesoproterozoic (ca. 1.4 Ga) quartz monzonite well known regionally as the Oracle Granite or Ruin Granite. Drewes (1977) recognized that the feldspar augen in this rock were porphyroclasts representing the remains of the very large feldspar phenocrysts (up to 8 cm) that distinguish the Oracle and Ruin Granites. Davis (1987a, 1987b) reported the conclusion drawn by a number of workers that, indeed, this mylonite, with characteristically large porphyroclasts, is derived from Oracle granite. Dickinson (1991, 1992), in his map explanation, names it "mylonitic Oracle granite suite" (Fig. 2-2). In addition, Drewes (1977) mapped the other major granitoid rock unit as "Wrong Mountain Quartz Monzonite," a two-mica, garnet-bearing, medium-grained granitoid that he interpreted to be Mesoproterozoic in age as well. However, this mylonite is derived from Cenozoic granitoids, and the basis for this is described by Davis (1987a, 1987b). Accordingly, it is

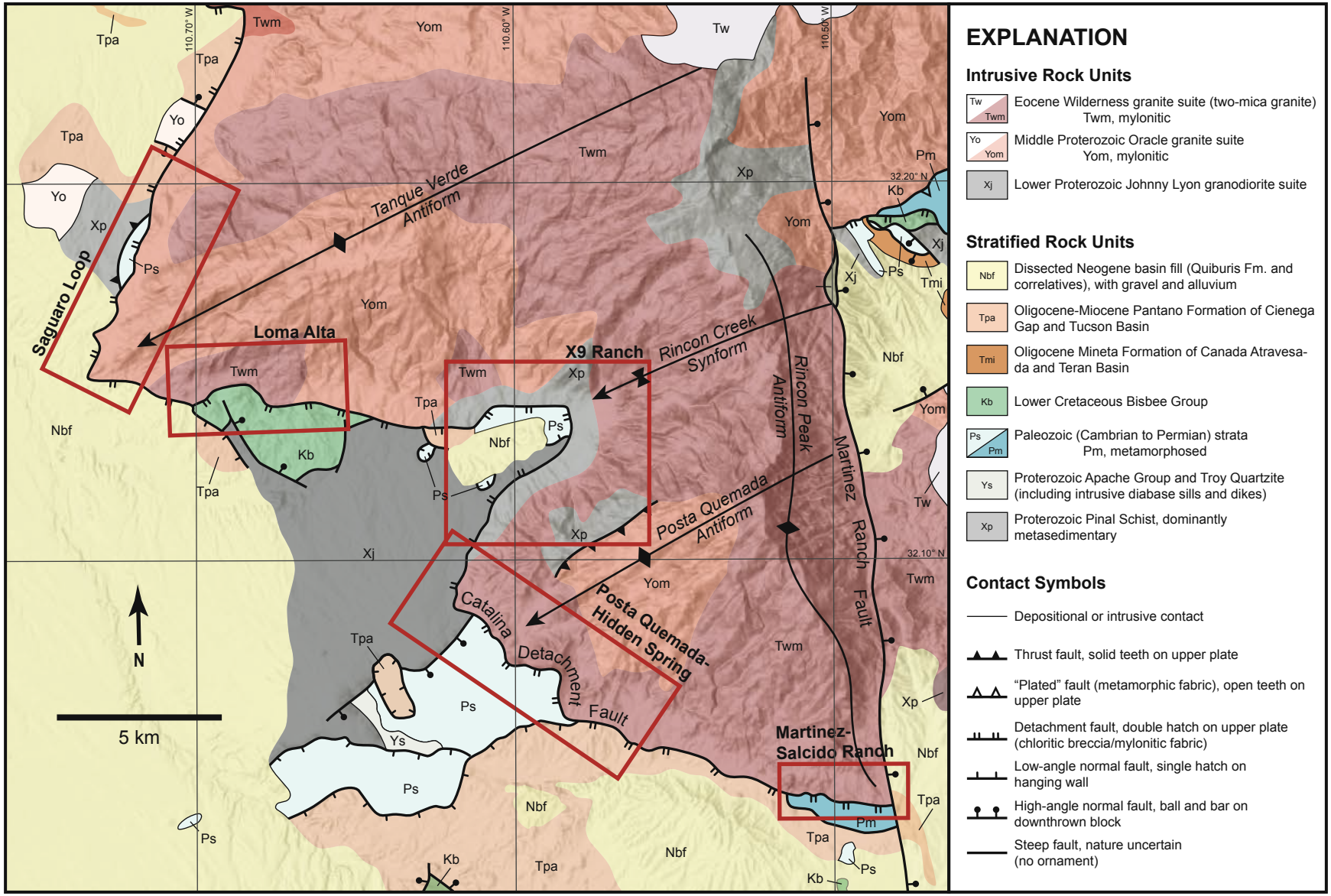


Figure 2-2. Geologic map of the Rincon Mountains, as adapted from Dickinson (1991, 1992, scale 1:125,000). Drewes' (1974, 1977) geologic maps provided the contacts for granitoid assemblages in the lower plate, and for Paleozoic and Mesozoic formations within the Paleozoic and Mesozoic cover. In this contribution, the Johnny Lyon Granodiorite Suite (Xj) is referred to as Rincon Valley Granodiorite. Yom and Twm are commonly referred to in this text as O-mylonite and W-mylonite, respectively (see text for explanation). Subareas are Saguaro Loop (SL), Loma Alta (LA), X9 Ranch (X9), Posta Quemada–Hidden Spring (PQ-HS), and Martinez-Salcido Ranch (MSR).

this rock body that Dickinson (1991, 1992) refers to on his map as "mylonitic Eocene Wilderness granite suite" (Fig. 2-2). In his interpretation, Drewes (1977) regarded these granitoid rocks as the autochthon of a regional thrust fault, one expression of which he considered to be the Catalina fault. Dickinson's (1992) map compilation, however, presents the Catalina fault as a detachment fault (Fig. 2-2), in accord with previous work following the discovery of metamorphic core complexes.

For shorthand in field work and conversation, we refer to O-mylonite as mylonite derived from Oracle-suite granites and W-mylonite as derived from Wilderness-suite granites (Davis, 2013). Mapped regions of O-mylonite commonly include abundant, largely concordant, thin bodies of W-mylonite and associated leucogranite. Similarly, mapped regions dominated by W-mylonite contain outcrop areas of O-mylonite. As commented upon by Force (2002), who mapped these rocks in the Agua Caliente area in the nexus between the Catalina and Rincon Mountains, this reality presents difficult practical challenges in the course of geologic mapping.

Mylonitic foliation orientations in the Rincon Mountains, and the form of the Catalina detachment fault itself, define the hinges and limbs of mountain-scale antiformal arches and synformal troughs (Fig. 2-2). The ~065°/245° trends of these structures coincide with the direction of penetrative lineation in O- and W-mylonites throughout the Catalina-Rincon metamorphic core complex, and also with the tectonic transport direction for ductile/brittle shearing (top-to-~240°) (Davis, 1980a, 1987a, 1987b; Spencer et al., 2019). The mountain-scale antiforms and synforms are Tanque Verde antiform, Rincon Creek synform, and Posta Quemada antiform (Fig. 2-2). These structures trend ~245° and plunge ~10–15°SW. The Saguaro Loop subarea occupies the lower part of the northwestern limb of Tanque Verde antiform, whereas the Loma Alta subarea lies near the base of its southeastern limb (Fig. 2-2). The X9 Ranch subarea lies within the tight, pinched Rincon Creek synform (Fig. 2-2). The Posta Quemada–Hidden Spring subarea lies on the plunging nose of Posta Quemada antiform, and to the east of it, at the southeast corner of the Rincon Mountains, there is the Martinez-Salcido Ranch subarea (Fig. 2-2), which contains the southern part of the N-S–trending Rincon Peak antiform, a post–core complex fault-bend fold produced during superimposed Basin and Range faulting (Davis et al., 2011) (Fig. 2-2).

Though for the most part not represented in Dickinson's (1992) geologic map, Drewes mapped a third unit—Proterozoic Pinal Schist—in the lower plate. It is largely restricted to the contact zones between O-mylonite and W-mylonite. It also, in places, occurs along the sole of the Catalina detachment fault (Fig. 2-2). Dickinson's (1992) geologic map only shows Pinal Schist at three locations within the lower-plate exposures of the Rincon Mountains. The rock type mapped as Pinal Schist by Drewes or by Dickinson (1992) has, for the most part, been reinterpreted as ultramylonite (Davis, 1987b). As shown on Dickinson's (1992) geologic map, one large synformal swath of this ultramylonite crops out directly beneath the Catalina detachment fault in the Rincon Creek synform (Fig. 2-2). To the southeast of this site, a second outcrop area of mapped Pinal Schist occupies part of the contact between O- and W-mylonite. The third mapped swath of this ultramylonite is in the summit area of the Rincon Mountains, where Pinal Schist marks the contact zone between O- and W-mylonite (Fig. 2-2).

As will become evident, our large-scale geologic mapping included certain rock formations that Drewes (1977) mapped but that were not incorporated in Dickinson's (1992) compilation. These include swaths of "Pinal Schist" on both limbs of Tanque Verde antiform as well as alignments of meters-scale pods and lenses of carbonate and calc-silicate rocks that are locally preserved within the lower-plate rocks in the X9 Ranch and Posta Quemada–Hidden Spring subareas (Drewes, 1977; Spencer et al., 2001; Richard et al., 2005).

Upper-Plate Geology

Upper-plate rocks residing above the Catalina detachment fault are nonmylonitic and noncataclastic, and they represent fault-bounded samplings of different parts of the southeastern Arizona geologic column. The largest contiguous upper-plate formation, as shown on Dickinson's (1991, 1992) geologic map, is the Johnny Lyon granodiorite suite (Fig. 2-2). Drewes (1977) mapped it as Rincon Valley Granodiorite, and here it is referred to as such. It extends from the southeast margin of the Loma Alta subarea to the western margin of the Posta Quemada–Hidden Spring subarea, including the area marking the southwest projection of Rincon Creek synform (Fig. 2-2). The largest contiguous upper-plate outcrop area of Paleozoic strata is southwest of the margin of the Posta Quemada–Hidden Spring subarea, i.e., along the southwestward projection of Posta Quemada antiform (Fig. 2-2). A large outcrop area of Cretaceous strata lies above the detachment fault at the southern margin of the Loma Alta subarea. In the region between the Posta Quemada–Hidden Spring and Martinez-Salcido Ranch subareas, there are expanses of Oligocene–Miocene upper-plate strata. The upper-plate rocks are dominantly Paleozoic strata in the Martinez-Salcido Ranch subarea proper. Finally, above the detachment fault along the northwest margin of the Tanque Verde antiform, the upper-plate rocks, though not extensively exposed, include (true) Pinal Schist and Rincon Valley Granodiorite (both Precambrian), Paleozoic strata, and Mesozoic strata.

The upper-plate rocks in the Rincon Mountains domain of the Catalina-Rincon metamorphic core complex were transported to their present sites from a location ~35 km northeast of their present location(s) (Krantz, 1983; Dickinson, 1992; Spencer et al., 2019), though Spencer et al. (2022) interpret the distance of transport to be as great as 60 km. Sense and direction of transport were ~240°. The brittle damage associated with this magnitude of tectonic transport is particularly dramatically displayed in the Precambrian Rincon Valley Granodiorite (Fig. 2-3A). Everywhere it crops out, this granodiorite is shattered by very closely spaced fractures. One can picture a progressive overprinting of fracturing of the granite during

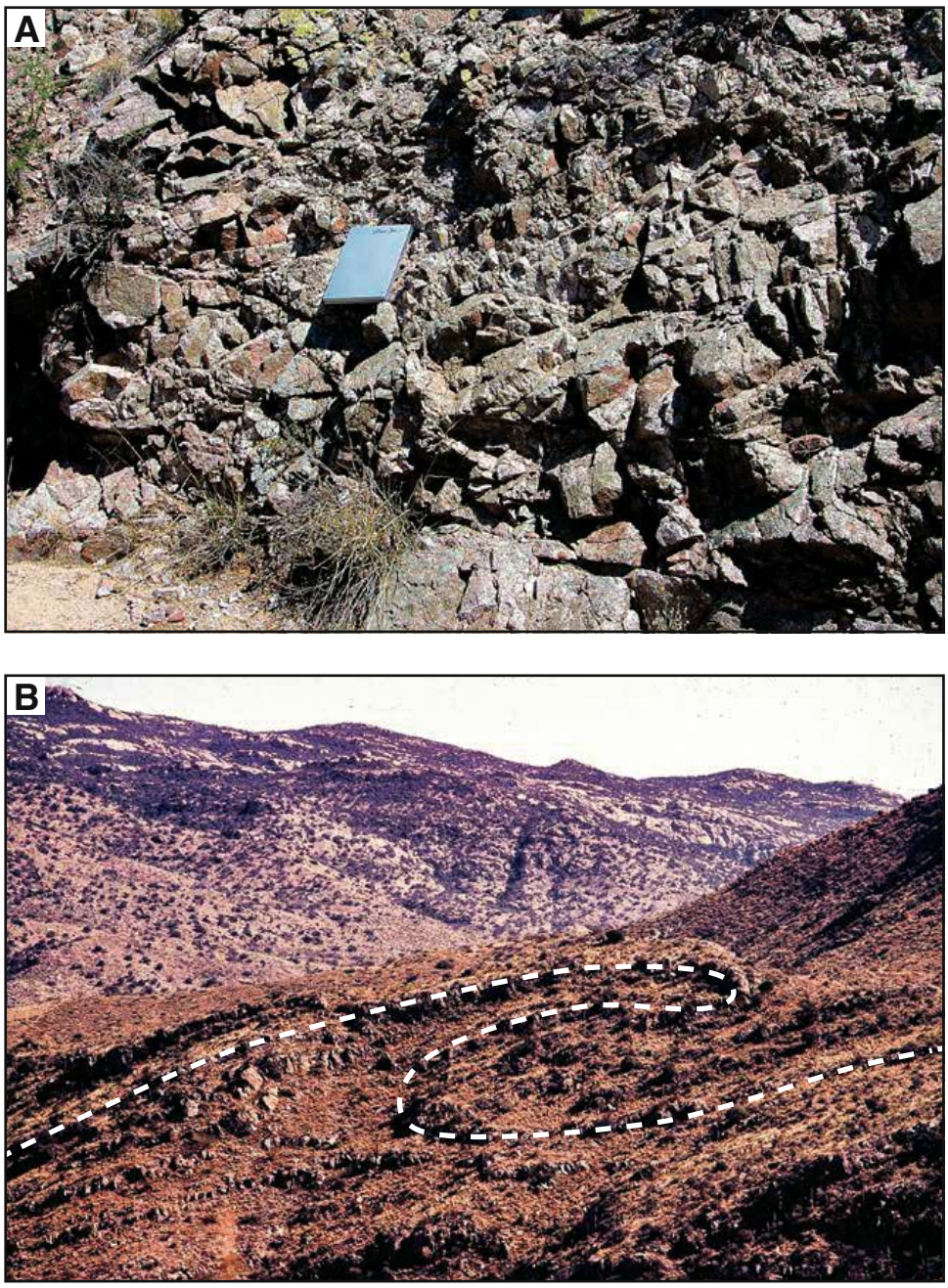


Figure 2-3. (A) Rincon Valley Granodiorite occupies the upper plate, and everywhere it is shattered by closely spaced fractures. Aluminum clipboard (34 cm × 23 cm) for scale. (B) Isoclinal recumbent fold, outlined in dashed white line, within upper-plate Pennsylvanian–Permian strata in the Posta Quemada–Hidden Spring subarea. View is to NE. Foreground width is ~200 m. Gently dipping mylonitic layering is expressed in landscape in background. Catalina detachment fault crops out beneath the stack of recumbent folds.

its translation along the Catalina detachment-fault deformation path. Its source outcrop region is in the eastern Rincon Mountains, where it was mapped as Johnny Lyon Granodiorite.

In contrast to the intensive fracturing of the Rincon Valley Granodiorite, the conspicuous structures in Paleozoic and Cretaceous upper-plate strata include abundant overturned to recumbent folds (Davis et al., 1974; Davis, 1975) (Fig. 2-3B). Davis (1975) originally interpreted these folds as products of "mid-Tertiary gravity-induced folding," and then later recanting the "gravitational origin" (Davis, 1987a) when he interpreted the folding as produced, at least in part, during top-to-the-SW shearing of the upper plate during tectonic transport. His reinterpretation emphasized overall SW vergence based on the orientations of poles (550) to fold axial surfaces falling directly on the 240° tectonic-transport direction. It thus seems more likely that the conspicuous folds in upper-plate Paleozoic and Cretaceous strata of the Rincon Mountains domain of the Catalina-Rincon metamorphic core complex were formed during Late Cretaceous to Early Paleogene time (Laramide deformation), and then transported, largely passively, as upper-plate

"passengers" during Oligocene–Miocene core complex shearing and detachment faulting. Laramide folding is well documented in southeastern Arizona (e.g., Hayes and Raup, 1968; Davis, 1979; Favorito and Seedorff, 2017). During this shearing and detachment faulting, originally Laramide fold shapes and orientations may have been modified into their largely SW-vergent, overturned to recumbent forms.

Of all the fault-bounded slices of upper-plate rock, the Oligocene–Miocene sedimentary strata were the most illuminating to the discovery of metamorphic core complexes and interpreting post-Laramide normal slip on detachment faults. Most of these strata are syntectonic layers that are tilted in a wide range of low- to steeply dipping inclinations. The tilted Oligocene–Miocene strata display a preferred strike of NNW (Dickinson, 1991, 1992), i.e., orthogonal to the SW tectonic-transport direction of upper-plate rocks. Of the 47 bedding-attitude measurements in panels of Oligocene–Miocene strata posted by Dickinson (1992), 28 dip NE and 19 dip SW, reflecting the kinematics of both synthetic and antithetic normal faulting.

MULTISPECTRAL EXPRESSION OF CATALINA DETACHMENT ZONE

It is revealing to compare Dickinson's (1992) mapping product with the expression of the landscape and rockscape captured in a multispectral remote-sensing analysis carried out during this research. The approach employed is described in the Supplemental Material, Appendix B: Multispectral Analysis Workflow. The false-color multispectral visualization product (Fig. 2-4) is a revealing image that complements Dickinson's (1992) geologic map (Fig. 2-2). The trace of the Catalina detachment fault is well defined by sharp contrasts in spectral response, especially along the southern margin of the Rincon Mountains, where the detachment fault is nearly continuously exposed for ~36 km from the Loma Alta to the Martinez-Salcido Ranch subareas. The detachment fault stands out because of contrasts in the combination of bedrock texture, rock composition, and landscape morphology on either side of the detachment fault, i.e., upper versus lower plate.

CPC is also revealed in the multispectral image (Fig. 2-4), recognizable as a broad yellow to light brown swath beneath the Catalina detachment fault. This distinction is pronounced in the Posta Quemada–Hidden Spring and X9 Ranch subareas. Eastward from the Posta Quemada–Hidden Spring subarea, the swath of CPC progressively thins toward the Martinez-Salcido Ranch subarea, where it is truncated at its easternmost end by the 350°-striking, steeply E-dipping Martinez Ranch fault.

The multispectral mapping of the lower contact of CPC coincides exactly with the trace of the subdetachment fault system as defined by large-scale structural mapping in each of the strategic subareas, permitting the opportunity to map this boundary beyond the extents of the subareas with confidence (Fig. 2-4). Mylonites throughout the Rincon Mountains display pervasive planar, parallel NNW-striking, high-angle joints and fracture zones oriented perpendicular to the overall stretching direction. The expression of this fracturing is quite profound when seen in Figure 2-5, a low-altitude aerial view of Tanque Verde Ridge, which is an antiform.

The multispectral image highlights the absence of the NNW-trending fracture grain in the mylonitic rocks within the swath of CPC, e.g., as traced westward across the Posta Quemada–Hidden Spring subarea and northward to the X9 Ranch subarea (Figs. 2-2 and 2-4). We conclude from this spectral difference that the pronounced NNW-striking jointing of mylonite was a very late-stage product in the development of the Catalina-Rincon metamorphic core complex. Jointing appears to have postdated the formation of CPC, which may extend and further support the conclusions of other studies of postmylonitization jointing (e.g., Fletcher et al., 1995). The high density of fractures in the CPC appears to have inhibited the propagation of systematic joints across this zone. Note that this fault rock is also spectrally distinct from the underlying mylonites of the lower plate due to its mineralogic alteration; therefore, it is distinguished by its more yellow color in this visualization.

Finally, the expression of W-mylonite in the multispectral image (Fig. 2-4) is quite dramatic given its distinctive bright turquoise hue, which is absent in areas underlain dominantly by O-mylonite (cf. Fig. 2-2 and Fig. 2-4). More importantly, the multispectral image conveys the contact positioning of W- versus O-mylonite quite accurately. This fact is surprising, given that both W- and O-mylonite are dominated by quartzofeldspathic assemblages. This visual color difference suggests compositional differences between the two rock units sufficient to produce a spectral differentiation.

TUCSON BASIN SUBSURFACE RELATIONS

To gain greater 3-D control for interpreting surface geology of the Catalina-Rincon metamorphic core complex, we studied and reassessed available seismic reflection and well data in the Tucson Basin. In particular, we examined the subsurface expression of the Catalina detachment fault, the synkinematic hanging-wall faulting in the subsurface, and the record of growth deposition in the Tucson Basin (Fig. 2-6). A first-order confirmation is provided by the subsurface record, which, like that of the surface geology, reveals that the Catalina detachment fault accommodated slip during late Oligocene–early Miocene time.

Interpretation of Seismic Reflection Profiles

Seismic relations and reflection patterns reveal clear evidence for two principal phases of basin development (Loy, 1990; Houser et al., 2004; Wagner, 2005; Arca, 2009; Arca et al., 2010), and these can be differentiated on the basis of older and younger sets of basin deposits separated by a pair of unconformities: the early Miocene unconformity and the mid-Miocene unconformity (Fig. 2-6). These unconformities are separated by a thin seismic interval marked by parallel reflectors (Figs. 2-6A, 2-6C). The first phase of basin development, which was coeval with

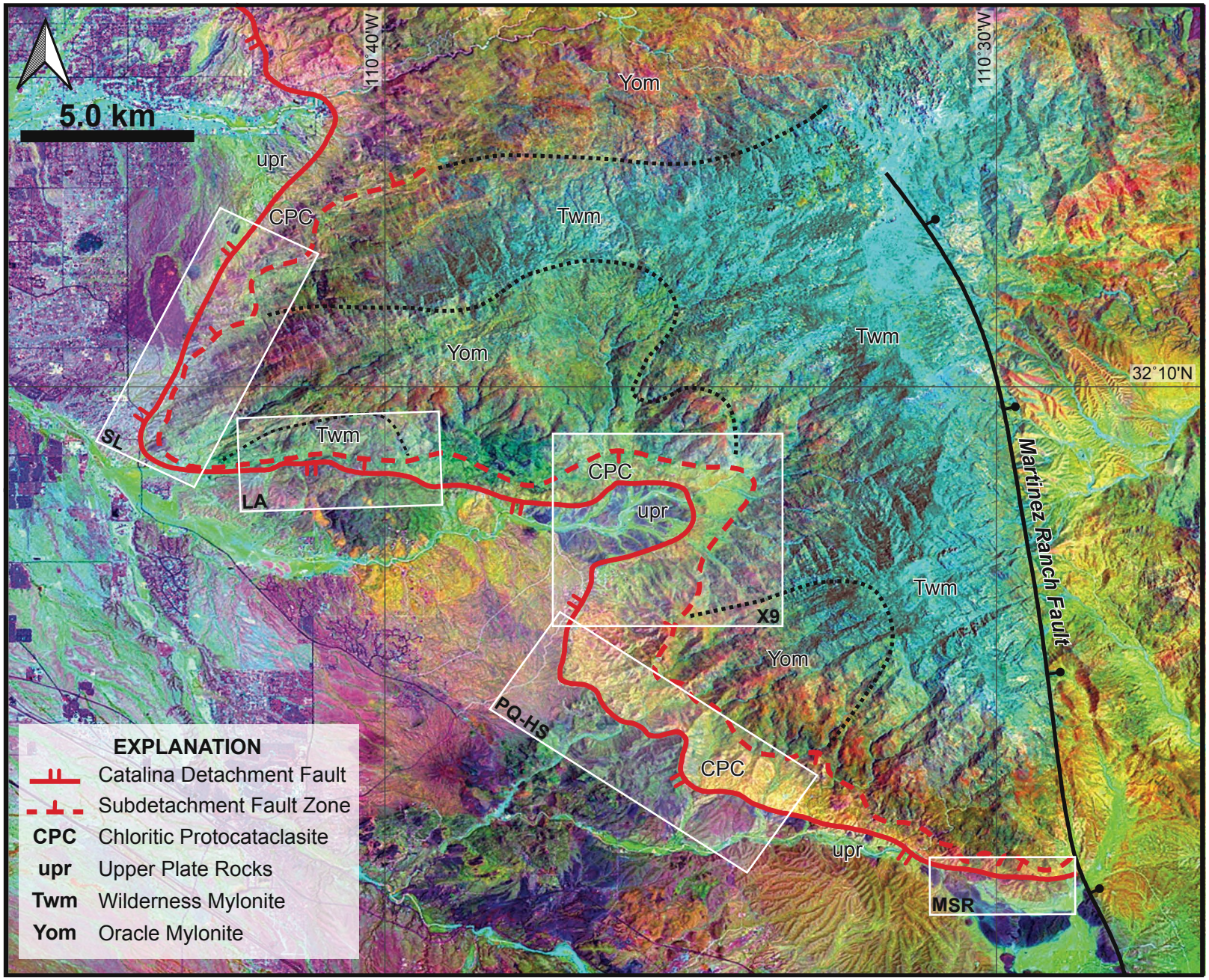

5.0 km
110°40'W
110°30'W
32°10'N
Yom
upr
CPC
Twm
Yom
Twm
Yom
Twm
SL
LA
CPC
upr
X9
Twm
Martinez Ranch Fault
Yom
PQ-HS
CPC
upr
MSR
EXPLANATION
Catalina Detachment Fault
Subdetachment Fault Zone
CPC Chloritic Protocataclasite
upr Upper Plate Rocks
Twm Wilderness Mylonite
Yom Oracle Mylonite

Figure 2-4.

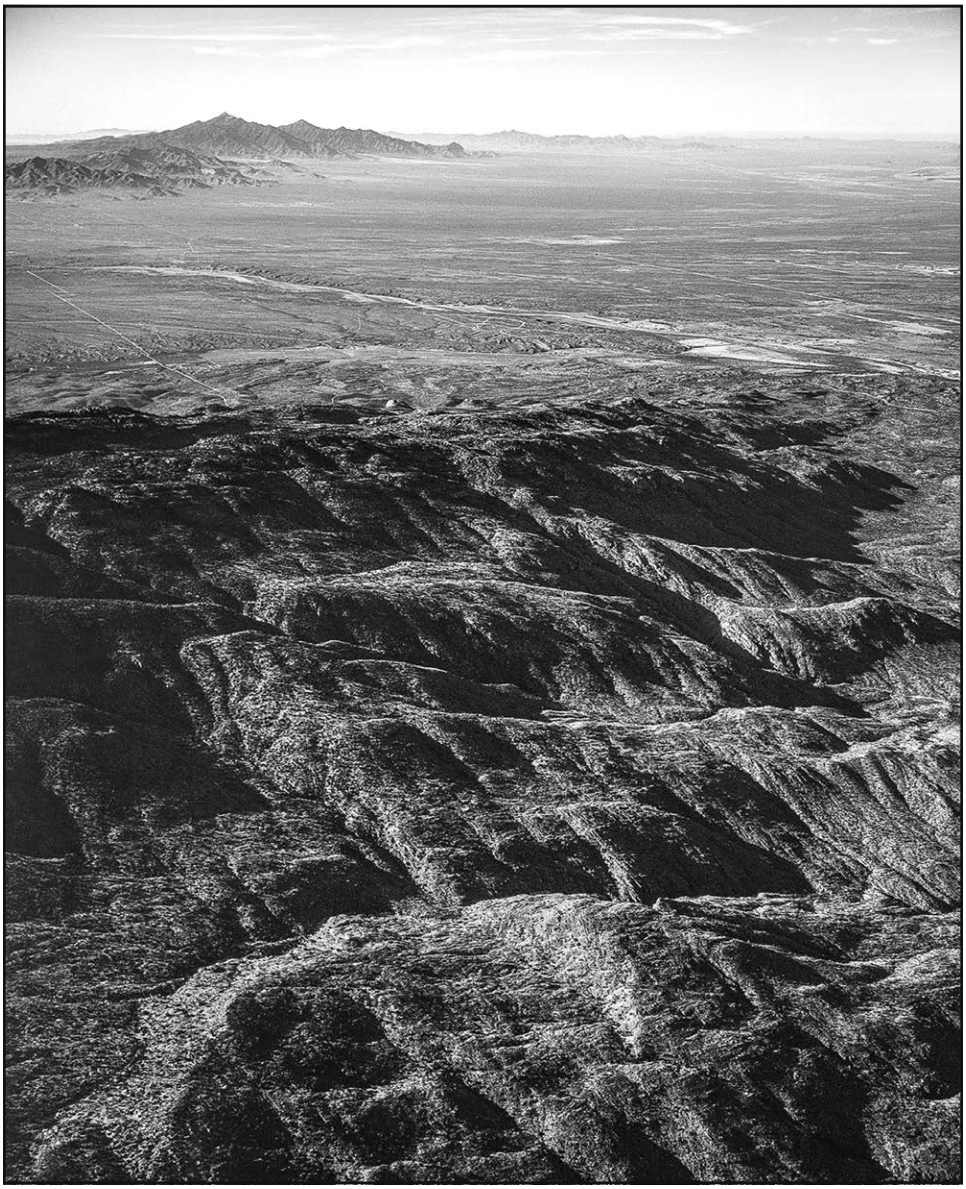


Figure 2-5. South-directed oblique aerial image of Tanque Verde Ridge (antiform) showing the expression of pervasive jointing in mylonites. This near-vertical fracturing strikes NNW, perpendicular to penetrative mineral lineation within the mylonites. Santa Rita Mountains are in background. Highest peak is Mt. Wrightson, ~60 km away. An annotated version of this photograph appeared as figure 2 in Davis (2013). Aerial photograph is by Peter L. Kresan © www.kresanphotography.com.

Figure 2-4. False-color multispectral image of the geology of the Rincon Mountains, produced in this study as a guide to mapping the full extent of the Catalina detachment zone. See text for explanation. Solid red line is trace of the Catalina detachment fault. Dashed red line is the trace of the subdetachment fault/fault zone, which in some locations is a discrete fault, but in others is a branching fault system. Dashed black line is approximate contact trace between O-mylonite (Yom) and W-mylonite (Twm). See Figure 2-2 to compare with mapped geology. Subareas are Saguaro Loop (SL), Loma Alta (LA), X9 Ranch (X9), Posta Quemada–Hidden Spring (PQ-HS), and Martinez-Salcido Ranch (MSR).

the Catalina detachment system, created a localized asymmetric depocenter strongly controlled by WNW-dipping listric normal faults. Discontinuous and diverging reflections are expressions of hanging-wall syntectonic deposits that dip toward the E-SE, consistent with having been deposited during offset on the Catalina detachment zone (Fig. 2-6C). The older, basin-center fault sets do not extend upward through the section above the early Miocene unconformity, indicating that their activity had ceased by that time. After a period of relative tectonic quiescence, the mid-Miocene unconformity defines the base for the overlying

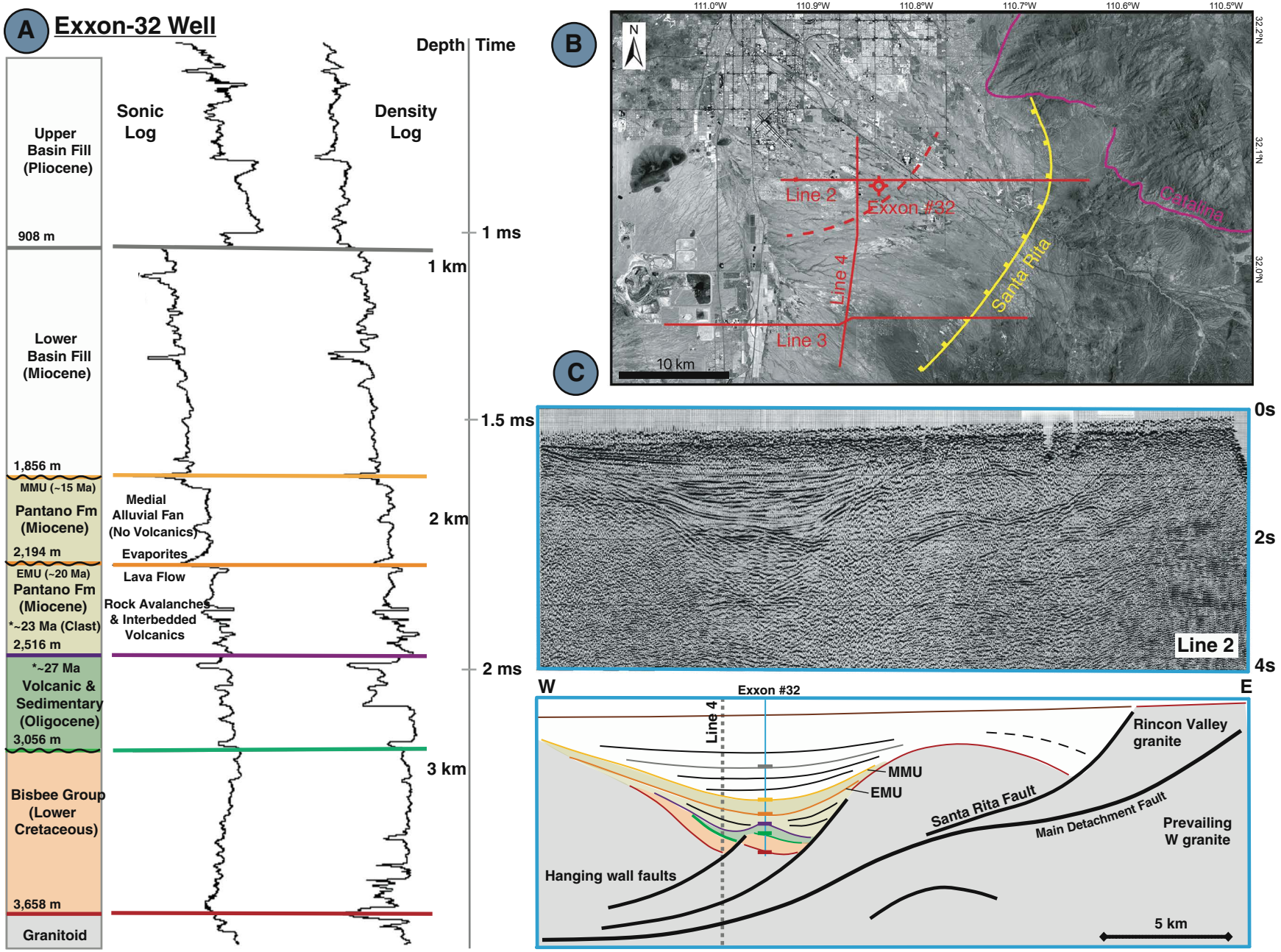

A
Exxon-32 Well
Depth
Time
Sonic Log
Density Log
Upper Basin Fill (Pliocene)
908 m
Lower Basin Fill (Miocene)
1,856 m
MMU (~15 Ma)
Pantano Fm (Miocene)
Medial Alluvial Fan (No Volcanics)
2,194 m
Evaporites
EMU (~20 Ma)
Lava Flow
Pantano Fm (Miocene)
Rock Avalanches & Interbedded Volcanics
*~23 Ma (Clast)
2,516 m
*~27 Ma
Volcanic & Sedimentary (Oligocene)
3,056 m
Bisbee Group (Lower Cretaceous)
3,658 m
Granitoid
1 ms
1 km
1.5 ms
2 km
2 ms
3 km
B
111.0°W
110.9°W
110.8°W
110.7°W
110.6°W
110.5°W
32.2°N
32.1°N
32.0°N
N
Line 2
Exxon #32
Line 4
Line 3
Santa Rita
Catalina
10 km
C
0s
2s
4s
Line 2
W
E
Exxon #32
Line 4
MMU
EMU
Rincon Valley granite
Santa Rita Fault
Main Detachment Fault
Prevailing W granite
Hanging wall faults
5 km

Figure 2-6.

growth section, which records evidence for further extension that progressively broadened the basin extent due to displacement on other faults.

Growth sediments were deposited above the mid-Miocene unconformity (Fig. 2-6A), the geometry of which is broadly consistent with slip and rollover along the W-dipping Santa Rita fault, which helped to accommodate post–mid-Miocene unconformity extension. At the surface, the Santa Rita fault juxtaposes recent alluvial and fluvial deposits against Rincon Valley Granodiorite (Fig. 2-6B). The Santa Rita and older faults, including the Catalina detachment, all converge downward toward a horizontal midcrustal detachment zone (Fig. 2-6C). Nearby basins (e.g., Altar and Safford Basins) also display similar intracrustal control and listric-fault geometries (Arca, 2009; Arca et al., 2010). The faults tip out ~8500 m below the reference datum (~7500 m below sea level), based upon a seismic dimension of 3.5 s two-way traveltime.

Interpretation of Well Control

Exxon well #32 was drilled to a depth of ~3.8 km, thus providing age and facies information within the sedimentary section in the Tucson Basin. This well terminates in crystalline basement (Figs. 2-6A, 2-6B). Houser et al. (2004) arrived at the following observations and interpretations. The deepest unit is nonmylonitic granitoid, located in the hanging wall of the main detachment. Detachment-contemporaneous basin deposits begin above 3056 m, where a first-order unconformity on top of Bisbee Group successions (Late Jurassic–Early Cretaceous) marks the base of Cenozoic deposition. The Cenozoic deposits are composed of alkaline lava flows at the base and andesitic tuffs interbedded with overlying limestone conglomerates. Total thickness is 540 m. The age of these deposits is constrained near its upper boundary by an Ar/Ar dated tuff at 26.9 ± 0.2 Ma. The age at or near the base is likely 29 Ma or older, depending on assumptions regarding regional magmatic constraints (e.g., Favorito and Seedorff, 2021).

Together with the first Cenozoic deposits, the age and character of the Pantano Formation (Figs. 2-6A) are particularly relevant to supporting the timing of activity on the Catalina detachment fault as ca. 29–21 Ma. The Lower Pantano Formation includes rock avalanches of intermediate volcanic rocks (from 2516 to 2194 m), with clasts dated at ca. 23 Ma (Houser et al., 2004). Therefore, faulting and mechanical subsidence persisted until ca. 21 Ma, likely accompanying slip along the Catalina detachment fault. The Upper Pantano Formation is a gypsiferous muddy conglomerate, separated from the Lower Pantano Formation by a lava flow and a 3.7-m-thick anhydrite bed at the interface. Its deposition reflects a period of relative tectonic quiescence accompanying core complex exhumation and the onset of Basin and Range extension. The contact between Lower and Upper Pantano Formation strata is the early Miocene unconformity, located in the well at 2194 m. The top of the Upper Pantano Formation at 1880 m was interpreted as the mid-Miocene unconformity by Houser et al. (2004). Above the mid-Miocene unconformity, the basin stratigraphy transitions to washouts and muddy sediments deposited after ca. 17–15 Ma (Houser et al., 2004), associated with synkinematic basin accommodation associated with displacement on the Santa Rita fault.

SUMMARY

Previous 1:48,000 geologic mapping of the Rincon Mountains, combined with 1:24,000 and much larger-scale geologic mapping, has established a context for investigating the structure and fabric characteristics of this major metamorphic core complex detachment zone. A particularly important fault-rock unit is CPC, which represents the structural-behavioral linkage between the crystal-plastic creation of mylonites and the semibrittle to brittle overprinting of the mylonites. The Rincon Mountains domain of the Catalina-Rincon metamorphic core complex displays especially abundant and well-preserved exposures of CPC. Through the combination of detailed structural mapping in the five subareas and multispectral analysis of the entire Rincon Mountains, the full distribution of CPC is now mapped completely in the Rincon Mountains domain of the Catalina-Rincon metamorphic core complex.

Figure 2-6. Data germane to assessment of subsurface relationships in the Tucson Basin, directly west of the Rincon Mountains. (A) Stratigraphic column based on well records and logs (sonic and density). (B) Location map showing trace of Catalina detachment surface (purple), buried fault bounding older depocenter (dotted red), and Santa Rita normal fault (yellow). Note projection of older fault toward Tanque Verde antiform. Locations of traces of seismic lines and the Exxon #2 well are shown. (C) Seismic reflection profile line 2 (top) and interpretation (bottom) of subsurface structure with emphasis on older faults in the hanging wall of the Catalina detachment fault, the seismic patterns for the two stages of basin fill and the transition between them (from early Miocene unconformity [EMU] to mid-Miocene unconformity [MMU]), and the younger Santa Rita fault and related rollover.

CHAPTER 3

Expression of the Catalina detachment zone in five key subareas

INTRODUCTION

Five subareas around the margin of the Rincon Mountains metamorphic core complex provide many of the geologic details that are essential to building an informed kinematic/mechanical interpretation of the progressive evolution of the Catalina detachment zone. These subareas are Saguaro Loop (SL), Loma Alta (LA), X9 Ranch (X9), Posta Quemada–Hidden Spring (PQHS), and Martinez-Salcido Ranch (MSR). With the exception of the X9 Ranch subarea, all are displayed in Google Earth Pro© perspective in Figure 3-1A. The X9 Ranch subarea is not included in Figure 3-1 because aerial oblique expression of the detachment zone components and upper plate is not particularly illuminating. The 1:48,000 and 1:24,000 scale geologic mapping of the Rincon Mountains cited in Chapter 2 is fundamental to grasping the basic geology of these subareas, including their structural positioning within the Catalina-Rincon Mountains metamorphic core complex. The additive facts and interpretations essential to this contribution were obtained through large-scale structural geologic mapping and analysis, including but not limited to this study (Table 3-1). Excellent exposures express the Catalina detachment fault surface and detachment zone sequence of cataclasite, CPC, and mylonite. Subdetachment faults and fault zones mark the interface between CPC and mylonite. Figures 3-1B through 3-1E are oblique Google Earth Pro© views of the basic detachment zone architecture within the Saguaro Loop, Loma Alta, Posta Quemada–Hidden Spring, and Martinez-Salcido Ranch subareas.

An important emphasis throughout Chapters 3–6 is the degree to which, within each subarea, mylonitic foliations and lineations, regardless of protolith, are marked by identical orientations, and the Catalina detachment fault and underlying subdetachment fault are likewise subparallel to one another and to mylonitic foliation. This is evident in Table 3-2, which is a summary of orientations of structures and fabrics for each subarea.

SAGUARO LOOP SUBAREA

Saguaro Loop subarea occupies the northwest limb of Tanque Verde antiform (Fig. 3-1B), a foliation arch that plunges very gently to the W-SW (Chapter 2, Fig. 2-2). Note that the distributions of the mylonites, CPC, and upper-plate rocks are identified in Figure 3-1B. Mylonite and CPC, both of which reside in the lower plate, are separated by a subdetachment fault, whereas lower-plate and upper-plate rocks are separated by the Catalina detachment fault (Fig. 3-1B).

The Catalina detachment fault in the Saguaro Loop subarea (bold red line in Fig. 3-2) strikes 206° and dips 16°SW (Table 3-2) and separates upper-plate Precambrian and Phanerozoic rocks (on the west) from detachment zone fault rocks (on the east). Paleozoic strata are predominantly limestone with interbedded shale and siltstone. In places, these strata are intensely folded (Davis, 1975; Davis and Frost, 1976). Not shown are minor exposures of upper-plate Jurassic–Cretaceous strata. Part of the western margin of the Paleozoic strata shown is overthrust by Pinal Schist (Fig. 3-2). This deformation is the Laramide

TABLE 3-1. DETAILED LARGE-SCALE MAPPING AND STRUCTURAL ANALYSES IN THE RINCON MOUNTAINS THAT CONTRIBUTED TO THIS WORK

Saguaro Loop
G.H. Davis (1975, 1980a, 1980b, 1987b, 2013); DiTullio (1983); Gregorski et al. (2019); Wright (1978); this study
Loma Alta
G.H. Davis (1975); Research workshop (2017)*: G. Davis, H. Brooks, C. Clinkscales, J. Foster, R. Grieg, K. Guns, S. Lingrey, S. Stickroth; this study
X9 Ranch
Research workshop (2017*): G. Davis, H. Brooks, C. Clinkscales, J. Foster, R. Grieg, K. Guns, S. Lingrey, S. Stickroth
Posta Quemada–Hidden Spring
G.H. Davis et al. (1974); G.H. Davis (1975, 1980a, 1980b); Krantz (1983); this study
Martinez-Salcido Ranch
G.H. Davis (1975); G.H. Davis et al. (2011); Liming (1974)

*Department of Geosciences, The University of Arizona, Practicum in Tectonics, GEOS. 494-594, Spring Semester, 2017.

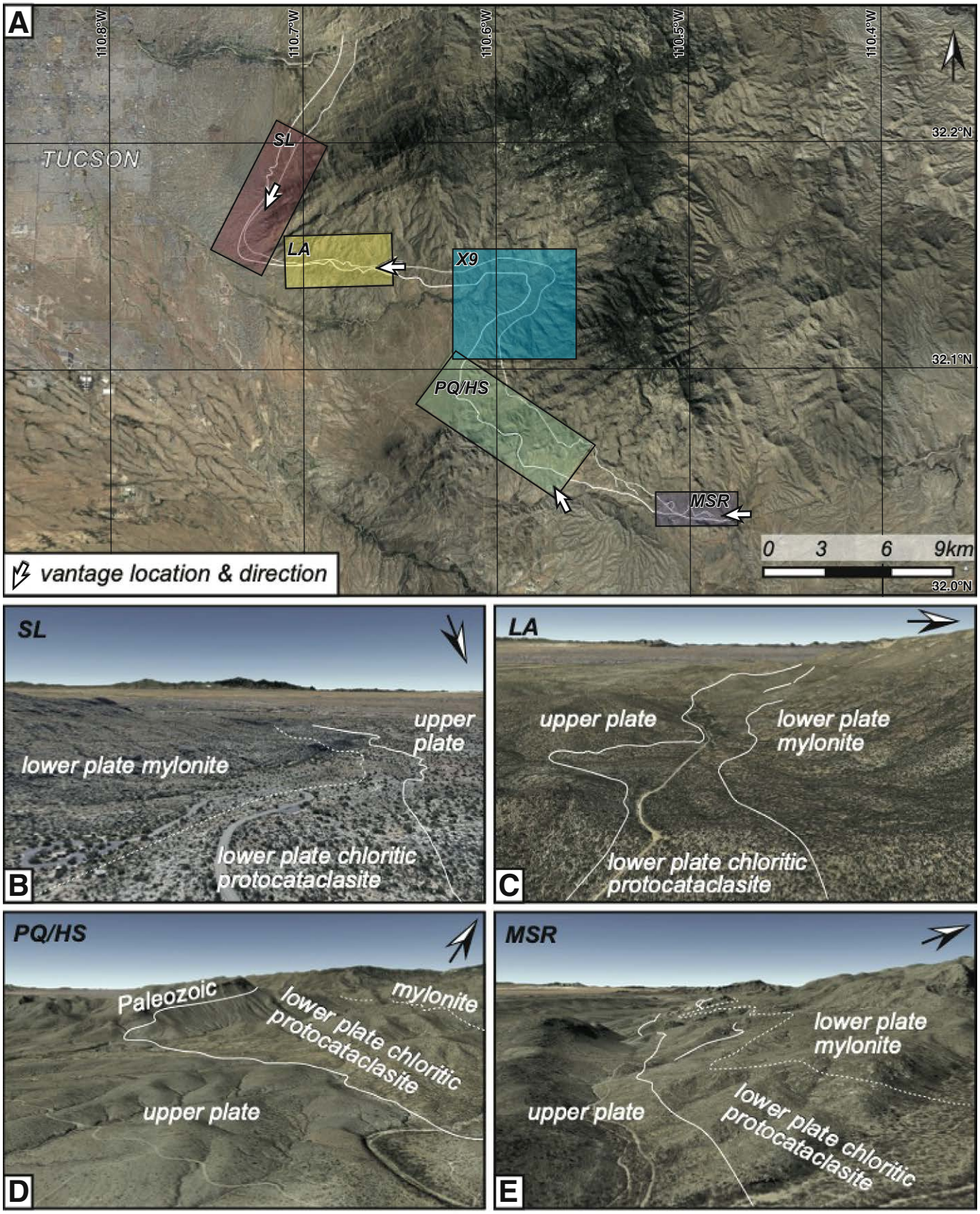

A
110.8°W
110.7°W
110.6°W
110.5°W
110.4°W
32.2°N
32.1°N
32.0°N
TUCSON
SL
LA
X9
PQ/HS
MSR
0 3 6 9km
vantage location & direction
SL
upper plate
lower plate mylonite
lower plate chloritic protocataclasite
B
LA
upper plate
lower plate mylonite
lower plate chloritic protocataclasite
C
PQ/HS
Paleozoic
mylonite
lower plate chloritic protocataclasite
upper plate
D
MSR
lower plate mylonite
upper plate
lower plate chloritic protocataclasite
E

Figure 3-1.

TABLE 3-2. ORIENTATIONS OF STRUCTURAL FEATURES IN THE RINCON MOUNTAINS

Area/subarea	Structural feature	Average azimuth (°)	Average inclination (°)	*n*	Comments
Regional	Detachment	124	14	88	All subareas
SL		206	16	6	
LA		91	10	12	
X9		169	15	6	
PQ/HS		107	15	32	
MSR		112	22	7	
Regional	Subdetachment	115	19	47	All subareas
SL		215	8	1	Calculated from global positioning system (GPS) traverse
LA		95	11	9	
X9		72	15	1	
PQ/HS		111	13	2	
MSR		104	24	21	
Regional	Mylonitic foliation	135	13	321	Excludes X9 and PQ/HS data
SL		189	24	123	
LA		102	16	66	
X9		153	12	22	Excludes NE-dipping planes
PQ/HS		103	26	11	Excludes NE-dipping planes
MSR		115	20	76	
Regional	Mylonitic lineation	241	14	299	Excludes X9 and PQ/HS data
SL		241	17	112	
LA		244	10	114	
X9		257	10	17	Excludes NE-plunging lineations
PQ/HS		219	20	7	Excludes NE-plunging lineations
MSR		235	15	74	
Regional	Back-rotated foliation	320	15	129	Excludes SW-dipping planes; no data from LA
SL		291	18	85	Excludes SW-dipping planes
LA		—	—	—	No back-rotation in LA?
X9		12	19	16	Excludes SW-dipping planes
PQ/HS		350	20	11	Excludes SW-dipping planes
MSR		19	24	17	Excludes SW-dipping planes
Regional	Back-rotated lineation	60	15	93	No data from LA
SL		59	16	47	Excludes SW-plunging lineations
LA		—	—	—	No back-rotation in LA?
X9		67	14	23	Excludes SW-plunging lineations
PQ/HS		51	13	7	Excludes SW-plunging lineations
MSR		55	14	16	Excludes SW-plunging lineations

Note: SL—Saguaro Loop; LA—Loma Alta; X9—X9 Ranch; PQ/HS—Posta Quemada–Hidden Spring; MSR—Martinez-Salcido Ranch.

Figure 3-1. (A) Google Earth Pro© view of the Rincon Mountains, showing the locations of the five subareas emphasized in this volume, namely, Saguaro Loop (SL), Loma Alta (LA), X9 Ranch (X9), Posta Quemada–Hidden Spring (PQ/HS), and Martinez-Salcido Ranch (MSR). (B–E) Google Earth Pro© aerial-oblique images of landscape expressions showing detachment fault (heavier white line), subdetachment fault zone (dotted white line), lower-plate chloritic protocataclasite (CPC) versus mylonite, and upper-plate rocks in four of the five subareas (X9 not included). (B) SL—Saguaro Loop subarea. Width of field of view in middle ground is ~1.5 km. (C) LA—Loma Alta subarea. Width of field of view in middle ground is ~1.5 km. (D) PQ/HS—Posta Quemada–Hidden Spring subarea. Width of field of view in middle ground is ~3.5 km. (E) MSR—Martinez-Salcido Ranch. Width of field of view in middle ground is ~2.5 km. Direction of view in the four labeled images (B–E) is depicted by arrow.

thrust-fault relationship identified by Drewes (1977). The overall attitude of the thrust (Drewes, 1977) is 200°/25°NW. Direct outcrop measurements show an attitude of ~161°/24°SW.

A thin fault-rock unit of cataclasite (up to ~5 m thick) occurs along the base of the Catalina detachment fault. Its expression in the landscape is commonly a resistant ledge. At the plunging nose of Tanque Verde antiform, however, the cataclasite is replaced by an expanse of ultracataclasite (Fig. 3-2). CPC is abundantly exposed in the Saguaro Loop subarea. It is crudely tabular as a fault-rock unit and separates cataclasite or ultracataclasite from mylonite. Davis (2013) reported a 215°/08°NW three-point determination of the orientation of the subdetachment fault at the base of CPC for most of the length of the Saguaro Loop

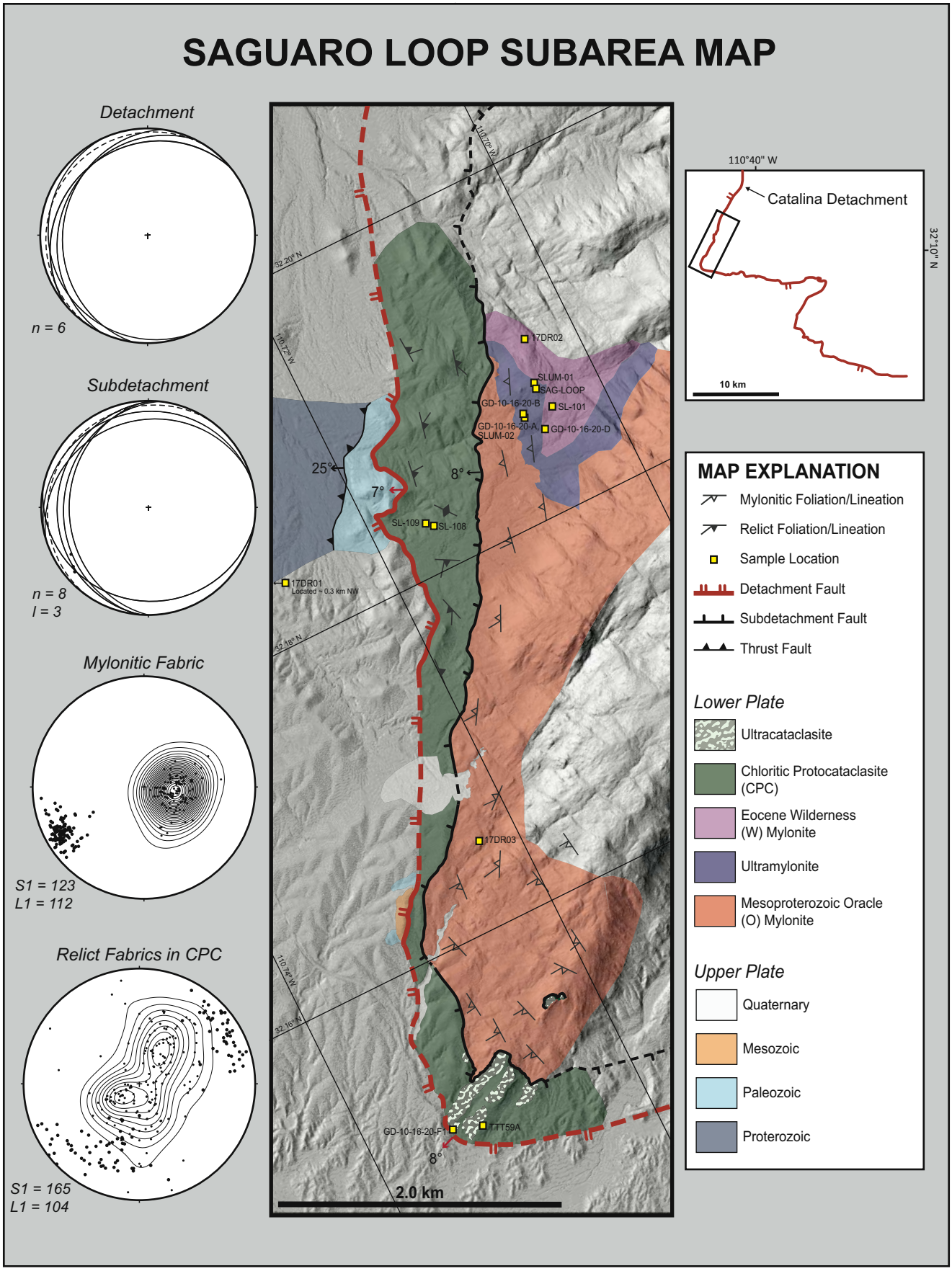

SAGUARO LOOP SUBAREA MAP
Detachment
n = 6
Subdetachment
n = 8
l = 3
Mylonitic Fabric
S1 = 123
L1 = 112
Relict Fabrics in CPC
S1 = 165
L1 = 104
110°40' W
Catalina Detachment
32°10" N
10 km
17DR02
SLUM-01
SAG-LOOP
GD-10-16-20-B
SL-101
GD-10-16-20-A
SLUM-02
GD-10-16-20-D
25°
8°
7°
SL-109
SL-108
17DR01
Located ~ 0.3 km NW
17DR03
GD-10-16-20-F1
17T59A
8°
2.0 km
MAP EXPLANATION
Mylonitic Foliation/Lineation
Relict Foliation/Lineation
Sample Location
Detachment Fault
Subdetachment Fault
Thrust Fault
Lower Plate
Ultracataclasite
Chloritic Protocataclasite (CPC)
Eocene Wilderness (W) Mylonite
Ultramylonite
Mesoproterozoic Oracle (O) Mylonite
Upper Plate
Quaternary
Mesozoic
Paleozoic
Proterozoic

Figure 3-2.

subarea. This average strike is more northeasterly than the average strike of subdetachment fault orientations plotted in Figure 3-2 (160°/10°SW) because of the range of strikes of the detachment fault and subdetachment fault around the plunging nose of the Tanque Verde antiform. Even though the maximum thickness of the CPC is just 50–75 m, outcrop breadth ranges up to ~500 m because of its very low dip angle. The CPC possesses relict mylonitic fabrics (foliation and lineation), which survived total obliteration by cataclasis.

As emphasized earlier, two main mylonites (O-mylonite and W-mylonite) reside beneath the subdetachment fault (Fig. 3-2). The average foliation attitude of the mylonites (189°/24°NW) conforms to the overall orientation of the northwest limb of the Tanque Verde antiform. Mineral lineations consistently plunge 17° toward 241° (Table 3-2; Fig. 3-2). Note that relict fabrics in CPC have dispersed orientations compared with those of the non-overprinted mylonites (Table 3-2; Fig. 3-2). Poles to relict mylonite foliation are generally distributed along a great-circle representing a steeply dipping zone striking 035°, while shallowly to moderately plunging relict lineation orientations are distributed across a plunge-trend range of 025°/205° to 075°/255°. The conclusion drawn is that the fabric orientations are scattered in ways that conform to a gently NW-plunging axis of rotation.

W-mylonite is separated from O-mylonite by a thin (~50 m) screen of ultramylonite, which, as reported in Chapter 2, was mapped by Drewes (1977) as Pinal Schist (ca. 1.65 Ga) (Davis, 2013) (Fig. 3-2). The protolith is largely W-mylonite. The attitudes of the upper and lower contacts of the ultramylonite, as well as the orientations of foliation and lineation within it, are identical to those of foliation and lineation within O- and W-mylonite (Davis, 2013). Microstructures in mylonite and ultramylonite reveal a top-to-the-SW sense of shear.

LOMA ALTA SUBAREA

The Catalina detachment fault (solid white line in Fig. 3-1C) within the Loma Alta subarea marks the base of the upper plate, and its attitude is 091°/10°S (Table 3-2; Fig. 3-3). CPC and mylonite underlie the Catalina detachment fault. The subdetachment fault at the base of CPC strikes 095°/11°S (Table 3-2; Figs. 3-1C and 3-3). West of the Loma Alta subarea, the Catalina detachment fault is covered along the 3 km distance to the toe of Tanque Verde Ridge. To the east, there is near-continuous exposure through the X9 Ranch, Posta Quemada–Hidden Spring, and Martinez-Salcido Ranch subareas (Fig. 3-1A).

The trace of the Catalina detachment fault (bold red line in Fig. 3-3) encompasses underlying cataclasite. Though the ~2-m-thick cataclasite fault-rock unit underlies most of the exposed trace length of the detachment fault, only the outcrop area of black ultracataclasite is shown in Figure 3-3, where it is up to ~15 m thick. The map pattern of the black ultracataclasite reveals an overall tabular form that closely parallels the E-W strike and gentle southerly dip of the Catalina detachment fault at this location (Fig. 3-3). Directly beneath cataclasite and ultracataclasite, there is CPC (Fig. 3-3), followed by a subdetachment fault (black line) that marks the truncated upper surface of the mylonites. The average attitude of the subdetachment fault in the Loma Alta subarea is almost perfectly parallel to that of the detachment fault. The position of this subdetachment fault is readily identified because of the striking contrasts both in rock fabric/structure and landscape expression (Fig. 3-4). CPC is as thick as ~75 m. Outcrops of foliated, lineated mylonite directly beneath the subdetachment fault weather to smooth, expansive exfoliated surfaces. In contrast, the highly fractured, altered, faulted CPC weathers and erodes to landscape that Force (2002) described as "scabrous" (i.e., covered with raised, roughened patches). In contrast to the Saguaro Loop area, where relict fabrics in CPC are rotated into dispersed orientations, attitudes of these overprinted mylonitic fabrics in the Loma Alta subarea are parallel to those of underlying mylonite, namely 102°/16°SW, with lineation oriented 10°/244° (Table 3-2).

Mainly interested in capturing the geology of upper-plate rocks and structures in the Loma Alta area at 1:24,000 scale, Richard et al. (2005) lumped the lower-plate granitoids as mixed granitoid and gneiss (Proterozoic, Cretaceous, and Tertiary). Based on the geologic mapping by Drewes (1977), we anticipated and confirmed that mylonite in the eastern third of the Loma Alta subarea is dominated by O-mylonite, marked by porphyroclasts of orthoclase feldspar up to 7 cm long; mylonite in the western two thirds of the subarea is W-mylonite, featuring white mica and garnet (Fig. 3-3). We discovered a distinctive third variety of mylonite, which presents itself as beige-weathering, quartzofeldspathic, medium-grained, and equigranular mylonite that contains biotite, chlorite, and accessory apatite and titanite. Absent are the diagnostic large porphyroclasts of O-mylonite and the two-mica garnet–bearing essential mineralogy of W-mylonite. We call it "Loma Alta mylonite." Its U-Pb zircon–derived age is late Oligocene (Chapter 8). Where the sense of shear could be determined in outcrop and thin section, it is consistently top-to-the-SW, based on indicators such as S-C fabrics, rotated porphryoclasts, imbrication of mica fish, and asymmetrical overturned folds (Chapter 6).

Upper-plate rocks in the Loma Alta subarea are mainly Late Jurassic–Early Cretaceous Bisbee Group sedimentary rocks

Figure 3-2. Structural geologic map of the Saguaro Loop subarea. Position of this subarea with respect to the trace of the Catalina detachment fault in the Rincon Mountains is shown in index map at upper right. Stereographic projections show measured detachment fault orientations (great circles) and orientation determined through three-point method (dashed great circle); measured subdetachment fault orientations (dashed great circles), with slickenlines (points), and best-fit orientation of subdetachment fault zone (dashed great circle); poles to mylonitic foliation (points, Kamb contoured) and mylonitic lineation (points); and poles to relict mylonitic foliation in chloritic protocataclasite (CPC) (points, Kamb contoured) and relict mineral lineation (points). Fault-rock stratigraphy is presented in the explanation legend. Rock sample locations are shown (see also Fig. A-1; Table A-1 [Supplemental Material, Appendix A]).

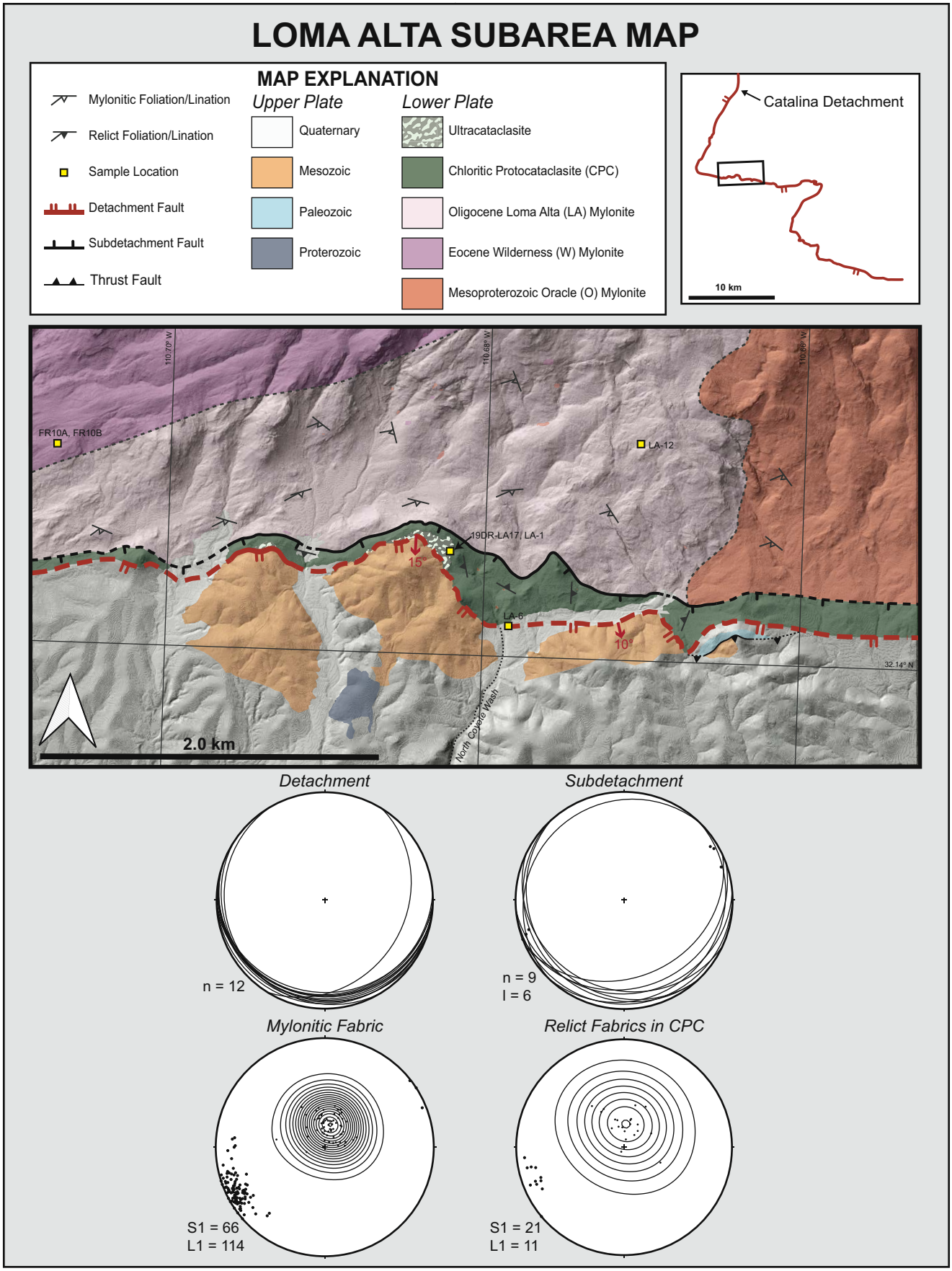

LOMA ALTA SUBAREA MAP
MAP EXPLANATION
Mylonitic Foliation/Lination
Relict Foliation/Lination
Sample Location
Detachment Fault
Subdetachment Fault
Thrust Fault
Upper Plate
Quaternary
Mesozoic
Paleozoic
Proterozoic
Lower Plate
Ultracataclasite
Chloritic Protocataclasite (CPC)
Oligocene Loma Alta (LA) Mylonite
Eocene Wilderness (W) Mylonite
Mesoproterozoic Oracle (O) Mylonite
Catalina Detachment
10 km
110.70° W
110.68° W
110.66° W
32.14° N
FR10A, FR10B
LA-12
19DR-LA17/ LA-1
LA-6
15°
10°
North Coyote Wash
2.0 km
Detachment
n = 12
Subdetachment
n = 9
l = 6
Mylonitic Fabric
S1 = 66
L1 = 114
Relict Fabrics in CPC
S1 = 21
L1 = 11

Figure 3-3.



Figure 3-4. Northwest-directed view of part of the Loma Alta subarea showing the contrast in landscape expression between mylonite (right half) vs. chloritic protocataclasite (left half). Subdetachment fault separates the two. Width of field of view in middle ground is ~150 m.

(shale, sandstone, and conglomerate), though Precambrian Rincon Valley Granodiorite (ca. 1.62 Ga) is present as well (Drewes, 1977; Richard et al., 2005). The Bisbee Group strata are replete with overturned-to-recumbent mesoscopic folds (Davis, 1975), products of pervasive shearing within these sedimentary strata. Richard et al. (2005) discovered a (Laramide) thrust-fault contact of Precambrian on Jurassic/Cretaceous strata within the upper plate (Fig. 3-3). Spencer et al. (2019) recognized this thrust relationship as a hanging-wall piercing point, corresponding to a footwall equivalent located ~35 km to the east. This relation provides control for minimum distance of post-Laramide tectonic transport accommodated by the Catalina detachment fault.

X9 RANCH SUBAREA

The X9 Ranch subarea occupies the narrow synformal keel of the Rincon Creek synform (Figs. 2-2, 3-1, and 3-5). The synformal shape of the Catalina detachment fault (red line) is so tight in the X9 Ranch subarea that its trace has the form of a hairpin.

Figure 3-3. Structural geologic map of the Loma Alta subarea. Position of this subarea with respect to the trace of the Catalina detachment fault in the Rincon Mountains is shown in index map at upper right. Stereographic projections show measured detachment fault orientations (great circles), three-point–determined subdetachment fault orientations (dashed great circles), slickenlines on subdetachment faults (points), poles to mylonitic foliation (points, Kamb contoured), mylonitic lineation (points), poles to relict foliation in chloritic protocataclasite (CPC) (points, Kamb contoured), and relict mineral lineation in CPC (points). Fault-rock stratigraphy is presented in explanation legend. Rock sample locations are shown (see also Fig. A-1; Table A-1 [Supplemental Material, Appendix A]).

The synformally folded form of the Catalina detachment fault surface (red line in Fig. 3-5) is marked by a hinge line with an orientation of 15°/240.

Alluvium covers much of the upper plate in the very keel of the synform, but bedrock exposures document upper-plate Rincon Valley Granodiorite (Paleoproterozoic), Paleozoic strata, and Oligocene–Miocene sedimentary rocks (Drewes, 1977; Richard et al., 2005). Drewes (1977) mapped Pinal Schist (Paleoproterozoic) directly beneath the detachment fault (Fig. 3-5), though Richard et al. (2005) mapped this same rock as "heterogeneous gneiss and mylonite." Reconnaissance mapping led us to conclude that this swath of bedrock, deformed along the sole of the Catalina detachment fault, is a combination of ultramylonite and CPC. Though we did not carry out sufficient fieldwork in this area to explore for and map the subdetachment fault, we positioned the trace of the subdetachment fault (Fig. 3-5) based on the expression of the outcrop breadth of CPC in the multispectral image (Fig. 2-4).

Drewes' (1977) map and rock descriptions of most of the granitoids on the northwest limb of Rincon Creek synform reveal it to be O-mylonite, whereas W-mylonite dominates the southeast limb (Fig. 3-5). Upslope on the southeast limb, the W-mylonite is in contact with O-mylonite. At or near that interface, Drewes (1977) mapped Pinal Schist, which is largely ultramylonite derived from W-mylonite. Mylonitic lineation plunges 10°/257° in the X9 Ranch subarea (Table 3-2), based on the measurements of Drewes (1977) and Richard et al. (2005). This plunge/trend orientation is subparallel to the orientation of the hinge of the Rincon Creek syncline (Fig. 3-5).

One of the most curious geologic features tucked within the mylonites at several locations in the Rincon Mountains, and made

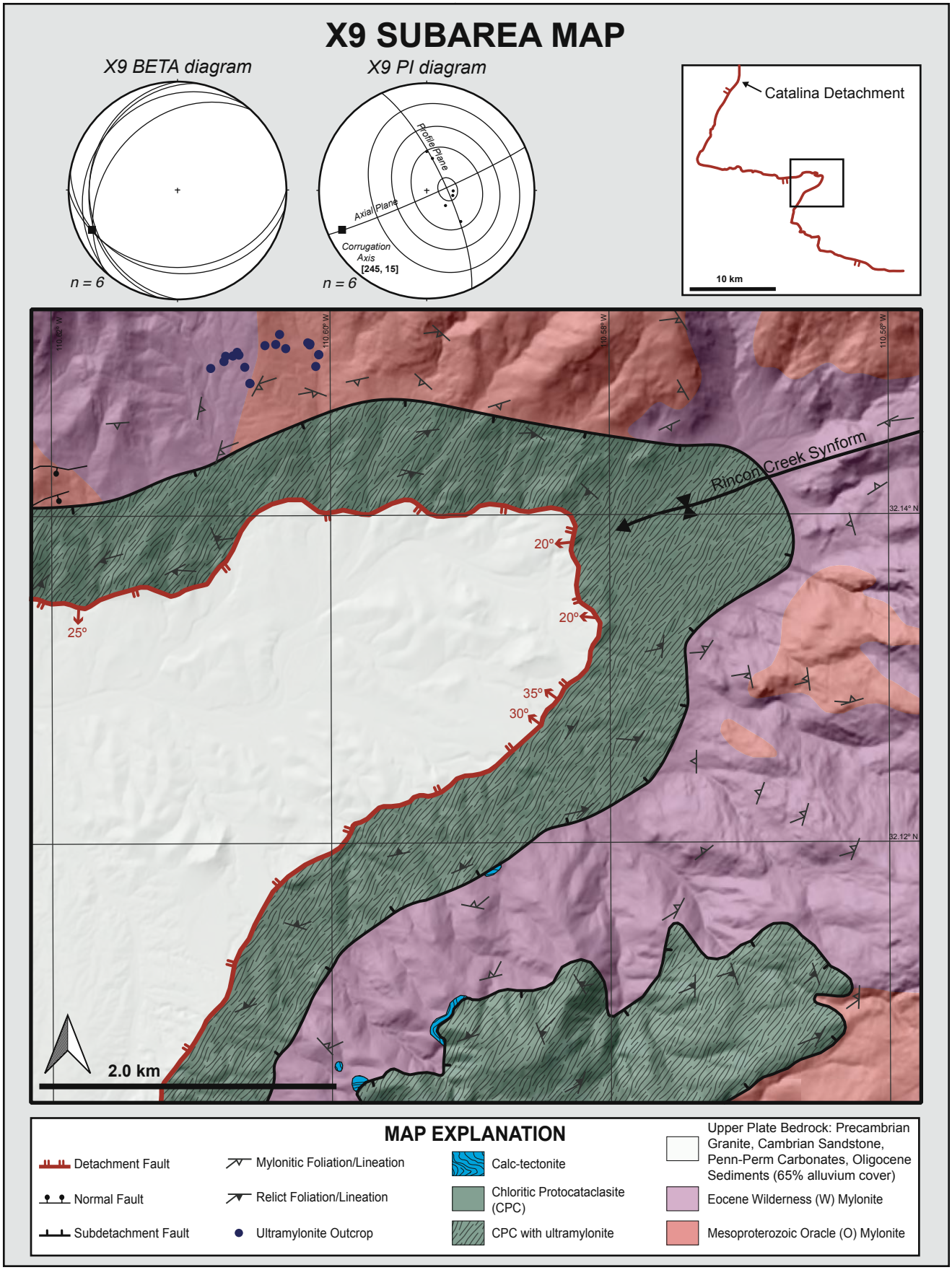

X9 SUBAREA MAP
X9 BETA diagram
n = 6
X9 PI diagram
Profile Plane
Axial Plane
Corrugation Axis
[245, 15]
n = 6
Catalina Detachment
10 km
110.62° W
110.60° W
110.58° W
110.56° W
32.14° N
32.12° N
Rincon Creek Synform
20°
20°
25°
35°
30°
2.0 km
MAP EXPLANATION
Detachment Fault
Normal Fault
Subdetachment Fault
Mylonitic Foliation/Lineation
Relict Foliation/Lineation
Ultramylonite Outcrop
Calc-tectonite
Chloritic Protocataclasite (CPC)
CPC with ultramylonite
Upper Plate Bedrock: Precambrian Granite, Cambrian Sandstone, Penn-Perm Carbonates, Oligocene Sediments (65% alluvium cover)
Eocene Wilderness (W) Mylonite
Mesoproterozoic Oracle (O) Mylonite

Figure 3-5.

evident on the geologic maps of both Drewes (1977) and Richard et al. (2005), is a string of disconnected outcrops of marble, quartzite, and calc-silicate rocks (middle Proterozoic, Paleozoic, Cretaceous, and Tertiary) (Fig. 3-5). Where these alignments of exotic rocks occur, Drewes (1977) mapped Laramide thrust faults. He interpreted them as tectonic horses. The mapped trace of alignment of these marble/calc-silicate outcrops reveals that this feature is planar to slightly curviplanar and gently dipping. Its attitude is essentially parallel to mylonitic foliation and layering on the northeastern limb of Posta Quemada antiform.

POSTA QUEMADA–HIDDEN SPRING SUBAREA

Within the Posta Quemada–Hidden Spring subarea, the thickest and highest reaches of upper-plate rocks are dominated by Paleozoic strata (largely limestone with interbedded shale and sandstone), though in addition, the upper plate consists of Rincon Valley Granodiorite (Paleoproterozoic) and Oligocene–Miocene sedimentary and volcanic rocks (Figs. 3-1D and 3-6). The Catalina detachment fault (solid white line in Fig. 3-1D) separates upper-plate rocks from lower-plate CPC. Beneath CPC, there are mylonites, and the contact between them is a subdetachment fault zone (dotted white line in Fig. 3-1D).

The trace of the Catalina detachment fault is exposed nearly continuously for a distance of >5 km across the full length of the Posta Quemada–Hidden Spring subarea (Fig. 3-6). The attitude of the Catalina detachment fault along most of its length is 107°/15°SW (Table 3-2; Fig. 3-6), except where it twists to an E-W strike in the easternmost part. A broad expanse of CPC separates the trace of the Catalina detachment fault from mylonites deeper in the lower plate. The contact between mylonites and CPC is a subdetachment fault zone composed of anastomosing splays (Fig. 3-6). The overall attitude of the subdetachment fault zone is 111°/13°SW (Table 3-2; Fig. 3-6), thus parallel to the Catalina detachment fault. Lenses and pods of calc-silicate tectonite, derived apparently from Paleozoic protolith, occur along the subdetachment fault zone (Drewes, 1977; Spencer et al., 2012).

Panoramic photographs convey the landscape expression of the Catalina detachment zone (Figs. 3-7 and 3-8). These images make clear that the overall form and landscape expression of the Rincon Mountains domain of the Catalina-Rincon metamorphic core complex are controlled by the orientation and properties of the Catalina detachment zone.

Though Drewes (1977) mapped the mylonites in the Posta Quemada–Hidden Spring subarea as gneissic "Wrong Mountain Quartz Monzonite," which we consider W-mylonite (Fig. 3-6), Spencer et al. (2001) lumped the lower-plate rocks as mylonitic Cretaceous–Tertiary granitoids. These lower-plate mylonitic rocks are quite heterogeneous, marked by foliated and commonly lineated metamorphic and/or banded mylonitic rocks that range from melanocratic to leucocratic and coarse to fine grained. Compositional banding and foliation tend to be shallowly to moderately dipping (Fig. 3-6). Mylonitic foliation tends to be quite variable based on our plotting of foliation readings by Drewes (1977) and Spencer et al. (2001), though gently plunging mylonitic lineation shows a preferred trend of ~230° (Fig. 3-6, "Mylonitic fabric" stereographic projection). Most of the granitoids residing above the subdetachment fault zone are CPC marked by chlorite-epidote-hematite alteration, cataclasis, and conspicuous fracturing and shattering. The average orientation of relict mylonitic foliation is 100°/40°SW.

MARTINEZ-SALCIDO RANCH SUBAREA

Upper-plate rocks in the Martinez-Salcido Ranch subarea are sharply separated from CPC by the Catalina detachment fault (solid white line in Fig. 3-1E). Similar to the other subareas, CPC is separated from mylonites by a subdetachment fault system. The landscape expression of these elements is profound—the finest in the entire Rincon Mountains (Fig. 3-9). The most eye-catching landscape feature is the uniform ~10°S-dipping inclination of the land surface, controlled by the position and orientation of the Catalina detachment fault. The projected trace of this fault barely clears the topographic profile. The kilometers-thick, brittlely deformed, upper-plate rocks have been removed by erosion, and most of the CPC beneath this fault was removed as well. The slightly scalloped nature of this eroded slope may be due to "survivor patches" of CPC.

Davis et al. (2011) mapped its geology along a 4 km strike length of the Catalina detachment zone, which strikes ~112° and dips 22° (SW) (Table 3-2; Fig. 3-10). Upper-plate rocks occur in a foothills ridge composed almost exclusively of Paleozoic strata dipping ~35°S. The largely homoclinal configuration of strata is marked by individual formations that are in proper stratigraphic order but profoundly thinned in comparison to full thicknesses measured in nearby ranges (Liming, 1974; Davis, 1975; Drewes, 1977). Shearing is expressed in pervasive, strongly asymmetric S-SW–verging chevron-like folds (Davis, 1973, 1975; Liming, 1974). Near the base of the upper plate, thin tectonic slices (~15 m thick) of Precambrian formations (Pinal Schist and Rincon Valley Granodiorite) crop out for 500 m along one stretch of the detachment fault. These rocks are ground to gouge (in a zone up to 15 m thick) directly above the detachment fault.

Figure 3-5. Structural geologic map of the X9 Ranch subarea. Position of this subarea with respect to the trace of the Catalina detachment fault in the Rincon Mountains is shown in index map at upper right. Traces of the detachment fault and subdetachment fault are shown. Fault-rock stratigraphy is presented in explanation legend. Stereographic projections present curviplanar form of the Catalina detachment fault in the X9 Ranch area. Beta diagram is based on plotting detachment fault attitudes shown as great circles. Pi-diagram is based on plotting poles to fault attitudes (points, Kamb contoured). The corrugation axis is the trend and plunge of the Rincon Creek synform. Penn-Perm—Permian–Pennsylvanian.

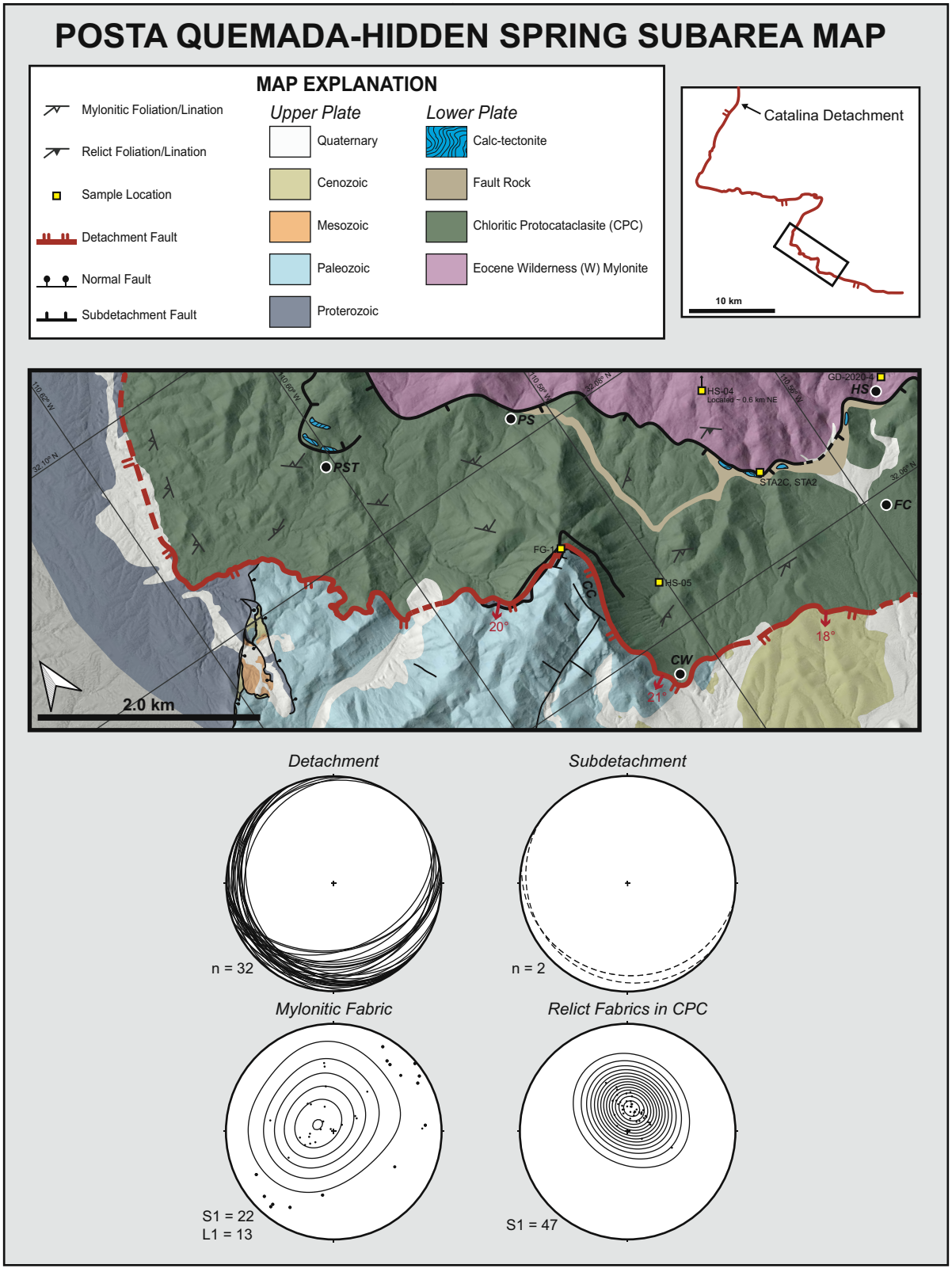


Figure 3-6. Structural geologic map of the Posta Quemada–Hidden Spring subarea. Position of this subarea with respect to the trace of the Catalina detachment fault in the Rincon Mountains is shown in index map at upper right. Stereographic projections show measured detachment fault orientations (great circles), three-point–determined subdetachment fault orientations (dashed great circles), poles to mylonitic foliation (points, Kamb contoured), mylonitic lineation (points), and poles to relict foliation in chloritic protocataclasite (CPC) (Kamb contoured). Fault-rock stratigraphy is presented in explanation legend. Rock sample locations are shown (see also Fig. A-1; Table A-1 [Supplemental Material, Appendix A]). Also, the locations of Charlie's Cliff (CC), Charlie's Wash (CW), Hidden Spring (HS), Papago Springs (PS), and Papago Springs Trailhead (PST), and Fault City (FC) are marked.

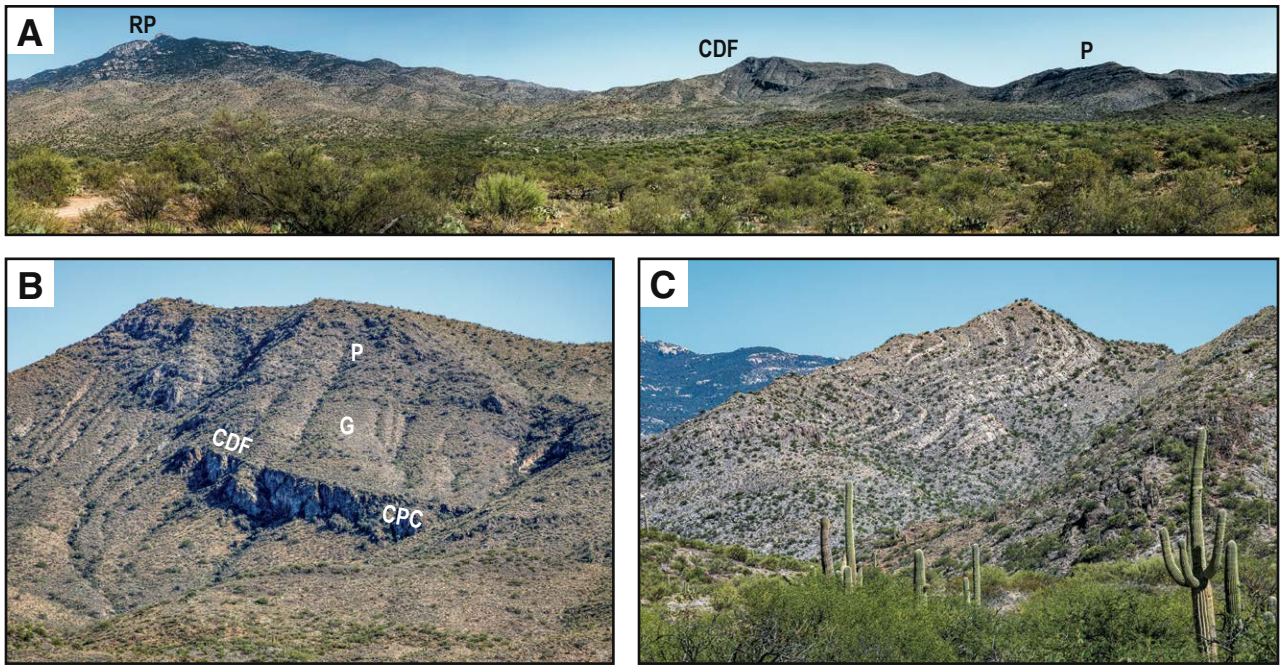


Figure 3-7. (A) East-directed view showing the location of the Posta Quemada–Hidden Spring subarea in relation to the broad landscape of the Rincon Mountain metamorphic core complex. The left half of the image captures mylonites sloping gently southward from Rincon Peak (RP, highest elevation). This landscape slope reflects the inclination of the Catalina detachment fault, which parallels but projects above the sloping landscape. The Catalina detachment fault (CDF) is well exposed as the gently southward-inclined planar top of the shadowed cliff of chloritic protocataclasite in the middle of the panorama. On the right are upper-plate Paleozoic strata (P). Width of field of view is ~12 km. (B) Closer image of the Catalina detachment fault (CDF) underlain by cliff of chloritic protocataclasite (CPC). Upper-plate rocks include Precambrian granite (G, smooth slope) and Paleozoic strata (P, rougher slope). Width of field of view in middle ground is ~1 km. (C) North-directed view of overturned to recumbent folding in Pennsylvanian–Permian strata in the upper plate, mapped by Davis et al. (1974). Mylonites comprise the main range in the far upper-left background. Width of field of view in middle ground is ~1.5 km. Photographs are by Peter L. Kresan © www.kresanphotography.com.



Figure 3-8. (A) WNW-directed view of the Posta Quemada–Hidden Spring subarea. This location is Charlie's Cliff and its position is on the opposite side of the ridge shown in Figure 3-7A. Width of field of view in middle ground is ~6 km. (B) Expanded view (width of field of view is ~600 m) of black rectangle in part A, featuring tilted, faulted, upper-plate Paleozoic strata (gray; brownish gray). The trace of the Catalina detachment fault runs along the top of the white/silver-gray bench lower on the slope. The bench is composed of cataclasite and chloritic protocataclasite (CPC). Most of the landscape shown in part A beneath the trace of the Catalina detachment fault is CPC. Photographs are by Peter L. Kresan © www.kresanphotography.com.



Figure 3-9. West-directed annotated photograph of the eastern margin of the Rincon Mountains. Mountain is composed of mylonite (M), i.e., lower-plate rocks. The N-S–trending escarpment at far right is an E-dipping, high-angle normal fault, namely, the Martinez Ranch fault zone (MRFZ). The S-dipping landscape profile reflects the orientation of the Catalina detachment fault (CDF), which, along with upper-plate rocks, has been eroded from the main range. The Martinez-Salcito Ranch subarea (MSR) lies at the southern foot of this landscape declivity and preserves the entire Catalina detachment zone. Panoramic photograph is by Peter L. Kresan © www.kresanphotography.com.

Directly beneath the detachment surface, the characteristic 1–2-m-thick, resistant ledge of cataclasite is present. Directly beneath this fault rock, there is CPC, whose thickness ranges from ~30 to 300 m. The attitude of the subdetachment fault is 104°/24°SW, i.e., parallel to the Catalina detachment fault (Table 3-2; Fig. 3-10). Mylonites beneath the subdetachment fault are derived primarily from W-mylonite and lesser O-mylonite (Drewes, 1977). The strike of mylonitic foliation is 115°/20°, with lineation plunging 15°/235° (Table 3-2; Fig. 3-10). Sense of shear in the mylonites is top-to-the-SW. The attitude of relict foliations in CPC is 019°/24°SE (Table 3-2; Fig. 3-10), which departs from that of the underlying mylonites, though mylonitic lineations are subparallel to one another.

ORIENTATION SUMMARY

As emphasized earlier, the attitudes of the detachment fault, subdetachment fault, and mylonitic foliation are similar within each subarea (Table 3-2). However, the absolute orientation for a given subarea is related to positioning on the antiformal/synformal morphology of the Catalina-Rincon metamorphic core complex (Fig. 2-2). Regardless of subarea, direction and sense of shear are constant: top-to-240° (Fig. 3-11).

SUMMARY

This overview of the geologic and structural-geologic properties of each subarea creates context for the more detailed treatments that follow for the Catalina detachment fault and underlying cataclasite and ultracataclasite (Chapter 4); CPC and minidetachment faults (Chapter 5); subdetachment faults, ultramylonite, calc-tectonite, and mylonite (Chapter 6); and progressive structural evolution of the Catalina detachment zone (Chapter 7). The tectonic-transport direction and sense of transport along the Catalina detachment fault and the direction and sense of shear revealed in mylonite fabrics are uniformly top-to-~240° in the Rincon Mountains domain of the Catalina-Rincon metamorphic core complex. Nevertheless, each subarea offers different but complementary perspectives of the nature and history of the Catalina detachment zone. Variations in subarea geology relate to differences in (1) position with respect to the antiformal/synformal morphology of the mylonite and the detachment fault surface, (2) mylonite protolith, (3) degree of internal disruption of relict mylonite fabrics in CPC, (4) presence and degree of development of ultramylonite and calc-tectonite, (5) expressions of structures and fabrics in the landscape, and (6) state of preservation of upper-plate rocks.

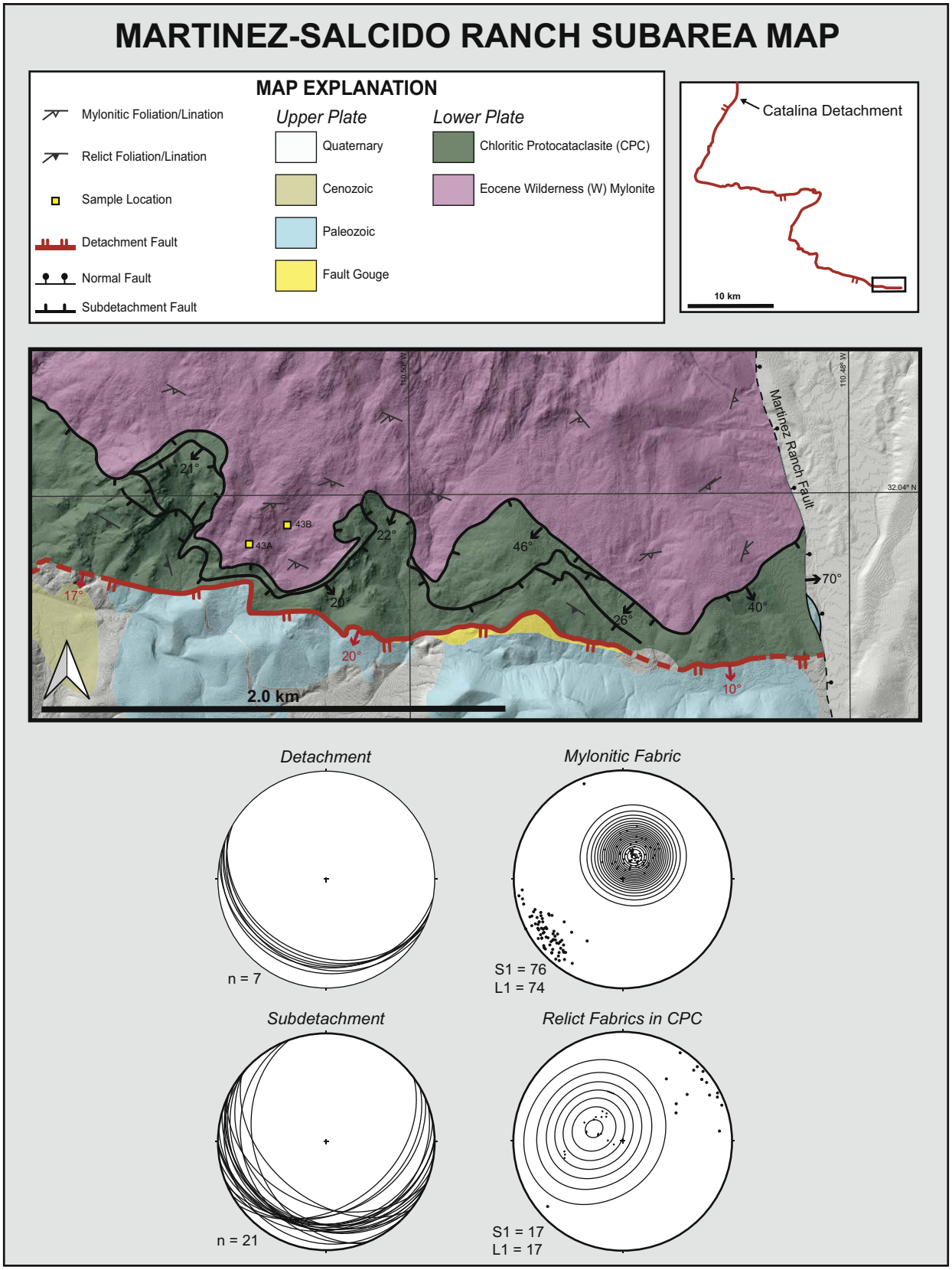


Figure 3-10. Structural geologic map of the Martinez-Salcido Ranch subarea. Position of this subarea with respect to the trace of the Catalina detachment fault in the Rincon Mountains is shown in index map at upper right. Stereographic projections show measured detachment fault and subdetachment fault orientations (great circles), poles to mylonitic foliation (Kamb contoured), mylonitic lineation (points), poles to relict foliation in chloritic protocataclasite (CPC) (points, Kamb contoured), and orientations of relict lineation in CPC (points). Fault-rock stratigraphy is presented in explanation legend. Rock sample locations are shown (see also Fig. A-1; Table A-1 [Supplemental Material, Appendix A]).

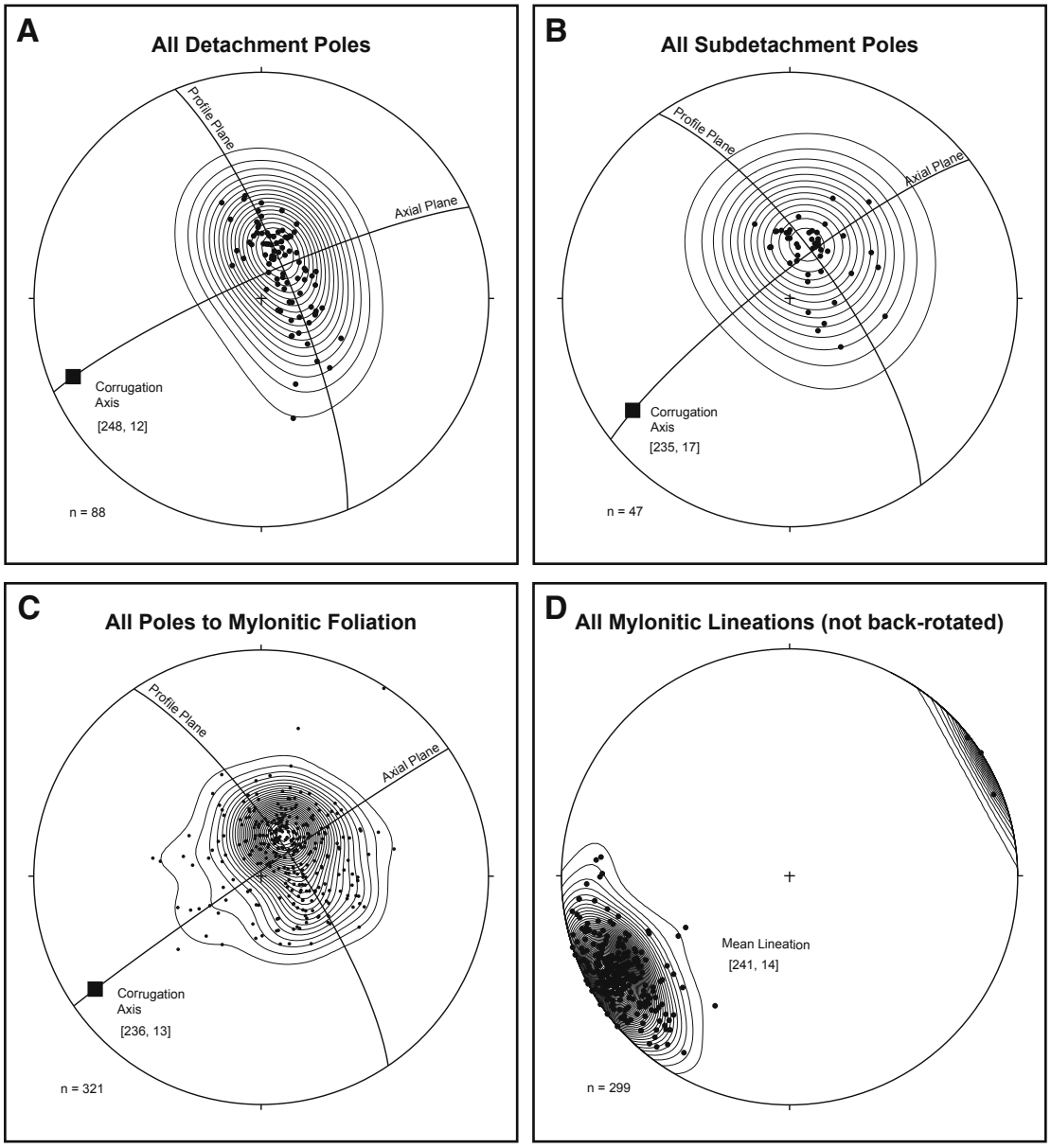


Figure 3-11. Synoptic stereographic projections drawing together all measurements from the five key subareas in the Rincon Mountains, for (A) Catalina detachment fault, (B) subdetachment fault, (C) mylonitic foliation, and (D) mylonitic lineation.

CHAPTER 4

Catalina detachment fault and subjacent cataclasite

INTRODUCTION

This is the first in a triad of chapters (Chapters 4, 5, and 6) that presents the structural and fabric features comprising the essential elements of the Catalina detachment zone. This chapter focuses on the Catalina detachment fault itself, along with immediately underlying fault-rock units, cataclasite and ultracataclasite.

MACROSCOPIC FORM OF THE CATALINA DETACHMENT FAULT

Though subplanar within given subareas, the Catalina detachment fault, at the scale of the Catalina-Rincon Mountains metamorphic core complex, is marked by a macroscopic antiformal/synformal cylindrical geometry (Fig. 1-1). Crests and troughs plunge 15°/235° (Fig. 3-11A). The most extreme expression of this curvature is seen in the X9 Ranch subarea along the trace of the Rincon Creek synform (Figs. 2-2 and 3-5). This overall macroscopic fold-form geometry is characteristic of detachment faults in most if not all metamorphic core complexes (G.A. Davis et al., 1980; Rehrig and Reynolds, 1980; Spencer, 1984; John, 1987; Frost and Heidrick, 1996).

The Rincon Mountains antiforms and synforms (aka, corrugations), as defined by mylonitic foliation orientations, display comparable form, scale, and map position to those of the overlying detachment fault surface. The crest and trough lines of each coincide (Fig. 2-2). For the entire Rincon Mountains, stereographic projections of poles to mylonitic foliation (Fig. 3-11C), in comparison to poles to Catalina detachment surface orientations (Fig. 3-11A), are quite similar, as are the orientations of fold hinge lines (Fig. 3-11C). Penetrative mineral lineation in mylonite (Fig. 3-11D) is, likewise, oriented parallel to the axes of these antiforms and synforms (Fig. 3-11C). The wavelength measured from the crest of Tanque Verde antiform to that of Posta Quemada antiform is ~13 km (Fig. 2-2).

The macroscopic folded forms of mylonites and detachments faults are typical of Cordilleran metamorphic core complexes. These macroscopic features have been interpreted in various ways: transverse buckling responses to profound extension (Fletcher et al., 1995); giant fault grooves (megamullions) produced by large-magnitude frictional translation (John, 1987); corrugations resulting from the continuous casting of plastically deforming mylonites ascending upward from beneath upper-plate rocks (Spencer, 1999); and brittle strain localization on a network of linked fractures (Parnell-Turner et al., 2018). In Chapter 7, these megastructural forms, and their origins, are integrated into our kinematic/mechanical model for the progressive evolution of the Catalina detachment zone.



Figure 4-1. South-directed photograph showing a Catalina detachment fault as well as a short segment of the subdetachment fault (white arrow, sd, points it out). Also identified is the location (white arrow, g) where gouge was sampled for purposes of dating latest movement on the detachment fault (Chapter 8). Though the detachment fault appears to be slightly curved (convex upward), this is an artifact of distortion in building this panoramic view. Width of field of view is ~750 m.

OUTCROP EXPRESSION OF THE CATALINA DETACHMENT FAULT SURFACE

The Catalina detachment fault at a number of locations in the Rincon Mountains metamorphic core complex displays its sharply planar expression (Fig. 4-1). There is negligible roughness or irregularity even at the outcrop scale. The prominence of the detachment surface in Figure 4-1 is due to the strength of the cliff-forming CPC in contrast to the erosional weakness of immediately overlying and shattered Rincon Valley Granodiorite.

Smeared on the surface of the Catalina fault from place to place is clay-rich gouge, though good exposures are rare because of the vulnerability of gouge to erosion. One exception is in the Martinez-Salcido subarea, where a narrow gouge zone is exposed along the fault trace for a distance of ~1 km (Fig. 3-10). Weathering and erosion of the weak gouge have laid bare the Catalina detachment fault. The light- to medium-gray clay-rich gouge contains abundant granule- to pebble-size faceted clasts (up to ~6 cm), the largest of which have friction-fashioned forms and shapes resembling ventifacts. The clast protoliths are primarily Rincon Valley Granodiorite.

An excellent outcrop area exposing the Catalina detachment fault surface is seen in the Posta Quemada–Hidden Spring subarea at a location known as Charlie's Wash (Fig. 4-2). The low-dipping fault surface at this location is oriented ~125°/15°SW and marks the upper boundary of the underlying resistant cataclasite. The Charlie's Wash exposure of the Catalina detachment fault displays hues of brown (iron oxides) coating the surface, beneath which are the bluish-green hues of cataclasite and CPC (Fig. 4-2A). The hues are expressions of low-grade hydrothermal chlorite-epidote alteration. Resistant cataclasite combined with the uppermost altered and comminuted CPC form a kind of resistive armor that presents itself as a fault-line scarp. Upper-plate strata in this arroyo setting have been completely stripped away by erosion. The detachment fault is evidently planar at outcrop scale, though at this particular location, it is part of a very slight curviplanar bend of the fault surface (Spencer et al., 2001) (Fig. 3-6). Although the fault surface may initially appear to be relatively smooth, in detail, there are meters-scale and 1–10-cm-scale mullions produced by facet-like steps in the otherwise smooth surface. The trends of these mullions conform closely to the overall ~240° tectonic-transport direction for the Rincon Mountains metamorphic core complex (see stereographic projection, Fig. 3-6).

OUTCROP AND FABRIC EXPRESSION OF SUBJACENT CATACLASITE

The Saguaro Loop subarea contains the type-locality expression of the Catalina detachment fault and its underlying cataclasite fault-rock unit. The cataclasite forms a resistant 7-m-thick ledge, the upper surface of which is the Catalina detachment fault surface (CDF in Fig. 4-3A). Upper-plate strata exposed at this location are Pennsylvanian–Permian limestone-dominated strata (P in Figs. 4-3A and 4-3B) (Davis and Frost, 1976). Directly beneath the detachment surface, there is cataclasite (C in Figs. 4-3A and 4-3B), the upper ~50 cm interval of which is coated with brown-weathering iron oxides. Most of the cataclasite ledge weathers gray and is marked by spaced listric faults of apparent normal separation (LF in Figs. 4-3B and 4-3C). Within the cataclasite, there are visible expressions of not-fully-overprinted brownish-weathering CPC. Beneath the cataclasite ledge is the CPC fault rock unit (Fig. 4-3B). The presence of this CPC is revealed by a subtle relict compositional banding, which is a vestige of the original mylonitic compositional banding that was overprinted by cataclastic deformation (CB in Fig. 4-3C). The apparent dip of the relict compositional banding is moderately steep to the north, in contrast to the base of the cataclasite ledge, which dips shallowly southwest.

Fresh gray cataclasite is particularly well exposed in a small abandoned "dog-hole" pit from which a small volume of the rock had been extracted in the late nineteenth and early twentieth centuries (Fig. 4-4A). The trace of the Catalina detachment fault passes along the top of the ledge of cataclasite. The texture of the cataclasite is that of a cohesive random-fabric fault rock, with rounded to angular quartzofeldspathic clasts set in a very fine-grained matrix (Fig. 4-4B). In outcrop, the cataclasite appears to be completely homogeneous, but the macrophoto of cataclasite (Fig. 4-4C) reveals a distinctive band of (largely) black ultracataclasite (*bu*), within the larger volume of cataclasite, suggesting that progressive faulting and comminution produced this fault rock. Late-stage fractures cutting the cataclasite are coated with epidote (e in Fig. 4-4C). At microscopic scale, mylonite fabric is preserved within some porphyroclasts (Fig. 4-5).

DiTullio (1983) described two basic varieties of the cataclasite in the Saguaro Loop area, one light colored and the other dark green to black. The lighter-colored variety has, on average, slightly less matrix (~50%–80%) than the darker variety (70%–90%). The matrix in both is very fine grained (1–5 μm). As determined through X-ray diffraction, the mineralogy in the lighter-variety matrix is quartz, feldspar, chlorite, and sericite. In the darker variety, the matrix contains disseminated very fine-grained (5–10 μm) chlorite; feldspar is absent. Tiny clasts in the light and dark varieties of the cataclasite are angular to rounded, averaging several millimeters.

ULTRACATACLASITE

Ultracataclasite substitutes for cataclasite in two outcrop areas in the Saguaro Loop and Loma Alta subareas, the only known outcrop areas of this fault-rock unit in southeastern Arizona. The outcrop exposure of ultracataclasite in the Saguaro Loop subarea is on the plunging nose of the Tanque Verde antiform (Fig. 3-2). Within the Loma Alta subarea, the outcrop expression of black ultracataclasite is located on the lower part of the southeast limb of the Tanque Verde antiform (Fig. 3-3). Though exclusively black in the Loma Alta subarea, the ultracataclasite in the Saguaro Loop subarea has some beige expressions



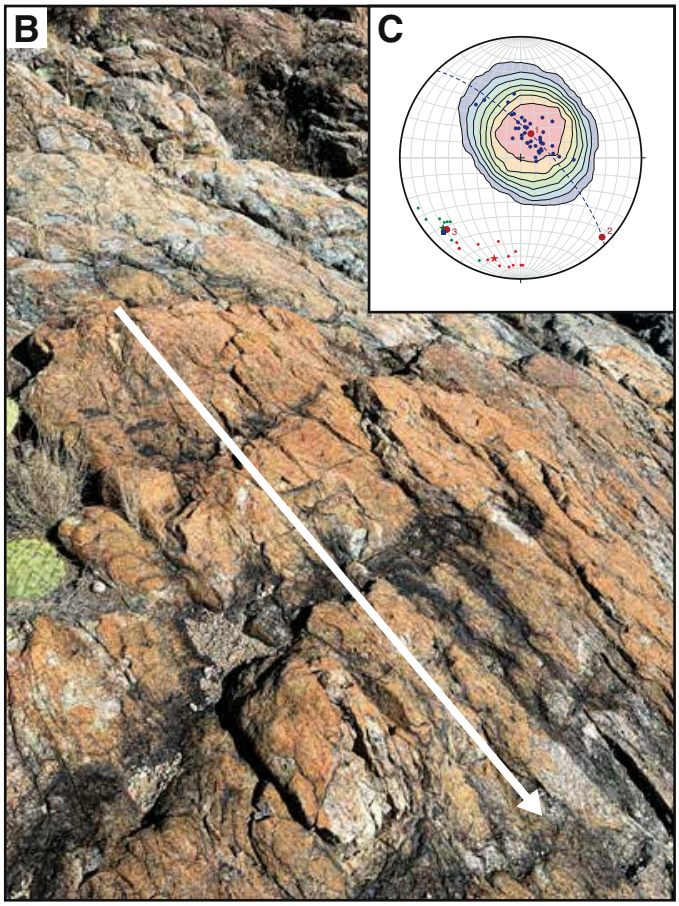


Figure 4-2. (A) Northwest-directed photograph of the Catalina detachment fault and underlying cataclasite and chloritic protocataclasite (CPC) in Charlie's Wash in the Posta Quemada–Hidden Spring subarea (Fig. 3-6). The trace of Catalina detachment fault lies at the interface of sand and blue-weathering bedrock in the middle-left part of photograph. Note geologist (circled) for scale. Lower-right corner of photograph captures the common outcrop character of CPC. (B) NE-directed photograph of polished mullion along upper surface of the Catalina detachment surface in Charlie's Wash. Photographs are by Peter L. Kresan © www.kresanphotography.com. (C) Stereographic projection presents 40 poles to mullion surfaces, which disclose an overall mullion orientation plunging ~15°/245°. Slickenlines (12) are also plotted, averaging ~195°, i.e., more southerly than the mullions proper. Scale length of white arrow, which represents sense and direction of transport, is equal to ~1 m.

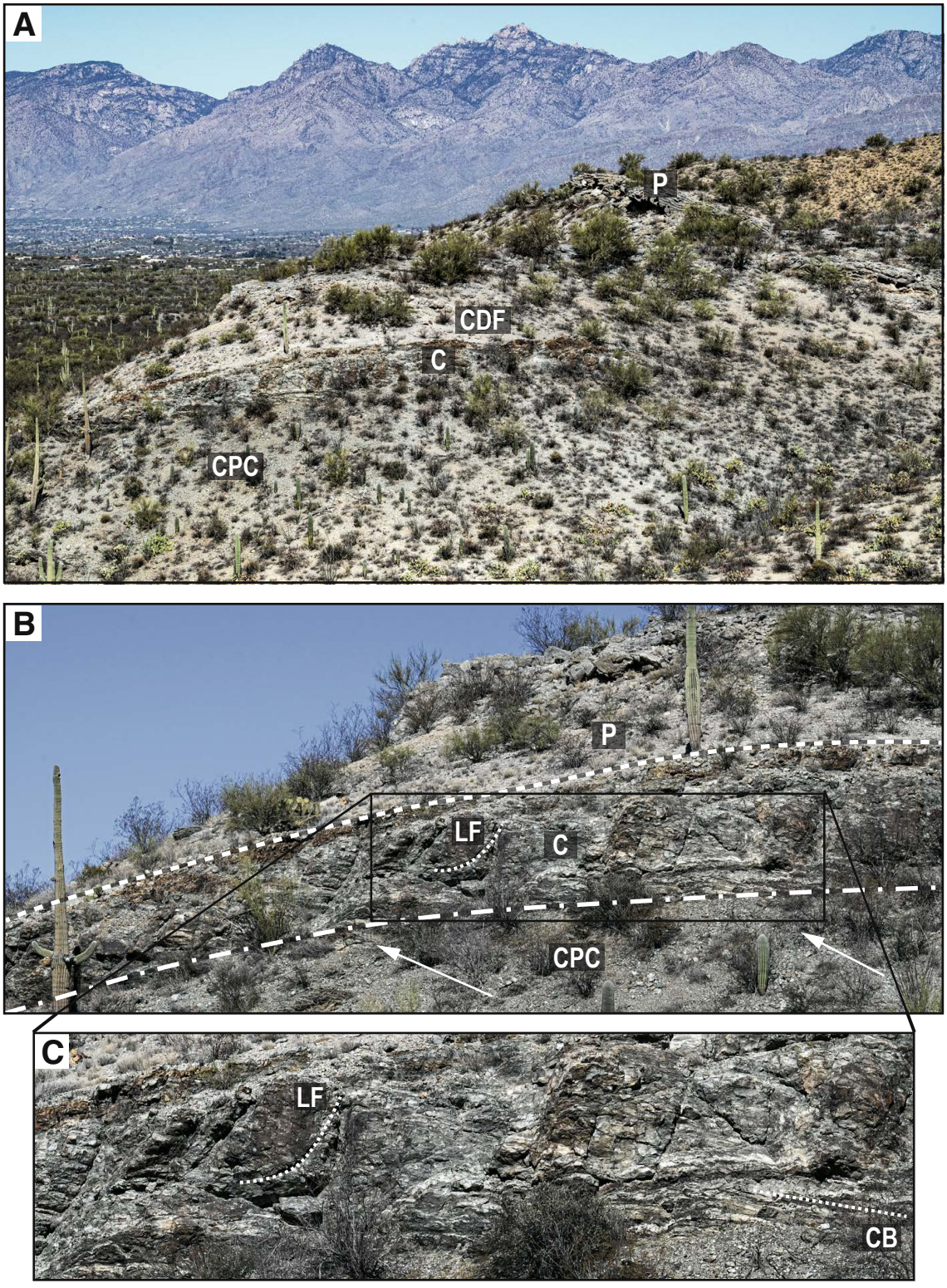


Figure 4-3. (A) NNW-directed photograph of Catalina detachment fault surface (CDF) in the Saguaro Loop subarea. The fault surface is underlain by a ledge of cataclasite (C) and overlain by upper-plate Paleozoic limestones (P). Chloritic protocataclasite (CPC) is poorly exposed within the frame of this photograph; it occupies the slope beneath the base of the resistant cataclasite ledge. The Catalina Mountains dominate the skyline. A similar photo of this ledge appears in Davis (2013, fig. 7). Width of field of view is ~125 m. (B) Closer view of the cataclasite ledge. Saguaro cactus on far-left stands ~5 m high. Trace of detachment fault is shown as dashed white line. Upper plate is the Paleozoic limestone (P). Note the underlying ledge of cataclasite (C), and chloritic protocataclasite (CPC) beneath the cataclasite. Height of rectangular box is ~3 m. (C) Numerous discrete listric normal faults (LF) cut the cataclasite. One is highlighted. On far right, along bottom of ledge, there is expression of overprinted mylonitic compositional banding (CB) within CPC. Note the angular discordance between this banding and the orientation of the base of the cataclasite.

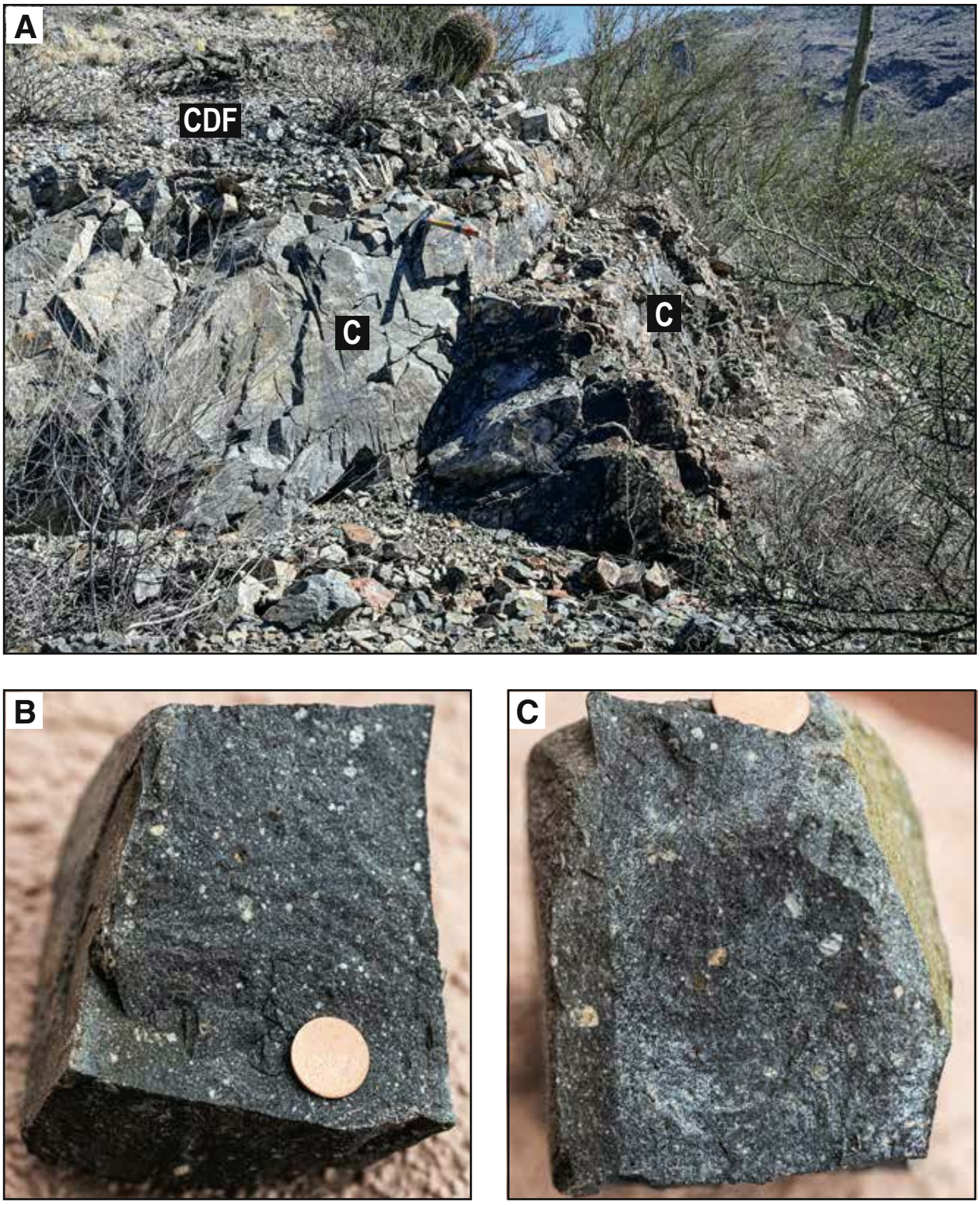


Figure 4-4. (A) Fresh cataclasite in tiny quarry pit directly beneath the Catalina detachment fault (CDF, highlighted). Rock hammer, for scale, lies just beneath the trace of the detachment fault. All of the resistant rock, including that which is "rusty" weathering, is cataclasite (C). (B) Macrophoto of hand specimen of the cataclasite. Copper disc is 1 cm in diameter. Random fabric of angular to rounded quartzofeldspathic clasts is embedded in an extremely fine-grained matrix. (C) This macrophoto of the cataclasite reveals a distinctive band along the left border that appears to be superposed cataclasis on the main volume of the rock (highlighted). Upper-right surface is coated with epidote (also highlighted). Height of sample is 6 cm; width of sample is 4.5 cm.



Figure 4-5. Photomicrograph of the cataclasite shown in Figure 4-4 under cross-polarized light. Porphyroclast in center is large enough to reveal overprinted mylonitic fabric. Rock is composed of fine-grained (~100 µm) highly angular small clasts suspended in a dark finer-grained matrix. Smaller clasts have distinctive angular morphologies compared to that of the larger clasts (200 µm–2 mm), which are more rounded. Clasts are predominantly feldspar or fine-grained quartz. Alteration of clasts commonly includes fine-grained muscovite and chlorite, which are mostly confined to clast boundaries. Small percentages of the clasts (<5%) are individual chlorite and epidote grains. Mylonitic fabrics are cataclastically and protocataclastically damaged.

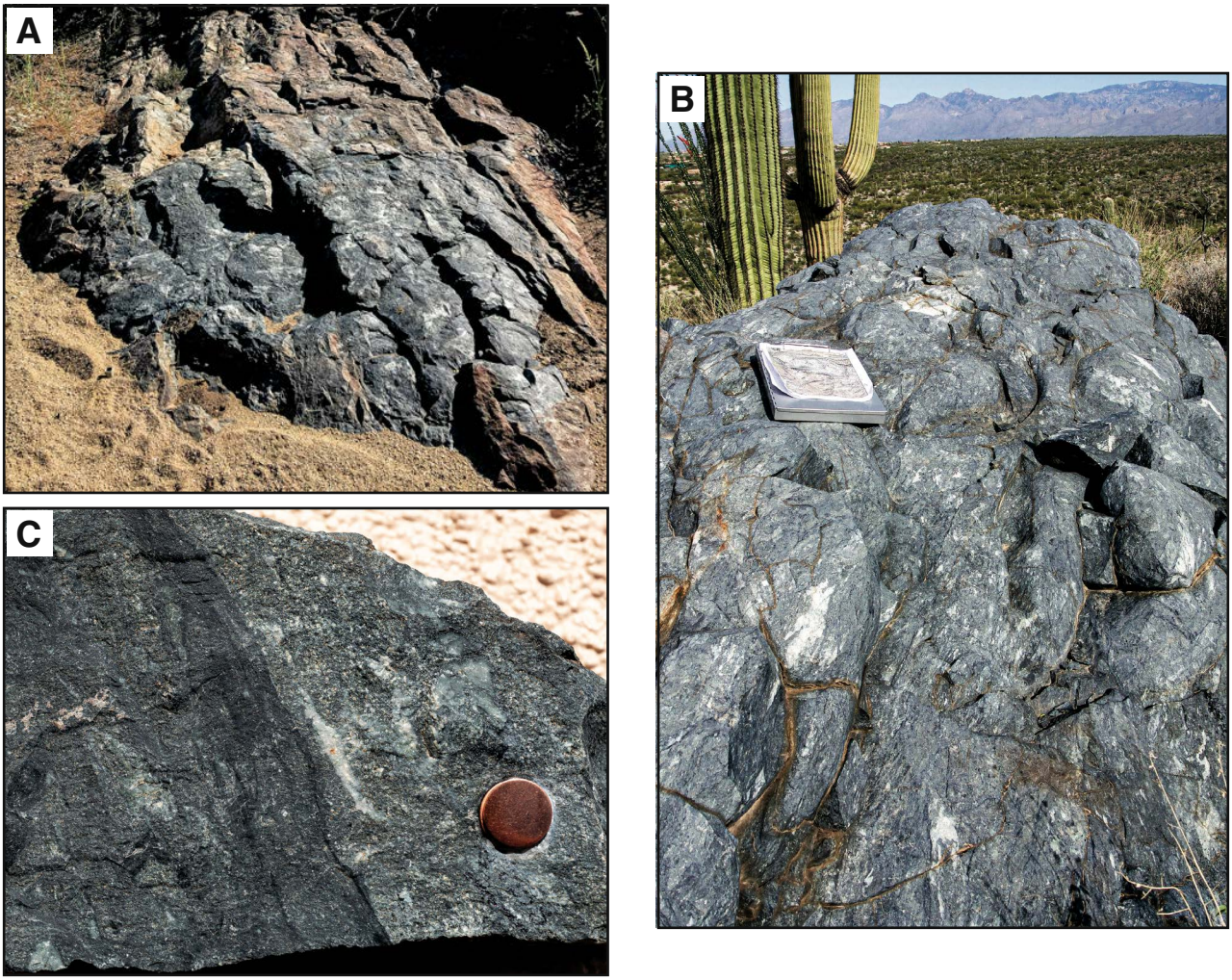


Figure 4-6. (A) NE-directed photograph of mullioned outcrop of black ultracataclasite at the very toe of Tanque Verde Ridge in the Saguaro Loop subarea (Fig. 3-2). This outcrop lies just 2 m below the Catalina detachment fault. Splotchy white relict protolith of cataclasite is evident on fresh surfaces, and this property is characteristic of the ultracataclasite. Note that at least some of the ultracataclasite weathers to a rusty brown. Width of outcrop is ~3 m. (B) Close-range photograph revealing the complexity of the internal fabric of the black ultracataclasite. The abundant silvery to white splotchy areas are cataclastic relicts of not-completely-overprinted quartzofeldspathic protolith, probably chloritic protocataclasite (CPC). (C) Macrophotograph of thin black shear zone seams of ultracataclasite that cut through the volume of rock and compartmentalize the ultracataclasite into tiny structural domains. Copper disc is 1 cm in diameter.

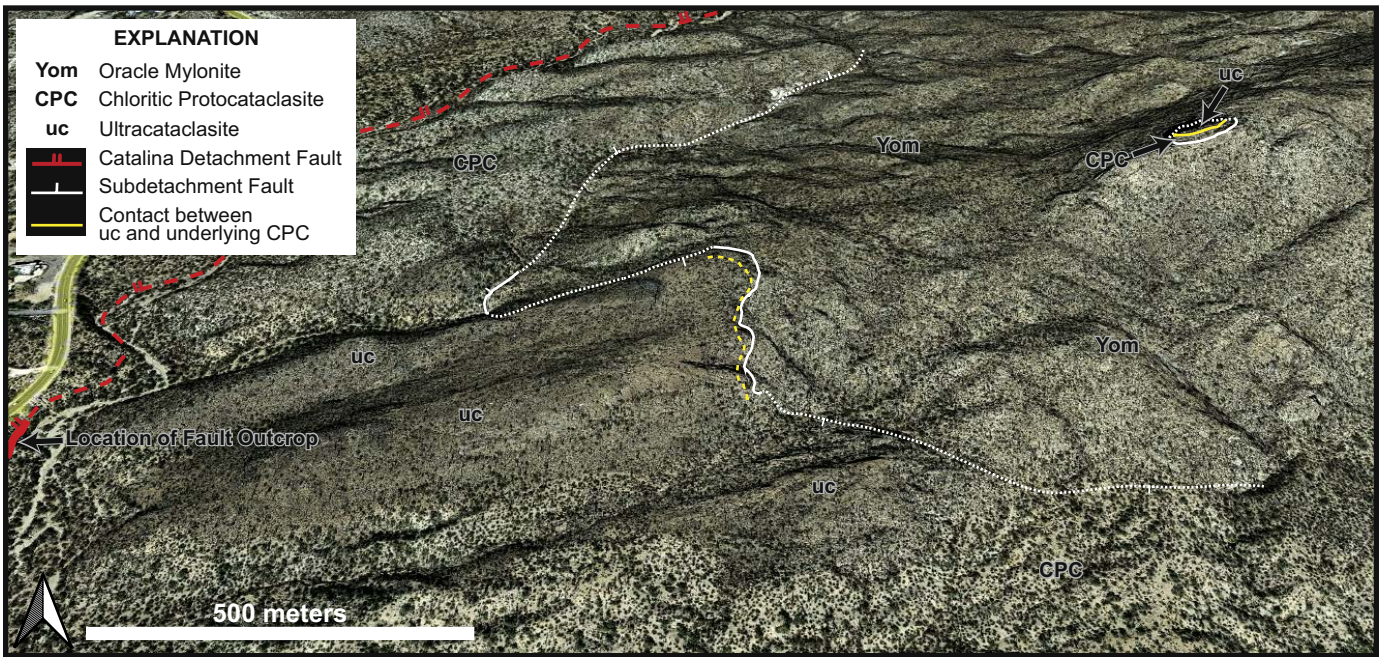


Figure 4-7. N-directed aerial-oblique Google Earth view of the "toe" region of the Tanque Verde antiform. Dark-weathering rock is ultracataclasite (uc), underlain by chloritic protocataclasite (CPC). The subdetachment fault separates CPC from underlying mylonite. Note extensional klippe higher on the ridge (right side of image). The geology of this area was mapped at large scale by DiTullio (1983) and Gregorski et al. (2019).

as well (DiTullio, 1983; Gregorski et al., 2019). The map pattern of the ultracataclasite in both of these subareas conveys a generally tabular form, parallel to the overall orientation of the detachment surface. The ultracataclasite ranges up to ~30 m thick, i.e., much greater than that of the cataclasite, which is typically no more than ~5 m thick.

Within the Saguaro Loop subarea, the exposed ultracataclasite fault-rock unit is ~30 m thick and expresses, locally, a rounded to crude mullion-like morphology (Fig. 4-6A). Thin (<0.5 cm) reddish-rust-brown Fe-rich oxidized rinds are commonly found on weathered surfaces. The ultracataclasite is neither foliated or lineated, nor marked by slickenlines. Within outcrops of the black variety of ultracataclasite, there are cm-scale silvery frosted wisps of cataclasite. These appear to be disrupted clasts of quartzofeldspathic cataclasite (Fig. 4-6B). Individual grains of feldspar and ribbons of quartz are recognizable with the aid of a 10× hand lens. Within these leucocratic cataclasite clasts, there are discrete, tiny, fold-like forms. Additionally, very thin (2 mm or less) black seams of extremely fine-grained ultracataclasite can be observed (Fig. 4-6C). These appear to be late-stage ultracataclasite shear zones that compartmentalized the ultracataclasite into small domains marked by contrasts in the abundance and character of relict clasts of quartzofeldspathic cataclasite.

Ultracataclasite is well exposed at the southwest plunge end of the Tanque Verde antiform (Fig. 4-7). DiTullio (1983) and Gregorski et al. (2019) mapped its distribution. Both mapping efforts determined that the ultracataclasite presents a subtle layering evident in some outcrop areas, and these were interpreted by DiTullio (1983) as representing superposed generations of ultracataclastic fault rock. Gregorski et al. (2019) distinguished beige and black expressions of ultracataclasite, though there does not appear to be a coherent ordered sequence. The black ultracataclasite at this location is finer grained than the beige variety, with 0.5–5 μm grains comprising 80%–90% of the rock (DiTullio, 1983). Ultracataclasite is in direct contact with underlying CPC, which in turn is separated from underlying O-mylonite by a subdetachment fault zone. Ultracataclasite occurs several hundred meters up the ridge as an extensional klippe (Fig. 4-7). The attitude of the ultracataclasite layering is essentially parallel to both the lower-plate mylonitic foliation and the overlying Catalina detachment fault surface. The preferred orientation of the penetrative mineral lineation in the O-mylonite, i.e., ~240°, is parallel to the plunge and trend of the Tanque Verde antiform and to the interpreted slip direction on the Catalina detachment fault.

In the Loma Alta subarea, the black ultracataclasite fault rock covers a broad area (Fig. 3-3) and produces a ledgy landscape (Fig. 4-8A). Rust-brown veneers coat the highly weathered surfaces, but spalling of the rock reveals the fresh black (though splotchy) ultracataclasite. The fresh rock displays an aphanitic matrix, within which tiny chips and clasts of quartzofeldspathic rock occur, as well as larger, irregular, splotchy fragments of not-fully-comminuted material (Fig. 4-8B).

In thin section, the ultracataclastic nature of this hard, dense rock is impressive given the pervasive comminution (Fig. 4-9).

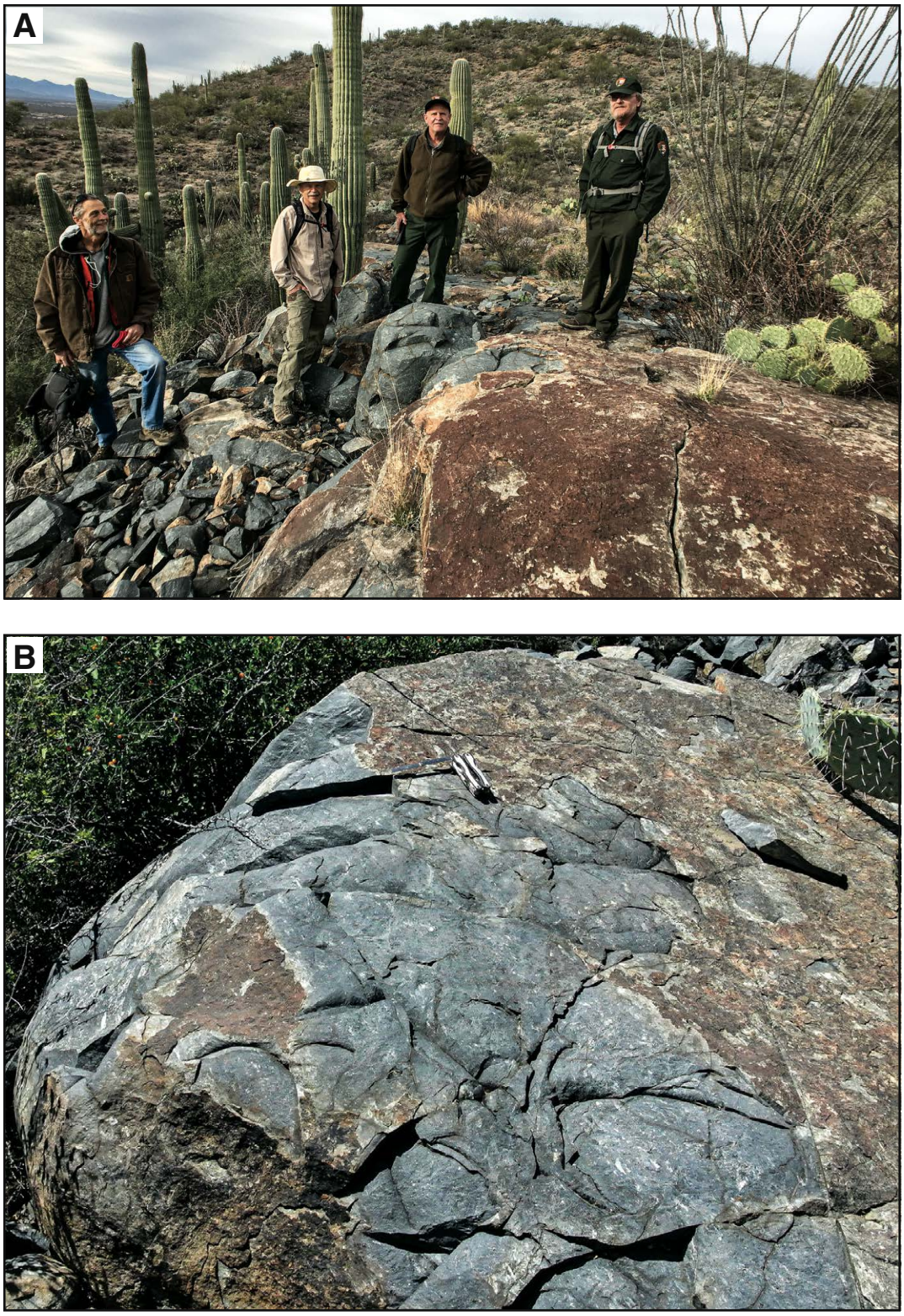


Figure 4-8. (A) Ledgy expression of black ultracataclasite in the Loma Alta subarea. This strong massive fault rock, which is black and shiny on fresh surfaces, weathers in a way marked by Fe-rich rust-colored rinds. The investigators (from left to right) are George Gehrels (University of Arizona LaserChron Laboratory), Jon Spencer (Arizona Geological Survey), Don Swann (National Park Service biologist), and Ron Beckwith (National Park Service archaeologist). (B) Close-range photograph showing relict patches of incompletely comminuted cataclasite protolith (white "fragments"). Knife for scale is 12 cm long.

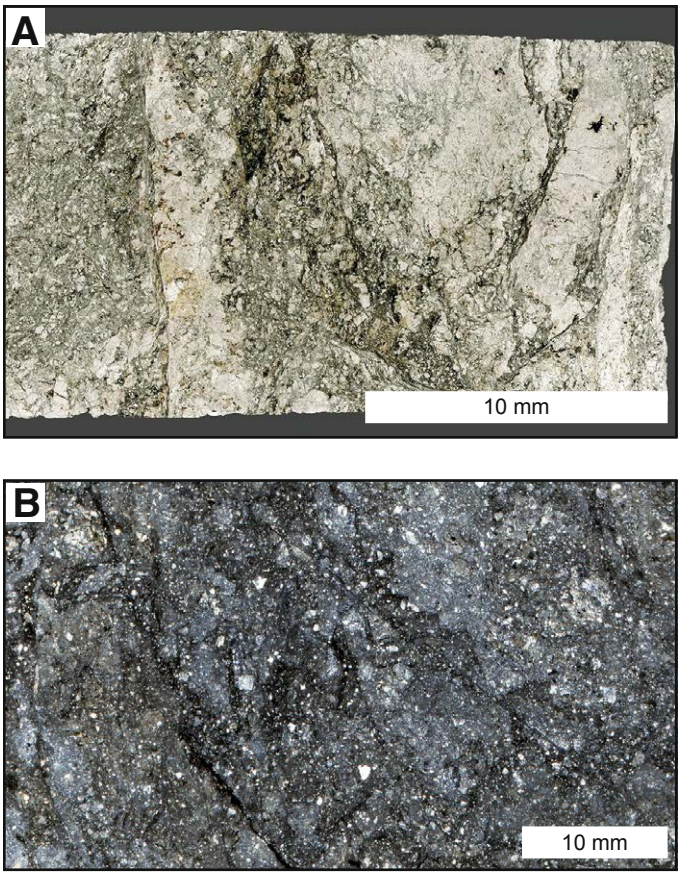


Figure 4-9. (A) Full thin-section scan of fabric character of beige ultracataclasite collected in the Saguaro Loop subarea on plunge nose of the Tanque Verde antiform. Internal faulting and shearing are evident within the fault rock, displaying a domainal internal structure marked by different degrees of comminution. Banded appearance is derived from multiplicity of brittle shear zones. Sample TTT59A. (B) Full thin-section scan of fabric character of black ultracataclasite collected in the Loma Alta subarea. Thin shear bands are evident, as well as pervasive chips and clasts of quartzofeldspathic rock. Sample GD 10-16-20-F1. (C) Photomicrograph of beige ultracataclasite. The internal fabric of some of the clasts is revealed, notably displaying some preservation of mylonitic foliation. Location of sample is Saguaro Loop area. Sample TTT59A.



Figure 4-10. Photograph of outcrop of black ultracataclasite. Hohokam petroglyphs were scratched through desert varnish (rust color) that coats fresh black bedrock. Foreground contains abundant small sharp-edged rocks, some of which were used by Hohokam people as knives and scrapers. Published with permission of Saguaro National Park, Rincon Mountain District. Width of field of view is ~4 m.

Full thin-section scans of the ultracataclasite revealed an overall random-textured distribution of fine clasts of cataclasite, ghost-like light gray areas of original clasts, and ultracataclastic seams that superficially resemble pseudotachylyte (Figs. 4-9A and 4-9B). Other common features are angular to rounded porphyroclasts (30 μm to 2 mm) of quartz and feldspar set in a very fine-grained matrix (5–15 μm) (Fig. 4-9C). The clasts display relict ultramylonitic and mylonitic fabrics, though some clasts appear to be somewhat recrystallized random-fabric aggregates of μm-scale grains from the cataclastic protolith. Chlorite, as well as recrystallized quartz, pervades the very fine-grained matrix (DiTullio, 1983). Larger grains (several mm in diameter) terminate sharply at contacts with chlorite-rich matrix. Fragments are angular and overall do not display systematic alignment(s). Photomicrographic evidence of multiple generations of fragmentation events shows fragments within fragments, and clasts within clasts. This fine-grained matrix locally behaved as an injectite, creating ultracataclasite seams and veins (DiTullio, 1983).

SUMMARY

Cataclasite and ultracataclasite are random-fabric fault-rock units that were generated by extreme comminution associated with top-to-the-SW translation of upper-plate rocks on the Catalina detachment fault. Thin smears of gouge are preserved in places along the upper surface of the Catalina detachment fault, reflecting extreme grinding of upper-plate rock during tectonic transport. The protolith for the cataclasite and ultracataclasite was CPC, which had been fashioned through cataclastic deformation of mylonite.

The ultracataclasite was of practical value to the Hohokam People dwelling in the Rincon Mountains region ca. 500–1450 A.D. (Don Swann, 2022, personal commun.). The obsidian-like, black ultracataclasite fragments were used as very sharp blades. Outcrops commonly are coated with thin veneers of brown Fe-oxide patina, rendering the surfaces ideal for the Hohokam penchant for fashioning petroglyphs (Fig. 4-10).

CHAPTER 5

Chloritic protocataclasite and minidetachment faults

INTRODUCTION

In considering the progressive structural evolution of the Catalina detachment zone, the structural significance of the chloritic protocataclasite (CPC) (traditionally referred to as "chlorite breccia") fault-rock unit is one of the most strategic ingredients. In comparison with the state of understanding of fabrics and deformation mechanisms associated with mylonitization, cataclasis, and fault slip, the properties, origin, and significance of CPC are much less researched by the geoscientific community. Observations and interpretations are presented here regarding the nature of this core-complex fault rock, including upper and lower contacts, fabrics, alteration, fracturing, shattering, internal faulting (including minidetachments), and bulk fault rotation of original mylonites. To paraphrase and reemphasize a point made in Chapter 1, CPC represents a kinematic and rheological linkage between the structural transition from crystal-plastic deformation of underlying mylonites to elastic-frictional deformation of overlying cataclasite and ultracataclasite.

UPPER CONTACT OF CHLORITIC PROTOCATACLASITE

The upper contact of the unit of CPC, though generally sharp, is seldom exposed. It lies directly beneath cataclasite, though almost everywhere this contact is marked by poor outcrop due to weathering and degradation of the CPC. However, even where not discretely exposed, mapping of cataclasite and underlying CPC tightly constrains the position of this contact, which is parallel to the Catalina detachment fault. This is clear at the Saguaro Loop subarea "type locality" (Davis, 1987b, 2013), where the Catalina detachment fault and its underlying ~7-m-thick distinctive ledge of cataclasite are well exposed (Fig. 4-3). The upper contact of the CPC unit, located ~1 m below the base of this ledge, is recognizable because of its less-resistive form, bluish-green hue, and the presence of relict mylonitic compositional layering that dips more steeply than the base of the cataclasite.

A particularly compelling exposure of the upper contact of CPC occurs along Charlie's Cliff (CC in Fig. 3-6) in the Posta Quemada–Hidden Spring subarea (Fig. 5-1A). The trace of the Catalina detachment fault is positioned at the base of the upper-plate strata (predominantly Upper Paleozoic carbonates) and is expressed by the very gently inclined trace represented by a light-gray rock bench that directly underlies the fault trace (Fig. 5-1B). The rock bench reveals its typical mottled green and light-gray banding (Fig. 5-1C). The banding is a relict compositional banding that persevered through protocataclastic overprinting of mylonite. The angular discordance between the gently inclined Catalina detachment fault and the moderately inclined compositional banding in underlying CPC reveals that the detachment fault slashes through older, now discordant, fabrics and structures.

FABRICS AND ALTERATION

The CPC is blue/green in fresh exposures along drainages but weathers to a dark rusty brown (Figs. 5-2A and 5-2B). These hues reflect pervasive Fe- and Mn-oxides and the presence of chlorite and epidote as retrograde alteration products of the breakdown of K-feldspar and biotite. Because most outcrops are highly weathered and thus dark brown, quartz-rich compositional bands, which did not experience chlorite-epidote alteration, tend to be visible (Fig. 5-2C). Fault truncations and offsets of relict compositional bands underscore the degree of internal structural disruption and rigid-body rotation. These compositional bands are expressions of protocataclastically overprinted mylonite. Their presence confirms that the protolith is mylonite. Many outcrops display overprinted, though recognizable, mylonitic fabrics and structures (Fig. 5-3). The fabric orientations of relict foliation and lineation tend to be highly variable, departing from the tightly preferred orientations of foliation and lineation in underlying mylonite. This contrast underscores the subsequent rotation of mylonitic fabrics from that of original attitudes via brittle overprinting. Though constituting less than ~10% of the rock by volume, the most intensely deformed CPC is true cataclasite, marked by such a high degree of comminution that the rock is aphanitic, absent any macroscopic vestiges of relict mylonitic foliation and lineation.

At the microscale, varying degrees of protocataclastic and cataclastic deformation are evident within this CPC (Fig. 5-4). The preserved presence of relict mylonite fabrics is a reminder of the crystal-plastic fabrics, such as dynamically recrystallized quartz comprising quartz ribbons, that have been overprinted by brittle deformation. Protocataclastic deformation occurred in a lower-temperature environment in which both feldspar and quartz deformed via brittle mechanisms.

Masking of the original mylonite protolith is compounded by pervasive, synkinematic, low-grade, chlorite-dominated

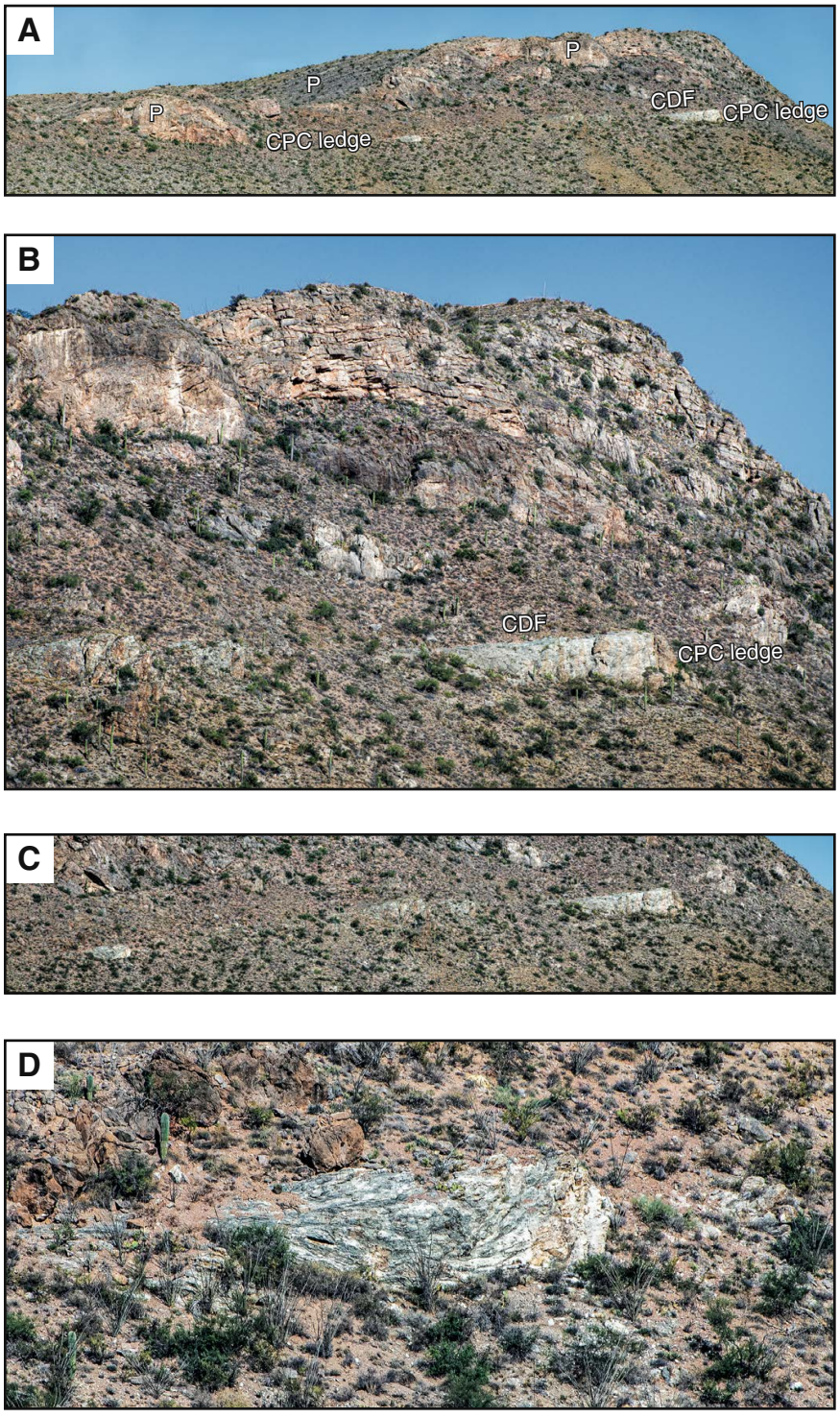


Figure 5-1. (A) East-directed photograph of Charlie's Cliff in the Posta Quemada–Hidden Spring subarea. Uppermost gray rocks are Paleozoic strata (P) of the upper plate of the Catalina detachment fault (CDF), the trace of which is inclined very gently leftward (to the south). The light-colored bench of resistant rock is uppermost chloritic protocataclasite (CPC). Width of field of view is ~900 m. (B) Closer view of the Catalina detachment fault surface, which runs along the top of the ledge of CPC and marks the base of upper-plate Paleozoic strata. Width of field of view is ~150 m. (C) This photograph captures the trace of the Catalina detachment fault, the underlying CPC, and the continuity of each. Width of field of view is ~250 m. (D) Enlargement of image of outcrop of CPC that appears on far left in part C. Note blue-green hue. Compositional banding in CPC is evident. Width of field of view is ~40 m. Photographs are by Peter L. Kresan © www.kresanphotography.com.

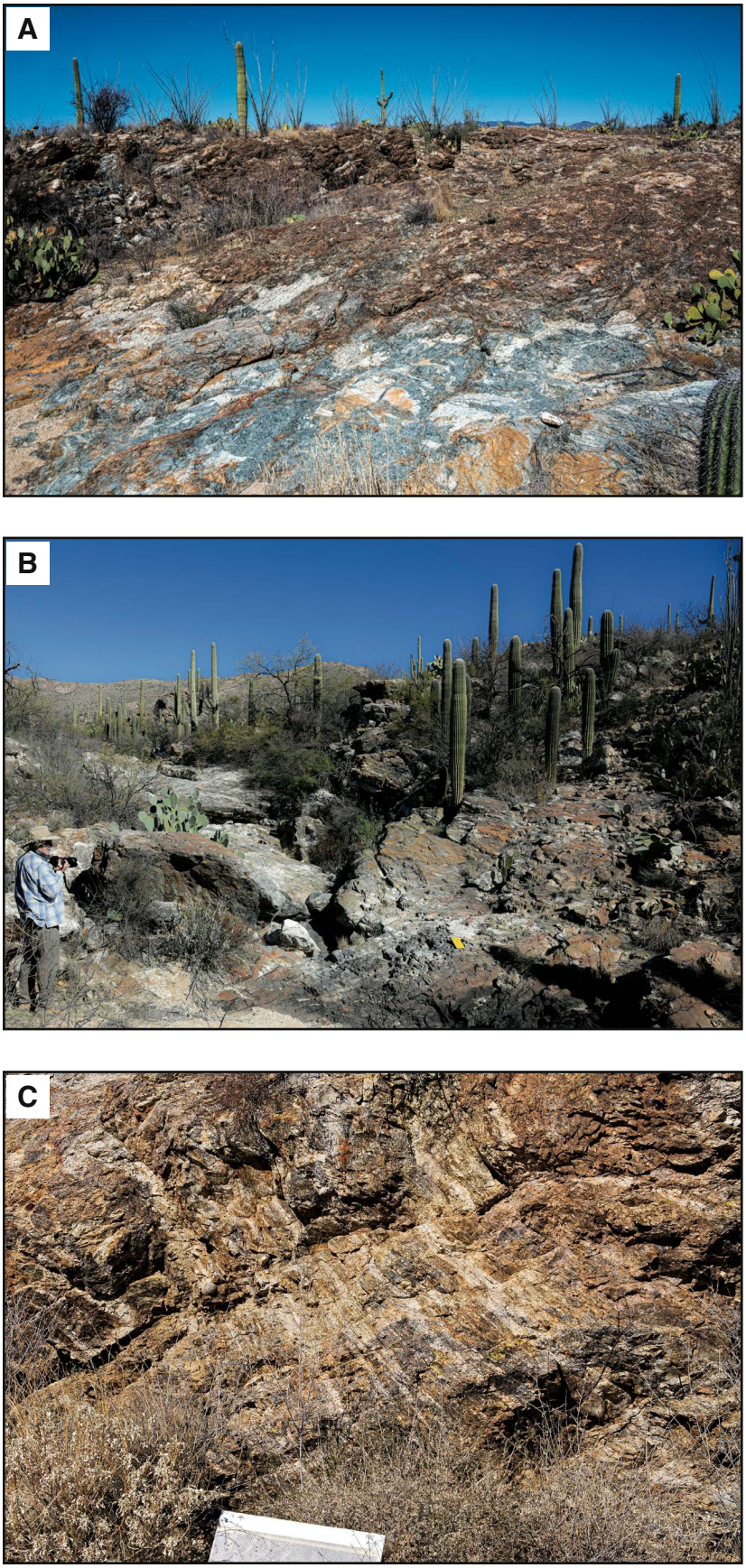


Figure 5-2. (A) Chloritic protocataclasite (CPC) in Saguaro Loop subarea. It is bluish green on fresh surfaces but weathers to a brown rust hue. Closest saguaro cactus (just left of center of photograph) is ~3 m tall, providing a reference for scale. (B) NE-directed view of rust-weathering CPC at the Charlie's Wash locality, Posta Quemada–Hidden Spring subarea. (C) Photograph of rust-weathering CPC with pervasive moderately to steeply dipping compositional banding in part related to original mylonitic fabric. Photographs are by Peter L. Kresan © www.kresanphotography.com.

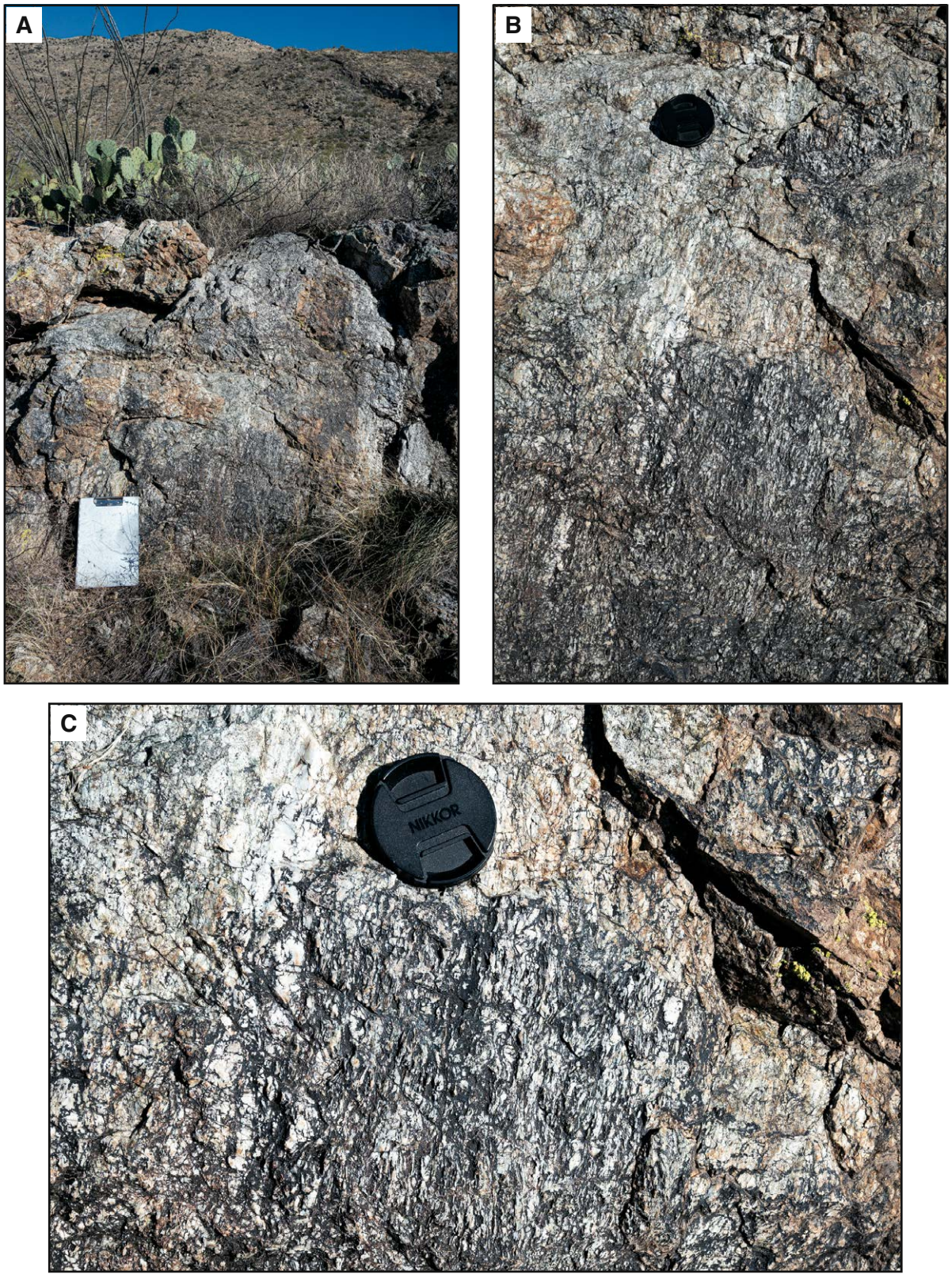


Figure 5-3. (A) Northeast-directed photograph of outcrop of chloritic protocataclasite (CPC) in Saguaro Loop subarea. Clipboard for scale (34 cm × 23 cm). Backdrop is the NW flank of the Tanque Verde antiform. The front surface of the outcrop is shown in the following parts of the figure. (B) Closer view (lens cap for scale) of the outcrop surface that reveals an intersection lineation produced by steeply dipping mylonitic foliation (trending orthogonal to strike of outcrop surface) and the weathered surface of the outcrop. (C) Yet-closer view that reveals the intersection lineation expressed as quartz ribbons truncated by the outcrop surface.

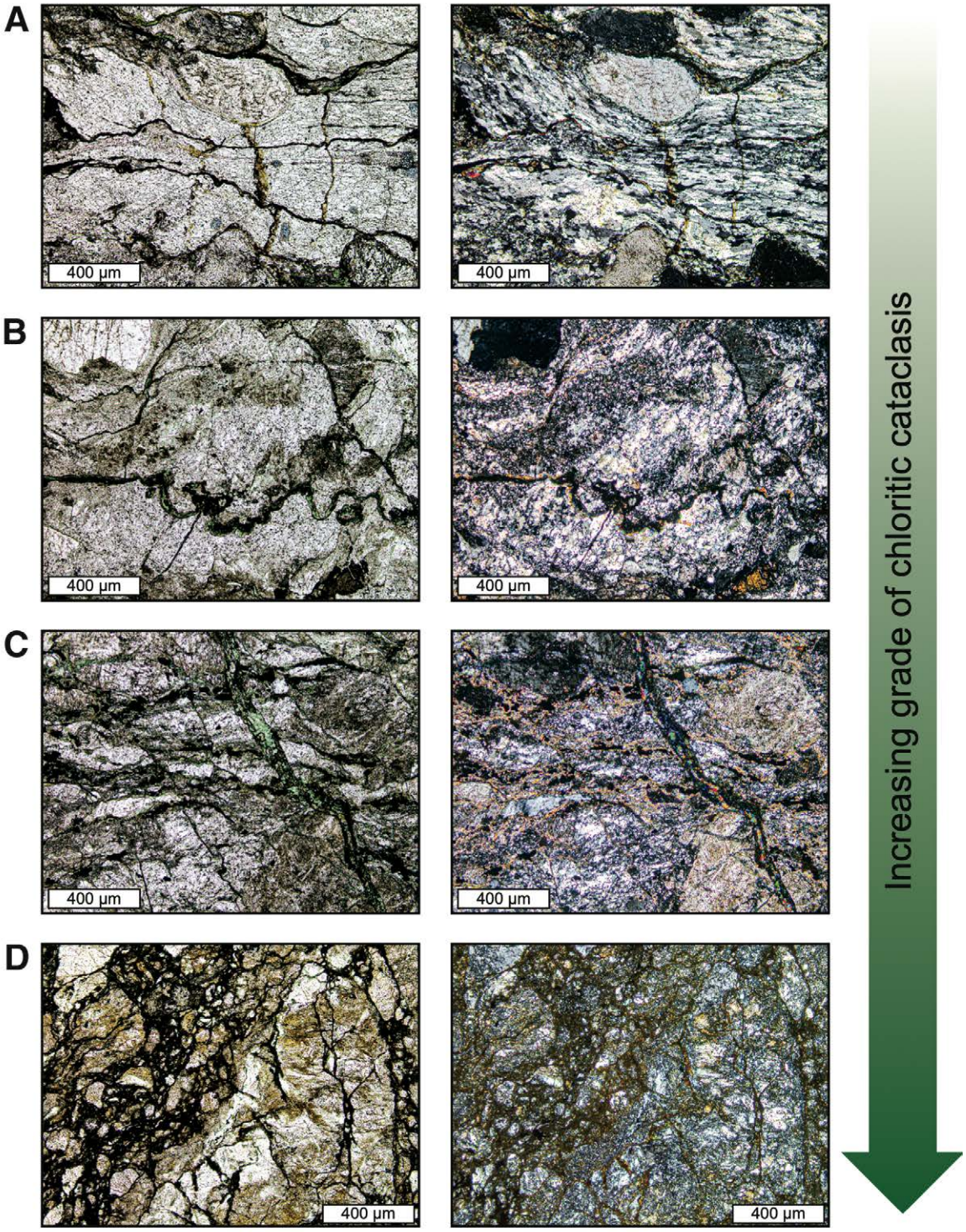


Figure 5-4. (A–D) Photomicrographs showing chloritic protocataclasite (CPC) arranged in increasing degree of fracturing and alteration. Left-hand images are in plane light; right-hand images are in cross-polarized light. (A) Mainly mylonitic foliation marked by dynamically recrystallized quartz and feldspar porphyroclasts. (B) Fractured protocataclastically overprinted mylonite. Note stylolites, which are products of dissolution creep, an aseismic deformation mechanism. The teeth-and-cone geometry of the stylolites reflects the direction of greatest principal stress. The chlorite linings are replacements of insoluble residue that collected along the sutures. (C) Thoroughly fractured and faulted mylonite and cataclastically overprinted mylonite. Note epidote veining. (D) Heavily comminuted CPC.

hydrothermal alteration (Fig. 5-4). Metamorphic core complex literature is replete with conclusions that the faulting, attrition, and comminution that fashioned "chlorite breccia" were carried out under conditions marked by voluminous circulation of hot fluids, causing hydrothermal alteration (e.g., Rehrig and Reynolds, 1980; Kerrich and Rehrig, 1987; Gottardi et al., 2018). DiTullio's (1983) investigations in the Saguaro Loop subarea included a detailed study of microfabrics and petrography of CPCs. She determined that quartz- and feldspar-dominated porphyroclasts, with or without recognizable mylonitic fabric, were reduced from sizes of ~3 cm to less than 0.1 mm. Consistent with the thin-section fabrics (Fig. 5-4), quartz expresses undulose extinction and microfracture traces. Feldspars are commonly cracked and broken along cleavage, and cleavage surfaces are sometimes kinked. Porphyroclasts float in a fine- to very fine-grained matrix of quartz, feldspar, and hematite. The percentage of matrix material increases with the degree of cataclastic damage. Alteration is primarily chloritic, but it also includes epidote, hematite, magnetite, pyrite, and manganese oxides. Chlorite occurs both as void fillings and as replacement of biotite. Release of iron to form oxides accompanied replacement of biotite and K-feldspar by chlorite, quartz, and sericite. Abundant fractures tend to be filled with 0.5- to 5-mm-sized recrystallized quartz, feldspar, chlorite, and hematite. The myriad healed microfractures and porphyroclast grain boundaries seal this brecciated rock and impart to it a cohesive integrity. Factors contributing importantly to this cohesion are the lower-temperature precipitation products, namely, Fe- and Mn-oxides, which likely are products of deep mixing of hydrothermal fluids with oxidizing meteoric waters (Morrison and Anderson, 1998; Haines et al., 2016).

INTENSIVE FRACTURING

Beyond color, alteration, and cataclasis, another dominant outcrop signature of CPC is its intensely fractured state. The overall shattered appearance of CPC is the collective expression of these pervasive, closely spaced, often irregularly oriented fractures (Fig. 5-5A). The degree of alteration is consistent with the myriad fractures that served as channels for hydrothermal fluid during protocataclastic deformation. The fractures tend to be exceedingly closely spaced and exhibit significant dispersion in their orientations and number of sets, though some regularly oriented sets are locally observed (Fig. 5-5B). While conventional joint sets typically show a systematic relationship between fracture spacing and the thickness and strength of individual mechanical units, the fractures in CPC typically display spacings much smaller than would be predicted by trace lengths or thicknesses of mechanical units. Fracture spacing is hypersaturated (Fig. 5-6A). Hypersaturated fracture densities (range IV in Bai and Pollard, 2000) generally are interpreted to reflect conditions of significant overburden, high fluid saturation, and nucleation on local mechanical heterogeneities, all of which are consistent with field observations for the CPC overprint of mylonitic fabric in this structural unit. Moreover, fracture sets in some outcrops curve and bend (Fig. 5-6B). Rarely, outcrops of CPC display penetrative parallel planar sets that might be described as joints, though once again, they exhibit hypersaturated fracture-spacing ratios. The fracture pattern captured in Figure 5-6C is such an example, and it appears to be an example of hydraulic fracturing. In addition, some outcrops are shattered into cohesive breccias (Fig. 5-6D). Such intensive fracturing appears to have been produced by evolving dynamic fluid-pressure conditions, where sustained and repeated fracturing saturated and thus continuously and pervasively damaged the mylonite protolith and its successor protocataclasite. The presence of this shattering is consistent with formation in an environment marked by voluminous hydrothermal fluids and fluxes in fluid pressure (Halfkenny et al., 1989; Kerrich and Rehrig, 1987; Morrison and Anderson, 1998).

The largest and thickest exposures of CPC are within the Posta Quemada–Hidden Spring subarea (Fig. 3-6). The dominant protolith was leucocratic protolith composed of coarse-grained plagioclase, quartz, and white mica; the protolith was locally pegmatitic. Superimposed protocataclastic deformation was achieved by brittle mechanisms marked by particularly intense fracturing. Closer to the underlying subdetachment fault system, foliation within this leucocratic CPC becomes more prominent, although still relatively weak. In places, the leucocratic rock becomes associated with banded gneissic rock displaying a strong mylonitic foliation, though the gneiss is highly fractured within the CPC. Organized slickenlined fault surfaces within CPC are rare. However, one such occurrence exists in the Posta Quemada–Hidden Spring subarea within an outcrop area we call "Fault City" (Fig. 3-6). The outcrop exposure has the rusty-weathering fracture-textured surface typical of CPC (Fig. 5-7A). Within this exposure, small-scale, discrete, and slickenlined fault and fracture surfaces are abundant. The kinematics of these faults and fractures are normal slip, based upon the combination of slickenlines, chattermarks, and small observable offsets by subsequent crosscutting slip surfaces. Many of the fault surfaces are coated in epidote, such as the conjugate normal fault surfaces shown in Figure 5-7B. Minimullions are fashioned along fault surfaces that display meter-scale offsets (Fig. 5-7C). The stereographic plot (Fig. 5-7D) of our field measurements reveals slickenlined surfaces striking ~345°, mostly dipping SW, but a number dipping NE. Slickenlines consistently trend ~245°, completely in keeping with ENE/WSW extension and southwestward tectonic transport. This kinematic record of fault-related deformation undoubtedly matches that which occurred throughout much of the progressive deformation that created the CPC fault rock unit. These particular "last-gasp" structures represent features that were never overprinted by further cataclasis. Similar such structures that formed earlier were likely overprinted by further cataclasis such that they are now difficult to recognize.

"SLOT FAULTS" WITHIN CHLORITIC PROTOCATACLASITE

Subhorizontal and somewhat irregularly curviplanar fissure-like faults of short trace lengths (up to several tens of meters)

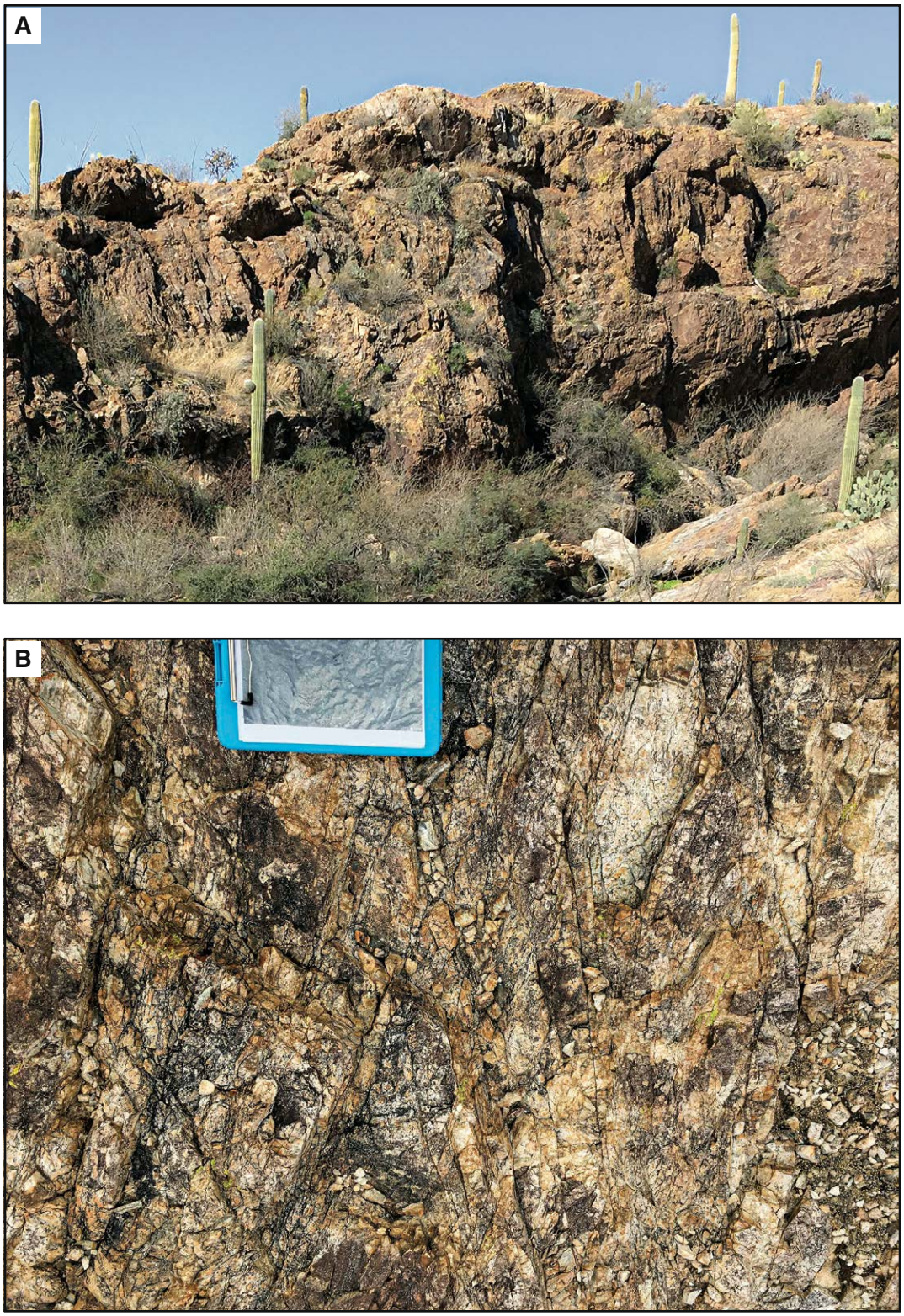


Figure 5-5. (A) Outcrop of chloritic protocataclasite (CPC) in the Loma Alta subarea. The entire rock body is marked by rust-brown weathering, disclosing the richness of its pervasive chloritic alteration. In spite of the intensity of this fracturing, the CPC in this outcrop retains a crude, gently dipping layering, perhaps reflecting original mylonitic layering. (B) Typical outcrop of altered and intensely fractured CPC. Clipboard for scale; length is ~30 cm. Protolith is mylonite. Loma Alta subarea.

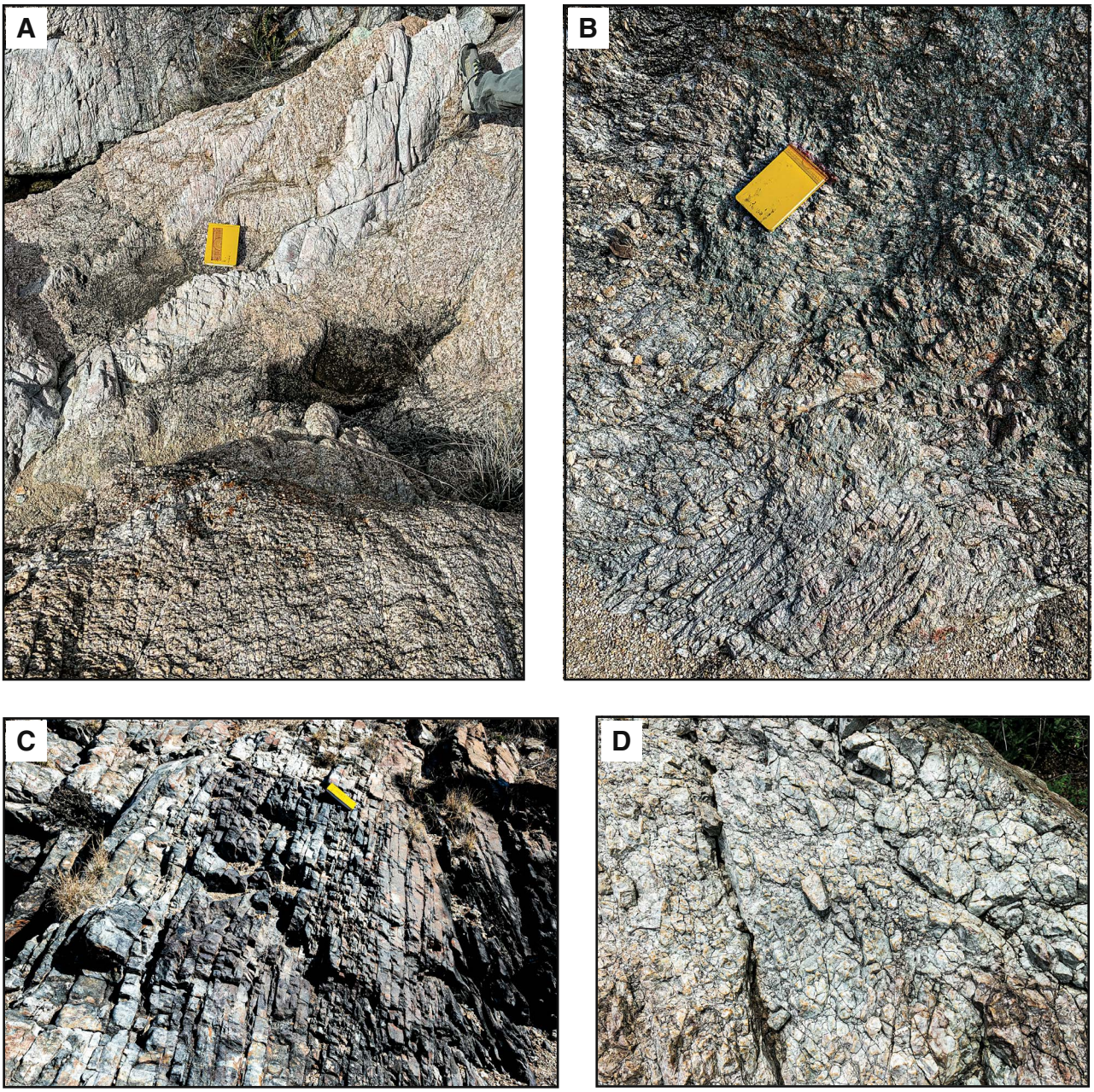


Figure 5-6. Outcrop photographs of fractured, shattered, and brecciated chloritic protocataclasite (CPC). (A) View looking downward vertically showing different degrees of fracturing and shattering within leucocratic sill-like bodies (white) and mylonite (slight orange/brown). Closest rock (lower front) is cohesive but intensely fractured. Field notebook is 19 cm long. Posta Quemada–Hidden Spring subarea. (B) Exceedingly closely spaced curviplanar fracturing in slightly bluish-green CPC in the Posta Quemada–Hidden Spring subarea. Notebook is 19 cm long. (C) Example of penetrative, planar parallel, closely spaced fractures in CPC. Such fracturing is rarely observed. The fractures are probably products of hydraulic fracturing. Field notebook for scale is 19 cm long. Loma Alta subarea. (D) Intense fracturing, bordering on brecciation, of leucocratic rock within CPC in the Posta Quemada–Hidden Spring subarea. Width of field of view is 1 m.

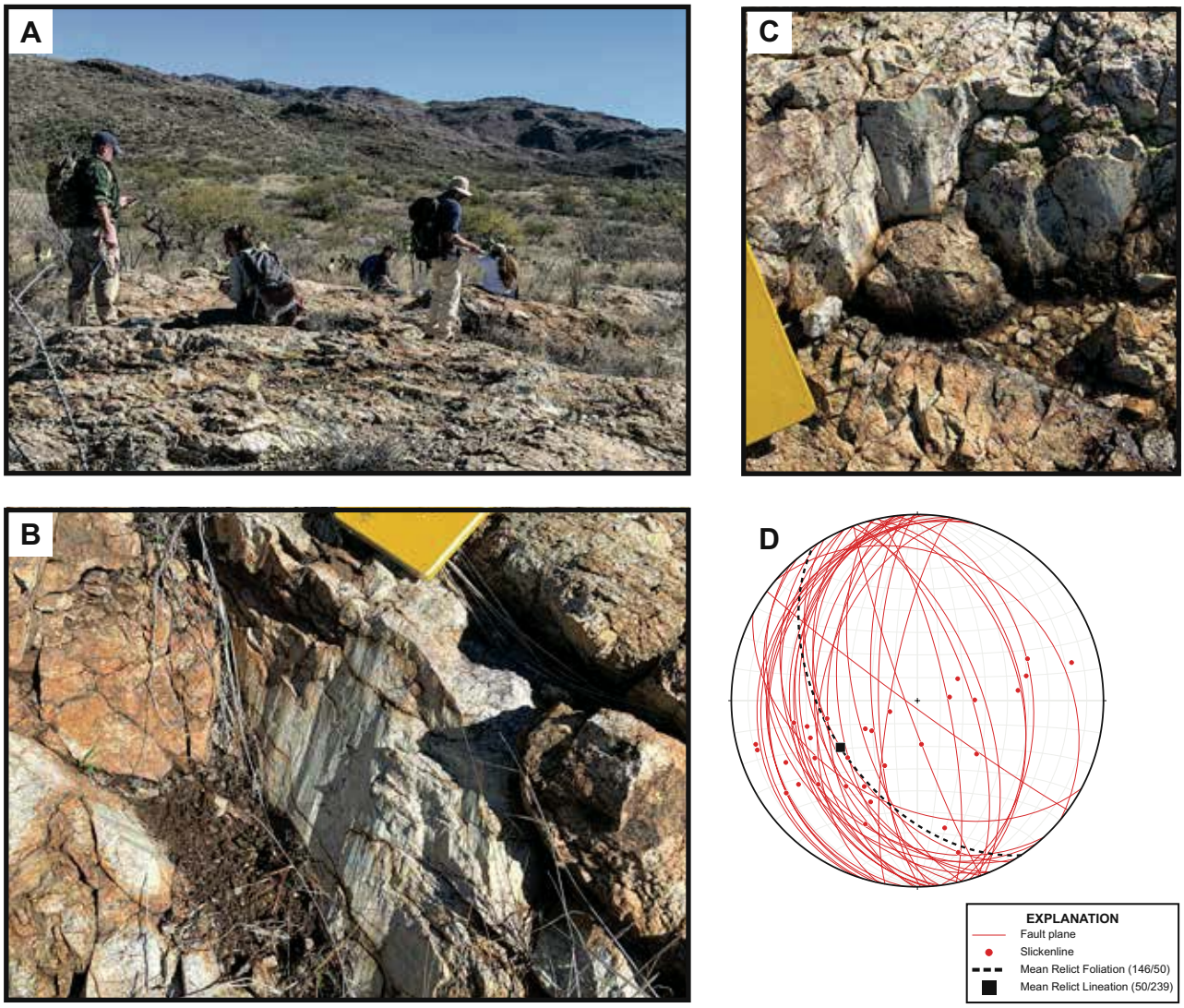


Figure 5-7. (A) Photograph of part of the "Fault City" outcrop in Posta Quemada–Hidden Spring subarea. Fault rock is chloritic protocataclasite (CPC). (B) Close-up photograph of conjugate slickenlined faults. Fault surfaces show epidote coatings. Width of field notebook is 13 cm. (C) Minimullion structures along normal-fault surface. (D) Stereographic projection of orientations of slickenlined fault surfaces and the slickenlines proper. Slickenlines trend consistently ~245°, occurring on fault surfaces that strike ~345°; dip direction is SW for most but NE for some.

are among the signature characteristics utilized in distinguishing CPC (Fig. 5-8). We call them "slot faults." Along these faults, weathering and erosion have created slot-like reentrants into the bedrock on the order of ~50 cm high and up to ~2 m deep (Fig. 5-8A) (Davis, 1980a, 1987a, 1987b, 2013). Standard fault properties such as slickenlines, grooves, or polish are absent on these features. Therefore, confirmation that they are faults is not possible through conventional criteria. However, some outcrops reveal that relict foliation (including compositional banding) preserved in the rock above and below a given slot fault is discordant, suggesting fault-related offset (Fig. 5-8B).

Slot faulting is interpreted to have taken place in a reasonably continuous, sustained manner during the creation of CPC. As a consequence, early-formed faults not only cut and rotated mylonites, but also became dismembered, accounting for the short trace lengths. The shortest and most irregularly curviplanar examples of slot faults appear to be fault-truncated, abandoned fault segments that were once much more continuous (Fig. 5-8B). The depth of slots along these faults is captured in Figure 5-8C, as is the highly damaged condition of rock both above and below the slot fault. The slots are utilized as habitat niches by desert creatures, such as desert tortoises, pack rats, and rattlesnakes.

Certain vertical exposures of CPC reveal what may be an approximation of the original properties of this faulting. Figure 5-9 shows such an example of features interpreted to be some

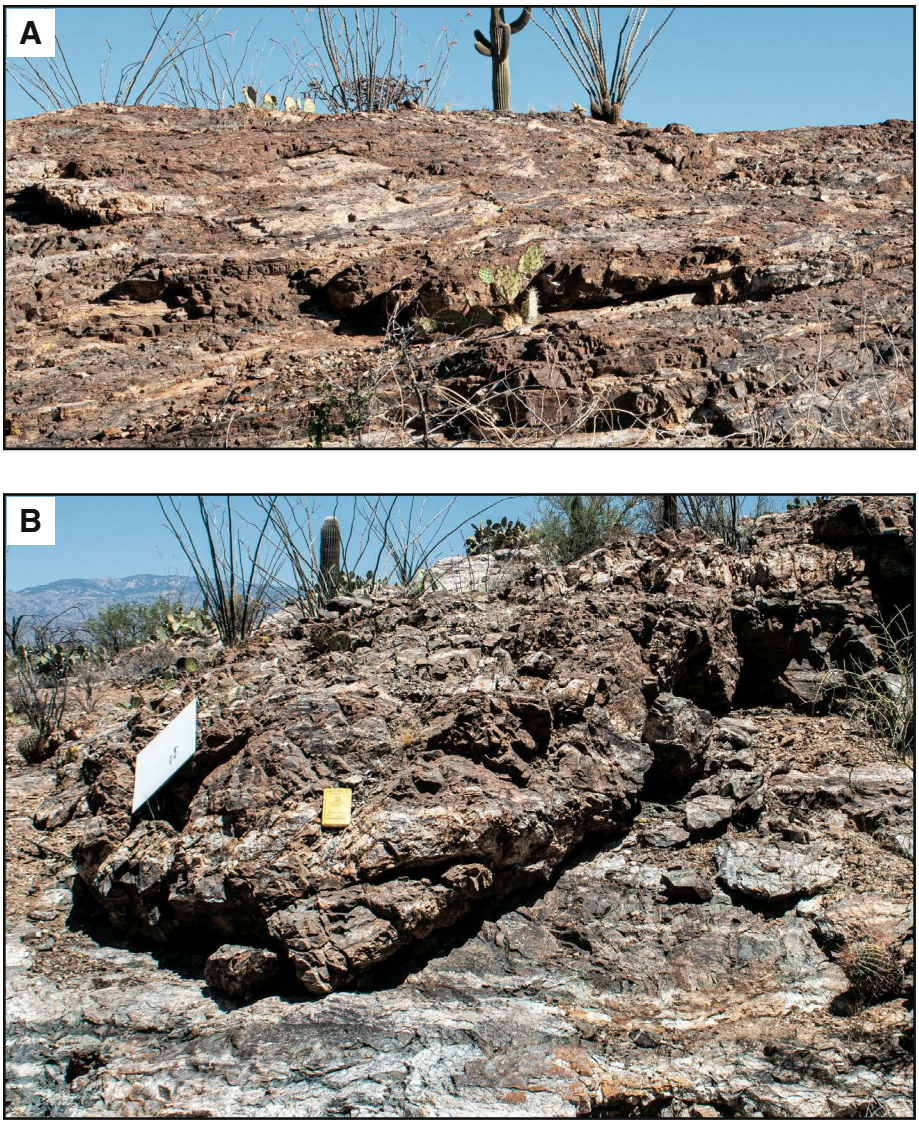


Figure 5-8. (A) Photograph of typical physical expression of "slot fault" in chloritic protocataclasite (CPC) in the Saguaro Loop subarea. In this example, the attitude of the slot fault is essentially parallel to overprinted compositional layering in CPC. (B) Photograph of irregularly curviplanar slot fault in CPC. Trace of the minidetachment is essentially the black shadow rimming the edge of this upper plate. Note discordance between compositional layering in rock above and below the fault in the Saguaro Loop subarea. (C) Photograph of slot fault in CPC in the X9 Ranch subarea. Like most examples, this slot fault is very shallowly dipping. Weathering and erosion along the trace of the fault penetrates more than 1 m. Note fractured, if not brecciated, character of the bedrock.

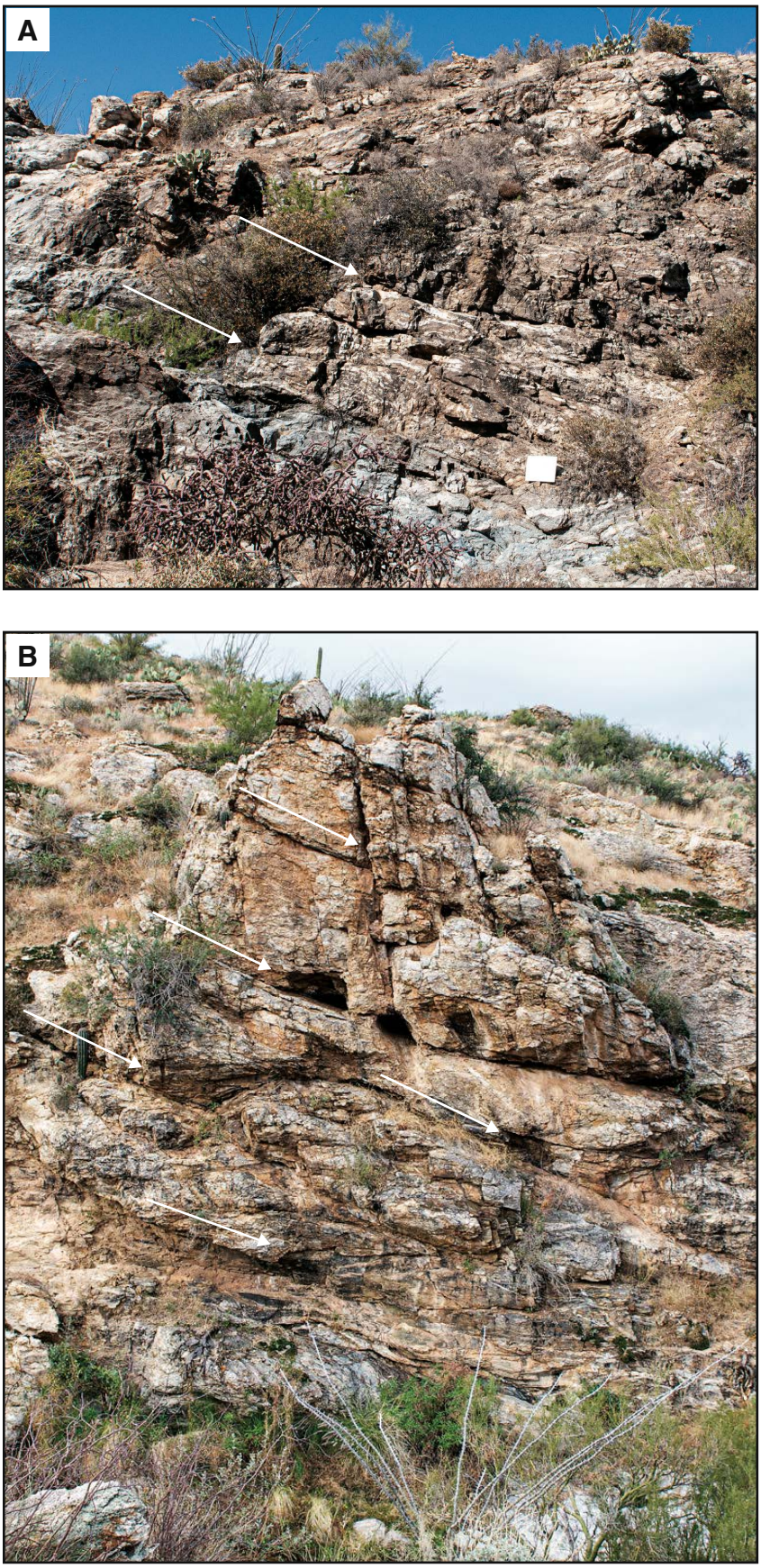


Figure 5-9. (A) South-directed photograph of minidetachment faults (noted by white arrows) in dark-weathering chloritic protocataclasite (CPC) in the Saguaro Loop subarea. Protolith is banded mylonite. The height of this outcrop is ~12 m. Several gently east-dipping minidetachment faults can be identified in this outcrop. Attitude of minidetachment faults is parallel to that of the Catalina detachment fault, the trace of which clears the top of this cliff exposure. (B) South-directed photograph of the stacking of gently east-dipping minidetachment faults in CPC. Arrows are positioned above traces of faults. Note how CPC is weathered into reentrants along parts of these faults. Height of this exposure is ~10 m. Saguaro Loop subarea.

of the latest faults to form during the progressive overprinting of mylonite by CPC. Multiple, spaced, subparallel faults are evident. The orientations of these faults are subparallel to the Catalina detachment fault, which projects above each of these outcrop areas by no more than 25 m.

Largely absent in CPC are slot faults that dip steeply or moderately. Almost always the slot-fault inclinations are less than 25°. In contrast, rotated mylonitic foliation, now expressed as relict foliation, not uncommonly dips at steep angles. This combination of observations suggests that slot faults, by and large, helped accommodate bulk rotation of mylonite without themselves being rotated to a marked degree. Alternatively, only the youngest faults created during the protocataclastic deformation are now recognizable in outcrop.

MINIDETACHMENT FAULTS

The slot faults described above are interpreted to be minidetachment faults. The expression "minidetachment" was coined by Axen and Selverstone (1994) in reference to planar to slightly curviplanar faults that are subparallel to and no more than ~200 m beneath the Whipple Mountain detachment fault. Slip directions are parallel to the vector of translation of the upper plate of the Whipple detachment fault. Upper and/or lower selvages of the minidetachments are not uncommonly marked by cataclastic deformation, including mosaic and chaotic breccias (Axen, 2020, fig. 3). Selverstone et al. (2012) emphasized that the minidetachments themselves tend to be fault-truncated, abandoned segments, traceable for distances ranging from 1 m to ~1 km. They

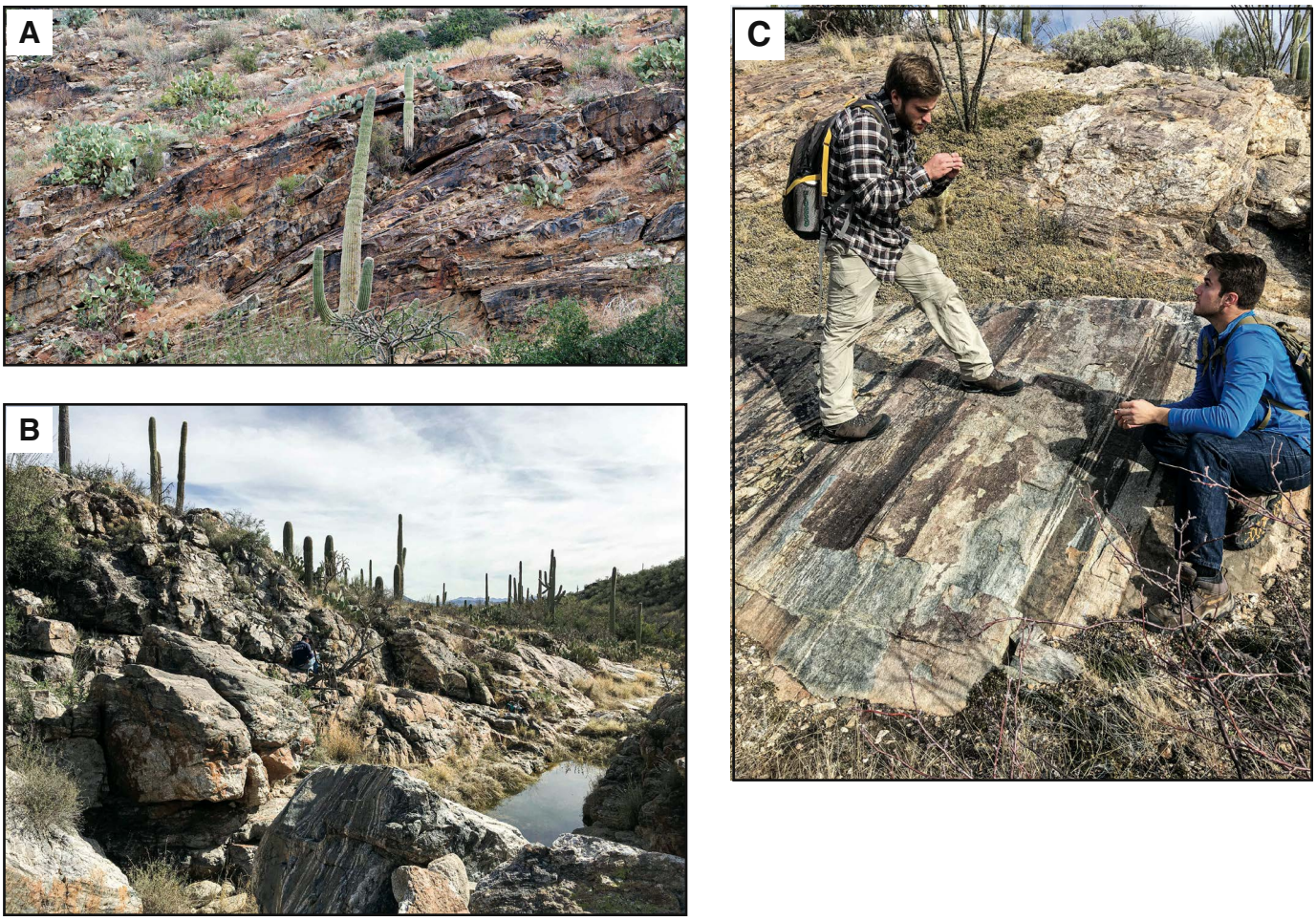


Figure 5-10. Photographs of minidetachment faults. In all cases, the attitudes of the minidetachment faults are parallel to those of the Catalina detachment fault surface. (A) North-directed photograph of discrete minidetachment faults "emerging" from protocataclastically overprinted ultramylonite in the Saguaro Loop subarea. Height of two-arm saguaro cactus in center of photograph is ~8 m. (B) Southeast-directed photograph of discrete, planar, minidetachment fault in chloritic protocataclasite (CPC) in the Loma Alta subarea. Barely recognizable in the center of photo, along the trace of the fault, there is a kneeling geologist (useful here for scale). (C) Discrete groove and rusted minidetachment surface within CPC in the Saguaro Loop subarea. Geologists are Alan Gregorski (left) and Aaron Alke (right).

were found to be parallel or subparallel to the attitude of the Whipple Mountain detachment, without direct physical linkage to the principal detachment fault. Epidote and chlorite alteration is intimately associated with these minidetachments. Pseudotachylyte is evident in places along or just below the slip surface.

Within the Rincon Mountains, some minidetachment faults have remained intact (Figs. 5-10A and 5-10B). They cut CPC as discrete and planar surfaces oriented parallel to the local orientation of the Catalina detachment fault. Only in rare instances, such as that shown in Figure 5-10C, are these faults marked by kinematic indicators such as grooves and slickenlines. These are interpreted to be very late-stage faults that escaped superposed intensive fracturing and alteration as well as disruption by yet-younger faults.

The finest display of minidetachment faulting in the Catalina-Rincon metamorphic core complex is seen at Lower Tanque Verde Falls, located ~7 km north of the Saguaro Loop subarea (Figs. 1-1 and 3-2). Details on location, access, and geologic context of Lower Tanque Verde Falls are available in Davis et al. (2019). The locality serves as part of the subdetachment system and occupies the contact between CPC and underlying mylonites. The exposure is ~20 m beneath the projected position of the Catalina detachment fault. Figure 5-11A is a panoramic view of the panel of minidetachment faulting, exhibiting the continuity and horizontality of this zone. The faults cut protocataclastically overprinted banded mylonitic gneiss. Selvages of the faults are marked by cataclasis and ultracataclasis, typically in zones no thicker than 10 cm (Fig. 5-11B). Listric normal minidetachment faults sole into the principal minidetachment surface (Fig. 5-11B). The upper-plate rocks of the principal minidetachment were back-rotated, westward, due to bulk rotation via faulting within CPC. Back-tilting above minidetachment faults in some locations was sufficient to flip small-scale normal faults into apparent reverse faults (Fig. 5-11C). In places along the main zone, well-developed breccia zones are evident (Fig. 5-11D). Also, releasing bends occur at shifted interfaces of the principal detachment surface and synthetic normal faults (Fig. 5-11E).

The mosaic/jigsaw breccia zone pictured in Figure 5-11D is particularly revealing with respect to the interplay of brittle/ductile deformation mechanisms. As evident in Figure 5-12, the sharp-edged angular clasts within this breccia zone are composed of slightly mylonitic granitoid. The clasts are suspended within a cataclastic matrix. The uppermost part of this breccia zone is truncated and distorted by a shear zone, within which the cataclastic matrix is transformed to ultramylonite, and the tops of the uppermost breccia fragments are mylonitized. One fragment, in particular, is profoundly distorted, such that shearing produced a "tail" that reflects the sense of shear. This combination of brittle/ductile behavior illustrates the effects of fault-valve behavior (Sibson, 1990, 1992, 2020a, 2020b).

Within a distance of 2 m or less along and directly beneath the sole of the principal minidetachment fault, glassy black seams and blobs of rock appear to be pseudotachylyte. Allen (2014) studied these rocks, photographed their various outcrop expressions, and investigated the microscale properties in thin section. He referred to the material as glassy but was not able to unequivocally identify the presence of true glass. The fault-rock expressions of these black glassy materials closely resemble pseudotachylyte and occur in the classic forms associated with unequivocal pseudotachylyte: fault seams (Fig. 5-13A) up to several cm thick, traceable for a few meters to as much as 8 m; injection veins (Fig. 5-13B) no more than 6 cm at their widest that splay off of the fault veins; isolated pockets with radiating expressions (Fig. 5-13C); and stubby, vein-like, fault-truncated gashes (Fig. 5-13D). Such expressions are consistent with those most commonly reported in the literature (e.g., Sibson, 1975; Lin, 1996; Spray, 1992; Barker, 2005). Viewed petrographically at the microscale, sharp contacts between the black glassy material and host rock (cataclastically overprinted mylonite) are commonplace, as are chilled margins (Fig. 5-14).

However, much of what appears to be pseudotachylyte, as seen in outcrop and thin section, was observed under backscattered-electron imaging to be almost entirely ultracataclasite with less than 1% preserved glass fractions (Fig. 5-15). This revelation raises the need for systematic interrogation of these black glassy rocks to distinguish true pseudotachylyte from ultracataclasite, which had the capacity, in an environment of high fluid pressures, to be injected as seams. The overall close association of the black glassy material, including tiny blebs of true glass, is consistent with pseudotachylyte developing from "prepared" ultracataclasite and not directly from mylonite or granitoid rock (Magloughlin, 1992; Bjørnerud, 2010).

FAULT-ACCOMMODATED BULK ROTATIONS

Overprinted (relict) mylonitic fabrics (both foliation and lineation) in CPC are highly variable in orientation. Very detailed 1:600 structural geologic mapping in the Saguaro Loop subarea by Davis (Davis and Anderson, 1981) and DiTullio (1983) documented bulk rigid-body rotations of the foliation and lineation that were accomplished during pervasive faulting and protocataclastic deformation. The mapped orientations of the relict mylonitic fabrics disclose the presence of discrete structural domains, each characterized by preferred L- and S-fabric orientations. Though the boundaries between structural domains are minidetachment faults, there is very little physical ground expression along any of these fault traces. Instead, the fault positions are identified by the sharp changes in relict fabric orientations from one internally homogeneous domain to the next. Within each structural domain, relict foliation and lineation depart from the preferred orientation of mylonitic fabrics in the lower plate. These aberrant mylonitic fabric orientations resulted from progressive superposed faulting during which a sustained sequencing of younger faults cut and rotated the mylonitic fabrics. It is likely that faulting cut and rotated some preexisting faults as well.

Detailed structural geologic mapping and structural analysis are required to explore bulk rotations within CPC. Tracking the combination of fracture intensity and the attitudes of overprinted foliation and lineation is insightful (Fig. 5-16). For

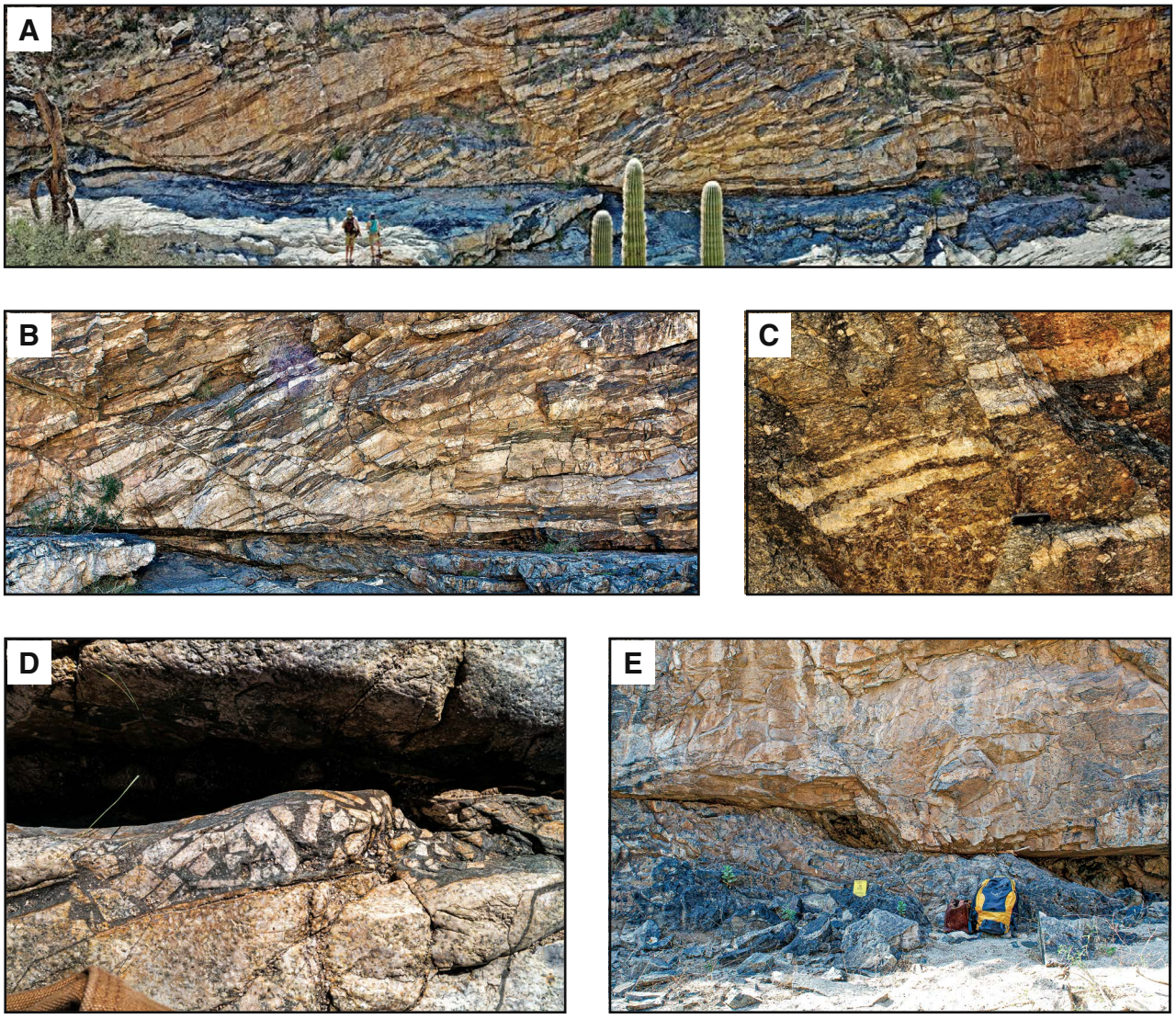


Figure 5-11. (A) South-directed panoramic photograph of minidetachment fault in the Lower Tanque Verde Falls area just north of the Saguaro Loop subarea. (This photo also appears as fig. 17 *in* Davis, 2013). Protocataclastically overprinted banded mylonitic gneisses have been back-rotated (by faulting) westward from their presumed original east-dipping attitude. Listric normal faults "sole" into the minidetachment. Panoramic photograph stitched together and enhanced by Peter L. Kresan © kresanphotography.com. (B) Closer view of back-rotation rollover and relationship of minor faults to principal minidetachment fault. Vertical field of view is ~6 m. (C) This apparent reverse fault was originally a left-dipping (east-dipping), high-angle normal fault, though now back-rotated along with the layering that it cuts and offsets. Note black pocket knife for scale; it is positioned above white band in lower-right corner. (D) Mosaic breccia along the base of the principal minidetachment fault. Photograph is by Warren Allen. Vertical field of view is ~1 m. (E) South-directed photograph of releasing bend that formed where the minidetachment abruptly stepped down by ~75 cm. Sense of transport of the minidetachment is top-to-the-right (SW). Parts D and E are good examples of slot-fault segments, due to weathering and erosion, along minidetachment faults.

example, DiTullio (1983) reported that weakly altered CPC with recognizable mylonitic fabrics (both foliation and lineation) is marked by ~25 fracture traces per linear meter. Fracture intensity increases to 40 or more fracture traces per linear meter where CPC is strongly altered, and only subtle relicts of mylonitic foliation are recognizable. Where extremely damaged and utterly altered, DiTullio (1983) noted that the number of fractures per linear meter may exceed 100. DiTullio's contouring of intensity of alteration and fracture density reveals that the greatest damage is directly beneath the cataclasites subjacent to the Catalina detachment fault and directly above the subdetachment fault (Fig. 5-16). Davis (1981) interpreted the bulk rotations as operating about a NNW-SSE horizontal axis of rotation. Sense of rotation, viewed NNW, was clockwise, consistent with top-to-the-SW tectonic transport. The range of rotated mylonitic fabrics suggests that maximum rotation in places approached 90° (Fig. 5-16).

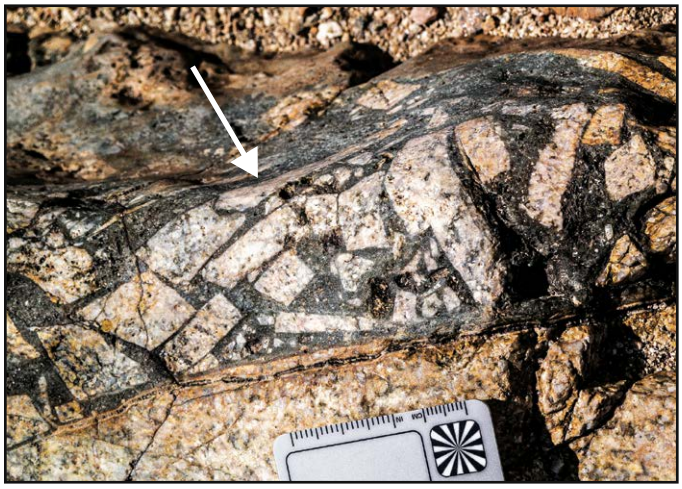


Figure 5-12. South-directed photograph of mosaic breccia (see Fig. 5-11D) that crops out in places along the sole of the principal minidetachment fault at Lower Tanque Verde Falls. Breccia fragments are composed of lightly foliated granitoid rock. Upper boundary of this breccia seam is marked by ultramylonite. Uppermost parts of breccia fragments are overprinted by intense mylonitization. White arrow points to breccia fragment that became profoundly sheared rightward (westward) as a result of shear zone deformation. Note tail. Photograph is by Warren Allen.

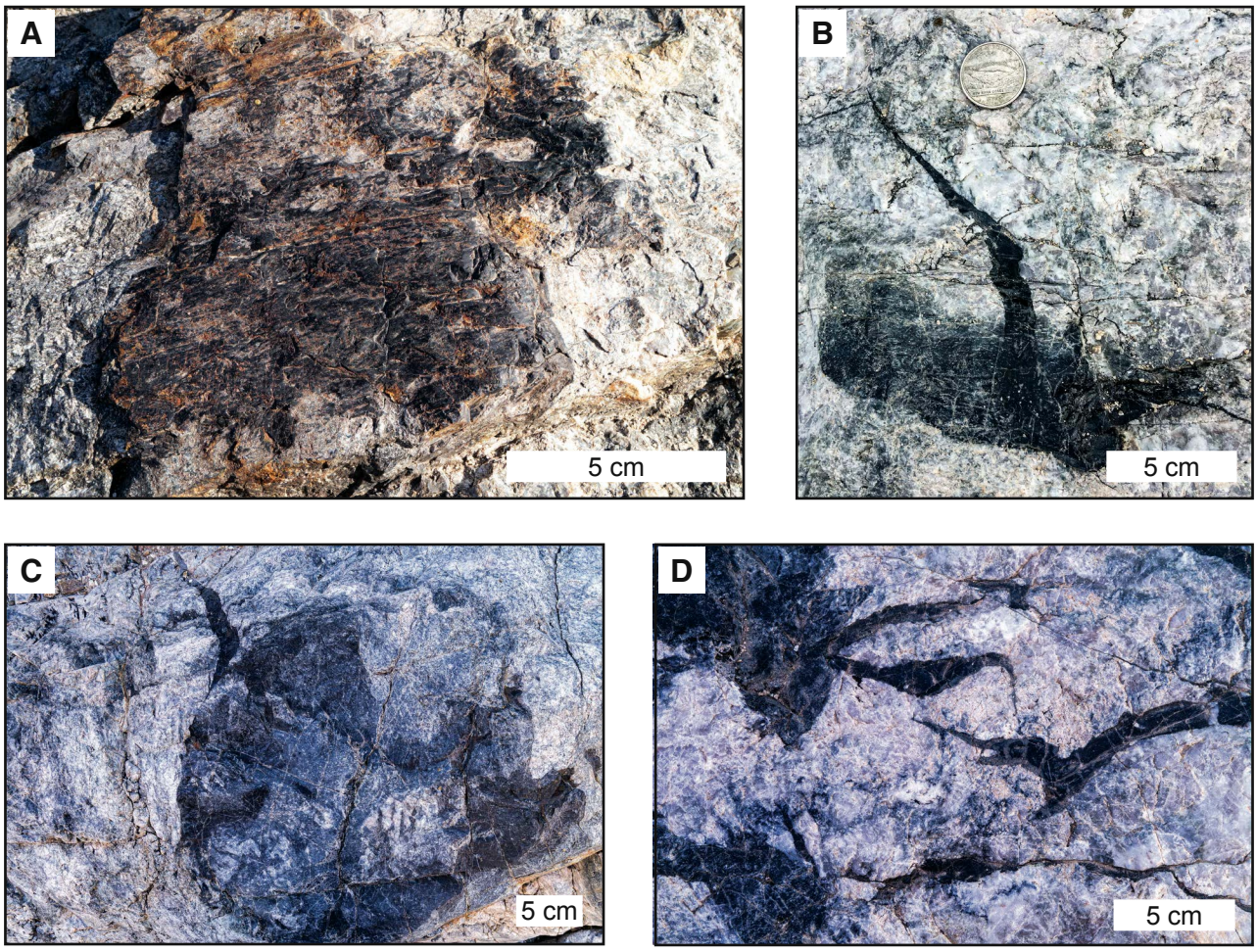


Figure 5-13. Expressions of black glassy rock at Lower Tanque Verde Falls. (A) Vertically downward directed photograph of subhorizontal fault seam in brittlely overprinted quartzofeldspathic rock. (B) Injection vein occupying gash fracture in quartzofeldspathic host. (C) Pod-like mass containing splotchy ghost-like relicts of comminuted rock. It closely resembles black ultracataclasite documented in the Loma Alta and Saguaro Loop subareas. Injection-like seam branches upward from pod on upper left. (D) Array of vein-like fault seams and/or injection veins. Photographs are courtesy of Warren Allen.

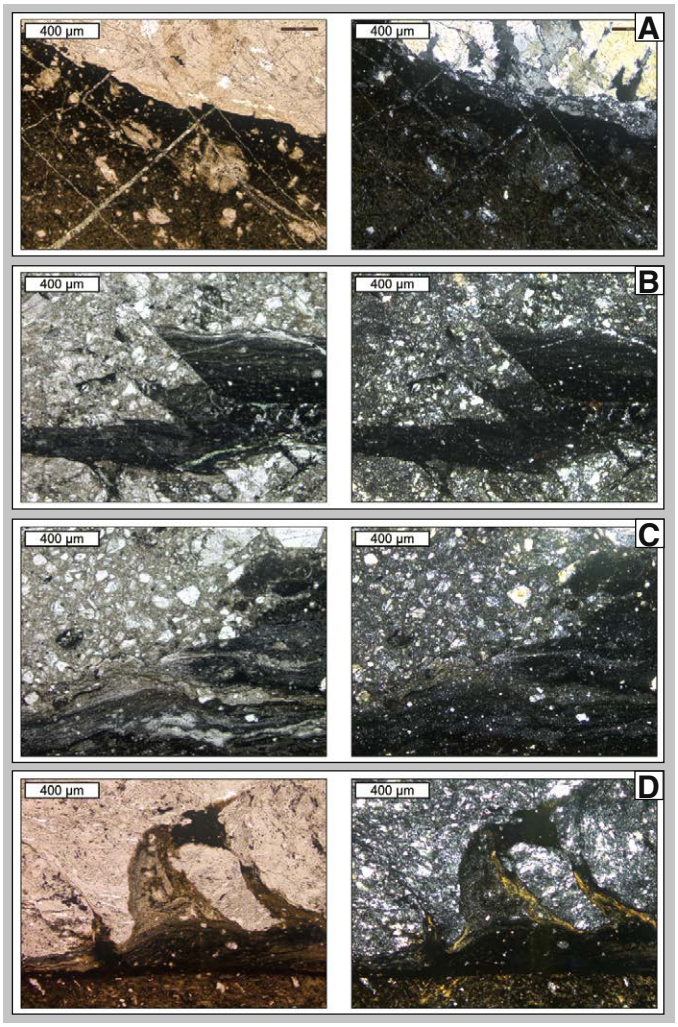


Figure 5-14. Photomicrographs of the extremely fine-grained black glassy rock at Lower Tanque Verde Falls. Left column, plane light; right column, cross-polarized light. (A) Amorphous black chill zone at boundary between black seam and mylonitic rock. A very thin selvage of ultramylonite borders (above) the black glassy rock. Late-stage chlorite veins slant through the black seam. (B) Faulted black glassy seam possesses ultramylonitic foliation. Host rock is cataclasite. (C) Mylonitic and/or glassy flow texture in black injection seam within cataclasite host. (D) Flame-like injection seams into cataclasite.

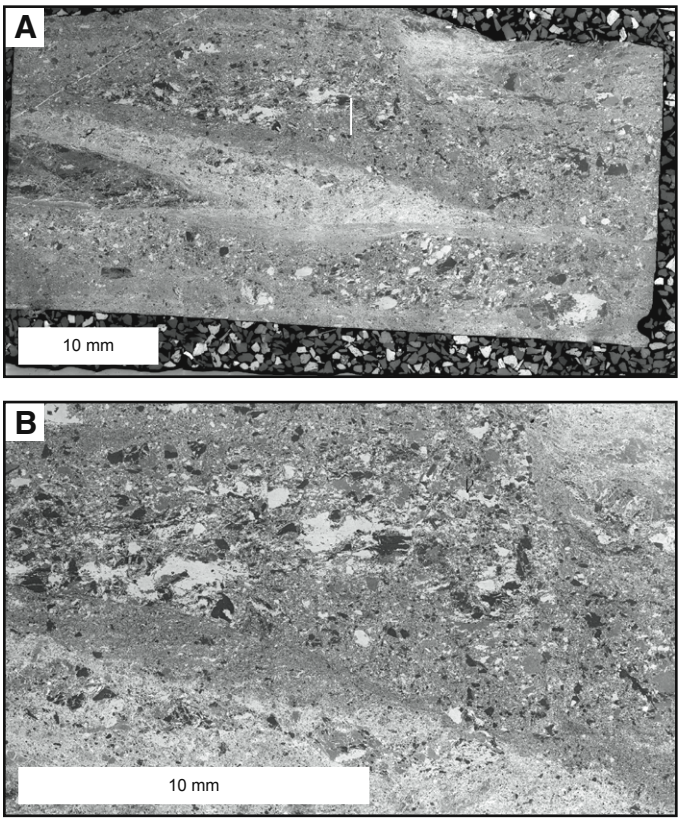


Figure 5-15. Mosaics of backscattered-electron images of what was thought to be pseudotachylyte but proves to be nearly exclusively ultracataclasite. The grayscale images highlight different phases and structural domains in the section. The images for each mosaic were acquired on a Hitachi S-3400N scanning electron microscope in full-vacuum mode using 15 kV at a working distance of ~15 mm.

The Posta Quemada–Hidden Spring subarea presents another example of fault-generated rigid-body bulk rotation. The exposed area occupied by rock impacted by this bulk rotation is on the order of 5 km^2. At Posta Quemada-Hidden Spring, the zone of CPC sandwiched between the Catalina detachment fault and the subdetachment fault zone is on the order of 1 km thick (Figs. 2-4 and 3-6). Geologic maps by Drewes (1977), Krantz (1983), and Spencer et al. (2001) all demonstrate that the preponderance of mylonite foliation readings measured in the lower-plate plunge-nose region of the Posta Quemada antiform dip northeastward, exactly the opposite of attitudes expected on the nose of a SW-plunging Posta Quemada antiform. Figure 5-17 stereographically conveys the back-rotated NE dip inclinations of foliation, as well as the back-rotated NE plunge of lineation, based on measurement data collected by Krantz (1983), supplemented by data extracted from the maps of Drewes (1977) and Spencer et al. (2001). The aberrant inclination directions of both foliation and lineation derive from faulting and attendant bulk rotation of the original SW- to S-dipping foliation, the original orientations of which conformed to the geometry of the antiform (Fig. 2-2).

SUMMARY

The combined thickness of cataclasite and ultracataclasite represents damage in response to tectonic transport of upper-plate rocks. Within this zone, CPC was transformed to the cataclasite and ultracataclasite. In contrast, the CPC represents transformation of mylonite and ultramylonite as these rocks, during top-to-the-SW shearing, moved from ductile to brittle conditions of deformation. The CPC is thus pervasively fractured, hydrothermally altered, and dissected by minidetachment faults, which are, for the most part, truncated and dismem-

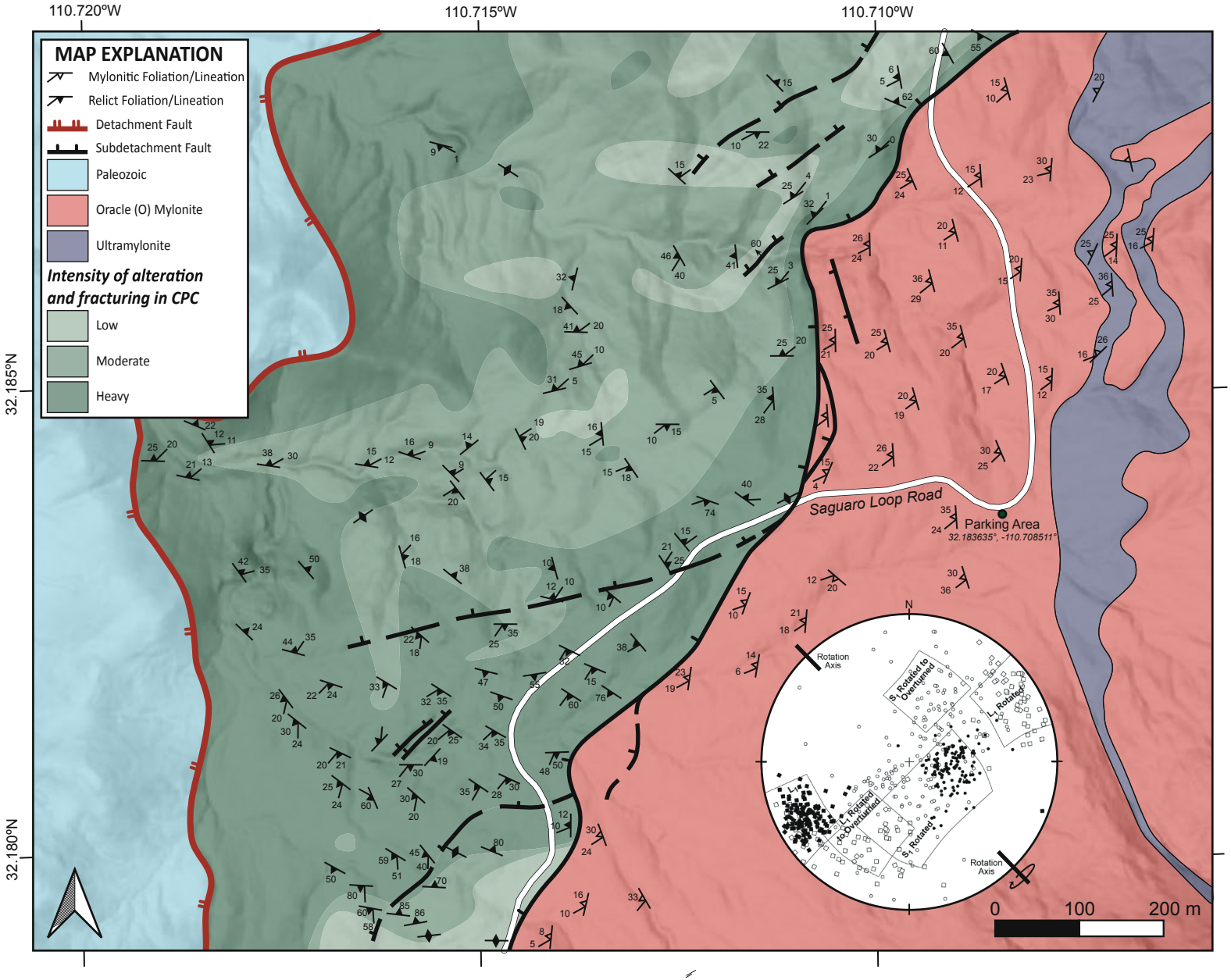


Figure 5-16. Structural geologic map of the Catalina detachment zone within a part of the Saguaro Loop area featured in Davis (1987b). The map is a composite of work by Davis (1987b) and DiTullio (1983). It conveys the degrees of intensity of alteration and fracturing in chloritic protocataclasite (CPC), as well as the departure of mylonitic fabric orientations (in CPC) from the norm in mylonite beneath the subdetachment fault. Embedded stereographic projection reveals that relict mylonitic fabrics were back-rotated in way a that fits a horizontal NNW-trending axis of rotation. [Stereographic projection was presented in Davis (2013) as fig. 16.]

bered. Slip along minidetachment faults helped accommodate the observed and measured bulk rotations of mylonitic fabrics within the zone of CPC. Some minidetachments are well preserved and have attitudes parallel to the Catalina detachment surface. An especially well-exposed minidetachment fault system preserves listric and/or domino-style faults that feed into the principal minidetachment zone, and these faults accommodated back rotation of mylonitic fabric. Closely associated with this minidetachment system is a black glassy rock that perfectly resembles pseudotachylyte in outcrop and hand specimen, though when viewed at high magnification, it is seen to be almost exclusively ultracataclasite.

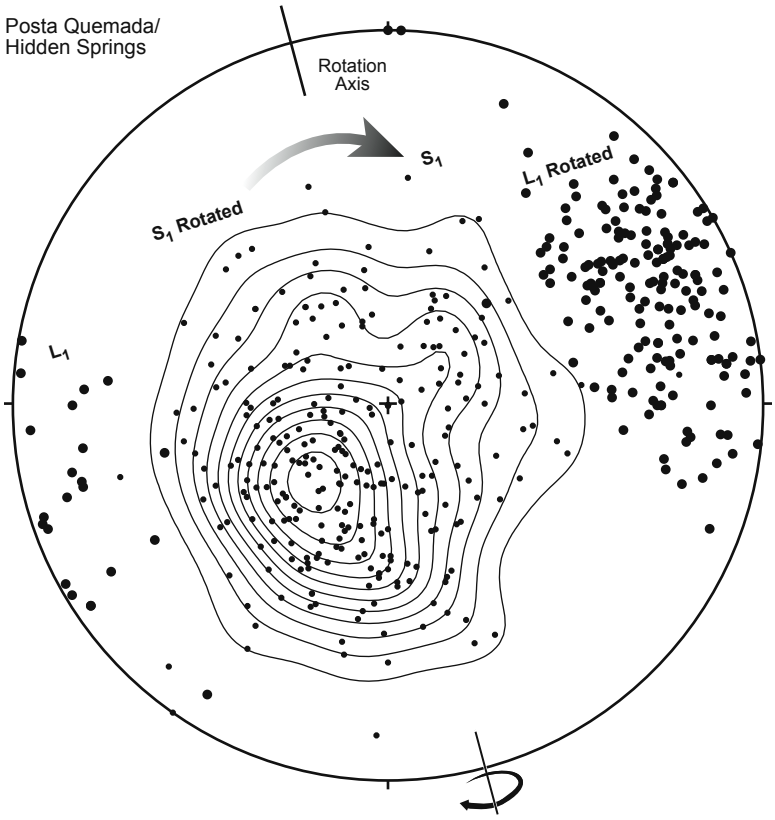


Figure 5-17. Lower-hemisphere stereographic projection of poles (smaller black dots) to largely NE-dipping mylonitic foliation and NE-plunging mylonitic lineation (larger black dots) based on measurements by Krantz (1983), supplemented by measurements from Drewes (1977) and Spencer et al. (2001), within the SW-plunging nose region of Posta Quemada antiform. Relict mylonitic foliation is gently NE dipping, the opposite of what is expected on the SW-plunging nose of the antiform. Original foliation was back-rotated as chloritic protocataclasite (CPC) evolved. Similarly, relict mylonitic lineation in CPC is plunging northeastward. Rotation was about a horizontal NNW-trending axis of rotation, with sense as shown by arrows. Magnitude of rotation ranges up to ~50°.

CHAPTER 6

Subdetachment faults, ultramylonite, calc-tectonite, and mylonite

INTRODUCTION

It is clarifying to bundle subdetachment faults, ultramylonite, calc-silicate tectonite, and the *uppermost* mylonite in a single chapter. Either as a single discrete fault or as a fault zone, the subdetachment fault continuously and consistently separates chloritic protocataclasite (CPC) from underlying lower-plate mylonites. An important tangible accomplishment of this research effort was documenting the full trace expression of subdetachment faulting at the base of CPC for the entire Rincon Mountains (Fig. 2-4), for it is not recognized on the principal geologic maps of the Rincon Mountains (Drewes, 1974, 1:48,000 scale; Drewes, 1977, 1:48,000 scale; Dickinson, 1991, 1992, 1:125,000 scale; Richard et al., 2005, 1:24,000 scale). Two exceptions are Spencer et al. (2001, 1:24,000 scale) and Force (2002, 1:48,000 scale). Discovery and map positioning of the subdetachment fault system benefited from detailed structural mapping (Table 3-1) and multispectral remote-sensing analysis. The position and orientation of the subdetachment fault zone appear to be controlled by the placement and orientation of ultramylonite and/or calc-silicate tectonite within mylonite. Strain localization along ultramylonite was proposed for the Saguaro Loop subarea by Davis (2013), but it was unclear, at the time, whether such control might apply to the Rincon Mountain as a whole.

SUBDETACHMENT FAULTING

Saguaro Loop Subarea

A brief recounting of the findings of Davis (2013) provides context. Everywhere in the Saguaro Loop subarea (Fig. 3-2), the base of CPC is sharply demarcated by a discrete fault and underlain by lower-plate mylonites. Field-measured attitudes of subdetachment fault surfaces in the Saguaro Loop subarea match best-fit orientations yielded from global positioning system elevation control along the map trace. The attitude was found to be 215°/08°NW (Davis, 2013). The subdetachment fault, in turn, is subparallel to the overlying Catalina detachment fault, for which the average attitude in this subarea is 206°/16°NW (Table 3-2; Fig. 3-2).

An exposure of the subdetachment fault along the Cactus Forest Drive in the Saguaro Loop subarea presents a very gently dipping, smooth, planar, dark-gray to brown rusted surface coated with Fe- and Mn-oxide alteration (Fig. 6-1). The stripped structural surface of the subdetachment fault slopes gently and uniformly (Fig. 6-1A). The top surface of this outcrop is marked by very strongly lineated ultramylonite that is protocataclastically overprinted. Both O-mylonite and W-mylonite crop out in profile view (Fig. 6-1B). Another excellent outcrop of the subdetachment fault in the Saguaro Loop subarea is exposed in a ravine near the toe of Tanque Verde Ridge (Fig. 6-1C). There, the subdetachment fault contact is knife-sharp, marked by fresh, penetratively foliated and lineated mylonite below and altered and highly fractured to shattered CPC above.

Loma Alta and X9 Ranch Subareas

The subdetachment fault mapped in the Saguaro Loop subarea is folded over the Tanque Verde antiform (Fig. 2-2), and because this is a plunging fold, the trace of the subdetachment fault wraps around the nose of the fold before projecting easterly toward the Loma Alta subarea (Fig. 3-3). The subdetachment fault runs E-W through the entire length of the Loma Alta subarea, and its attitude is 095°/11°S (Table 3-2; Fig. 3-3), again parallel to the attitude of the Catalina detachment fault, oriented 091°/10°S (Table 3-2; Fig. 3-3). The location of the subdetachment fault is straightforward to map because of the abrupt change from CPC above to mylonite beneath (Fig. 6-2). In places, the contact reveals a 1–2-m-thick layer of black ultramylonite. Protocataclastically overprinted mylonitic foliation within CPC and foliation in underlying ultramylonite are parallel to one another (Fig. 3-3). This concordance is qualitatively evident in Figure 6-2. Measured orientations of mylonite foliation and protocataclastically overprinted mylonite foliation bear this out. Average orientations for both are 102°/16°SW (Fig. 3-3).

The subdetachment fault projects eastward from the Loma Alta subarea and into the X9 Ranch subarea (Fig. 3-5), where it abruptly becomes tightly folded along the Rincon Creek synform (Fig. 2-2). Though the X9 Ranch subarea was mapped by Drewes (1977) and Richard et al. (2005), their maps do not delineate CPC or any subdetachment faulting. We examined parts of the X9 Ranch area in reconnaissance but did not directly explore for expressions of subdetachment faulting in this subarea. However, our multispectral image (Fig. 2-4) discloses the areal extent of CPC and the positioning of the subdetachment (Fig. 3-5).

Posta Quemada–Hidden Spring Subarea

From the X9 Ranch subarea southward and southeastward, the Catalina detachment zone is folded over the plunging nose

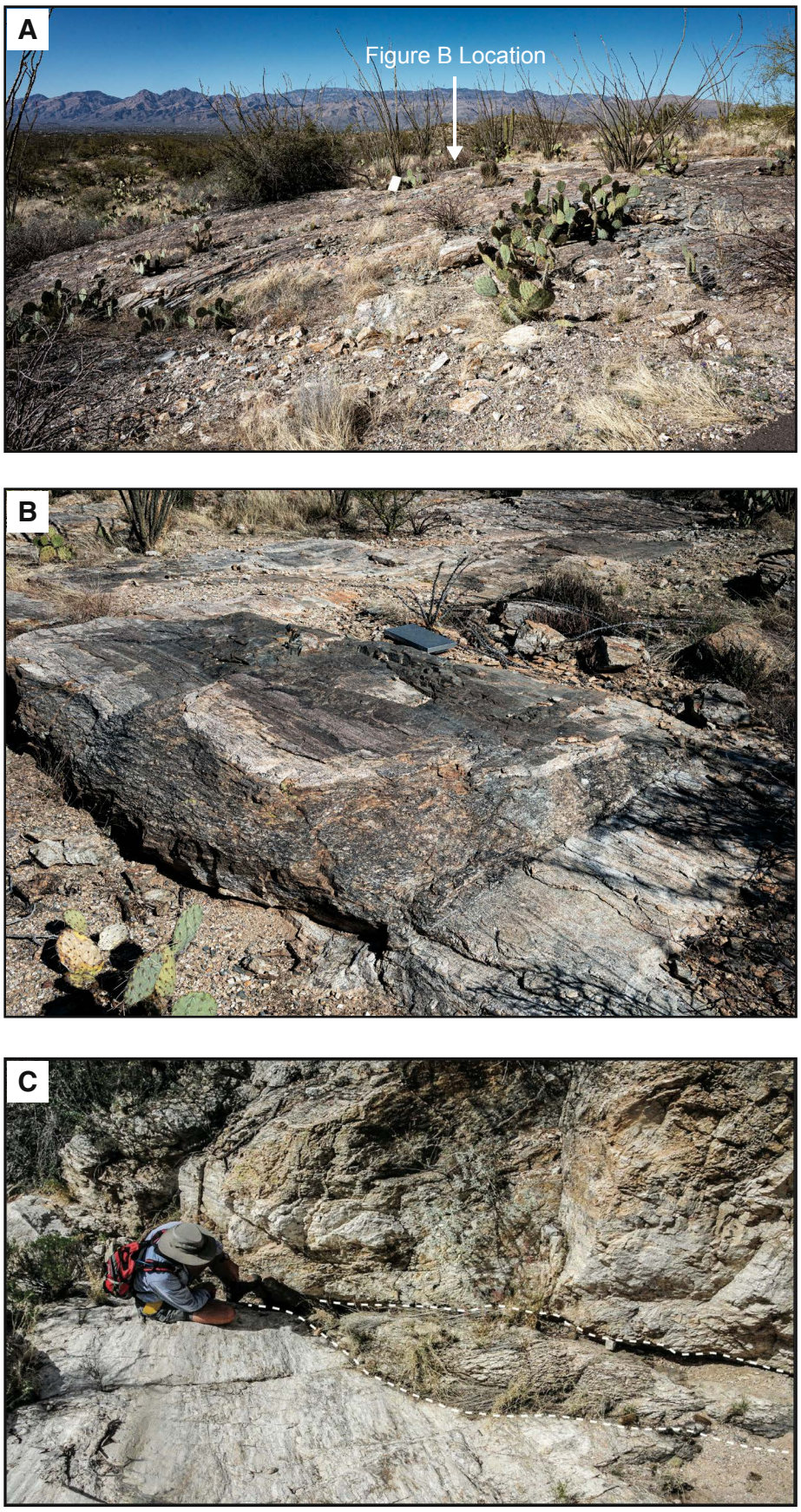


Figure 6-1. (A) North-directed photograph of the outcrop expression of the Javelina Rocks subdetachment fault exposed along Cactus Forest Drive in the Saguaro Loop subarea. Aluminum clipboard for scale. (B) Close-up view of the top surface of part of the subdetachment surface. The dark selvage is cataclastically overprinted, lineated ultramylonite. The protolith is O-mylonite (dark-weathering augen gneiss forms the discrete tabular layer), and W-mylonite (light-weathering finer-grained mylonite) is seen in lower-right corner of photograph. (C) SW-directed photograph of Javelina subdetachment fault zone in the Saguaro Loop subarea near toe of Tanque Verde Ridge. Dashed white lines demarcate an extensional horse in this fault zone. Below the fault, there is strongly lineated leucocratic mylonite. The overlying rock is shattered, consisting of chloritic protocataclasite derived from mylonite. Photograph by Alan Gregorski.



Figure 6-2. Northwest-directed photograph of subdetachment fault along North Coyote Wash in the Loma Alta subarea. Foreground is tan-weathering mylonite. Gently south-dipping mylonitic foliation is paralleled by trace of subdetachment fault, which separates the mylonite from dark-weathering chloritic protocataclasite above. Note the slot reentrant along the subdetachment fault.

of the Posta Quemada antiform (Fig. 2-2). Thus, the Posta Quemada–Hidden Spring subarea largely occupies the hinge zone and southeastern limb of the Posta Quemada antiform (Fig. 3-6). The subdetachment system is revealed best by the mapping by Spencer et al. (2001), which displays a branching, bifurcating fault system about 7 km in trace length. Figure 6-3A presents a simplified structural geologic map of this system and is accompanied by a down-plunge cross-sectional view (Fig. 6-3B). The NW-striking, SW-dipping low-angle subdetachment fault system is completely contained beneath the Catalina detachment fault. Spencer et al. (2001) mapped it as bifurcating near its northwest end and trifurcating near the southeastern termination. Based on a three-point determination, the overall attitude of this subdetachment fault system was found to be 100°/12°SW (Fig. 3-6), i.e., subparallel to the orientation of the Catalina detachment fault. The horizontal map distance between the trace of the subdetachment faulting and the Catalina detachment fault is as wide as ~2 km. Toward the southeast, this horizontal map distance reduces to less than 200 m (Fig. 6-3A). Nowhere do the traces of the Catalina detachment fault and subdetachment fault zone come into contact.

Martinez-Salcido Ranch Subarea

The subdetachment system exposed in the Posta Quemada–Hidden Spring subarea projects easterly into the Martinez-Salcido Ranch subarea (Figs. 2-2 and 3-10). The Catalina detachment zone is clearly expressed in the landscape (Fig. 6-4) due to the erosional resistance of CPC in comparison to underlying mylonites. In places, the expression of the principal subdetachment surface resembles a paved road (Fig. 6-5). The contacts mapped in the field perfectly coincide with the geometric expressions in the multispectral image, where the CPC stands out in hues of gold and red (Fig. 2-4).

As in the Posta Quemada–Hidden Spring subarea, subdetachment faulting in the Martinez-Salcido Ranch subarea is represented by anastomosing faults instead of a single discrete subdetachment fault (Fig. 3-10). In the westernmost and easternmost parts of the map area, the principal subdetachment fault surface marks the very base of the CPC. However, in some places, the rock below the principal subdetachment surface is also CPC, with additional subtle underlying subdetachment faults separating protocataclastic fault rock from underlying mylonite. The interlinked subdetachment system of faulting, for which the overall attitude is 104°/24SW°, is roughly parallel to that of the Catalina detachment fault proper: 112°/22SW° (Table 3-2; Fig. 3-10). Nowhere does subdetachment faulting physically link with the Catalina detachment fault. The lower contact of the subdetachment system resembles a complex fault-mullioned surface, which is best appreciated in a down-plunge view (Fig. 6-6).

Comparison of Attitudes of Subdetachment Faulting and Catalina Detachment Fault

There is a close parallelism between the overall geometric form of the Catalina detachment fault in the Rincon Mountains and the geometric forms revealed by mylonitic foliation and the subdetachment fault. Based on 88 measurements, Figure 3-11A reveals that the Catalina detachment surface is cylindrical in form, with a corrugation axis trending 12° toward 248°. Though the 321 poles to mylonitic foliations plotted in Figure 3-11C show much greater scatter than the 88 poles to the Catalina detachment fault surface orientations, they yield a corrugation axis (13° toward 236°) essentially parallel to that determined on the basis

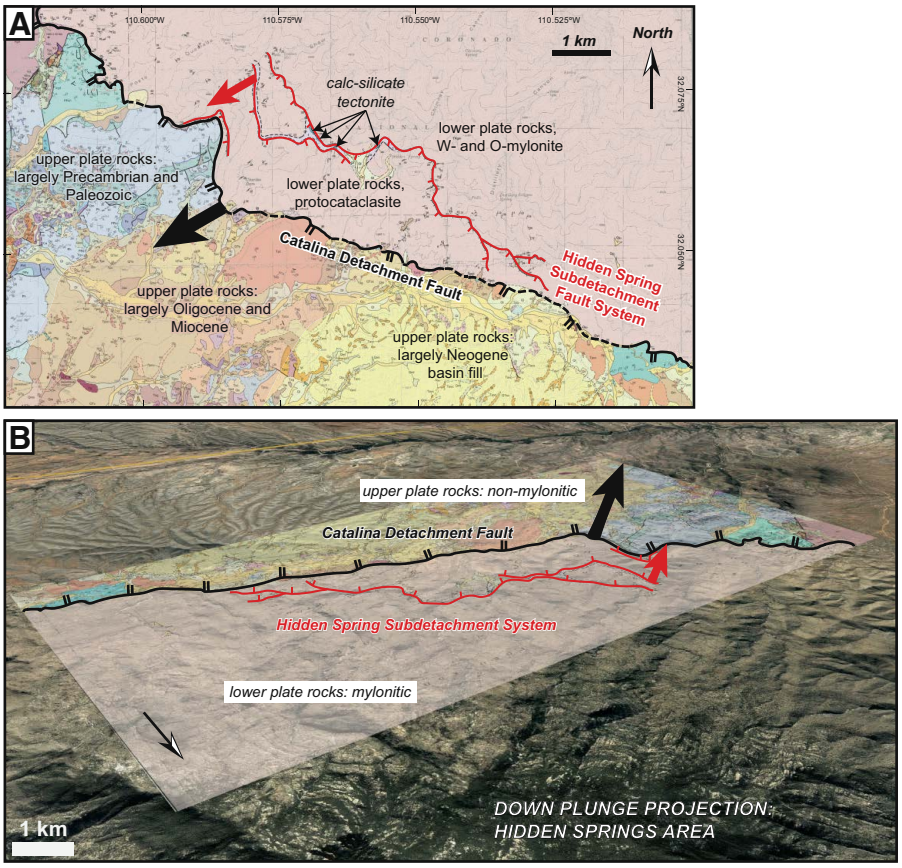


Figure 6-3. (A) Simplified structural geologic map of the Posta Quemada–Hidden Spring subarea based upon Spencer et al. (2001). The NW-trending trace of the Catalina detachment fault trace is shown in black; it separates lower-plate and upper-plate rocks. The red fault traces in the lower plate represent the subdetachment fault system. The expression of the subdetachment system is marked by branching. Small black arrows reference the locations of some of the calc-silicate tectonite pods and lenses. Large black and red arrows show tectonic-transport directions for the Catalina detachment fault and the subdetachment fault system, respectively. (B) SW-directed down-plunge view of the Catalina detachment zone, including the subdetachment fault zone. Note the mullioned nature of subdetachment faults. This view is based upon the geologic map by Spencer et al. (2001).

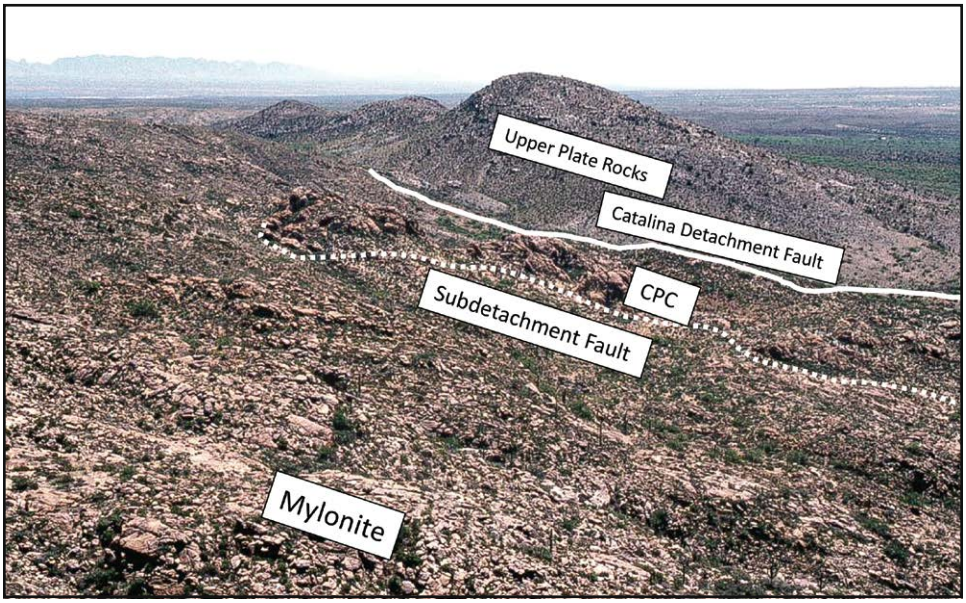


Figure 6-4. SE-directed photograph of the expression of the Catalina detachment zone as expressed in the landscape of the Martinez-Salcido Ranch area. Upper-plate rocks are separated from chloritic protocataclasite (CPC) by the Catalina detachment fault. The subdetachment fault (dotted white line) separates CPC from mylonite. Photograph is by Kurt Constenius.

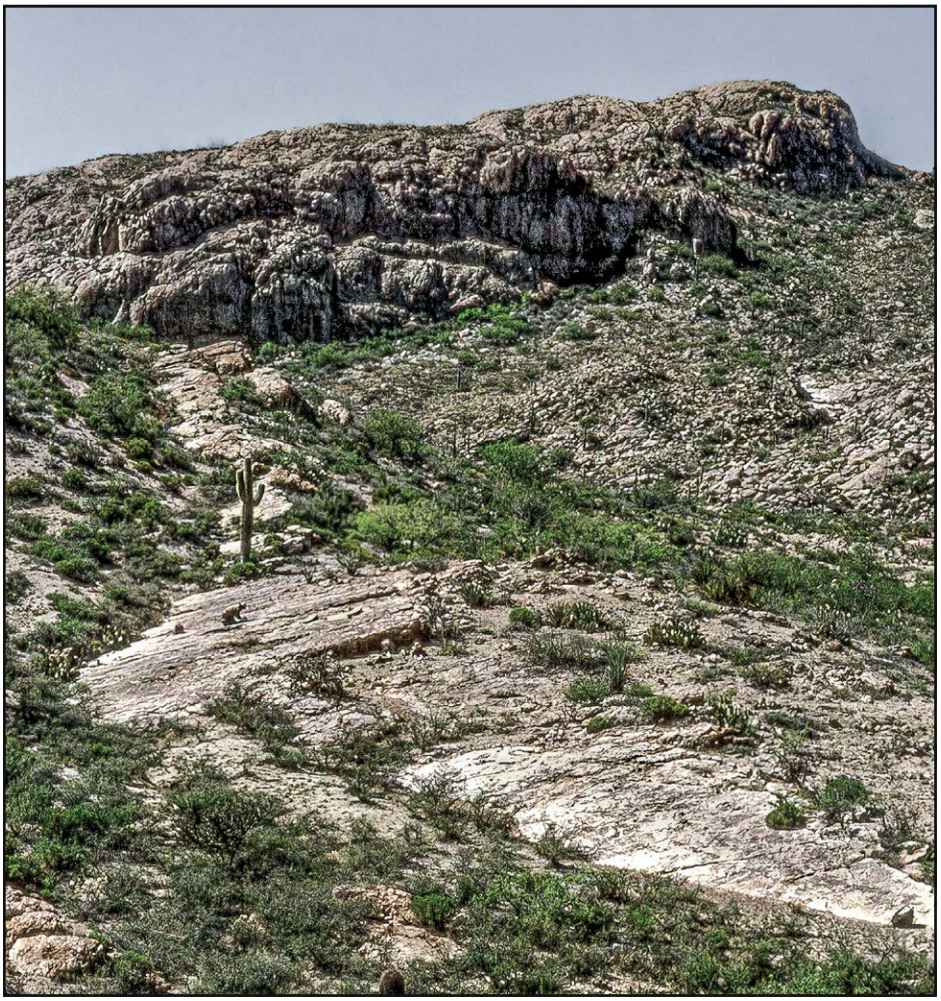


Figure 6-5. West-directed photograph of "paved-road" expression of a segment of the subdetachment fault system in the Martinez-Salcido Ranch subarea. Note geologist for scale just below large saguaro, center-left of image. Cliffs of chloritic protocataclasite are visible in background. Base of cliff coincides with the trace of the subdetachment fault, inclined to the left (south). Overall quality of original 1990s photograph was improved by Peter Kresan. Private-land access is impossible at this time.

of Catalina detachment fault measurements (Fig. 3-11A). Moreover, the orientation of the corrugation axis (17° toward 235°) based on poles to the 47 subdetachment fault measurements closely parallels the orientation (14° toward 241°) of penetrative lineation in underlying mylonite (Fig. 3-11D). The overall geometric/kinematic cohesiveness, crossing ductile through brittle fabrics and structures, is not only remarkable, but it underscores a progressive deformation within which the dominant variable was rheological response to a common loading condition.

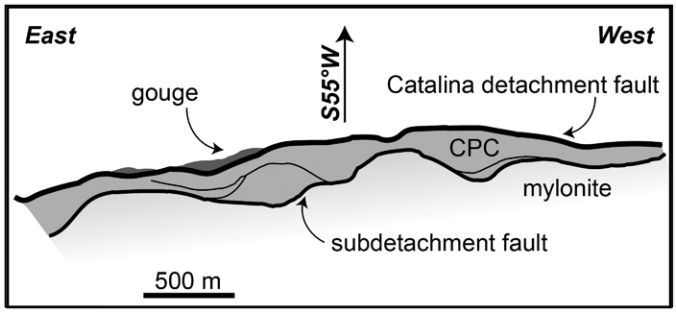


Figure 6-6. SW-directed down-plunge sketch of Catalina detachment zone in Martinez-Salcido Ranch area, adapted from Davis et al. (2011, fig. 5, p. 13). CPC—chloritic protocataclasite.

ULTRAMYLONITE AND CALC-SILICATE TECTONITE

Ultramylonite in Saguaro Loop, Loma Alta, and X9 Ranch Subareas

In the Saguaro Loop subarea (Fig. 3-2), mapping revealed that the subdetachment fault coincides closely in attitude and position with a fault-rock unit of ultramylonite. The strain-localization relation was described in detail by Davis (2013). In this study, samples of ultramylonite were collected for geochronology and thermochronology (Chapter 8). One variety has a schistose fabric (Figs. 6-7A and 6-7B). A full thin-section scan revealed abundant phyllosilicates arranged in a structural fabric that includes S-C relations with top-to-the-SW shear (Figs. 6-7C and 6-7D). The second, and more dominant, variety of ultramylonite is silver-gray to very dark-gray and platy, and it is marked by a fine-scale

laminated foliation (Fig. 6-8). It erodes into thin platelets of fresh rock, the surfaces of which sparkle with light reflecting from tiny muscovite porphyroclasts. Tiny feldspar and mica porphyroclasts are evident. Derived mainly from W-mylonite, the platy ultramylonite reveals the significant degree to which the granitoid protolith experienced grain-size reduction and penetrative shearing.

The general character of the platy ultramylonite fabric can be appreciated in full thin-section scans (Fig. 6-9A), where it is quite evident that mica fish are abundant in this ultramylonite (Fig. 6-9B). The S-C fabric defined by micas in relation to the penetrative foliation (C) conveys the sense of shear, which is consistently top-to-the-SW. Porphyroclasts of feldspar and garnets

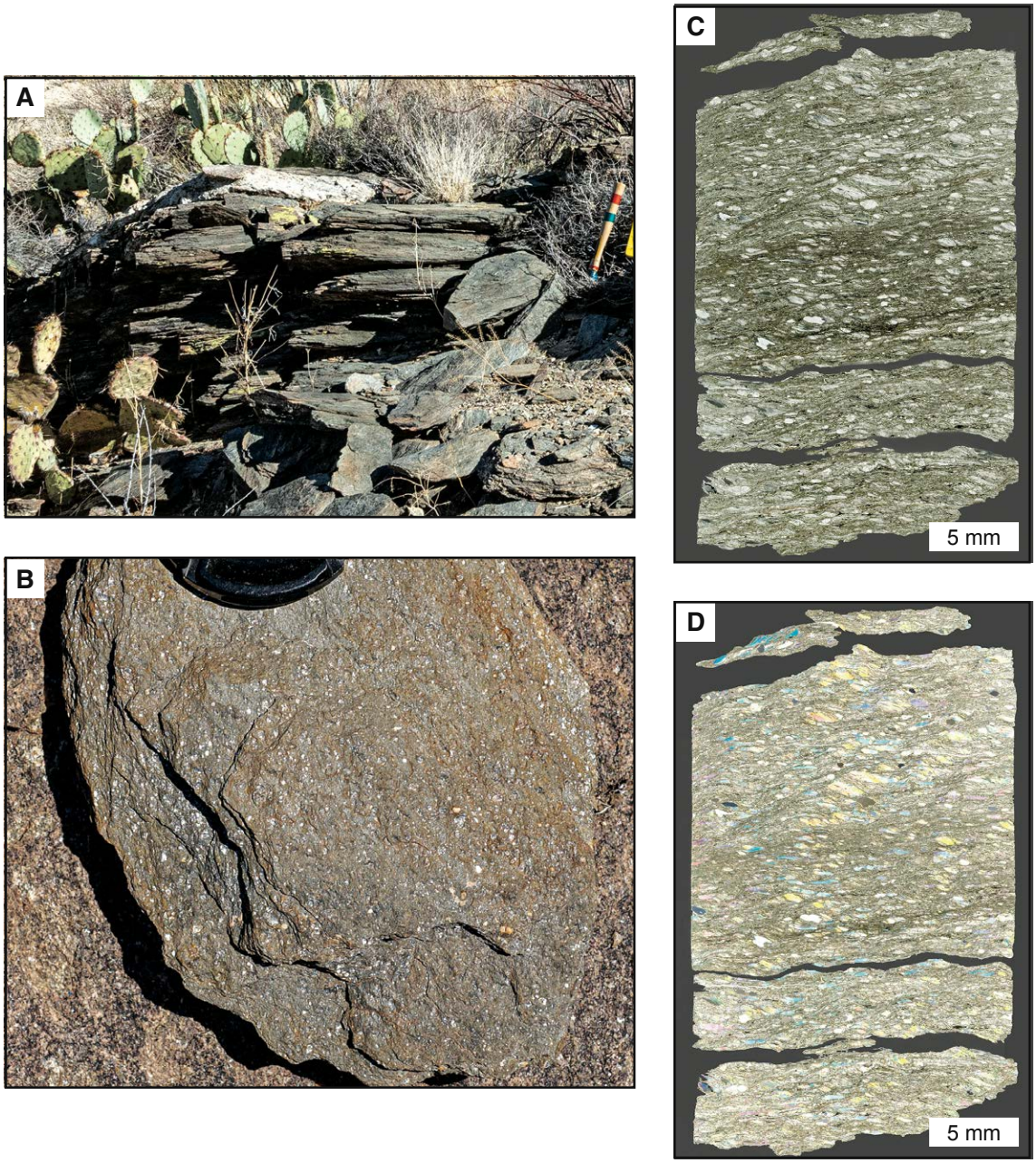


Figure 6-7. Ultramylonite in the Saguaro Loop subarea. (A) Photograph of outcrop expression of schistose ultramylonite. Rock hammer for scale. (B) Macrophotograph of the "plane" of foliation and the abundant white mica. Lens cap (black) for scale. (C) Full thin-section scan of schistose ultramylonite. Plane light. Section is oriented such that SW is on left margin. S-C fabric is well expressed. S fabric is defined by gently NE-inclined whitish mica fish, whereas C surfaces are gently inclined SW and marked by thin dark hues. (D) Full thin-section scan in cross-polarized view. Sample GD 10-16-20 (Fig. A-1; Table A-1 [see text footnote 2]).



Figure 6-8. Photograph of outcrop of the platy variety of ultramylonite in the Saguaro Loop study area. Lens cap for scale. Rock is lustrous gray and exhibits myriad tiny porphyroclasts of quartz/feldspar. Lineation is present, trending ~240°. Mylonitic protolith is evident in lower-left corner of photo.

and their attached tails (i.e., delta clasts) commonly reveal a sense of rotation that complements the use of mica fish in determining the sense of shear (Fig. 6-9C). There are two lines of evidence showing that the ultramylonite was largely derived from W-mylonite: first, the presence of garnet porphryoclasts, which average ~500 µm in diameter, and second, the muscovite mica, which displays undulose extinction. Feldspars show recrystallization around their edges. The groundmass of the ultramylonite is an extremely fine-grained (<10 µm) mixture of muscovite and chlorite, and it also includes laminae of quartz ribbons with entrained fragments of feldspar porphyroclasts.

Ultramylonite is the only fault-rock unit within the Catalina detachment zone that is marked by outcrop-scale folding (Davis, 1987a, 1987b, 2013). The folds are sheared to strongly overturned and locally recumbent and isoclinal forms (Fig. 6-10). The folds kinematically conform to a top-to-the-SW sense of shear, with an azimuth identical to sense-of-shear indicators observed in the underlying mylonite coinciding with the transport direction on the Catalina detachment fault surface (Davis, 1980b).

Exposures of ultramylonite in the Loma Alta subarea (Fig. 3-3) occur along a bedrock ravine in North Coyote Wash, right along the base of the CPC fault rock unit. There, the ultramylonite

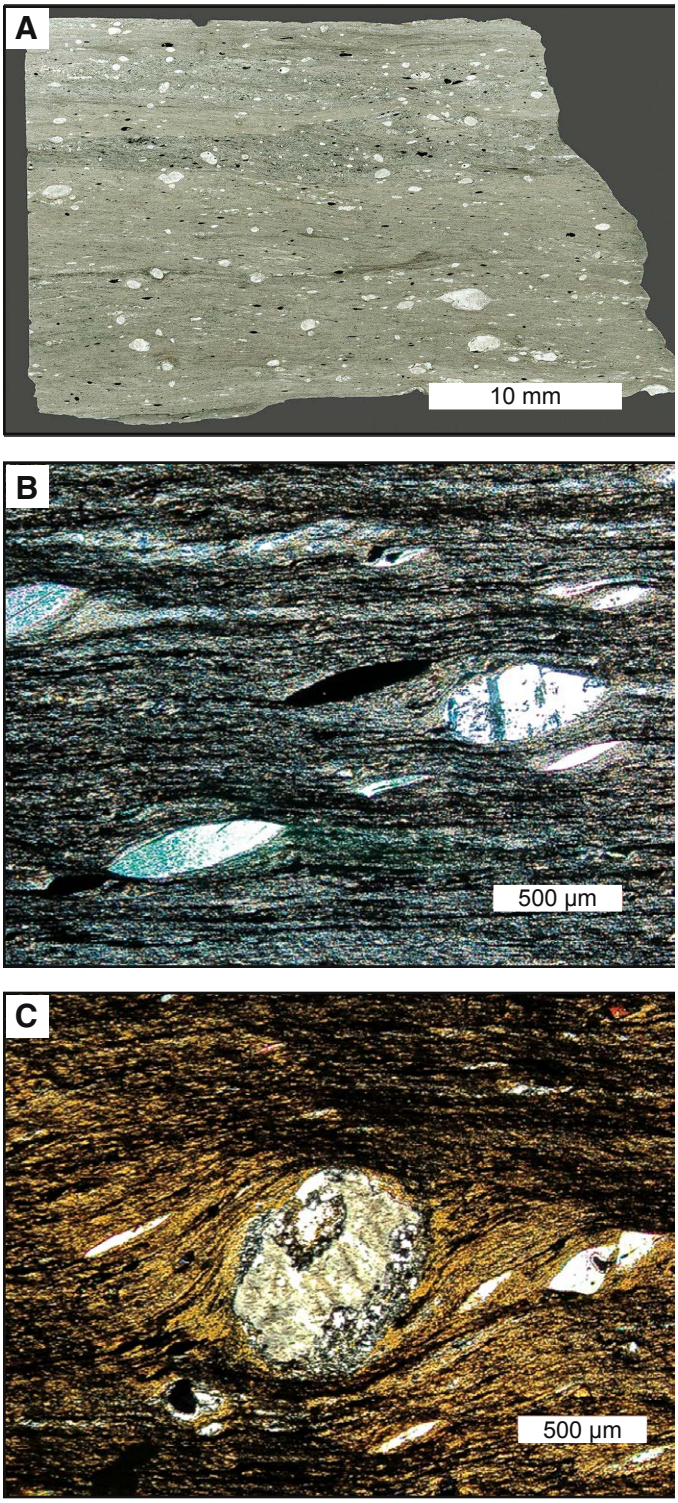


Figure 6-9. (A) Full thin-section scan of platy ultramylonite from Saguaro Loop area, showing quartz/feldspar porphyroclasts (white) in very fine-grained matrix of quartz and phyllosilicates. Tiny mica fish (black) are distributed through rock. Sample GD 10-16-20 (Fig. A-1; Table A-1 [see text footnote 2]). (B) Photomicrograph of the ultramylonite revealing mica fish (white) that constitute the S fabric in this S-C mylonite. Sense of shear is top-to-the-right (SW). (C) Photomicrograph showing rotated porphyroclast of quartz/feldspar. Sigmoid tails indicating top-to-the-right sense of shear.



Figure 6-10. North-directed photograph of overturned fold in ultramylonite in the Saguaro Loop subarea. Brunton compass for scale.

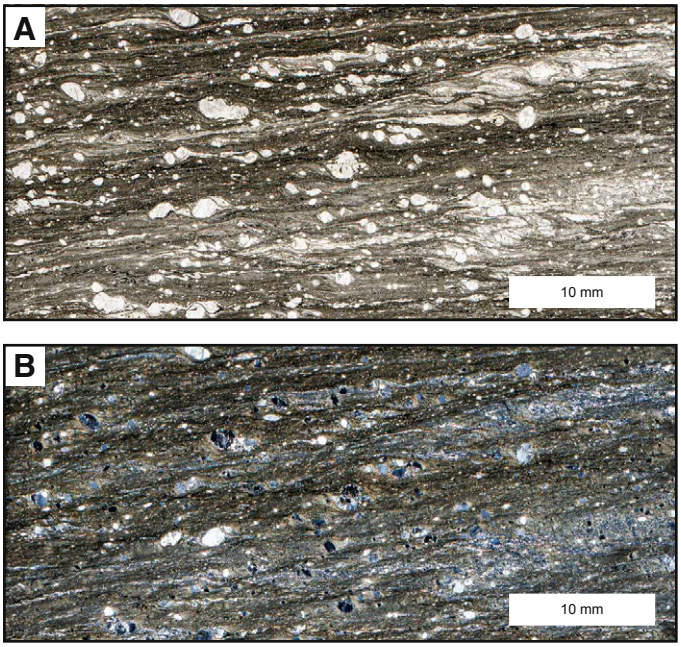


Figure 6-11. Full thin-section scans of ultramylonite from the Loma Alta subarea in (A) plane light and (B) cross-polarized light. Tiny porphyroclasts of feldspars float in a very fine matrix of quartz and phyllosilicates. They are inclined with respect to the dominant pervasive C surfaces, yielding a top-to-the-SW sense of shear. Thin wispy relicts of quartz ribbons are locally folded. Width of field of view is 46 mm. Sample LA1 (Fig. A-1; Table A-1 [see text footnote 2]).

(~2 m thick) is locally embayed due to its erosional weakness. The ultramylonite can be tracked for a distance of ~100 m. The attitude of ultramylonitic foliation is 137°/16°SW, with lineation plunging 11°/249°. The typically black ultramylonite is quite striking in thin section (Fig. 6-11). In places, white leucocratic mylonitic rock has been transformed to ultramylonite, with S-C fabric also revealing top-to-the-SW sense of shear. A thick (~40 m) ultramylonite occurs in the far northwestern corner of the Loma Alta subarea at sample locations FR10A and FR10B (Fig. 3-3). It resides in W-mylonite close to the contact with Loma Alta mylonite. Its W-mylonite protolith is evident due to the abundance of garnet both in outcrop and thin section (Fig. 6-12).

Ultramylonite and Calc-Tectonite in the Posta Quemada–Hidden Spring Subarea

It was especially challenging to depict and decipher the subdetachment system in the Posta Quemada–Hidden Spring subarea, requiring focused field work guided by previous geologic mapping and observations by Drewes (1977), Spencer et al. (2001), and Richard et al. (2005). It required determination of equivalencies of rock units named differently by the different workers, and recognition of equivalencies in disparate map-explanation symbology. We present the details of the synthesis we accomplished. An additional challenge lay in interpretation of the tectonic-mélange–like character of some of the tectonites that occupy the subdetachment system.

What we describe as the subdetachment fault system can be recognized in the mapping by Spencer et al. (2001) (Fig. 6-3A) in the Posta Quemada–Hidden Spring subarea. It closely coincides with the contact between O-mylonite and W-mylonite as mapped by Drewes (1977) (Fig. 2-2). Though Drewes (1977) did not map a fault separating these two mylonites of different protoliths, he mapped the interface between O- and W-mylonite as a schistose rock that he interpreted to be Pinal Schist (Paleoproterozoic). In the map explanation, he notes that this rock is "typically strongly and probably multiply deformed through dynamic and thermal events." We observed that this rock is largely ultramylonite.

Spencer et al. (2001) mapped discontinuous pods and lenses of calc-silicate tectonites along this same zone of ultramylonitic rock (Figs. 3-6 and 6-3A). In their map explanation, Spencer et al. (2001, p. 28) described these rocks as "[c]alc-silicate tectonite (probably Paleozoic protolith age with probable Mesozoic to Tertiary deformation)" and stated that they reside within "[f]ault rocks (Proterozoic to Tertiary protolith with probable Mesozoic to Tertiary deformation)." Drewes (1977) identified a single large "block of limestone" at a location just west of Hidden Spring proper (HS in Fig. 3-6). This block occurs along a part of the same fault system mapped by Spencer et al. (2001). The two fault branches marked by these fault rocks converge northwestward as they approach Papago Springs (note location PS in Fig. 3-6). The "Pinal Schist" (in reality, ultramylonite) mapped by Drewes (1977) along the contact between O-mylonite and W-mylonite also projects through Papago Springs. To the west of Papago Springs, near the Papago Springs trailhead (note location PST in Fig. 3-6), outcrops containing dark-weathering elliptical to rounded calc-silicate masses are completely enveloped in protocataclastically overprinted leucocratic sill-like bodies (Fig. 6-13).

As described earlier, farther west of Papago Springs (location PS in Fig. 3-6), in the X9 Ranch subarea (Fig. 3-5), Drewes (1977) mapped yet another string of lenses and pods

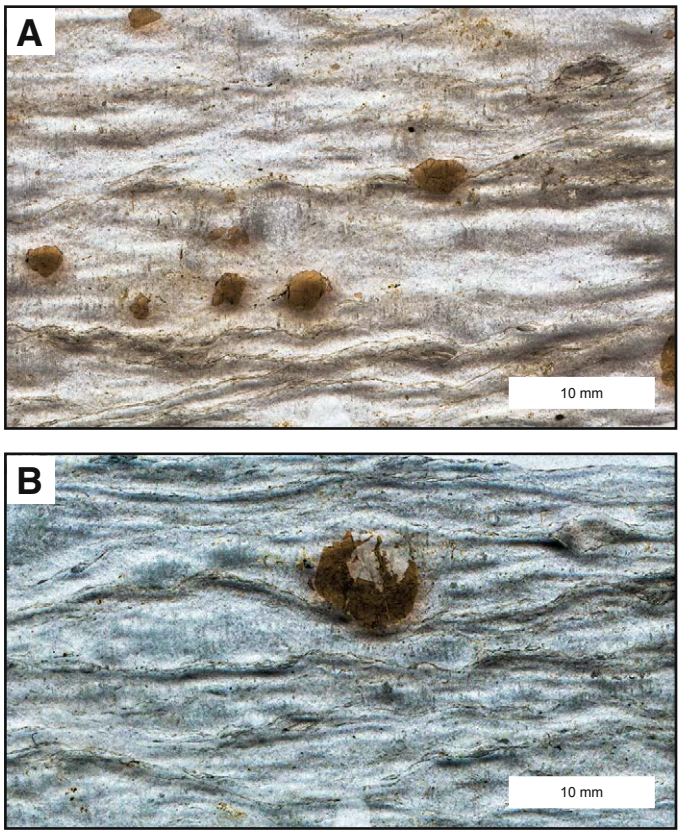


Figure 6-12. Thin-section scans of ultramylonite derived from W-mylonite protolith in the Loma Alta subarea. Garnets are enveloped by quartz-rich ribbons. Samples FR10A and FR10B (Fig. A-1; Table A-1 [see text footnote 2]).

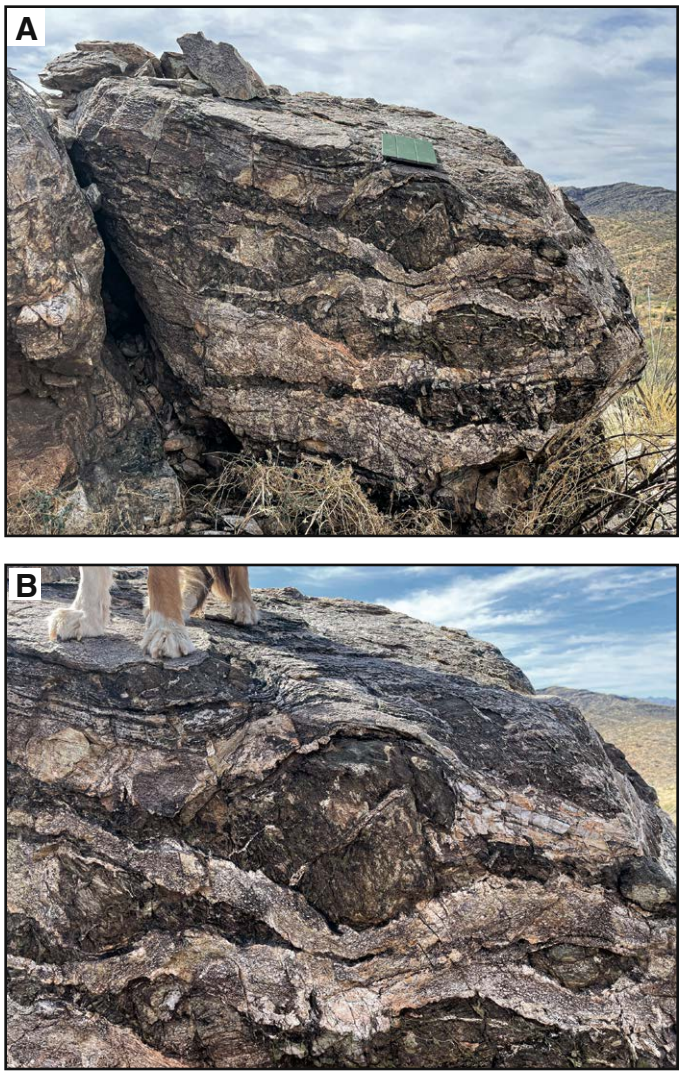


Figure 6-13. (A) East-directed photograph of outcrop of banded gneiss composed of white sill-like layers of coarse-grained leucocratic rock that envelop pods and lenses of dark-gray calc-silicate tectonites, which are vestiges of Paleozoic protolith. Computer pad for scale. (B) Closer view shows the cataclastically overprinted condition of the leucocratic rock and the penetratively faulted and fractured condition of the metamorphosed calc-silicate rocks. Dark-weathering elliptical to rounded calc-silicate masses are completely enveloped in cataclastically overprinted leucocratic sill-like bodies. Each dog paw is ~6 cm across. Location is Papago Springs trailhead in Posta Quemada–Hidden Spring subarea (Fig. 3-7).

of heterogeneous bedrock. He concluded that they occupied a thrust fault about 7 km long in trace length and were completely embedded within Wrong Mountain Quartz Monzonite (i.e., W-mylonite). Richard et al. (2005) interpreted the protolith of these lenses and pods as Paleozoic and Neoproterozoic sedimentary rock, including marble, quartzite, calc-silicate hornfels, and arenite. Rather than confirming the presence of a thrust, Richard et al. (2005) interpreted these enigmatic outcrops as representing dismembered skarn pendants in Laramide intrusive rocks, rearranged along a NE-trending zone created during Late Cretaceous to Early Paleogene (Laramide deformation) or middle Tertiary deformation.

Fault rock resembling mélange tectonite occurs from place to place along the main fault elements of the subdetachment zone (Fig. 6-3) as mapped by Spencer et al. (2001). This tectonite contains boudinaged, flattened, faulted, and folded lithologies that normally would not be found together in a single outcrop of sheared rock (Fig. 6-14). Though the matrix is largely marble, the boudins and fragments are composed of coarse-grained porphyroclastic mylonitic gneiss (resembling O-mylonite), fine-grained tectonite aplite and leucogranite, quartzite, calc-silicate metamorphic rocks, and carbonate. Foliation fabric is generally very gently dipping and contains a lineation that represents a standard, though crude, mineral lineation in the rheologically soft marble matrix. A more pronounced linear structure is evident in the alignment of nonequidimensional boudins of stiffer rock.

It is evident at the outcrop scale that the calc-silicate tectonite was subjected to intense flow and deformation in the solid state. The structural associations are bizarre (Fig. 6-15). On the one hand, angular chunks of granitoids, including mylonite, float

in a matrix of marble (Fig. 6-15A). On the other hand, boudined and pinch-and-swelled granitoids, including mylonite, are enveloped by marble. Most astonishingly, isoclinally folded layers of mylonite are completely contained in marble (Fig. 6-15B).

The main subdetachment fault passes through the location of Hidden Spring proper (location HS in Fig. 3-6). The outcrops are protocataclastically overprinted mylonites. Some outcrops display slickenlined surfaces that are unusually abundantly coated with epidote (Fig. 6-16A). Other outcrops resemble tectonite mélanges of mylonite, ultramylonite, and what appears to be pseudotachylyte (Fig. 6-16B). At one location, what appears to be pseudotachylyte (or ultracataclasite) occupies a set of faults and/or injection seams (Fig. 6-16C).

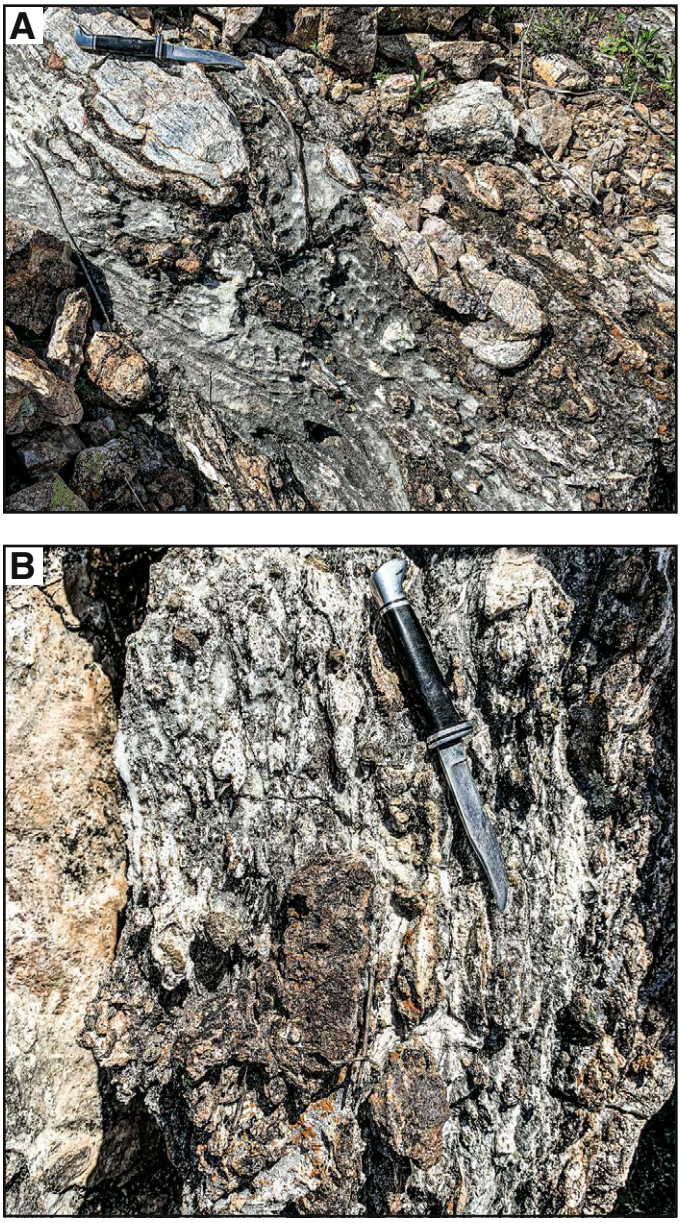


Figure 6-14. Outcrop photographs of calc-silicate tectonite in Posta Quemada–Hidden Spring subarea. These rocks and fabrics are found within the subdetachment fault zone. (A) Photograph of a mélange of mylonitic gneiss blocks suspended in a tectonite carbonate matrix. The largest block (upper left) is a boudin. The smaller block (near right-center edge) is a thin layer of mylonite that is isoclinally folded. Knife for scale is 19 cm long. (B) Photograph directed vertically downward at foliation-parallel surface in this tectonite. Note pervasive lineation defined by the subparallelism of ellipsoidal white mylonite clasts and brown blocky siliceous "clasts" floating within the marble tectonite matrix. Knife for scale is 19 cm long and happens to trend ~30° counterclockwise from the lineation.

MYLONITE

Introduction

The heterogeneous granitoid gneisses, at the scale of the entire Rincon Mountains, have received less attention than their complexity and geoscientific importance require. Only Drewes (1974, 1977) has mapped the entire range (1:48,000 scale), and this was a decade-long effort. Multiyear 1:24,000 scale geologic mapping by the Arizona Geological Survey addressed two large subregions of the Rincon Mountains. Spencer et al. (2001) mapped the Narrows quadrangle, which includes, but goes well beyond, the Posta Quemada–Hidden Spring subarea; Richard et al. (2005) mapped the Rincon Valley area at 1:24,000 scale, which includes both the Loma Alta and X-9 Ranch subareas. Their mapping, however, focused mainly on upper-plate rocks. They addressed the heterogenous lower-plate crystalline granitoids in more of a reconnaissance approach and chose to combine lower-plate rocks as a single unit comprising a number of rock types and ages.

Mylonites in the Saguaro Loop Subarea

The landscape expression of O-mylonite (belonging to the Oracle Granite Suite) within the Saguaro Loop subarea (Fig. 3-2) is ledgy, forming step-like benches controlled by differential weathering and erosion of the shallow-dipping mylonite layering (Fig. 6-17). O-mylonite weathers relatively dark and displays a highly penetrative mineral lineation (Fig. 6-18A). In weathered-surface expressions, the mylonitic foliation is slightly irregular due to quartz ribbons wrapping around large feldspar porphyroclasts (Figs. 6-18B and 6-18C). Full thin-section scans of O-mylonite revealed the overall fabric character (Fig. 6-18D). Additional descriptions of O-mylonite are found in Davis (2013).

W-mylonite (belonging to the Wilderness Granite Suite) is also observed in outcrop in the Saguaro Loop subarea. W-mylonite, which displays smooth weathering, has a light-beige to light-gray hue. Its foliation expression lacks the large augen porphyroclasts diagnostic of O-mylonite (Fig. 6-19A). Its pre-mylonite protolith texture was granular, not porphyritic. Diagnostic minerals of W-mylonite are garnet and muscovite







mica. In thin section, W-mylonite presents a distinctive S-type granite mineralogy dominated by quartz and feldspar but including essential garnet and muscovite (Fig. 6-19B). We sampled both O-mylonite and W-mylonite for purposes of geochronology and thermochronology within this subarea (Chapter 8).

Foliation and lineation in W-mylonite within the Saguaro Loop subarea are penetrative and oriented identically to foliation and lineation in the O-mylonite (Fig. 3-2). The attitude of mylonitic foliation in both rocks is generally 189°/24°NW, with lineation plunging 17°/241° (Table 3-2; Fig. 3-2). Moreover, the sense of shear is consistently top-to-the-SW. The sense of shear in W-mylonite is most evident in the alignment of mica fish and S-C fabrics. Some garnets exhibit a top-to-the-SW sense of rotation, a polarity highlighted in thin-section observations of micas wrapping around garnets. Similar fabrics were observed around feldspar porphyroclasts of similar size.

Mylonites in the Loma Alta Subarea

In addition to the O-mylonite and W-mylonite exposed within the Loma Alta subarea (Fig. 3-3), there is also the Loma Alta mylonite. It is a beige-weathering, medium-grained, and relatively equigranular granite. Its penetrative low-dipping foliation exerts a strong geometric control on weathering and erosion of the landscape (Fig. 6-20). Feldspar porphyroclasts are enveloped within a much finer-grained matrix dominated by quartz, phyllosilicates, and tiny feldspar porphyroclasts. Quartzofeldspathic in composition, it also contains biotite, chlorite, apatite, and tiny porphyroclasts of titanite. Loma Alta mylonite lacks the diagnostic large porphyroclasts of O-mylonite or the essential white-mica garnet–bearing mineralogy of W-mylonite. As described earlier, this mylonite was first identified and named in the Loma Alta subarea during this research; we also recognized it in the X9 Ranch subarea. As will be reported in Chapter 8, the U-Pb zircon age for the Loma Alta mylonite conforms with the 27–25 Ma age range of Catalina Intrusive Suite Granites. The microfabric characteristics in the Loma Alta mylonite include well-developed S-C relationships, as seen in the full thin-section scan (Fig. 6-21). Regardless of protolith, all mylonites in the Loma Alta subarea share common fabric orientations: the attitude of mylonitic foliation is 102°/16°, with lineation plunging 10°/244° (Table 3-2; Fig. 3-3).

Figure 6-15. Additional outcrop-scale photographs of calc-silicate tectonite in the Posta Quemada–Hidden Spring subarea. (A) White granitoid chunks and blocks floating in matrix of marble tectonite. Some of the clasts have broken shapes as if pulled apart by predominantly brittle fracturing. Others are more ellipsoidal, suggesting some plastic attenuation during shearing. Outlines of the clasts suggest some degree of brittle breakdown. Length of largest block is 60 cm. (B) The white granitoid chunks and blocks in this image are mostly mylonitic, and they display lensoidal (boudin) shapes and pinch-and-swell structure. Length of knife (for scale) is 19 cm. (C) This mylonite layer, embedded within marble tectonite, is isoclinally folded. Width of field of view is 28 cm.



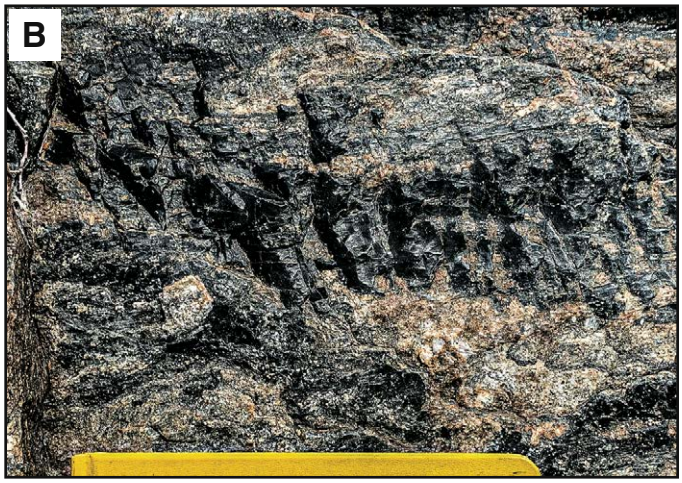




Figure 6-16. Photographs of outcrops at Hidden Spring. (A) Abundant slickenlined epidote coatings on fault surface. Hand and map board in upper-right corner indicate scale. (B) Black glassy pseudotachylyte and/or ultracataclasite. Note edge of field notebook (19 cm in length). (C) Tectonite mélange marked by granitoid clasts floating in pseudotachylyte and/or ultracataclasite.



Figure 6-17. SE-directed photograph of ledgy landscape of O-mylonite in the Saguaro Loop subarea near the Javelina Picnic Ground. Note the contrast between the foliated bedrock (O-mylonite) and the massive expression of chloritic protocataclasite (CPC) and dark-weathering ultracataclasite along back-right skyline area. Width of field of view at midrange is ~200 m.

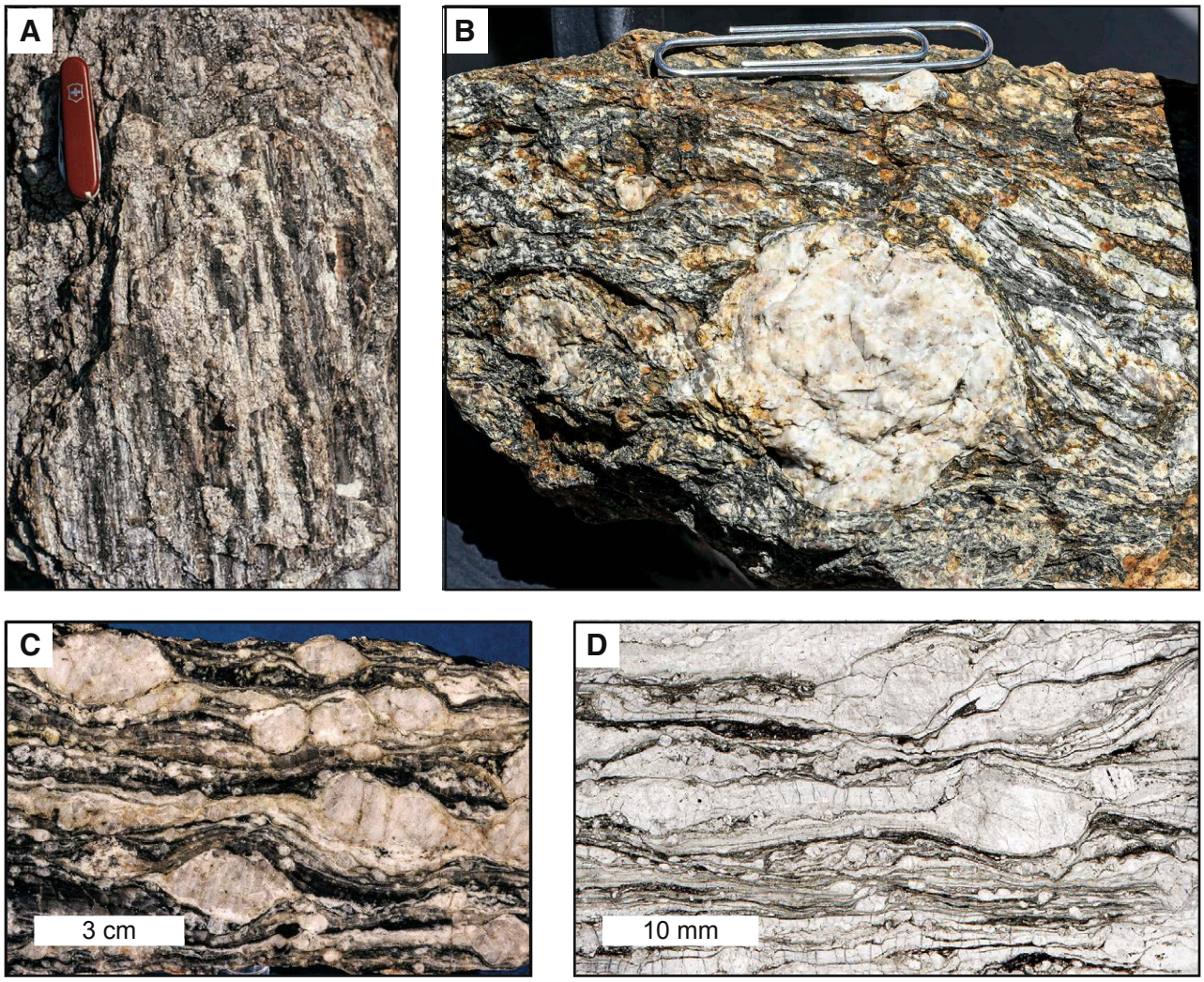


Figure 6-18. Physical nature of O-mylonite in the Saguaro Loop subarea. (A) Penetrative mineral lineation is largely controlled by sheared quartz ribbons. (B) Photograph of hand specimen of O-mylonite displaying large porphyroclast of feldspar with sigma tail. Foliation is defined by quartz ribbons and augen-shaped porphyroclast of feldspar. The Oracle Granite protolith for this rock is characterized by very large phenocrysts, up to 12 cm in length. Length of paper clip is 5 cm. (C) Photograph of slab of O-mylonite, with foliation defined primarily by quartz ribbons and lenticular feldspar porphyroclasts. Photographs A–C are by Peter L. Kresan © www.kresanphotography.com. (D) Full thin-section scan of O-mylonite showing pronounced quartz ribbons and feldspar porphyroclasts. Quartz ribbons are broken by closely spaced tension fractures. Field of view is 46 mm.

Mylonites in the X9 Ranch and Posta Quemada–Hidden Spring Subareas

We did not examine the mylonites and other lower-plate gneisses within the X9 Ranch and Posta Quemada–Hidden Spring subareas. However, the heterogeneity and complexity of these crystalline rocks were underscored in the work done by Richard et al. (2005) and Spencer et al. (2001). Richard et al. (2005) observed that the W-mylonite (Wrong Mountain Quartz Monzonite of Drewes, 1977) intrudes older igneous and metamorphic rocks in a lit-par-lit. Fabrics range from massive to strongly mylonitic, with mylonitic foliation becoming progressively stronger toward the Catalina detachment fault. Richard et al. (2005) evaluated the sense of shear in mylonites and found a dominant top-to-the-SW sense of shear, with some top-to-the-NE exceptions. Based on field measurements posted on the geologic map of Richard et al. (2005), mylonitic lineation plunges 10°/257°, i.e., parallel to this direction of transport.

Mylonite in Martinez-Salcido Ranch Subarea

Drewes (1974, 1977) regarded the mylonites of this subarea as Wrong Mountain Quartz Monzonite (W-mylonite). However, there are risks in assuming that this bedrock unit is equivalent to

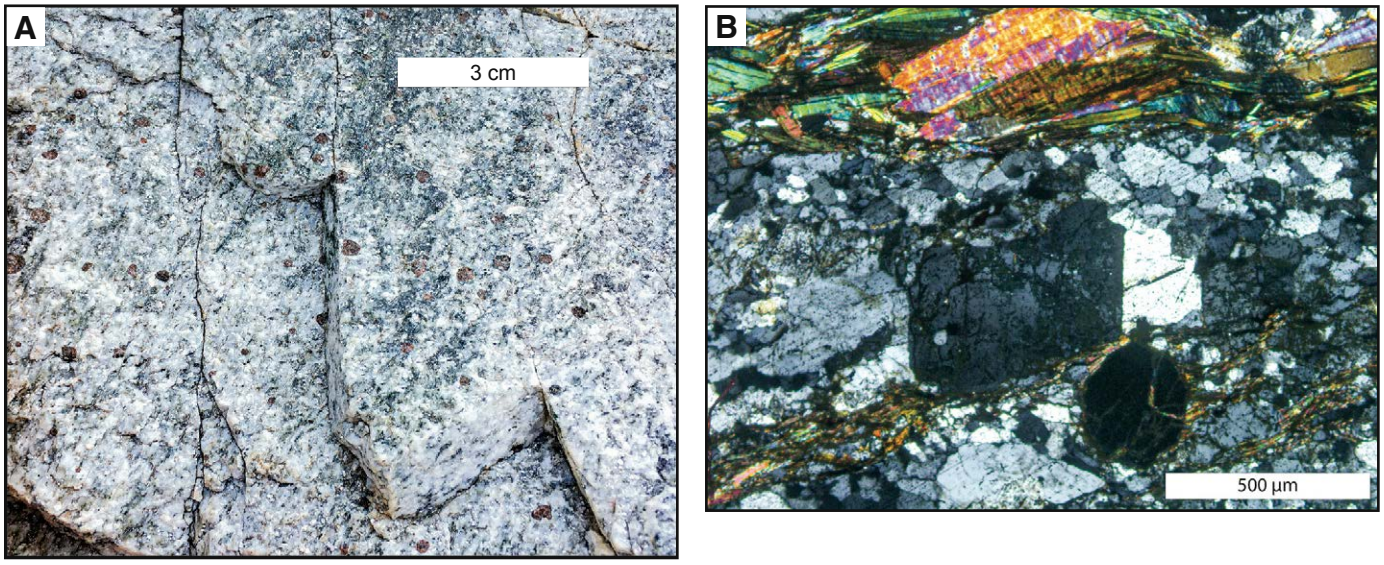


Figure 6-19. (A) Macrophoto of "plane" of foliation of W-mylonite with abundant garnet in a matrix of penetratively lineated quartz-feldspar mylonitic fabric. Lineation is penetrative. Garnet is anomalously large and abundant in this particular sample. (B) Photomicrograph of W-mylonite. Garnet in bottom right. Muscovite is abundant along top of this photomicrograph. Feldspar porphyroclast in center is bordered along top by strained quartz. Sample SL-101 (Fig. A-1; Table A-1 [see text footnote 2]).



Figure 6-20. East-directed photograph of outcrop expression of Loma Alta mylonite. Its color ranges from light brownish gray to slightly orange. Scale is based in relation to height of geologist to the left of the bar scale.



Figure 6-21. Full thin-section scan of Loma Alta mylonite, showing superb S-C relationships. C surfaces are inclined gently to the right. Feldspar porphyroclasts are inclined gently to the left. Sense of shear is top-to-the-right. Because the host rock for this thin section is float, the S-C fabric cannot be used to determine actual sense of shear. Sample LA-12 (Fig. A-1; Table A-1 [see text footnote 2]). Width of field of view is 46 mm.

W-mylonite. Liming (1974) did not observe garnet or essential white mica in describing the microscopic petrography of this rock, suggesting it may not have a Wilderness Suite protolith. Mylonitic foliation is oriented, on average, 115°/20°SW, with its pervasive penetrative streaky mineral lineation plunging 15°/235° (Liming, 1974) (Table 3-2; Fig. 3-10). Sense of shear is top-to-the-SW based upon S-C relations and comparable microstructural criteria (Davis et al., 1998, 2011).

STRAIN LOCALIZATION

Strain Localization by Ultramylonite in Saguaro Loop and Loma Alta Subareas

The ultramylonite formed beneath the brittle-ductile transition during core complex extensional tectonics as an accommodation to top-to-the-SW ductile shearing that brought O-mylonite and W-mylonite into shear zone contact (Davis, 2013). The transformation of mylonite to ultramylonite was marked by extreme grain-size reduction and an increase in the volumetric proportion of phyllosilicates. This process was the precursor to strain localization that led to ultramylonite becoming a strategic structural control for creating the subdetachment fault, which incised the CPC against mylonite (Davis, 2013). This is best displayed by the close juxtaposition (location and orientation) among the ultramylonite, the subdetachment fault, and the mylonite in the Saguaro Loop subarea (Davis, 2013) (Fig. 3-2).

A physical expression of this relation is evident in an extensional klippe of CPC whose basal contact is the subdetachment fault, beneath which is the ultramylonite (Fig. 6-22A). The same butte shown in Davis (2013, fig. 20) is pictured at a closer range and in a cross-sectional profile in Figure 6-22A. When viewed in the direction of tectonic transport (Fig. 6-22B), the ultramylonite projects SW along a surface just beneath the subdetachment fault and (beyond) to the trace of the Catalina detachment fault.

The argument for strain localization of the subdetachment fault by ultramylonite cannot be made as confidently in the Loma Alta subarea (Fig. 3-3). Yet the ultramylonite there coincides with the sole of the CPD fault rock unit, thus residing just beneath the subdetachment fault.

Strain Localization by Ultramylonite and Calc-Tectonite in the X9 Ranch and Posta Quemada–Hidden Spring Subareas

The entire tight synformal hinge of the Rincon Creek synform is lined with ultramylonitic fault rock, albeit commonly overprinted by cataclastic deformation (Fig. 3-5). It crops out beneath the Catalina detachment fault. Its thickness is ~200 m, which is comparable to that of the Saguaro Loop subarea and to the thickness of ultramylonite portrayed in cross-sections by Drewes (1977) for the Loma Alta subarea. The intensity of deformation of this rock in the X9 Ranch subarea was underscored by Drewes (1977) in his map explanation of units: "…typically strongly and multiply deformed through dynamic and thermal events." Its role as a strain localizer seems highly likely.

In the Posta Quemada–Hidden Spring subarea (Fig. 3-6), calc-silicate tectonites and calc-silicate rocks appear to have predetermined the locations of splays of the subdetachment fault system. The original "emplacement" of these enigmatic zones, marked by pods and lenses of Paleozoic and Neoproterozoic sedimentary protolith, seems to require tectonic heritage related to early Cenozoic magmatism and/or Laramide thrusting. An important exemplar for strain localization along calcite-rich mylonites is that of Singleton et al. (2018). Their research in the Buckskin-Rawhide metamorphic core complex documented the presence of thin (<1-m- to 100-m-thick) calc-rich mylonites, continuous for ~30 km in the tectonic transport direction along the Buckskin detachment fault. Protolith is Pennsylvanian–Permian sedimentary rock beneath a Cretaceous thrust fault. Though original tectonic-transport direction during thrusting was southeastward, shear in the calc-rich mylonites is northeastward, conforming to tectonic transport during detachment faulting. Singleton et al. (2018) conclude that even minor calc-mylonites can exert significant control on strain localization (including location and geometry) associated with detachment fault systems in metamorphic core complexes.

SUMMARY

Mapping and field observations disclosed that the contact interface between semi-brittlely to brittlely deformed CPC and underlying crystal-plastic mylonites is either a discrete subdetachment fault or a zone of subdetachment faulting. Rock units commonly found directly beneath or along the subdetachment fault or fault zone are quartzofeldspathic ultramylonites and vestiges of calc-silicate tectonites. It seems likely that the position and attitude of subdetachment faulting were strain-localized by the presence and rheological properties of the ultramylonite and

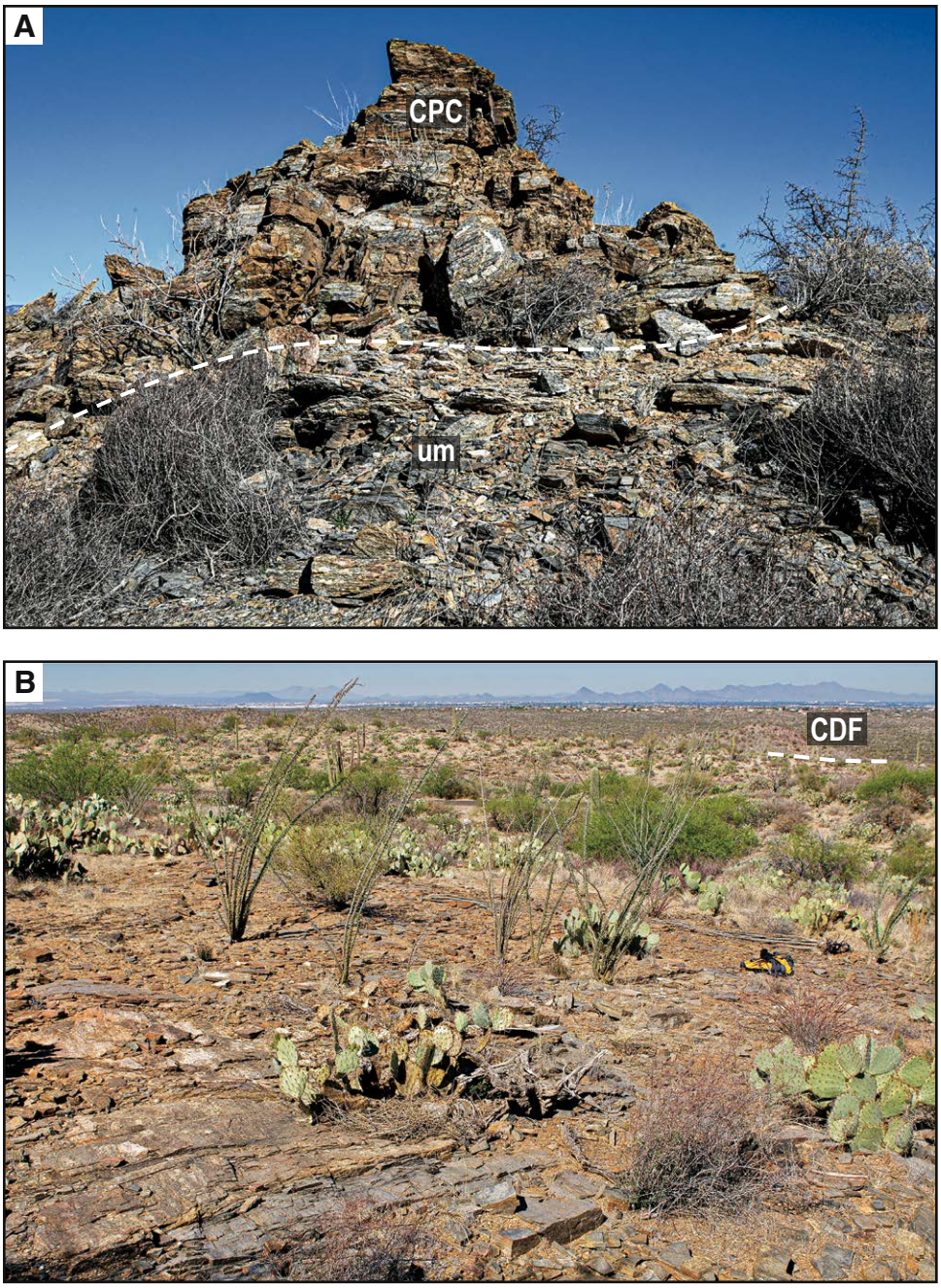


Figure 6-22. (A) North-directed photograph of tiny butte of chloritic protocataclasite (CPC) in the Saguaro Loop subarea. CPC in this outcrop is characteristically highly fractured, cataclastically overprinted mylonite. In the immediate foreground, there is ultramylonite (um), which weathers dark gray to black. The subdetachment fault (trace shown in dashed white line) separates ultramylonite (beneath) and CPC (above). Height of exposure above subdetachment fault is ~5 m. Same outcrop but different view is shown in figure 12 of Davis (2013). (B) SW-directed view of top of ultramylonite fault-rock unit in the Saguaro Loop subarea. It dips very gently westward, projecting into the subdetachment fault trace (not shown). Its attitude is parallel to that of the Catalina detachment fault (CDF), though it projects below the fault. The same outcrop but different view is shown in (Davis, 2013, fig. 12). City of Tucson and Tucson Mountains are visible in the distance.

calc-silicate tectonites. Strain localization is enhanced by deformation mechanisms that produce (1) extreme grain-size reduction (e.g., dynamic recrystallization; porphyroclastic breakdown of feldspar), (2) reaction softening (e.g., increase in phyllosilicates by alteration of feldspar to quartz and sericite; more interconnections among phyllosilicate-rich layers), and (3) geometric softening produced by enhancement of favorable shape and lattice alignments. In their review paper on metamorphic core complexes, Platt et al. (2015, p. 21) presented insight especially germane to the strain localization discussed here: "For several kilometers below the [brittle-ductile transition], ductile deformation is strongly localized in one or more shear zones with a cumulative width of a few tens of meters to 200 m (Behr and Platt, 2014). These processes generate a relatively thin layer of mylonite and ultramylonite that is genetically and geometrically related to the detachment (e.g., Behr and Platt, 2011, 2014), although it may be cut out during exhumation along the brittle section of the fault." In Chapter 7, we explore how these strain-localization processes fit into the overall structural-kinematic evolution of the Catalina detachment zone.

CHAPTER 7

Progressive structural evolution of the Catalina detachment zone

INTRODUCTION

This chapter presents a model that describes and explains the progressive ductile-through-brittle structural evolution of the Catalina detachment zone. The preceding chapters emphasized the physical, spatial, geometric, and kinematic character of the essential structures and fault-rock units, as well as the fabric and structural damage of the rocks within the various elements of the Catalina detachment zone. The model draws particularly upon the conditions whereby ductile deformation mechanisms within granitic crust shift to semibrittle and brittle deformation mechanisms. The physics of that shift is the focus of significant attention in the literature. A product of the model, referred to here as structural/fabric paragenetic sequencing, is consistent with observations made by Lister and Davis (1989), Roberts (2002, p. 3), and Platt et al. (2015, p. 20). This sequencing of deformation is one of progressive localization of strain and displacement. Chapter 8 integrates thermochronologic and geochronologic age constraints into this structural paragenesis.

DEPTH-DEPENDENT "CONVEYOR BELT" SHEAR ZONE MODEL

Establishing the contact relations of the structural components of the Catalina detachment zone led to a "shear zone model" for the progressive development of the fault-rock stratigraphy within a Cordilleran metamorphic core complex (Davis, 1981, 1983, 1987a). This model envisions a "conveyor belt" shearing process by which actively deforming lower-plate mylonites are lifted progressively from a ductile regime into a brittle regime (Fig. 7-1A). The model recognizes that deformation mechanisms that lead to mylonitization are thermally activated, whereas cataclasis, fracturing, and faulting obey constitutive laws anchored in frictional strength, including fluid overpressuring. For this reason, Rutter et al. (2001) equated the brittle-ductile transition to a frictional-viscous transition. The depth-dependent conveyor belt shear zone model as applied to metamorphic core complexes envisions the uppermost part of the lower-plate mylonites undergoing progressive transformation to chloritic protocataclasite (originally referred to as "chlorite breccia"; Fig. 7-1A) as it moves upward through the frictional-viscous transition. With time, and ever-shallower depth levels, the active zone of chloritic protocataclasite (CPC) becomes progressively thinner. During continued shear and slip, CPC directly beneath the Catalina detachment fault is converted into cataclasite and ultracataclasite within a thickness ranging from several meters to 15 m. In the final stage of extensional tectonic transport, all slip is concentrated on the detachment surface proper and along active faults within the upper plate. Lister and Davis (1989) illustrated this progression as a "time sequence of material response," showing cataclasis and brecciation overprinting mylonite and

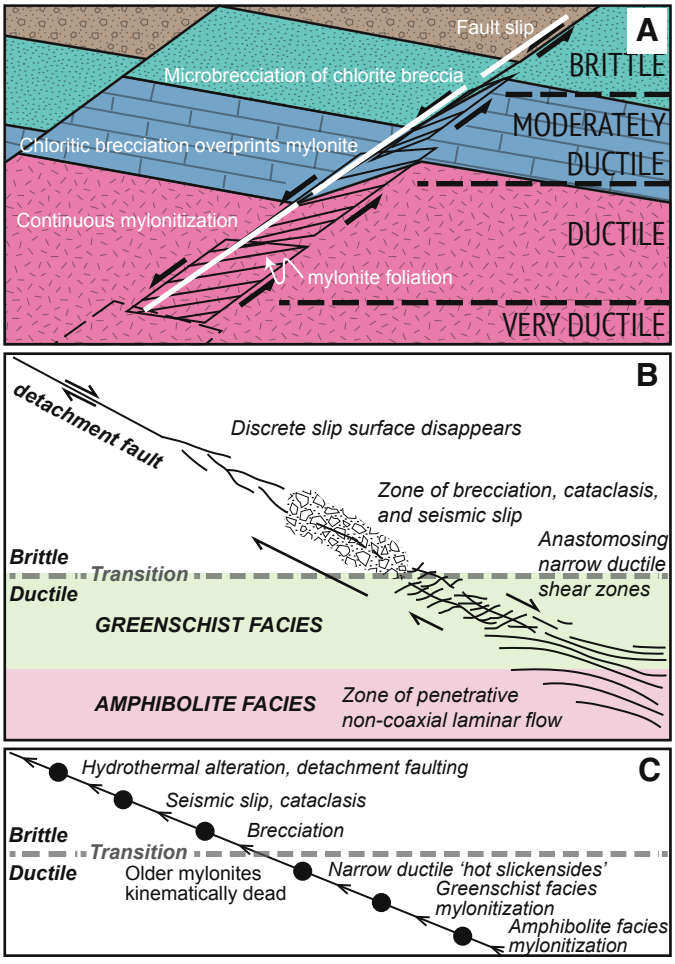


Figure 7-1. (A–C) Steady-state, depth-dependent models showing progressive deformation by extensional shear. As lower plate is lifted toward the surface, there is a natural fault-rock overprinting progression from mylonite to cataclasite to gouge. (A) Model from Davis (1981, 1983, 1987a). (B–C) Models from Lister and Davis (1989).

an upward replacement of these fault rocks by a discrete slip surface (Figs. 7-1B and 7-1C).

An important expansion of the shear zone model was presented by Lister and Davis (1989), one in which lower-plate doming, resulting from metamorphic core complex exhumation, causes earlier-formed protodetachment faults to bend and lock. As a consequence, younger detachment faults can develop in the upper reaches of the shear zone system. A new, active detachment fault continues to "root" into the principal brittle-ductile shear zone, but its efficacy relates to overall orientation and planarity, offering a frictional-sliding condition more favorable than the protodetachment fault that locked and became abandoned. Yet another relevant variant is that a younger detachment fault may cut and offset an older, now warped, detachment fault at an inclination, a position that causes "incisement," i.e., the propagation of faults into the uppermost lower plate and offset of the principal detachment fault (Lister and Davis, 1989).

Rutter et al. (2001, p. 3) emphasized that there may be departures from the fault-rock characterizations developed by Sibson (1977) and employed by Davis (1983), namely a systematic downward sequencing of gouge, cataclasite, mylonite, and mylonite gneiss. Departures from this idealized sequencing are the natural consequence of the heterogeneity of mechanical properties of initial protoliths, the modifications of these mechanical properties during shear, and the local environment and conditions of shear, especially fluid pressure and, thus, effective stress conditions (Rutter et al., 2001). It is likely that even below the zone of brittle-ductile transition, there can be spikes of elevated fluid-pressure conditions such that mylonitization is interrupted by short-lived episodes of brittle deformation, perhaps in the form of breccias or shattering.

FLUID-SOURCED REACTION-DRIVEN SHEAR ZONE MODELING

Selverstone et al. (2012) described the Davis (1983) shear zone model as a "gradual evolutionary model" of low-angle normal faults in which distributed viscous shearing gives way progressively to distributed brecciation and cataclastic flow, with thinning of the shear/fault zone occurring until a discrete principal slip surface forms considerably shallower than the brittle-plastic transition. An alternative model based on their research in the Whipple Mountains (California) was presented by Axen and Selverstone (1994) and expanded upon by Selverstone et al. (2012) and Axen (2020). These investigators set aside the conventional thinking that mylonite becomes brittlely overprinted when it ascends through a fixed-depth horizontal datum. Instead, they proposed that the viscous-brittle transformation occurs within a relatively thin interval controlled by fluid-sourced reaction-driven dynamics. Not only is this interval of high fluid influx not fixed in depth range, but they viewed it as a 3-D volume marked by significant topologic variability and relief (Selverstone et al., 2012). Strengthening due to the precipitation of alteration minerals (silica, chlorite, sericite, epidote, and titanite) triggers the transition from quasi-plastic flow to elastic-frictional deformation. While some of these mineral phases are typically mechanically weak (chlorite and sericite), randomly oriented fabrics and discontinuous lenses make these nominally weak minerals act as strengthening agents (e.g., Selverstone et al., 2012).

Though fluid-flow enhancement is most commonly associated with fault zones and damage-induced dilation, Rutter et al. (2001) pointed out that dilatancy can accompany shear-induced mylonitization, and as a result, mylonitic shear zones can be viable conduits for fluid transport. Mylonitization is superseded by progressive cataclastic overprinting of the mylonites, including the creation of slip surfaces in an environment of increased fluid pressure. Such recognition of abundant evidence for high fluid flow has been associated with interpretations of the origin of the chloritic protocataclasites (i.e., "chlorite breccias") from the beginning of core complex recognition (Davis and Coney, 1979; Crittenden et al., 1980), but most earlier works did not appreciate that rock strengthening, due to alteration and silicification (Selverstone et al., 2012), played an important role in triggering the formation of "chlorite breccia."

Consistent with Sibson (2020a, 2020b), the model emphasizes that the transition between crystal-plastic and elastic-frictional deformation is aided by sudden shifts in effective stress, such as those created through fault-valve behavior (Axen and Selverstone, 1994; Selverstone et al., 2012; Axen, 2019). Crystal-plastic shearing that creates the mylonites operates under relatively low differential stress conditions, whereas the formation of CPC proceeds in an environment of high differential stress modulated by elevated fluid pressure. This shift takes place within the lithosphere at an interval marked by maximum lithospheric strength.

Based on the fluid-sourced reaction-driven model (Selverstone et al., 2012), during the incipient stage of transition from crystal-plastic to elastic-frictional deformation, the "minidetachment faults" of Axen and Selverstone (1994) emerge, resulting in truncation, offset, and rotation of the mylonite. The initial orientations of minidetachment faults are controlled by orientations of C- and C′-surfaces in mylonite, because the minidetachment faults grow from these fabric elements (Selverstone et al., 2012). Most minidetachment faults are abandoned over time, after being progressively cut and offset by superimposed minidetachment faults. Some minidetachment faults coalesce, interconnect, and remain active within linked systems (Selverstone et al., 2012). This interconnectivity serves to dissipate fluid pressure, thus, enhancing hardening and embrittlement, leading locally to the creation of pseudotachylyte as quenched products of frictional melting. The effective hardening due to retrograde alteration not only leads to minidetachment faulting, but it also promotes the intensive fracturing of CPC. Selverstone et al. (2012) and Axen (2019) concluded that coalescing, linking, and smoothing of minidetachment faults lead to the emergence of the principal detachment fault surface.

PROPOSED ORIGIN OF FAULT ROCKS AND STRUCTURES: THIS STUDY

Introduction

We are attracted to integrating aspects of the "conveyor belt" shear zone model with the important insights developed in the Whipple Mountains detachment zone (Axen and Selverstone, 1994; Selverstone et al., 2012; Axen, 2019). Their observations and conclusions help to underscore the connections between so many of the fault-rock–related elements and structures observed in the Catalina detachment zone. For example, CPC is saturated with rock-strengthening alteration mineralogy. Minidetachment faults are part of the protocataclasite-forming dynamic system, and though not entirely confirmed through necessary microscopy, black glassy rock with outcrop expressions closely resembling pseudotachylyte is present along deeper minidetachments. The abundant "slot faults" identified in the Catalina detachment zone are simply expressions of abandoned minidetachments. The deeply recessed, weathered, and eroded slot-like character of these minidetachments reduces significantly the possibility of viewing fault-rock fabrics along the fault cores. We conclude that the model developed by Axen and Selverstone (1994) and Selverstone et al. (2012) in the Whipple Mountains metamorphic core complex is largely applicable to the CPC domain of the Rincon Mountains. Yet, there are other mechanical/rheological challenges that need to be addressed in the paragenetic sequencing, namely, the origin of the subdetachment fault system and its apparent strain-localization control by ultramylonite and calc-silicate tectonite.

Our model is presented in Figure 7-2. The depth level of the brittle-ductile transition zone is not specified for the crustal thermal gradient is not known. A standard depth of ~10–12 km is not presumed! In fact, a normal thermal gradient does not seem likely, given the fact that the southeastern Arizona region during the relevant period of time (Oligocene–early Miocene) was marked by the voluminous "mid-Tertiary ignimbrite flareup," and therefore, the brittle-ductile transition probably resided at a shallower depth, <10–12 km. We adopt the conclusion that the brittle-ductile transition controlling the shift from mylonitization to cataclasis was importantly determined by a combination of temperature gradient and fluid-sourced reaction-driven dynamics, as insightfully emphasized by Selverstone et al. (2012).

Mylonitization

As in the "conveyor belt" shear zone model, we picture a ductile-brittle shear zone as tapered upward, i.e., a tapered channel (Sibson, 1977; Davis, 1983, 1987a). Below the brittle-ductile transition, and following Selverstone et al. (2012), crystal-plastic shearing operated in lithostatic stress conditions marked by relatively low differential stress, producing mylonites marked by moderately high shear strain (Fig. 7-2A). Close to the brittle-ductile transition, but still beneath it, strain localization resulted in several thick (up to 200 m) ultramylonitic shear zones. Translation along the thickest of these (~200 m) produced kilometer-scale offsets and, from place to place, brought mylonites of different protoliths (namely W- and O-mylonites) into direct contact with one another. Features caught up in this shearing included Laramide skarn bodies and Paleozoic carbonates that had occupied lower-plate Laramide thrust positions to the northeast of the heart of the Rincon Mountains (Chapter 9). These carbonates were transformed into calc-silicate tectonites; during mylonitization the sense of shear throughout was consistently top-to-the-SW.

Initiation of Chloritic Protocataclastic Deformation and Minidetachment Faulting

As mylonites (and ultramylonites) were drawn upward through a ductile environment, they entered a fluid-sourced brittle-ductile transition environment within which crystal-plastic deformation mechanisms were replaced by elastic-frictional mechanisms (Fig. 7-2B). Differential stress of the mylonitic rock was elevated due to the temperature-imposed restrictions in the deformation mechanisms available to quartz. Quartz that formerly was transformed ductilely into ribbons now behaved brittlely. The high-volume influx of hydrothermal fluids saturated the brittlely deforming mylonite, resulting in a progressive strength-hardening due to reaction-driven precipitation of quartz, chlorite, sericite, epidote, and titanite (Selverstone et al., 2012). The incipient shift from crystal-plastic to more elastic-frictional shear became expressed in minidetachment faults emerging from positions and orientations of C surfaces (Axen and Selverstone, 1994; Selverstone et al., 2012). The combination of minidetachment faulting, intensive fracturing, and protocataclastic deformation of mylonite more fully generated significant thicknesses of CPC, which grew both up section and down section from the locus of fluid ingress and highest shear strain (Fig. 7-2B).

The formation of minidetachments within the CPC (Fig. 7-2B) was initially due to work hardening ("embrittlement"; Selverstone et al., 2012) attributable to the mineralogical shift produced by the production of alteration minerals (e.g., quartz and epidote) and neo-fault rocks. However, because there was steady shearing over a long period of time, the environment conducive to the ductile-to-brittle transition and the overall ascent of lower-plate rocks caused a continuous updip/downdip lengthening and widening of the CPC fault-rock unit and the detachment surface. During this process, older minidetachment faults became cut and offset and, in places, rotated by younger minidetachment faults.

Fault-valve behavior was operating throughout the time window when CPC was being fashioned (from mylonite) into a distinctive, mappable fault-rock unit. Effective stress fluctuated dynamically in magnitude and location within the large and growing volume of CPC. Simultaneously, rock cohesion in the mylonite and CPC fluctuated markedly in magnitude and location due to variability in mineralization, fluid involvement, and temperature gradients. Brecciation and cataclasis were triggered and enhanced by failure under low-effective stress conditions,

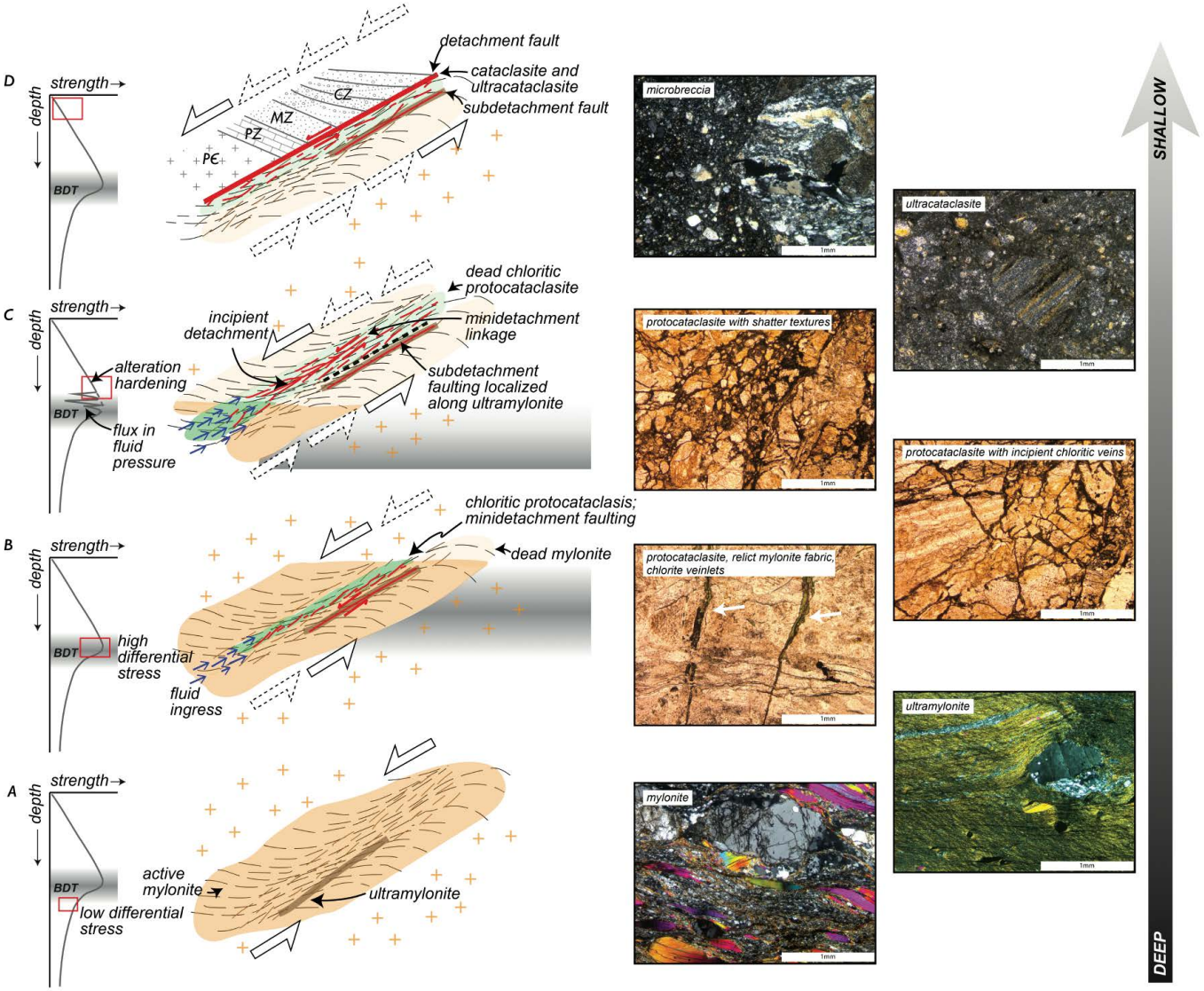


Figure 7-2. Model of progressive deformation, Catalina detachment zone. The time-sequence diagrams left of center portray the sequential evolution (structural paragenesis) of fabrics and structures within the Catalina detachment zone: (A) mylonite, ultramylonite, and calc-silicate tectonite (layers and pods too small to show but positioned within or near ultramylonite); (B) chloritic protocataclasite (including alteration and intensive fracturing) and minidetachment faults; (C) subdetachment fault and minidetachment linkage; and (D) the principal Catalina detachment fault and associated ultracataclasite, cataclasite, and gouge. Photographs right of center are reminders of the fabric characteristics imposed at successive stages during the progressive development of the Catalina detachment zone. On far left, there are portrayals of the positioning of each stage of progressive deformation relative to the zone of brittle-ductile transition (BDT); scale bars = 1 mm. The depth of this transition is not known, and positioning at the standard depth range of 10–12 km is not assumed. CZ—Cenozoic; MZ—Mesozoic; PZ—Paleozoic; P€—Precambrian.

and the cycle of failure and attendant (local) drop in fluid pressure caused precipitation of hydrothermal minerals, i.e., alteration and sealing. This began to occur in multiple seismic cycles within the seismogenic zone (Axen, 2020).

Subdetachment Faulting

CPC (still actively evolving) and the underlying mylonite remained coupled within a common shear zone until subdetachment faulting was initiated (Fig. 7-2B). The trigger for subdetachment faulting may have been macroscopic work hardening and embrittlement of the body of CPC, causing it to be more rigid. Discrete strain localization followed, concentrated along and/or near ultramylonite layers and calc-silicate tectonite. The strain-localizing qualities of the ultramylonite were derived from the combination of grain size reduction and abundance of phyllosilicates (Singleton et al., 2018). Additionally, carbonates offered geometric and thermal weakening of calcite. Subdetachment

faulting is an essential element of the entire Rincon Mountains domain of the Catalina-Rincon metamorphic core complex. There is only one such continuous subdetachment fault zone, though Force (2002) mapped multiple "subsidiary detachment faults" at the base of CPC (his "semi-breccia") in the Agua Caliente region between the Catalina and Rincon Mountains. The subdetachment fault fits the criteria of incisement (Lister and Davis, 1989), but what seems most important in explaining the development of the subdetachment fault is the strain-localizing control by tectonites, including calc-rich tectonites (Singleton et al., 2018), fashioned earlier during core complex extensional deformation.

The subdetachment fault in some ways fits the criteria of incisement, but there is no offset relationship with respect to the Catalina detachment fault. We conclude that the development of the subdetachment fault preceded the Catalina detachment fault and, thus, should be considered a "Catalina protodetachment fault." Thus, to the positional term, "subdetachment fault," is added a temporal term, "protodetachment fault." Down-plunge views underscore the observation that the protodetachment surface is by no means a planar low-angle normal fault; it has tens of meters of structural relief in area where the overlying detachment fault is strictly planar. Moreover, mapping demonstrates that the subdetachment fault is segmented and branching, characteristics that are not displayed by the map trace of the Catalina detachment fault. The Catalina detachment fault is everywhere unsegmented, nonbranching, and continuous. Slip along the Catalina protodetachment fault system conforms to the sense of shear in the underlying ultramylonite and mylonite. It also conforms to the top-to-the-SW slip on the Catalina detachment fault. The factor that seems to be most important in explaining the development of the subdetachment fault is the strain-localizing control by tectonites fashioned earlier during core complex formation.

We picture that the Catalina protodetachment fault system expanded in areal extent like a macro-dislocation, and as it did so, CPC became partially decoupled from underlying mylonite (Fig. 7-2C). Dynamic internal deformation of CPC directly above the subdetachment system simultaneously diminished. The duration of active slip along the subdetachment system may have been short-lived, partly because of the complexity and asperities within the anastomosing network of faults. Work hardening of the subdetachment fault system triggered the emergence of the principal detachment fault at a higher structural level (Selverstone et al., 2012). Conceivably, positioning was also influenced by what Selverstone et al. (2012) and Axen (2020) have emphasized: linking, coalescing, and smoothing of the youngest minidetachment faults that had emerged in CPC.

Detachment Faulting

As in the case of the Catalina protodetachment-subdetachment fault system, we envision the emergence of the Catalina detachment fault as analogous to a macro-dislocation with finite length. Growth and dominance of the detachment fault coincided with a decrease in slip and shear within the underlying CPC and cessation of activity on the Catalina protodetachment fault. As stated above, the Catalina detachment fault may well have emerged in part from the linking and coalescing of active minidetachment faults still being produced within the brittle-ductile transition zone (Selverstone et al., 2012; Parnell-Turner et al., 2018, p. 24) (Fig. 7-2C). Fault systems commonly evolve in ways marked by initial complexity (e.g., multiple, nonplanar, and/or misaligned segments) that "reorganize" into a single, master fault with smoother, planar geometry. The Catalina detachment fault would have achieved this through its many kilometers of slip, thus achieving much higher mechanical efficiency. Notwithstanding, it remains surprising that the principal detachment fault could not only be so smooth but also unsegmented over an exposed trace length of 80 km along the Catalina-Rincon metamorphic core complex. Everywhere, no matter its absolute orientation, the Catalina detachment fault is smooth, planar, and discrete in outcrop. No amount of fluid flow and alteration mineralization could seal the Catalina detachment fault as it localized slip for a sustained period of time. It appears that slip was managed with such mechanical efficiency that there never was work- hardening sufficient for branches or splays to develop.

Figure 7-2D depicts the final configuration in which upper-plate stratigraphy and basement rocks are juxtaposed with CPC along the detachment. Cataclasite and ultracataclasite formed as a direct expression of the "grinding load" of the tectonic transport of kilometers of upper-plate rock. Gouge and cohesionless breccias formed in places along the base of the upper plate, above the seismogenic zone (Axen et al., 2018). Even though gentle inclinations of fault-rock fabrics appear to be the rule within the Catalina-Rincon metamorphic core complex, the fashioning of the different fault rocks within different environments creates a subtle though significant structural disharmony within the Catalina detachment zone. To be sure, the attitudes of mylonite and the subdetachment fault are subparallel. But relict (mylonitic) compositional layering within CPC is discordant to both the subdetachment fault and underlying mylonite. Cataclasite and ultracataclasite layers are subparallel to mylonite foliation and the subdetachment fault, but commonly discordant to relict mylonitic foliation in underlying CPC. Axen et al. (2018) determined that cataclastic layers are youngest at the top and are generally older downward. We believe this holds true for the black ultracataclasites in the Rincon Mountains. Upper-plate bedding is typically discordant to the underlying detachment fault and cataclastic layering.

3-D Macroscopic Geometry through Time

In the Cordilleran metamorphic core complexes, including the Catalina-Rincon metamorphic core complex, mylonites and ultramylonites are deformed into doubly plunging upright antiforms and synforms. Upright antiformal/synformal folding of mylonitic foliation/layering is a buckling response to the profound ENE/WSW stretching that generated the metamorphic core complexes in the corridor running from SE California through

SE Arizona (e.g., Yin and Dunn, 1992; Singleton, 2013a). The folds were incrementally amplified as mylonitization proceeded. More than 200 large-scale core complex antiforms and synforms were identified and mapped by Frost et al. (1982) in the Colorado River area of southeastern California and west-central Arizona alone. Most trend within the tight range of 045°–055°. Axial traces are quite evenly spaced; fold wavelengths consistently average ~10 km, from ~5 to 15 km. The ~13 km wavelength for the spacing of the Tanque Verde and Posta Quemada antiforms falls within this range.

The antiforms and synforms in the Rincon Mountains consistently plunge gently southwestward, though the plunge direction reverses to the NE in the high country of the eastern third of the Rincon Mountains, (Drewes, 1977) (Fig. 7-3). This shift from SW-plunging antiformal/synformal folding to doubly plunging folding occurred relatively late. We interpret this transition to have been a consequence of doming of the mylonitic gneisses, which in turn was likely produced by rolling hinge–induced isostatic rebound of lower-plate rocks as upper-plate rocks were tectonically denuded (Spencer, 1984; Buck, 1988; Wernicke and Axen, 1988; Axen and Wernicke, 1991; Frost and Heidrick, 1996).

In a similar fashion, the detachment faults within Cordilleran metamorphic core complexes have a folded form, again marked by upright antiforms and synforms for which the axial traces match both in position and orientation those defined by the folding of mylonitic foliation. Fletcher et al. (1995) suggested that the folds may have continued to amplify throughout brittle-ductile shearing, even during detachment faulting proper. They based this interpretation on the observation that antiformal/synformal folds defined by mylonitic foliation are tighter than the folds defined by the spatially proximate detachment fault. Force (2002) noted that in the Catalina-Rincon metamorphic core complex, the antiformal/synformal mylonitic structure has ~500–600 m of structural relief, whereas the relief on the antiformal/synformal profile of what he calls "the subdetachment arch" (which closely parallels the Catalina detachment fault) is no more than 300 m. Fletcher et al. (1995, p. 1478) concluded that "the folds began forming in the ductile regime and continued to amplify in the brittle regime." Similar conclusions have been reached for other metamorphic core complexes in the region (Singleton, 2013a). We subscribe to the interpretation by Fletcher et al. (1995). However, we recognize that some of the smaller-scale irregularity of the trace of the Catalina detachment fault reflects mullions (e.g., John, 1987) that were produced through some combination of abrasion into lower-plate mylonites and the systematic kinematic linking of fault segments (Parnell-Turner et al., 2018).

Early development of foliation arches and troughs affected the core complex–scale morphology of both mylonite and ultramylonite. CPC began to be created after the mylonites had acquired their antiformal/synformal structural geometry, though perhaps not their full amplification. Consequently, the initial form of the CPC fault-rock unit was sinusoidal, not quasi-tabular. The Catalina protodetachment fault system, with locus and orientation controlled by the strain-localizing ultramylonites and calc-silicate tectonites, also developed with range-scale sinusoidal geometry. The template for this form had been established by the folded antiformal/synformal geometry of mylonitic foliation and layering. The Catalina protodetachment fault system has a corrugated roughness that exceeds that of the Catalina detachment surface. Parnell-Turner et al. (2018) noted that macroscopic corrugated fault geometries are indeed influenced by preexisting ductile fabrics.

The emergence of the Catalina detachment fault proper was accompanied by tectonic denudation of upper-plate rocks. Influenced by the first-order presence and orientation of the Catalina protodetachment fault system, and by exploiting linkages among minidetachment faults in CPC, the Catalina detachment fault formed with a slightly more subdued geometrical form of its present sinusoidal shape. During the process of synformal/antiformal folding attending extension, it is probable that modest amplification of upright folding in mylonite, the Catalina protodetachment fault system, and the Catalina detachment fault was achieved. In addition, given the minimum ~35 km of upper-plate transport, the Catalina detachment surface became further smoothed through mullion- and megamullion-creating attrition. The tens of kilometers of tectonic translation of upper-plate rocks resulted in load-bearing-induced brittle shearing of underlying CPC, yielding cataclasite and ultracataclasite along the sole of

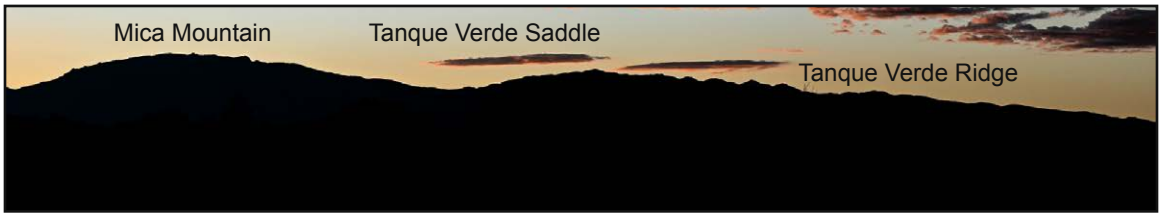


Figure 7-3. East-southeast–directed view of longitudinal profile of the Rincon Mountains metamorphic core complex. Mica Mountain is the domical summit (elevation is 2700 m). Doming was produced by late-stage flexural response to unloading associated with exhumation. Mica Mountain is separated from Tanque Verde Ridge by Tanque Verde Saddle. The elevation of the toe of Tanque Verde Ridge is 880 m. Tanque Verde Ridge is, structurally, the doubly plunging Tanque Verde antiform. The long rightward slope (SW of the culmination of Tanque Verde antiform) reflects the gentle SW plunge. We speculate that the serration seen along the ridge represents resistant patches of chloritic protocataclasite. Width of field of view is ~15 km.

the Catalina detachment surface. In particular, the narrow crest of the arched Tanque Verde antiform became a stress concentrator, accounting for the ultracataclasite that is localized along that structure. This spatial association supports the concept that the Tanque Verde corrugation/antiform had already developed to a significant extent prior to upper-plate transport and the fashioning of ultracataclasites.

During tectonic denudation, the characteristic domed geometry of the Rincon Mountains was achieved (Crittenden et al., 1980). A consequence was a shallowing of the Catalina detachment fault in its upper reaches. Another consequence was the development of the closely spaced NNW/SSE jointing that pervades the Tanque Verde antiform. Fletcher et al. (1995) reported such fracturing/jointing attending rolling-hinge bending associated with the Mojave core complex region. By the time this late-stage jointing was being created, the CPC now exposed at the surface had already acquired such intense damage that it was incapable of systematically fracturing in a manner akin to the jointing of mylonite. Force (2002) noted that jointing in mylonites is best and most intensely developed where the reconstructed detachment location is less than 200 m above.

SUMMARY

Our model attempts to place the development of the Catalina detachment zone into shear zone evolution context. The ductile fabrics and frictional damage produced in space and time and at nested scales were governed by the deformation mechanisms available to protoliths as crustal-scale normal faulting elevated lower-plate rocks through the brittle-ductile transition. During conveyance through the brittle-ductile transition, fault-valve behavior in a fluctuating environment of fluid pressure had a profound influence on frictional failure. Though imperfect, models of progressive structural evolution, such as the one presented here, underscore feedback loops that produced the properties of the Catalina detachment zone. For example, early-formed ultramylonite and calc-silicate tectonite controlled the position and attitude of the Catalina protodetachment fault. The overall form and position of the Catalina protodetachment fault exerted a strong control on the position of the Catalina detachment fault. Minidetachment faults emerged from oriented C and C′ fabric elements within mylonites. Coalescing, linking, and smoothing of minidetachment faults influenced the final positioning and attitude of the Catalina detachment fault. On the one hand, the body of CPC was weakened by pervasively frictionally controlled fracturing and faulting; on the other hand, the silicification and alteration accompanying fluid-induced fracturing strengthened the body of CPC. Such feedback loops and linkages must have a certain "universal" quality in the evolution of metamorphic core complexes. Why else would Cordilleran metamorphic core complexes be so nearly identical to one another?

CHAPTER 8

Geochronology- and thermochronology-based temporal framework

The content of the previous chapter reflects a major goal of this project: to develop an integrated kinematic-mechanical model explaining how the principal structures and fault rocks of the Rincon Mountains metamorphic core complex were fashioned during brittle and ductile shearing. In this chapter, we integrate this model into a reliable temporal framework, spanning formation of mylonites to exhumation of the detachment zone. A part of testing the efficacy of this timing relates to stratigraphic and basin analysis records (Chapter 9).

Here, we establish and/or confirm protolith ages of O-mylonite, W-mylonite, and Loma Alta (LA-) mylonite; the timing of mylonitization, cataclasis, slip, and exhumation; and the age of a post-CPC (chloritic protocataclasite) mafic dike. Overall, the objective is to add to existing thermochronology results for the Catalina-Rincon metamorphic core complex using a variety of techniques and methods. In this section, we primarily focus on the results of new geochronology and thermochronology analyses carried out for this study. Table 8-1 is a summary of the geochronology and thermochronology data. In Chapter 9, we place the results of the geochronology and thermochronology analyses in structure-tectonic context.

ZIRCON U-Pb GEOCHRONOLOGY: MYLONITE AND PINAL SCHIST

Samples of O- and W-mylonite were collected within the Saguaro Loop subarea, and a sample of LA-mylonite was collected within the Loma Alta subarea. The geologic map context for each of these samples is well established, and these samples conform to the mineralogy and fabric of the units they represent. Zircon extracted from these rocks was dated at the University of Arizona, Arizona LaserChron Center, following the U-Pb geochronologic protocols detailed in Gehrels et al. (2008) and Gehrels and Pecha (2014). Backscattered-electron (BSE) and cathodoluminescence (CL) images of the zircons were acquired on a Hitachi S-3400 N scanning electron microscope with a Gatan Chroma CL 2 attachment. The zircon ages for this study were acquired using a Photon Machine Analyte G2 excimer 193 nm laser-ablation system connected to a Thermo Element 2 single-collector high-resolution inductively coupled plasma–mass spectrometer (ICP-MS). Samples with >20% discordance were not included in the analyses.

Zircon U-Th-Pb (ZUPb) geochronology was performed on samples 17DR01, 17DR02, 17DR03, and 19DR-LA17 (sample locations shown in Supplemental Material, Appendix A). Results are presented in Wetherill concordia diagrams as well as weighted mean age plots (Fig. 8-1). O-mylonite sample 17DR03 and Loma Alta mylonite sample 19DR-LA17 gave consistent crystallization ages of 1448 ± 10 Ma (n = 57/60, mean square of weighted deviates [MSWD] = 1.15) and 26.87 ± 0.72 Ma (n = 230/245, MSWD = 5.0), respectively. W-mylonite sample 17DR02 yielded inherited core ages of 1663 ± 13 Ma (n = 36/39, MSWD = 1.6) and a rim age of 42.7 ± 1.0 Ma (n = 8/9, MSWD = 6.8). Pinal Schist sample 17DR01 yielded a multimodal kernel density estimation (KDE) out of 306 zircon analyses with peaks at ca. 1.70 Ga, ca. 1.85 Ga, ca. 2.56 Ga, and ca. 3.29 Ga. Sri Lanka (SL) zircon reference material (563.5 ± 2.3 Ma; Gehrels et al., 2008) was run as a secondary standard for accuracy checks (SL = 563.8 ± 1.8 Ma). The results of this accuracy check underscore good reproducibility of standards and, thus, a reliable analytical run. The U-Th-Pb analytical data for laser-ablation (LA) ICP-MS spot analyses on the zircon grains are presented in Supplemental Material, Appendix C, Table C-1.

Zircons from the W-mylonite record igneous and metamorphic overgrowths on inherited cores. U/Th ratios greater than 10 indicate zircon growth in the presence of metamorphic fluids (Black et al., 1986; Rubatto, 2017). Proterozoic inherited cores (dominantly ca. 1.65 Ga with some ca. 1.44 Ga ages) had U concentrations ranging from 100 to 2300 ppm and U/Th ratios from 0 to 20. In contrast, the Eocene rims had U concentrations ranging from 1200 to 3300 ppm and U/Th ratios ranging from 120 to 280.

APATITE U-Pb GEOCHRONOLOGY: W-MYLONITE AND O-MYLONITE

In order to constrain the onset of detachment and upper-crustal exhumation, four samples were collected for apatite U-Pb (AUPb) and fission-track (AFT) double dating. Samples HS-05, STA2, STA2C, and HS-04 were collected in a transect perpendicular to the trace of the Catalina detachment fault in the Hidden Spring subarea (sample locations shown in Supplemental Material, Appendix A). Sample HS-05 was W-mylonite collected ~1 km from the trace of the Catalina detachment fault. Sample STA2 was extracted from W-mylonite surrounding the carbonate tectonite locality; STA2C was taken from a mafic granitoid lens within the carbonate tectonite ~2.3 km from the Catalina detachment fault. Sample HS-04 was O-mylonite collected at a location ~3.5 km from the Catalina detachment fault.

TABLE 8.1. SUMMARY TABLE OF GEOCHRONOLOGY AND THERMOCHRONOLOGY AGES OBTAINED ON DEFORMATIONAL FABRICS AND ROCK PROTOLITHS AS WELL AS POSTDEFORMATIONAL MAFIC DIKES IN THE STUDY AREA IN THE RINCON MOUNTAINS

Sample	Type of rock	Subarea	Lat (°N)	Long (°W)	Mineral	Technique	Type of age	Comments	Age (Ma) ± error*
17DR01	Pinal Schist	Saguaro Loop	32.18548	110.73109	Detrital zircons (DZ)	U-Pb	Age peaks (n = 306)	Ca. 1.70, ca. 1.85, ca. 2.56, and ca. 3.29 Ga	
17DR03	Oracle (O)-mylonite	Saguaro Loop	32.16486	110.72284	Zircon	U-Pb	Crystallization	MSWD = 1.15; n = 57/60	**1448 ± 10**
17DR02	Wilderness (W)-mylonite	Saguaro Loop	32.19008	110.70429	Zircon (cores)	U-Pb	Inheritance	MSWD = 1.6; n = 36/39	**1663 ± 13**
					Zircon (rims)	U-Pb	Crystallization	MSWD = 6.8; n = 8/9	**42.7 ± 1.0**
19DR-LA17	Loma Alta (LA)-mylonite	Loma Alta	32.14561	110.68264	Zircon	U-Pb	Crystallization	MSWD = 5.0; n = 230/245	**26.87 ± 0.72**
STA2C	Granitoid boudin within calc-silicate tectonite	Posta Quemada–Hidden Spring	32.06708	110.56753	Apatite Apatite	U-Pb FT	Lower intercept Central	MSWD = 0.8; n = 21 P(chi-square) = 0.0; n = 17	**27.3 ± 2.1** **29.4 ± 6.5**
HS-05	Wilderness (W)-mylonite	Posta Quemada–Hidden Spring	32.06425	110.58077	Apatite Apatite	U-Pb FT	Lower intercept Central	MSWD = 1.0; n = 19 P(chi-square) = 0.0; n = 10	**26.6 ± 2.3** **26.3 ± 6.8**
HS-04	Wilderness (W)-mylonite	Posta Quemada–Hidden Spring	32.08089	110.56321	Apatite Apatite	U-Pb FT	Lower intercept Central	MSWD = 1.2; n = 12 P(chi-square) = 0.37; n = 11	**24.2 ± 9.8** **29.5 ± 4.6**
STA2	Wilderness (W)-mylonite near calc-silicate tectonite	Posta Quemada–Hidden Spring	32.06708	110.56753	Apatite Apatite	U-Pb FT	Lower intercept Central	MSWD = 1.0; n = 21 P(chi-square) = 0.76; n = 18	**18.4 ± 7.5** **27.1 ± 3.2**
SAG-LOOP	Flinty ultramylonite	Saguaro Loop	32.18722	110.70500	Bulk white mica fish	Ar-Ar	Plateau	MSWD = 1.55; 75.1% of gas	**24.13 ± 0.07**
					Dark groundmass	Ar-Ar	Mini-plateau	MSWD = 11.6; 34.0% of gas	**24.12 ± 0.12**
GD10-16-20A	Flinty ultramylonite	Saguaro Loop	32.18596	110.70668	Dark groundmass	Ar-Ar	Weighted mean	MSWD = 2.24; 68.8% of gas	**23.99 ± 0.08**
					Bulk white mica fish	Ar-Ar	Mini-plateau	MSWD = 1.7; 27.5% of gas	**23.85 ± 0.05**
					Thick single white mica book	Ar-Ar	Weighted mean	MSWD = 3.6; 89.1% of gas	**24.08 ± 0.05**
					Thin single white mica flake/fish	Ar-Ar	Plateau	MSWD = 0.72; 56.9% of gas	**23.95 ± 0.04**
					Thin single white mica flake/fish	Ar-Ar	Plateau	MSWD = 0.42; 100% of gas	**24.04 ± 0.04**

(*Continued*)

TABLE 8.1. SUMMARY TABLE OF GEOCHRONOLOGY AND THERMOCHRONOLOGY AGES OBTAINED ON DEFORMATIONAL FABRICS AND ROCK PROTOLITHS AS WELL AS POSTDEFORMATIONAL MAFIC DIKES IN THE STUDY AREA IN THE RINCON MOUNTAINS (*Continued*)

Sample	Type of rock	Subarea	Lat (°N)	Long (°W)	Mineral	Technique	Type of age	Comments	Age (Ma) ± error*
GD10-16-20B	Schistose ultramylonite	Saguaro Loop	32.18613	110.70669	Fine-grained groundmass	Ar-Ar	Mini-plateau	MSWD = 1.28; 21.5% of gas	**24.13 ± 0.07**
					Bulk white mica fish	Ar-Ar	Plateau	MSWD = 1.51; 60.8% of gas	**23.74 ± 0.04**
					Thick single white mica book	Ar-Ar	Mini-plateau	MSWD = 2.64; 44.2% of gas	**23.71 ± 0.04**
					Thin single white mica flake	Ar-Ar	Plateau	MSWD = 1.54; 43% of gas	**24.07 ± 0.04**
					Thin single white mica flake	Ar-Ar	Plateau	MSWD = 0.86; 97.3% of gas	**23.73 ± 0.04**
GD-2020-4	Ultracataclasite	Posta Quemada–Hidden Spring	32.06803	110.55247	Glassy veinlets (one grain)	Ar-Ar	Mini-plateau	MSWD = 1.86; 17.5% of gas	**23.90 ± 0.07**
					Glassy veinlets (two grain)	Ar-Ar	Mini-plateau	MSWD = 1.12; 13.2% of gas	**23.81 ± 0.07**
					Glassy veinlets (five grain)	Ar-Ar	Mini-plateau	MSWD = 1.90; 21.7% of gas	**23.92 ± 0.06**
GD10-16-20D	Mafic dike cutting mylonite	Saguaro Loop	32.18477	110.70571	Volcanic groundmass (60–80 mesh)	Ar-Ar	Plateau	MSWD = 1.43; 60.0% of gas	**22.03 ± 0.06**
					Volcanic groundmass (80–100 mesh)	Ar-Ar	Mini-plateau	MSWD = 0.60; 48.5% of gas	**22.03 ± 0.05**
					Volcanic groundmass (80–100 mesh)	Ar-Ar	Weighted mean	MSWD = 4.64; 48.1% of gas	**21.85 ± 0.06**
FG-1	Fault gouge Catalina detachment	Posta Quemada–Hidden Spring	32.07139	110.58778	Illite	K-Ar	Linear regression	r^2 = 0.995	**13.8 ± 8.1**
JR-02	Protocataclasite of W-mylonite	Saguaro Loop	32.17406	110.71808	Zircon	U-Th-Sm/He	Weighted mean	MSWD = 13, n = 3	**16.9 ± 0.1**
JR-01	Protocataclasite of W-mylonite	Saguaro Loop	32.17406	110.71808	Apatite	U-Th-Sm/He	Weighted mean	MSWD = 14, n = 5	**14.9 ± 0.2**

Note: FT—fission track;; MSWD—mean square of weighted deviates.
*Errors in the age are reported at 2σ level except for the apatite fission-track ages, which are reported at 1σ.

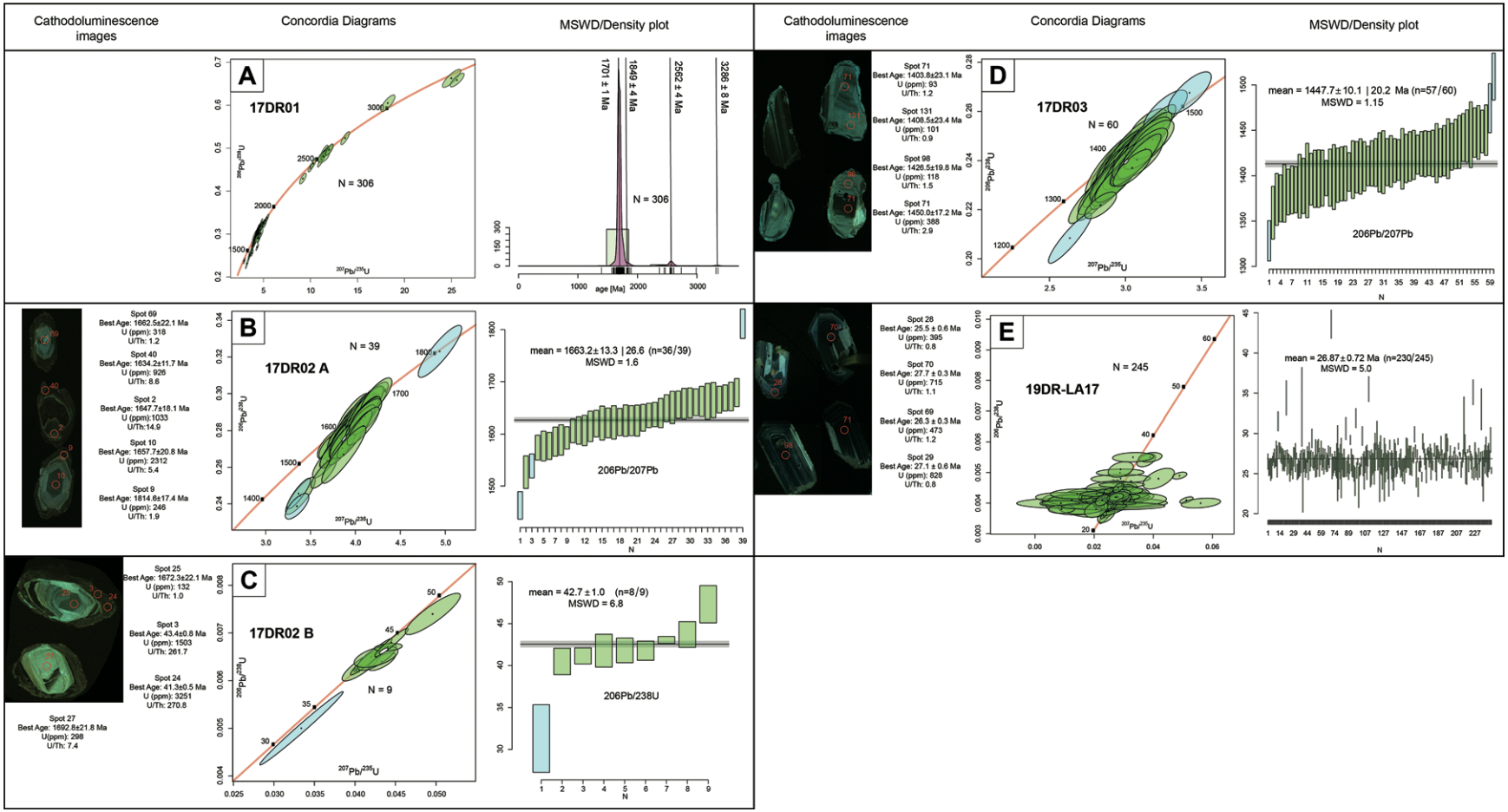


Figure 8-1. Zircon U-Pb results, including scanning electron microscope–cathodoluminescence images of representative dated zircons, Wetherill concordia diagrams, and weighted mean age plot/density plots. (A) Pinal Schist (17DR01). (B) The inherited core of the W-mylonite (17DR02A). (C) The associated younger rim age (17DR02B). (D) O-mylonite (17DR03). (E) Loma Alta mylonite (19DR-LA17). Red circles indicate spot size (20 μm) and location. Analyses in blue were excluded from weighted mean age. MSWD—mean square of weighted deviates. Sample locations are presented in Figure A-1 and Table A-1 (see text footnote 2).

The apatite U-Pb method was selected for these analyses because its use has been successful in dating upper-greenschist- to lower-amphibolite-facies mylonitization, constraining the onset of detachment faulting in other metamorphic core complexes (Odlum and Stockli, 2020; Jepson et al., 2021). Estimates of the closure temperature of the apatite U-Pb system are between ~550 and 370 °C depending on cooling rates and apatite crystal sizes (Chew and Donelick, 2012; Cochrane et al., 2014). However, temperatures of ~450–550 °C are more typically reported (e.g., Schoene and Bowring, 2007; Blackburn et al., 2011), though the onset of mylonitization in the case of the Catalina detachment zone was certainly lower. Apatite grains that were selected for AFT analysis were also targeted for same-grain apatite U-Pb analyses.

During apatite U-Pb analysis, the Mt. McClure primary reference material (523.98 ± 0.12 Ma; Schoene and Bowring, 2006) was measured repeatedly throughout the session to correct for instrumental drift and downhole fractionation, and the Madagascar (MAD2) apatite reference material (474.2 ± 0.4 Ma; Thomson et al., 2012) was analyzed as a secondary standard for accuracy checks (MAD2 = 475.3 ± 8.0 Ma). Data reduction was performed using the "VizualAge_UcomPbine" data reduction scheme in Iolite (Paton et al., 2011; Chew et al., 2014). Isotopic data ($^{238}U/^{206}Pb$ and $^{207}Pb/^{206}Pb$ ratios) were plotted and apatite U-Pb ages were obtained using a Tera-Wasserburg lower-concordia intercept based on a unique upper ($^{207}Pb/^{206}Pb$) intercept with a relevant nonradiogenic Pb regression line (Fig. 8-2). Tera-Wasserburg plots and concordia intercepts were calculated using the IsoplotR package v. 2.3 (Vermeesch, 2018) in R v. 3.5.2.

All four samples, which were collected in the lower plate in the Posta Quemada–Hidden Spring subarea, clearly define linear arrays in Tera-Wasserburg concordia space (Fig. 8-2). Using the lower intercept, samples STA2C, HS-04, and HS-05 yielded Oligocene ages of 27.3 ± 2.1 Ma (n = 21, MSWD = 0.8), 24.2 ± 9.8 Ma (n = 12, MSWD = 1.2), and 26.6 ± 2.2 Ma (n = 19, MSWD = 1.0), respectively. Sample STA2 yielded a younger Miocene age of 18.4 ± 7.5 Ma (n = 21, MSWD = 0.3) (Table 8-1).

$^{40}Ar/^{39}Ar$ GEOCHRONOLOGY: ULTRAMYLONITE, ULTRACATACLASITE, AND MAFIC DIKE

Introduction

In order to constrain the onset of mylonitization, and the subsequent ultracataclastic event, as well as assess the cessation of deformation, we collected representative samples from the Saguaro Loop and the Posta Quemada–Hidden Spring subareas. We collected both types of ultramylonite (flinty and schistose) in the Saguaro Loop (Figs. 6-7, 6-8, and 6-9), and ultracataclasite (with black obsidian-like matrix) in the Posta Quemada–Hidden Spring subarea. In addition, to constrain the cessation of deformation, we collected a mafic dike that crosscuts the mylonitic fabrics in the Saguaro Loop subarea (sample locations are shown in the Supplemental Material, Appendix A). Also in the Supplemental Material, Appendix D, we provide detailed descriptions of mineral separation and cleaning, the removal of finer fractions produced from cleaning, irradiation of the samples, and calculation protocols. Age spectra are shown in Figure 8-3 and tabulated in Table D-1 in the Supplemental Material, Appendix D.

Ultramylonite

For sample SAG-LOOP (flinty ultramylonite), we ran step-heating experiments on both the dark matrix and on white mica fish porphyroclasts (Fig. 8-3A). An accepted closure temperature for Ar systematics of white mica (muscovite) is ~350 °C (e.g., McDougall and Harrison, 1999), but in some particular cases, closure temperatures could be as high as 400 °C (Harrison et al., 2009). For the purpose of this study, a muscovite closure temperature of 350 ± 25 °C was assumed.

The ultramylonite dark matrix (SAG-LOOP), which resulted from extreme grain-size reduction due to dynamic recrystallization of the original mineral constituents, yielded a disturbed age spectrum (Fig. 8-3A, yellow spectrum) with the initial 16% degassing returning young ages between ca. 23 and 14 Ma, perhaps due to argon loss related to a subsequent regional thermal disturbance (i.e., postdeformation mafic dikes). We were able to calculate a mini-plateau age at 24.12 ± 0.12 Ma using ~34% of the total $^{39}Ar_K$ released (Table 8-1). The remaining steps, accounting for ~50% of the gas, climbed from ca. 24 to close to 30 Ma, possibly representing a pattern of excess argon. On the other hand, a pure white mica flake aliquot from a porphyroclast yielded a very flat spectrum, allowing the calculation of a plateau age at 24.13 ± 0.07 Ma, with 75% of the total $^{39}Ar_K$ released gas (Table 8-1; Fig. 8-3A, red spectrum).

In order to reproduce these age results, we analyzed a second sample of the flinty ultramylonite from the same area (sample GD10-16-20A). The age spectrum of the dark matrix was very similar to the previous sample, and a combination of the two allowed for calculation of a combined weighted mean age of 24.03 ± 0.76 Ma (Fig. 8-3A). Aliquots of bulk white mica fish porphyroclasts, a thick single book, and single white mica flakes were analyzed and provided the same age results as the previous ultramylonite (Table 8-1). A weighted mean age at 23.99 ± 0.04 Ma, calculated using only four out of the five ages obtained for the white mica flakes (Table 8-1; Fig. 8-3A), is interpreted as a cooling age that represents an age of ongoing ultramylonite formation.

White mica porphyroclasts in schistose ultramylonite (GD10-16-20B) collected near the flinty ultramylonite samples were analyzed using a combination of bulk, thick booklet, and two single flake analyses (Table 8-1). All of the white mica age spectra were very well behaved (Fig. 8-3B); however, one of the thin single white mica flake degassing experiments provided an excellent plateau age at 23.73 ± 0.04 Ma, representing more than 97% of the total gas (Table 8-1). A combination of the best three white mica fish analyses of the schistose ultramylonite allowed us to calculate a stacked plateau age at 23.72 ± 0.04 Ma (Fig. 8-3B), which represents a cooling age constraining the timing of active formation of ultramylonite in the Saguaro Loop subarea. A

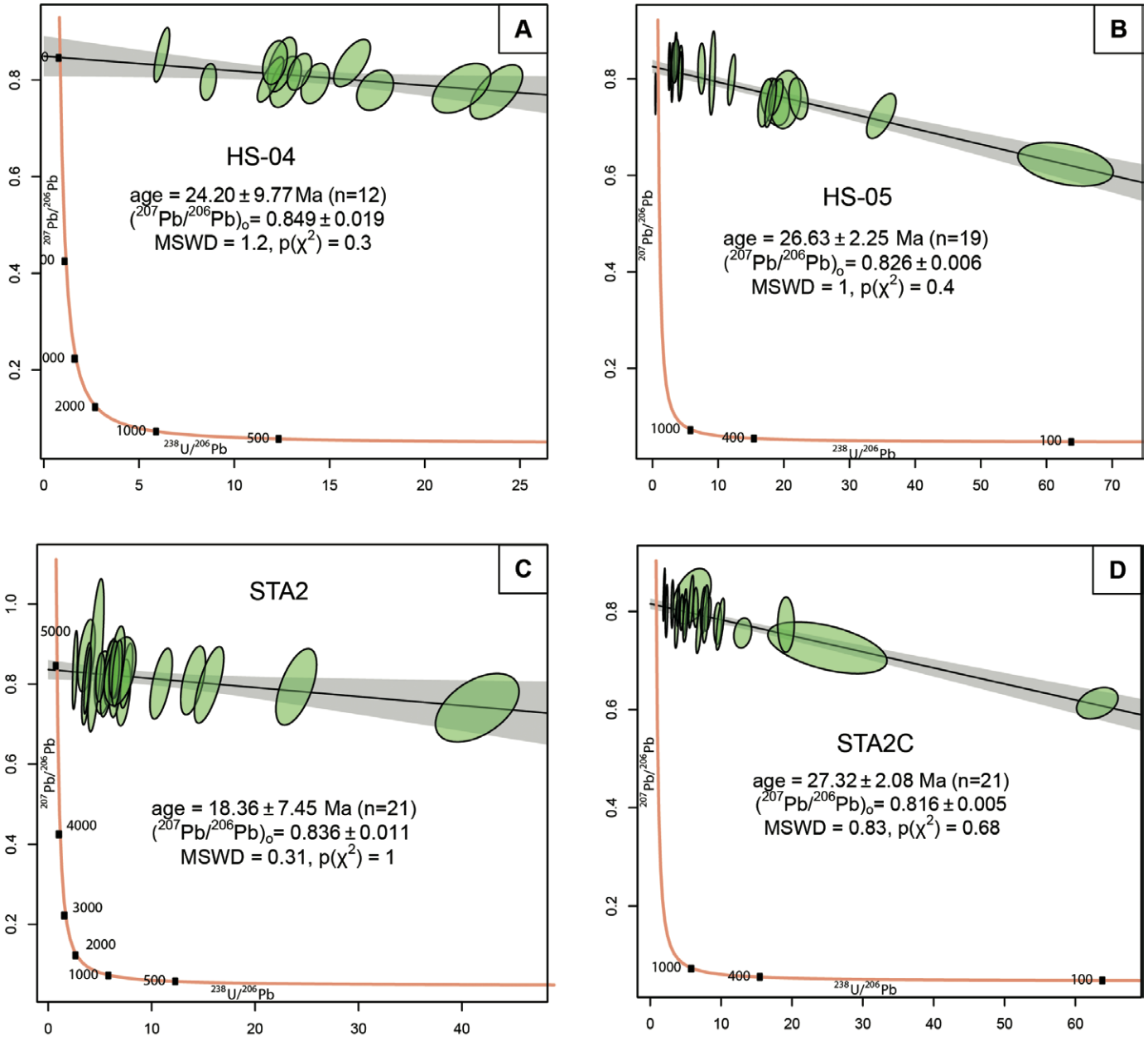


Figure 8-2. Tera-Wasserburg concordia diagrams of apatite U-Pb data from samples HS-04, HS-05, STA2, and STA2C (Fig. A-1; Table A-1 [see text footnote 2]). Ellipses are plotted at 2σ uncertainties. Solid black lines within gray envelopes correspond to linear regressions through the apatite U-Pb data that were used to obtain an estimate of the initial $^{207}Pb/^{206}Pb$ ratio (upper intersect with the concordia curve) and the apatite U-Pb (AUPb) date (lower intercept with the concordia curve). MSWD—mean square of weighted deviates; $p(\chi^2)$—chi squared test value.

sample of fine-grained matrix from this schistose ultramylonite yielded a slightly older mini-plateau age at 24.13 ± 0.07 Ma (Table 8-1; Fig. 8-1C).

It appears that protoliths for both the flinty and schistose ultramylonite were W-mylonite formed after intrusive units of the early Eocene Wilderness Sill Suite (ca. 57–43 Ma). In fact, sample 17DR02 of W-mylonite from the Saguaro Loop subarea yielded an age of 42.7 ± 1.0 Ma (Table 8-1; Fig. 8-3C). Therefore, the formation of ultramylonites in the Saguaro Loop subarea could be constrained between ca. 43 and 24 Ma. Yet, we know that mylonites from the nearby Loma Alta subarea were derived in part from protolith dated as 26.87 ± 0.72 Ma on the basis of U-Pb geochronology (Table 8-1; Fig. 8-1E). At this point, it seems safe and plausible to propose that mylonitization in the Catalina detachment zone, including ultramylonite formation, occurred between ca. 27 and 24 Ma (late Oligocene).

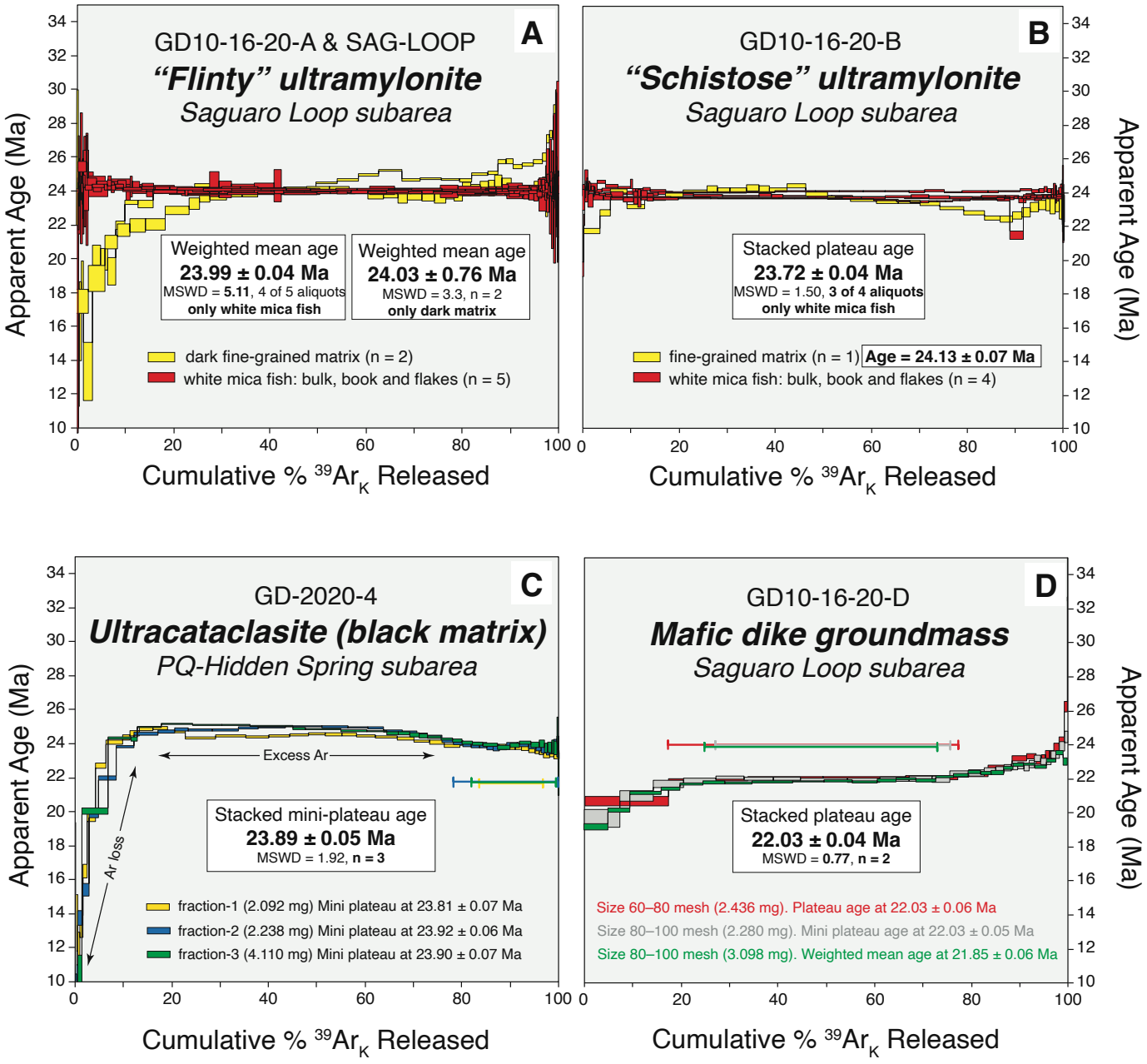


Figure 8-3. Ar-Ar age spectra for deformational fabrics (ultramylonite and ultracataclasite) and postdeformational mafic dikes in the Rincon Mountains study area. (A) Age spectra for various flinty ultramylonite white mica aliquots (bulk, thick mica book, and thinner single flakes) and dark fine-grained matrix samples from the Saguaro Loop subarea. (B) Age spectra for white mica aliquots and fine-grained matrix of schistose ultramylonite from the Saguaro Loop subarea. (C) Age spectra for black glassy aliquots of ultracataclasite veinlets from the Posta Quemada (PQ)–Hidden Spring subarea. (D) Age spectra for three different groundmass size fractions from crosscutting mafic dikes from the Saguaro Loop subarea. MSWD—mean square of weighted deviates.

Ultracataclasite

The black obsidian-like matrix from ultracataclasite sample GD-2020-4, collected in the Posta Quemada–Hidden Spring subarea, was analyzed using three different weight fractions. The ultracataclasite matrix resulted from extreme grinding of the protolith, most likely the W-mylonite. The three Ar-Ar age spectra are nearly identical (Fig. 8-3C), and resemble the disturbed age spectra of the two dark-fine matrix analyses of the flinty ultramylonite (Fig. 8-3A). The initial ~12% of the $^{39}Ar_K$ released gas shows a staircase pattern returning young apparent ages ranging between ~10–24 Ma. These patterns are interpreted

as representing Ar loss out of the ultracataclasite matrix, perhaps due to a thermal disturbance event in the early Miocene (i.e., postdeformational mafic dikes). The following ~66% of the gas forms a hump-shaped section in the spectra (Fig. 8-3C), returning slightly older ages ranging between ca. 25 and 24 Ma, which most likely formed due to excess argon incorporated into the matrix. Only ages for the last ~22% of the released gas are considered to correspond to the ultracataclasite event. We calculated three identical mini-plateau ages for the three sample fractions, which, combined, produced a mini-plateau age of 23.89 ± 0.05 Ma (n = 3, MSWD = 1.92). We interpret this age as the best approximation for the formation of the ultracataclasite. Note that this age is indistinguishable, within analytical error, to the ages obtained from the ultramylonite samples collected in the Saguaro Loop subarea (Figs. 8-3A and 8-3B).

Mafic Dike That Cuts W-Mylonite

Last, we analyzed a mafic dike collected in the Saguaro Loop subarea (GD10-16-20D) that clearly cuts W-mylonite. Three groundmass aliquots of the dike, of slightly different size fractions and weights, provided similar argon degassing patterns (Fig. 8-3D). The best behavior was provided by the coarsest grain-size fraction (60–80 mesh), yielding a plateau age at 22.03 ± 0.06 Ma (Table 8-1), which we interpret as the age of crystallization of the dike. This Ar-Ar age at ca. 22 Ma provides the best approximation for cessation of mylonitization in the Saguaro Loop subarea, and most likely in the Rincon Mountains, where similar mafic dikes cutting deformational fabrics occur.

^{40}K-^{40}Ar DATING OF FAULT GOUGE

A fault gouge sample (FG-1) was collected along the Catalina detachment fault in the Posta Quemada–Hidden Spring subarea for illite K-Ar age analysis following the methods of Haines and van der Pluijm (2008) (sample location shown in Supplemental Material, Appendix A). The sample was hand crushed and sieved before separation into four clay-size fractions by density settling and centrifugation in water. Powdered X-ray diffraction (XRD) analysis was done for each size fraction using a Bruker D8 Advance diffractometer, and curves were fit using the Profex BGMN software (Döbelin and Kleeberg, 2015) to determine the amount of 1Md and 2M1 illite present. K was measured by ICP-MS in the Arizona Laboratory for Emerging Contaminants. Aliquots for Ar were leached in an acetic acid and sodium acetate solution (pH ~4) to remove calcite before being measured by laser ablation using the Ar extraction line in the Arizona Noble Gas Laboratory. The procedure outlined by Thirumalai et al. (2011) was followed to make weighted linear extrapolations through the data.

Illite age analysis was used on fault gouge to discriminate between authigenic 1Md illite formed at low temperature during fault movement and detrital 2M1 illite incorporated in the gouge from the surrounding wall rock. Size-fraction separation is a way to secure multiple samples from the same bulk gouge but with different amounts of each illite polytype. We then quantified the amount of 1Md and $2M_1$ illite using powdered XRD and dated each size fraction separately. Plotting age (as an exponential $e^{\lambda t} - 1$) against the normalized amount of $2M_1$ illite in each size fraction (Fig. 8-4) allowed us to extrapolate back to a purely authigenic $1M_d$ illite age of 13.8 ± 8.1 Ma, which is the last age of movement along the Catalina detachment fault. Table E-1 presents the raw data pertaining to this age determination (Supplemental Material, Appendix E).

ZIRCON AND APATITE (U-Th-Sm)/He THERMOCHRONOLOGY: PROTOCATACLASTICALLY DEFORMED W-MYLONITE

The (U-Th-Sm)/He thermochronometer relies on the accumulation and thermally activated diffusion of radiogenic ^{4}He. The closure temperature for apatite (U-Th-Sm)/He (AHe) is typically around 60 ± 20 °C, and for zircon (U-Th)/He (ZHe), it is 170 ± 10 °C, and, thus, the combination is valuable for determining middle- to upper-crustal cooling (Reiners, 2005). Apatite and zircon analyses were undertaken at the Arizona Radiogenic Helium Dating Laboratory at the University of Arizona and followed the protocols described in Reiners (2005).

Under ultra-high vacuum conditions, helium (^{4}He) was extracted at 900–1300 °C with a diode laser and measured via isotope dilution on an Element 2 mass spectrometer at the University of Arizona. Following ^{4}He extraction, tubes that contained

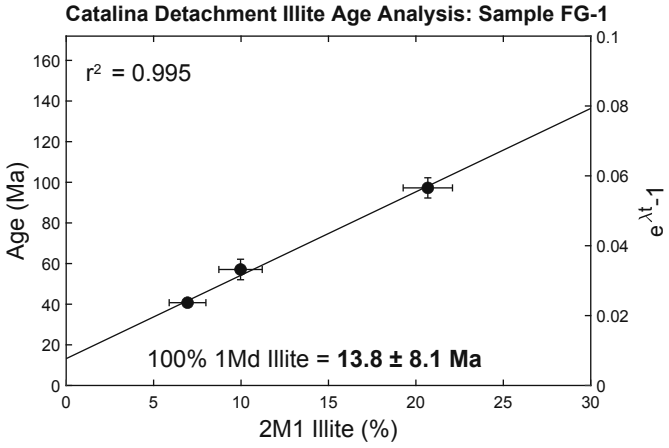


Figure 8-4. Plot of age vs. normalized percent of $2M_1$ illite in sample FG-1, a fault gouge in the Catalina detachment fault. Ages are plotted as an exponential ($e^{\lambda t} - 1$) because this value is more linearly related to the amount of $2M_1$ illite than time (Haines and van der Pluijm, 2008). A weighted linear regression was used to determine the 100% $1M_d$ illite age, which corresponds to the last movement along the fault. The 1–0.2 µm size fraction was omitted due to low radiogenic Ar yield. Mineralogy and K-Ar results for each size fraction can be found in the Supplemental Material (Appendix E).

apatite and zircon were retrieved from the laser cell, then spiked with ^{235}U and ^{230}Th, and dissolved. Blank sample and spiked standard solutions were subsequently analyzed for ^{238}U and ^{232}Th via isotope dilution and then, with an external calibration, for ^{147}Sm via ICP-MS (Reiners, 2005). Replicate analyses of Durango apatite performed as an internal standard (n = 1) yielded a mean (U-Th-Sm)/He age of 28.07 ± 0.4 Ma (1σ), slightly younger than the Durango (U-Th-Sm)/He reference age of 31.02 ± 1.01 Ma (McDowell et al., 2005).

One ZHe sample selected for analysis was collected from protocataclastically overprinted W-mylonite at Javelina Rocks in the Saguaro Loop subarea (Figs. 8-5A and 8-5B). The sample was collected no more than 5 m above the subdetachment fault, beneath which are non-brittlely overprinted mylonites. Three grains yielded a weighted mean age of 16.9 ± 0.1 Ma. The same sample from Javelina Rocks was selected for AHe analysis. Five apatite grains yielded a weighted mean age of 14.9 ± 0.2 Ma. Given the consistency of single-grain apatite and zircon helium dates, we suggest that these samples record the timing of relatively rapid cooling through the partial retention zones of ~180–200 °C and ~40–80 °C, respectively. Table F-1 presents zircon and apatite results (Supplemental Material, Appendix F).

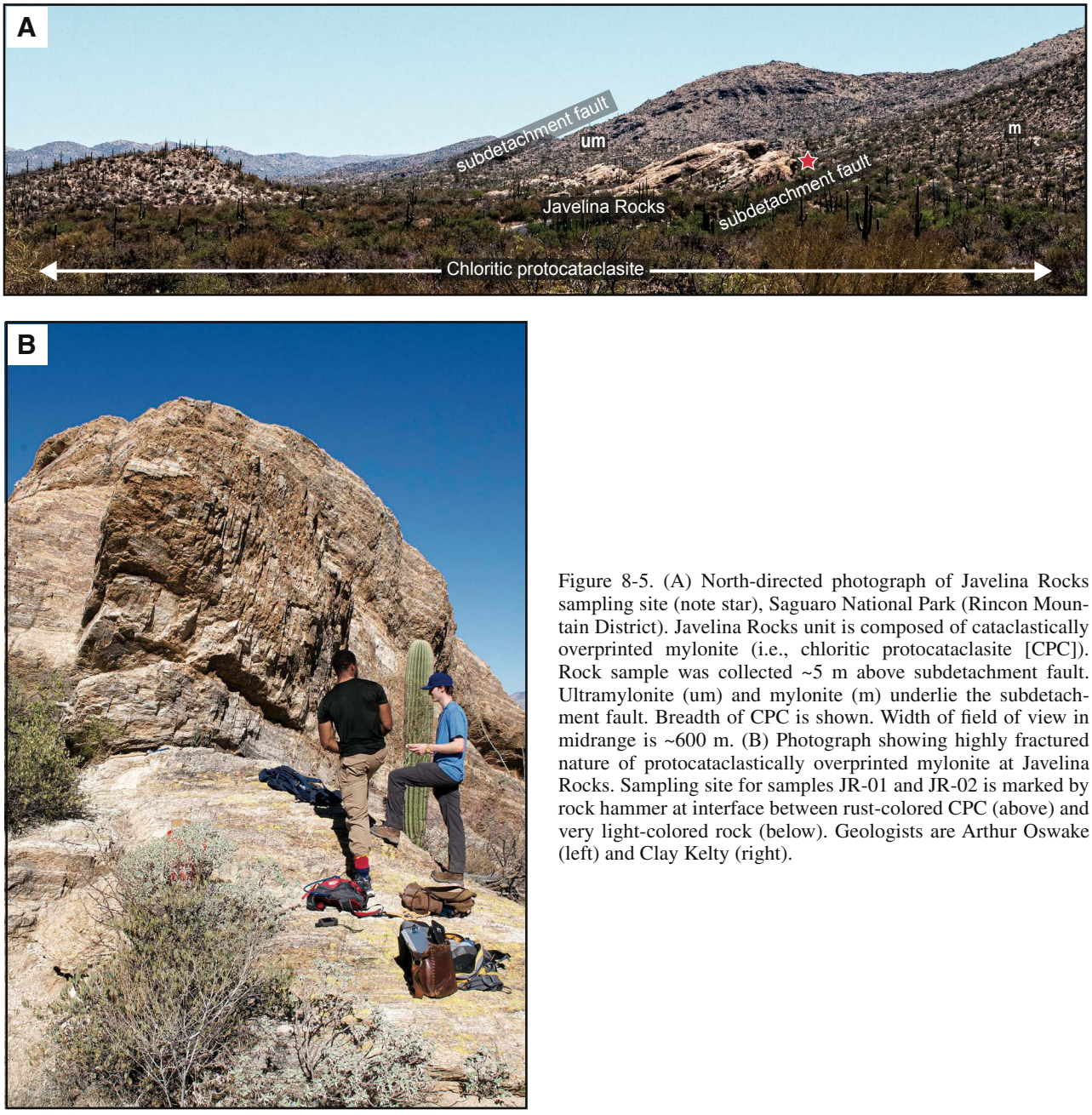


Figure 8-5. (A) North-directed photograph of Javelina Rocks sampling site (note star), Saguaro National Park (Rincon Mountain District). Javelina Rocks unit is composed of cataclastically overprinted mylonite (i.e., chloritic protocataclasite [CPC]). Rock sample was collected ~5 m above subdetachment fault. Ultramylonite (um) and mylonite (m) underlie the subdetachment fault. Breadth of CPC is shown. Width of field of view in midrange is ~600 m. (B) Photograph showing highly fractured nature of protocataclastically overprinted mylonite at Javelina Rocks. Sampling site for samples JR-01 and JR-02 is marked by rock hammer at interface between rust-colored CPC (above) and very light-colored rock (below). Geologists are Arthur Oswake (left) and Clay Kelty (right).

APATITE FISSION-TRACK THERMOCHRONOLOGY: W-MYLONITE AND O-MYLONITE

The fission-track thermochronometer relies on the spontaneous fission decay of ^{238}U (Hurford and Green, 1983). Spontaneous fission within apatite is annealed above ~120–60 °C, making the AFT system useful for constraining upper-crustal cooling (e.g., Braun et al., 2006, and references within). AFT analyses were performed using the laser-ablation method (Tagami, 1987). Apatite grains were mounted in epoxy and polished, and spontaneous fission tracks were revealed by etching with 5.5 *M* nitric acid for 20 s at 21 °C before laser ablation (after Donelick et al., 2005). The fission-track analyses were performed as part of U-Pb and fission-track double-dating at the Arizona Fission Track Laboratory in the University of Arizona following the procedure outlined in Jepson et al. (2021) (Supplemental Material, Appendix G).

The concentration of uranium (^{238}U) in the counted areas of apatite from samples STA2, STA2C, HS-04, and HS-05 was determined using LA-ICP-MS. Age calculation was carried out using an in-house R script following equations as described in Hasebe et al. (2004) and Vermeesch et al. (2017), using the

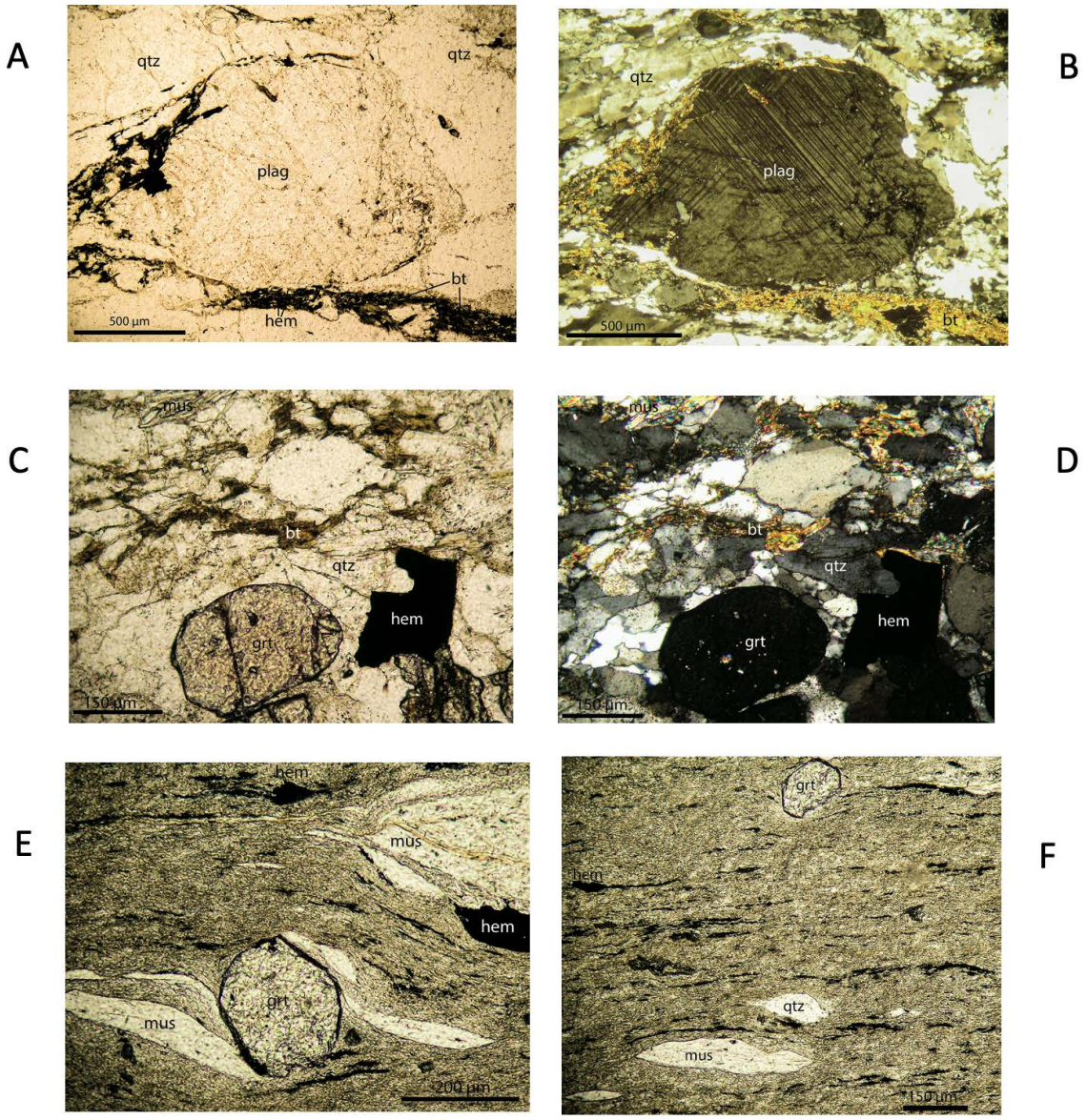


Figure 8-6. Photomicrographs of (A) O-mylonite, (C) W-mylonite, and (E, F) ultramylonite, all in plane light. (B, D) Cross-polarized photomicrograph equivalents of A and C, respectively. Mineral abbreviations: qtz—quartz; plag—plagioclase; bt—biotite; hem—hematite; mus—muscovite; grt—garnet.

Durango apatite (McDowell et al., 2005) to perform a session-zeta calibration (Vermeesch et al., 2017). All four samples (STA2, STA2C, HS04, and HS05) from the lower-plate Posta Quemada–Hidden Spring subarea yielded Oligocene AFT dates of 27.1 ± 3.2 Ma (corresponding AUPb age of 18.4 ± 7.5 Ma), 29.4 ± 6.5 Ma (corresponding AUPb age of 27.3 ± 2.1 Ma), 29.5 ± 4.6 Ma (corresponding AUPb age of 24.2 ± 9.8 Ma), and 26.3 ± 6.8 Ma (corresponding AUPb age of 26.6 ± 2.2 Ma), respectively (sample locations are shown in Supplemental Material, Appendix A). Table G-1 in the Supplemental Material, Appendix G, presents a summary of apatite fission-track data.

SUMMARY

Mapping and structural analysis of the fault-rock stratigraphy within the Catalina detachment zone, followed by interrogation of the microscopic petrography (Fig. 8-6), created an informed basis for geochronology and thermochronology applications (Fig. 8-7; Table 8-1). Figure 8-7 is in part a paragenetic succession chart that sets the stage for constraining the stages of temporal evolution of the Catalina detachment zone: mylonitization; faulting and cataclasis; and fault slip and exhumation. Chapter 9 elaborates on these analyses in relation to the overall history.

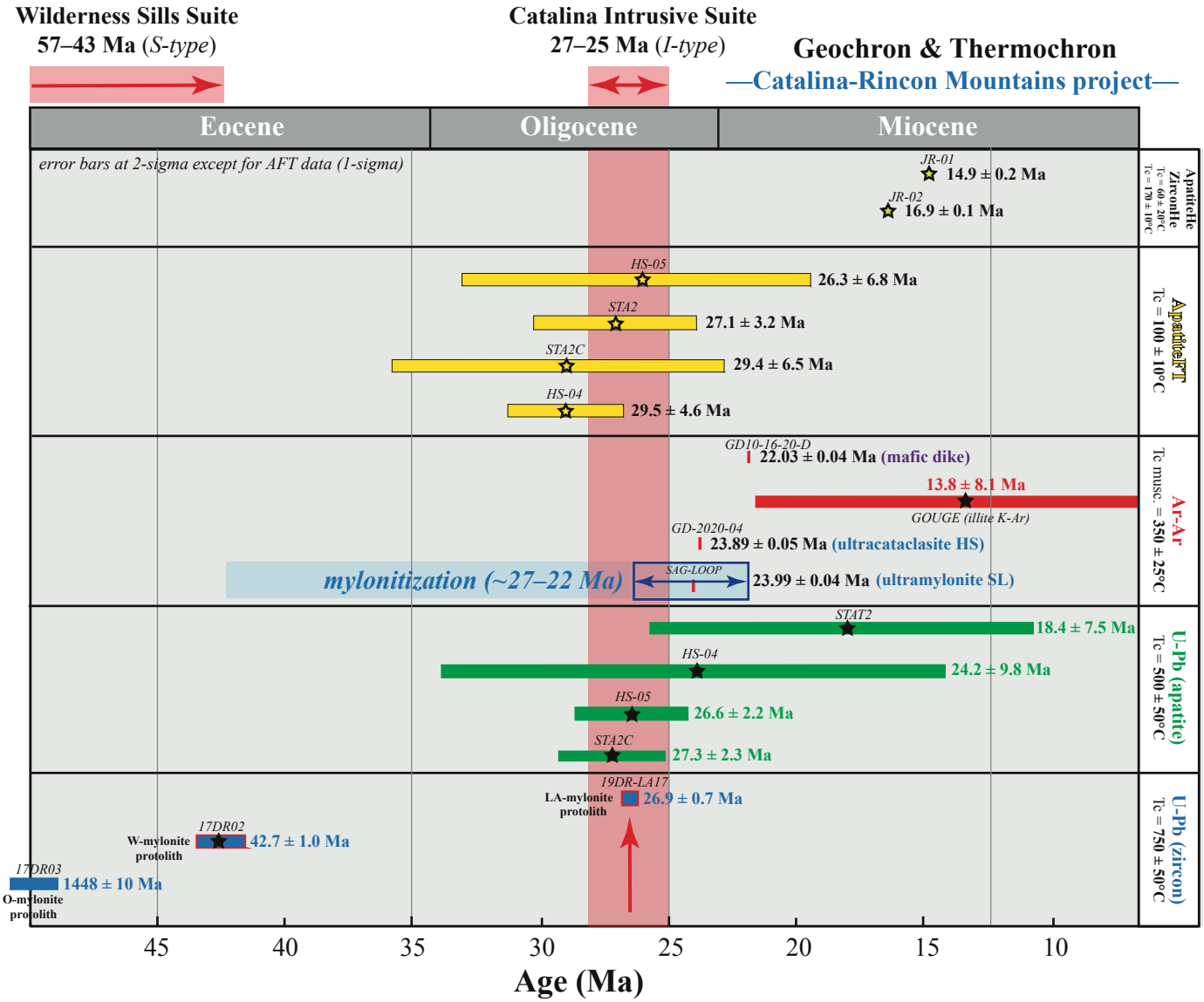


Figure 8-7. Age diagram of all the geochronology and thermochronology data (zircon U-Pb, apatite U-Pb, Ar-Ar, K-Ar, zircon He, apatite fission track [FT], and apatite He) obtained on deformational fabrics and rock protoliths (ultramylonite, cataclasite, and fault gouge), as well as post-deformational mafic dikes in the study area in the Rincon Mountains. LA-mylonite—Loma Alta mylonite; O-mylonite—mylonite derived from Mesoproterozoic Oracle Granite Suite protolith; W-mylonite—mylonite derived from Eocene Wilderness Suite Granite protolith; Tc—closure temperature for the different isotopic systematics; SL—Saguaro Loop; HS—Hidden Spring.

CHAPTER 9

Discussion

INTRODUCTION

Previous chapters focused on the exceptional exposures of the crustal-scale Catalina detachment zone, integrating new geologic, geophysical, and geochronologic analyses with updated reviews of more than four decades of published and previously unpublished research. A structural model was built with reference to specific deformation mechanisms that produced distinct structures and fabrics during progressive ductile to brittle evolution of the detachment footwall, with timing constrained by new geochronology and thermochronology.

Here we frame our model of the progressive structural evolution of the Catalina detachment zone in the context of the overall Laramide and Cenozoic tectonic history of the region now occupied by the Catalina-Rincon metamorphic core complex. We also compare the temporal history of the detachment zone of this metamorphic core complex to others in Arizona, California, and Sonora, Mexico. For the Catalina-Rincon core complex evolution, an important part of the discussion that follows deals with tectonic heritage. Past and present debates on tectonic significance of the Catalina-Rincon metamorphic core complexes have always centered on the degree to which structures and fabrics are late Cretaceous/early Paleogene (i.e., "Laramide") versus Oligocene–Miocene, or a hybrid of both. Part of the challenge is insufficient understanding of overall Laramide tectonics in southern Arizona. Unlike many parts of the North American Cordillera, there is no well-established, unified, and reasonably accepted model, but instead a number of focused interpretations of different aspects of Laramide history.

AGE AND SIGNIFICANCE OF THE WILDERNESS SUITE GRANITES

In Late Cretaceous and early Paleogene time, widespread shortening and crustal thickening took place across westernmost North America, related in part to flattening of the Farallon slab (e.g., Coney and Reynolds, 1977; Henderson et al., 1984; Bird, 1998; Saleeby, 2003; Humphreys, 1995, 2009; Liu and Gurnis, 2010; Best et al., 2016). Crustal thickening appears to have generated widespread emplacement of silicic, peraluminous granitoids, interpreted as products of crustal melt (Haxel et al., 1984; Miller and Barton, 1990; Fornash et al., 2013; Chapman et al., 2021). In the Catalina-Rincon metamorphic core complex, this plutonism is manifested in the emplacement of the Wilderness Suite rocks (ca. 57–43 Ma). Zircons within this suite yield Proterozoic inherited cores (ca. 1.6–1.4 Ga) overgrown with Paleogene rims (ca. 43 Ma).

The comparatively low values of U/Th in the Proterozoic inherited cores indicate igneous zircon growth, whereas the relatively high values for eU in the Eocene rims indicate metamorphic zircon growth. The ca. 1.65 Ga cores likely derive from the Pinal Schist, the ca. 1.44 Ga cores likely derive from the Oracle Granite, and the 42.7 Ma rims likely represent the youngest phase of Wilderness Suite intrusions (Fornash et al., 2013; Meijer, 2014) (Table 8-1; Fig. 8-7).

LARAMIDE THRUST FAULTS IN THE RINCON-MOUNTAINS REGION

Drewes (1981, 1991) referred to the Catalina detachment fault as the Santa Catalina complex fault and interpreted it as a Laramide thrust fault (ca. 75 Ma). He noted as well that this structure accommodated some postthrusting low-angle normal fault slip during reactivation in the Oligocene. The trace of Drewes' Santa Catalina complex thrust fault coincided with the convergence of his two inferred regional thrust fault systems, which he considered to be phases of Laramide deformation: the Hidalgo thrust fault, which was active in late Cretaceous in his "Piman phase," and the Cochise thrust fault, which formed during the Paleocene in his "Helvetian phase." Piman-related thrusting was northeastward and estimated to be marked by ~200 km of tectonic transport. Drewes (1981) considered the penetrative mylonitic and cataclastic fabrics of the Rincon Mountains to have formed during Laramide Cordilleran orogenic thrusting, though enhanced somewhat during Miocene deformation.

A late Cretaceous to Paleocene timing of the formation of the Catalina detachment zone, including the Catalina detachment fault, is contradicted by timing relationships emphasized in this study. NE-directed thrusting, on the order of 200 km, is contradicted by the consistent top-to-SW sense of shear for each structural component of the Catalina detachment zone: mylonite, ultramylonite, chloritic protocataclasite, and detachment fault. But there is some documented top-to-NE sense of shear as well in lower-plate rocks (Bykerk-Kauffman and Janecke, 1987; Naruk and Bykerk-Kauffman, 1990). In upper-plate rocks, there is clear evidence for older-on-younger thrust-fault heritage, expressed as fragmentary elements of thrust faults exist in scattered outcrops. Examples include: (1) In the northern Johnny Lyon Hills east of

the San Pedro Valley (Cooper and Silver, 1964), a gently east-dipping thrust fault places Precambrian Pinal Schist on top of Lower Cretaceous Bisbee Group strata; (2) in the Roble Canyon area of northeastern Rincons (Lingrey, 1982), a steeply ENE-dipping (50–75°) thrust fault places Precambrian granite and Pinal Schist above Bisbee Group strata; (3) in the Youtcy Canyon area of Redington Pass (Bykerk-Kaufman, 1990, 2008), a gently NE-dipping thrust fault places Precambrian basement and overlying Apache Group and Paleozoic strata above Bisbee Group strata; (4) in the Loma Alta subarea of Rincon Valley (Richard et al., 2005; Davis et al., 2019), a very gently E-dipping thrust separates Precambrian granite (above) from overturned Bisbee Group

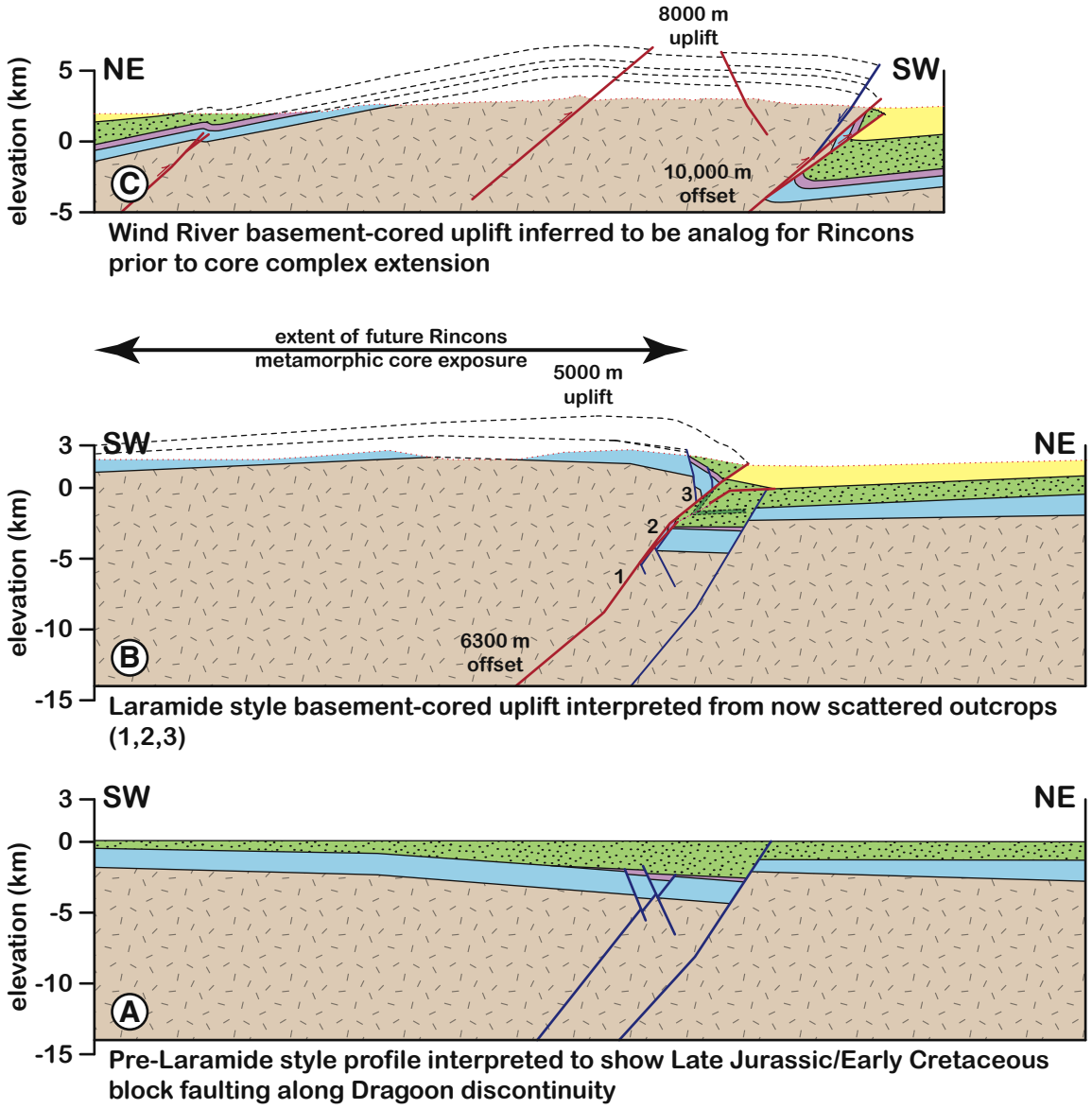


Figure 9-1. Interpretation of the tectonic framework of the Rincon Mountains region before metamorphic core complex development. (A) Late Jurassic–Early Cretaceous normal faulting zone, the position and offset of which conform to the Dragoon discontinuity (Titley, 1976). The faulting is an expression of Early Cretaceous back-arc to intra-arc extension (Dickinson, 1989). (B) NE-vergent basement-cored uplift bounded by SW-dipping reverse fault along its northeastern margin. This was a product of Laramide contractional inversion. Sites marked 1, 2, and 3 represent the original positions of outcrop occurrences of the Laramide thrust fault that are now scattered by core complex extension: 1—Youtcy, 2—Wildhorse, 3—Johnny Lyon (subdetachment) and Roble Canyon (supradetachment). These exposures were cited by Favorito and Seedorff (2021). (C) Comparison profile of the Wind River basement-cored uplift (Stevens et al., 2016) as an analog for the Rincon metamorphic core complex reconstruction. Profile is inverted to be viewed to the south. Units for all profiles: Precambrian basement (tan stipple), Paleozoic (blue), Triassic–Jurassic (purple), Cretaceous (green dotted), and early Tertiary (yellow).

strata (below); (5) in the Saguaro Loop subarea, a thrust fault separates Precambrian Pinal Schist (above) from Paleozoic and Cretaceous strata (below) (Drewes, 1977) (Fig. 3-2); and (6) in the Posta Quemada–Hidden Spring subarea, there are low-angle thrust faults that place Precambrian granite and Cambrian strata atop Bisbee Group strata (Krantz, 1983) (Fig. 3-3).

Favorito and Seedorff (2021) interpreted such older-over-younger relationships in the vicinity of the Rincon Mountains to be part of a large-scale basement-involved structure with multiple reverse faults along its NW margin. Based on their interpretive cross-sections, Favorito and Seedorff (2021) estimate ~9 km of net vertical uplift produced by ~12 km of total horizontal shortening. Then, post-Laramide extension was accommodated across progressively rotating normal faults, which denuded the former Laramide uplift. Our interpretation of the pre-extensional Laramide structure is shown in Figure 9-1, and emphasizes a single NE-vergent basement-cored uplift bounded by a SW-dipping (40°–50°) reverse fault along its northeastern margin. The principal Laramide reverse fault formed within and through reactivation of an older Jurassic normal fault zone, named the Dragoon discontinuity (Titley (1976), which separated fault blocks developed in a back-arc to intra-arc setting (Dickinson, 1989; Haxel et al., 2005). Later, we will return to interpretation of Laramide structural heritage.

AGE AND SIGNIFICANCE OF CATALINA INTRUSIVE SUITE GRANITES, INCLUDING LOMA ALTA

Based on our geochronologic and thermochronologic analyses of samples collected in the Saguaro Loop, Loma Alta, and Posta Quemada–Hidden Spring subareas (Table 8-1; Fig. 8-7), the final phase of plutonism in the Rincon Mountains occurred at ca. 27 Ma, coincident with the beginning of metamorphic core complex extension (Fig. 9-2A). The Loma Alta mylonite, derived from the Loma Alta granite, yielded consistent ca. 27 Ma core and rim ages, supporting Oligocene crystallization. These data are in agreement with zircon U-Pb dates from the Catalina Intrusive Suite, which Fornash et al. (2013) and Ducea et al. (2020) documented as consisting of shallowly emplaced crustal melts at ca. 27–25 Ma. Ducea et al. (2020) suggested an emplacement depth of ~6 km. These data underscore that the Catalina-Rincon metamorphic core complex experienced melting immediately preceding and contemporaneously with the onset of detachment faulting and core complex mylonitization in late Oligocene time.

CATALINA DETACHMENT ZONE MYLONITIZATION AND STRAIN LOCALIZATION

Intermediate-temperature (600–200 °C) thermochronology data suggest that the mylonitic fabrics directly beneath the Catalina detachment fault cooled between 27 and 24 Ma

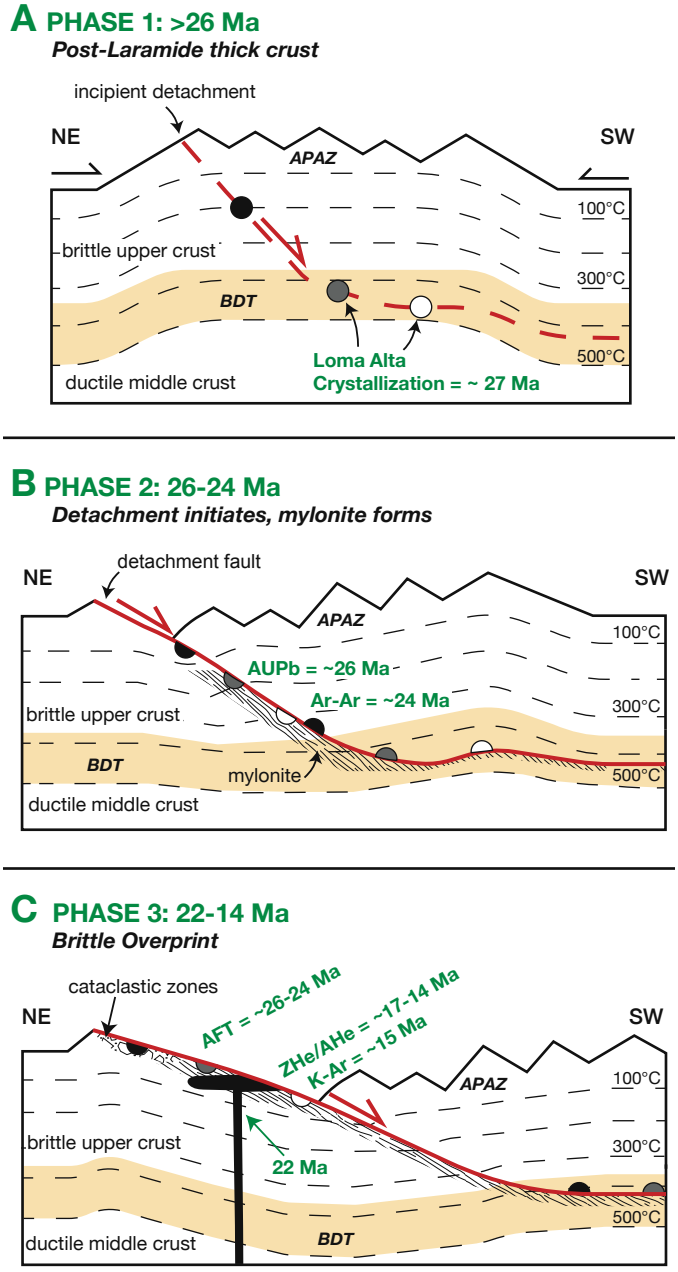


Figure 9-2. Schematic diagram of the Rincon Mountains metamorphic core complex illustrating the temporal evolution of the Catalina detachment system. (A) Following Late Cretaceous to early Cenozoic crustal thickening, extensional shearing initiated in late Oligocene time. (B) Mylonitization and detachment faulting were actively taking place between 26 and 24 Ma. (C) Semibrittle (chloritic protocataclasite [CPC]) and brittle overprinting (cataclasites) constituted latest stages of detachment faulting. Post-mylonite and post-CPC dike intrusion at 22 Ma. Continued detachment faulting between 22 and 17 Ma, and perhaps as young as 14 Ma. APAZ—apatite partial annealing zone; BDT—brittle-ductile transition; AUPb—apatite U-Pb dating; AFT—apatite fission-track dating; AHe/ZHe—apatite and zircon helium dating, respectively.

(Fig. 9-2B; see also Fig. 8-7). In the Posta Quemada–Hidden Spring subarea, a mean apatite U-Pb age from W-mylonite (samples STA2C, HS-04, and HS-05; see Table A-1 and Fig. A-1 in the Supplemental Material, Appendix A) is consistent with mylonitization at ca. 27 Ma. Previous studies have underscored the applicability of apatite U-Pb for dating mylonitization (Odlum and Stockli, 2020).

In the early stages of extensional ductile shearing, mylonites derived from Oracle suite granitoids became, at least in part, juxtaposed with Wilderness suite rocks, promoting strain-localized ultramylonite zones. Calc-silicate tectonites developed from bodies of sedimentary rocks that had been engulfed by intrusions, and/or structurally intermingled with basement, during Laramide deformation. It seems possible that the calc-silicate tectonites in the Posta Quemada–Hidden Spring subarea could be residual tectonite products of a Laramide thrust where the lower plate became smeared southwesterly during core complex deformation. Yet such shear localization did not coincide with the eventual structural position of the Catalina detachment fault, though it may have partly controlled the base of its precursor, the proto-Catalina detachment fault. Other possible sites for such strain localization are the carbonates described by Richard et al. (2005), where pods and lenses of calc-silicate tectonite embedded within W-mylonite that may originally have been Laramide skarn rocks. Spencer et al. (2022) emphasized weak tectonite carbonates as having had a controlling influence on the positioning of the upper-plate to lower-plate boundary of the core complex.

We suggest that mylonitization operated ca. 24 Ma within the Catalina detachment zone, though the timing of its onset was likely somewhat earlier than ca. 24 Ma. Muscovite porphyroclasts (i.e., mica fish) and groundmass Ar-Ar from the ultramylonite (sample SAG-LOOP) and ultracataclasite (sample GD-2020-04) document cooling to ~350 °C at ca. 24 Ma (Table A-1; Fig. A-1). Given the temperatures over which natural mylonites can occur (700–250 °C; Stipp et al., 2002), this suggests that the process of mylonitization was under way at this time. Based on a groundmass Ar-Ar age of 22.03 ± 0.04 Ma from an undeformed mafic dike crosscutting mylonitic fabric and cataclastically overprinted mylonite (sample GD10-16-20-D) (Table A-1; Fig. A-1), mylonitization must have ceased by ca. 22 Ma. Thus, intermediate-temperature thermochronology constrains mylonitization within the Catalina detachment zone to ca. 27–22 Ma (Fig. 9-2B), followed by creation of CPC from ca. 24 to 22 Ma. Because samples are from low elevations along the margin of the metamorphic core complex, we acknowledge that older dates could be revealed at greater distances from the detachment fault, now exposed at higher elevations.

CURRENT ALTERNATIVE HYPOTHESES FOR ORIGIN AND TIMING OF MYLONITIZATION

Other authors, such as Drewes (1981, 1991), have published alternative hypotheses that relate to the age, origin, and significance of mylonites in the Catalina-Rincon metamorphic core complexes. Keith and Rasmussen (2018) concluded that the overall SW-directed shear recorded in this Wilderness Suite mylonitic fabric reflects crustal-scale thrust faulting driven by NE-directed, intraplate, flat-slab subduction in the Eocene. They suggested that this tectonic process created a crustal-scale top-to-the-SW thrust system, which accomplished 100 km of SW-directed transport. Keith and Rasmussen (2019) in fact concluded that the preponderance of mylonites in the Catalina Mountains were formed in Late Cretaceous to Eocene time as a result of such flat-slab subduction. Keith and Rasmussen (2019) viewed the mid-Cenozoic "metamorphic core complex" crustal extension simply as a denudation effect of relative uplift of the Rincon and Catalina Mountains.

Ducea et al. (2020) also placed emphasis on an Eocene (ca. 46 Ma) time of origin for mylonites in the Wilderness Suite Granites. They pointed to the presence of dated synkinematic to late-kinematic leucocratic dikes emplaced into the mylonitic fabric. Ducea et al. (2020) concluded that most of the mylonitic fabrics in the Catalina Mountains were formed during the Eocene (ca. 46 Ma), and that Oligocene–Miocene mylonites formed locally as a result of pluton emplacement–induced ductile deformation. They concluded that ductile fabrics did not develop during low-angle normal shearing in the latest Oligocene; that similarities in orientation of ductile fabrics in Wilderness Suite Granites and the brittle fabrics of the Catalina detachment zone are coincidental; that brittle fabric development associated with extensional denudation exploited earlier fabric; and that doming of the Catalina and Rincon Mountains was driven by intrusion of the Catalina Intrusive Suite (ca. 27–25 Ma). Deemphasis of Oligocene–Miocene mylonitization in the models of Keith and Rasmussen (2018) and Ducea et al. (2020) bears similarity with the aforementioned interpretation by Drewes (1981).

Interpretation of the Oligocene–Miocene mylonites as dominantly a late-stage Laramide, pre-extensional denudation effect is, for us, an unfulfilling proposition. The penetrative mylonitic fabrics in the Rincon metamorphic core complex were imposed on granite as young as 27 Ma, and the physical, geometric, and kinematic characteristics of these young mylonites are an identical match to the mylonitic fabrics imposed on older protoliths. In the case of the South Mountain metamorphic core complex (Reynolds et al., 1986), an entire suite of core complex–typical structures developed in Oligocene–Miocene plutonic rock, eliminating the possibility that they were somehow influenced by Laramide structures. Loma Alta mylonite, whose protolith is post-Laramide, provides the basis for the same argument Reynolds et al. (1986) applied in the South Mountain metamorphic core complex. The tightly consistent geometric and kinematic properties of Catalina detachment zone fabrics and structures in the Rincon Mountains (Fig. 3-11) argue for progressive deformation and not a polyphase deformation, especially given the temporal pinning provided by the age of the Loma Alta mylonite.

PROGRESSIVE DISPLACEMENT AND STRUCTURAL EXHUMATION OF THE MYLONITES

Mylonitic fault rock cooled to upper-crustal temperatures almost immediately following mylonitization (Fig. 8-7). Core complex footwall exhumation of the Rincon Mountains, based on analysis of the Catalina detachment zone, occurred rapidly in the late Oligocene, ca. 27–22 Ma. The mylonite samples yielded AFT ages of ca. 29–26 Ma, within error of apatite U-Pb ages (ca. 26 Ma). We suggest the slightly older ages yielded by AFT are a product of low spontaneous track densities; however, the overlapping AFT and apatite U-Pb ages combined with an absence of a spatial trend suggest rapid upper-crustal cooling between 26 Ma and 22 Ma. This is also supported by the Ar-Ar geochronology.

Viewed in the context of progressive deformation, the temporal framework for development of mylonitic fabrics connects harmoniously with previous low-temperature thermochronometric investigations of the Catalina-Rincon metamorphic core complex. In the discovery phase of Cordilleran metamorphic core complex geology, Keith et al. (1980) were among the first researchers to apply low-temperature thermochronology to the Catalina-Rincon metamorphic core complex, using apatite, titanite, and zircon FT dates to constrain upper-crustal cooling to between 30 Ma and 20 Ma. However, the absence of sample coordinates and a map in the publication by Keith et al. (1980) makes it difficult to resolve individual cooling events from the overall tectonic history. However, Fayon et al. (2000) carried out sampling along a detailed transect and derived apatite and zircon fission-track data from rocks structurally highest (closer to the detachment) to samples structurally deeper (farther from the detachment). Through this approach, Fayon et al. (2000) resolved three clear periods of cooling; a minor period older than 26 Ma recorded by zircon fission-track, a major phase occurring between 26 and 21 Ma, and a final phase of cooling younger than or ca. 20 Ma. Using these results, Fayon et al. (2000) interpreted a period of postmagmatic cooling prior to 26 Ma, followed by tectonic exhumation via detachment faulting at 26–21 Ma, and subsequent normal faulting at or after 20 Ma. More recent low-temperature studies into the Catalina-Rincon metamorphic core complex (e.g., Terrien, 2012; Scoggin et al., 2021; Jepson et al., 2022) have largely refined the periods of upper-crustal cooling determined by Fayon et al. (2000). Our data are within error of previously published AFT data from the Catalina-Rincon metamorphic core complex (Keith et al., 1980; Fayon et al., 2000; Jepson et al., 2021, 2022).

SYNTHESIS OF SEQUENCING OF BRITTLE OVERPRINTING

Chloritic Protocataclasite, Minidetachments, and the Subdetachment Fault Zone

As mylonites were brought updip through the "fluids-sourced reaction-driven" brittle-ductile transition (Selverstone et al., 2012), deformation mechanisms changed at both the crystal scale and the macroscopic scale. Quartz especially began to fail brittlely instead of ductilely. The transition is especially well captured in CPC, within which cataclasis overprinted original mylonite and ultramylonite fabrics in an environment of fluid-induced overpressuring and alteration. Minidetachment faulting proceeded essentially synchronous with shear-induced cataclastic overprinting of mylonites, with the tempo of faulting regulated by localized overpressuring. Deeply weathered slot-fault exposures are the most prominent outcrop expressions of the minidetachments. Minidetachment faulting overall helped accommodate rotation of deformed mylonites, generally around NNW-SSE axes, sympathetic to ENE-WSW displacement.

Through time, the CPC volume of the evolving Catalina detachment zone work hardened as a result of increased internal cohesion due to alteration mineralogy, and this in turn set the stage for evolution of the subdetachment zone, i.e., the Catalina protodetachment fault. The locations of protodetachment fault elements were controlled by loci of strain-localizing fault-rock units, namely, ultramylonites and calc-silicate tectonites. Incremental protodetachment fault slip progressively translated CPC as a body southwestward relative to mylonites beneath the subdetachment zone. The 3-D form of the protodetachment zone, at the scale of the entire Catalina detachment zone, was somewhat branching and corrugated though sympathetic to the antiformal/synformal configuration expressed in underlying mylonite.

Catalina Detachment Fault, Breccias, and Regional Joints

At an even shallower level, and as progressive shearing continued during extension, further strain localization focused slip on minidetachment faults still operating within CPC. As emphasized by Selverstone et al. (2012) and Axen (2020), the linking, coalescing, and smoothing of youngest minidetachments ultimately produced the Catalina detachment fault. This master fault eventually grew laterally into the remarkable continuous length seen today, i.e., 85 km, and accommodated many kilometers of normal slip. These large displacements juxtaposed folded and faulted Paleozoic and Mesozoic strata against the exhumed footwall. Large-magnitude slip of upper-plate rocks on the Catalina detachment fault severely damaged subjacent CPC, transforming it to cataclasite and ultracataclasite directly beneath the detachment surface.

Final movement of the Catalina detachment fault (brittle stage) in the Rincon Mountains to ca. 17–14 Ma (mid-Miocene) is constrained through a combination of K-Ar dating of fault gouge (Fig. 9-2C) and zircon and apatite helium dating from Javelina Rocks. Overall, detachment faulting, and associated core complex exhumation, occurred rapidly in the late Oligocene, ca. 26–22 Ma, with final increments in the early Miocene.

Ubiquitous joints, striking NNW-SSE, define a penetrative fabric across the Rincon Mountain mylonite exposures (Figs. 2-4 and 2-5). These joints, and associated small-displacement normal faults, also formed during late-stage, brittle ENE-WSW

extension. Insights on the timing of late-stage jointing are provided by results of (U-Th)/He and $^{4}He/^{3}He$ thermochronology of secondary oxides in faults and fractures, as reported by Scoggin et al. (2021). On Tanque Verde Ridge, Scoggin et al. (2021) collected specular hematite blades from three quartz/hematite veins in fault breccia and along fracture planes. They dated these iron oxides by exploiting the (U-Th)/He system, reporting ages of 12.8 ± 4.4 Ma, 14.9 ± 3.4 Ma, and 9.5 ± 1.0 Ma. These fit the cluster of helium thermochronometric dates reported in this study (ZHe = ca. 17 Ma and AHe = ca. 15 Ma) and previously published work centered on ca. 15 Ma, which has been interpreted to represent a Basin and Range fracture/fault-controlled fluid-flow episode (Scoggin et al., 2021; Jepson et al., 2022). Perhaps these dates capture the late-stage ENE-WSW extensional deformation that produced the conspicuous systematic jointing so evident in the mylonites of Tanque Verde Ridge (Figs. 2-2 and 2-3).

TRANSITION TO BASIN AND RANGE EXTENSION

High-angle normal faults truncate and offset the Catalina detachment fault. On the west side of the Catalina Mountains, the Pirate fault (listric in profile) dips 55° to 70° to the WNW, with offset of at least 4 km (Davis et al., 2004, 2019). On the east side, the steeply dipping Martinez Ranch fault dips to the east (Fig. 2-2) (Drewes, 1974, 1977; Davis et al., 2011, 2019). Favorito and Seedorff (2021) reported other high-angle faults exposed in the San Pedro Valley. We interpret these faults, including the Santa Rita fault (Fig. 2-6), as expressions of Basin and Range deformation. The Santa Rita fault strikes NNE, and although steep near the surface, it displays a listric geometry that is responsible for most of the subsidence of the Tucson Basin.

The transition from metamorphic core complex deformation to Basin and Range faulting represents a tectonic regime change. Across southwestern North America, continental extension became more broadly distributed. In southern Arizona, Basin and Range deformation spans the entire state, over a width of at least 300 km. In the Catalina-Rincon area, N-S–striking Basin and Range faults accommodated E-W extension, similar to modern geodetic motions (Broermann et al., 2021). Initiation of steep Basin and Range faulting in southern Arizona began around 13–12 Ma (Menges and Pearthree, 1989; Dickinson, 1991; Hoxie, 2012).

TIMING OF DETACHMENT FAULTING IN RELATION TO STRATIGRAPHY AND BASIN EVOLUTION

Data cited above on faulting and exhumation are consistent with stratigraphic constraints, both surface and subsurface. Relevant mid-Cenozoic stratigraphy includes extensive alluvial and braid-plain fluvial deposits, along with integrated volcanic and local lacustrine rocks, ranging in age from middle Oligocene through late Miocene and early Pliocene (Balcer, 1984; Dickinson, 1991; Spencer et al., 2001). Facies, paleocurrents, thicknesses, geometries, and especially clast lithologies reflect an active tectonic system. Late Oligocene volcanic and volcaniclastic rocks (Galiuro Formation and Cloudburst Formations, respectively) were faulted and rotated into half grabens, creating localized accommodation for additional fluvial and braid-plain clastic rocks (e.g., San Manuel Formation and Pantano Formation) (Balcer, 1984; Dickinson, 1991). None of these units, as young as middle Miocene, contains mylonite clasts in their conglomerate facies. In contrast, Upper Miocene Quiburis Formation conglomerates (Dickinson, 1991), and equivalent rocks in the Tucson Basin, contain mylonite clasts, thus revealing that erosion of lower-plate rocks was being accomplished by that time. Degree of faulting and back-rotation decreases in the exposed Upper Miocene units (Favorito and Seedorff, 2021).

Subsurface data (Chapter 2) provide constraints for the timing of basin development related to major detachment fault activity and nearby basins. From dating of syntectonic units in the Tucson Basin, subsidence accompanied by normal faulting began before ca. 27 Ma (Houser et al., 2004). Regionally, magmatic "flareups" quasi-synchronous with detachment faulting, and coeval clastic deposits, roughly span in time from ca. 30 to 21 Ma (e.g., Favorito and Seedorff, 2021, and references therein). Accommodation space for lava flows and conglomerates in the Tucson Basin was achieved by fault splays linked to the Catalina detachment fault. Tectonic activity is considered to be consistent with the timing of the Galiuro and Cloudburst Formations, reaching its apex during ca. 28–21 Ma. Major extension ceased at the early Miocene unconformity, estimated at ca. 21 Ma, and the onset of a new tectonic regime followed the middle Miocene unconformity (ca. 17–15 Ma according to Houser et al., 2004), when subsidence was renewed by Santa Rita fault activity and deposition of the Quiburis Formation (Chapter 2).

DETACHMENT FAULT SYSTEM 3-D MODEL

Figure 9-3 shows our 3-D descriptive model of the Rincon Mountains metamorphic core complex. Outcrop data were integrated in ArcGIS and MOVE. Mapping of the Catalina detachment fault and the Catalina protodetachment fault constrained the trace (relative to topography) and provided local control on the dip of these detachment faults. The main elements of the Catalina detachment zone were then projected updip above the ground surface and downdip into the subsurface, using as a basis our subarea maps and subsurface interpretation for control. The fundamental geometry was projected to a series of 25 cross sections constructed in 3DMOVE. Triangulated 3-D fault surfaces were constructed in GoCAD and then interpolated and modified locally to better adhere to topography/surface trace constraints. Further calculations of dip, azimuth, thickness, and visualization were completed in GoCAD using these surfaces. The 3-D model presents the Catalina detachment fault as a shallowly dipping (10°–20°) fault along the lower margin of the Rincon Mountains. Descending into the subsurface, it first steepens but then becomes shallow and listric to merge with other faults into a midcrustal detachment at ~7–8 km depth.

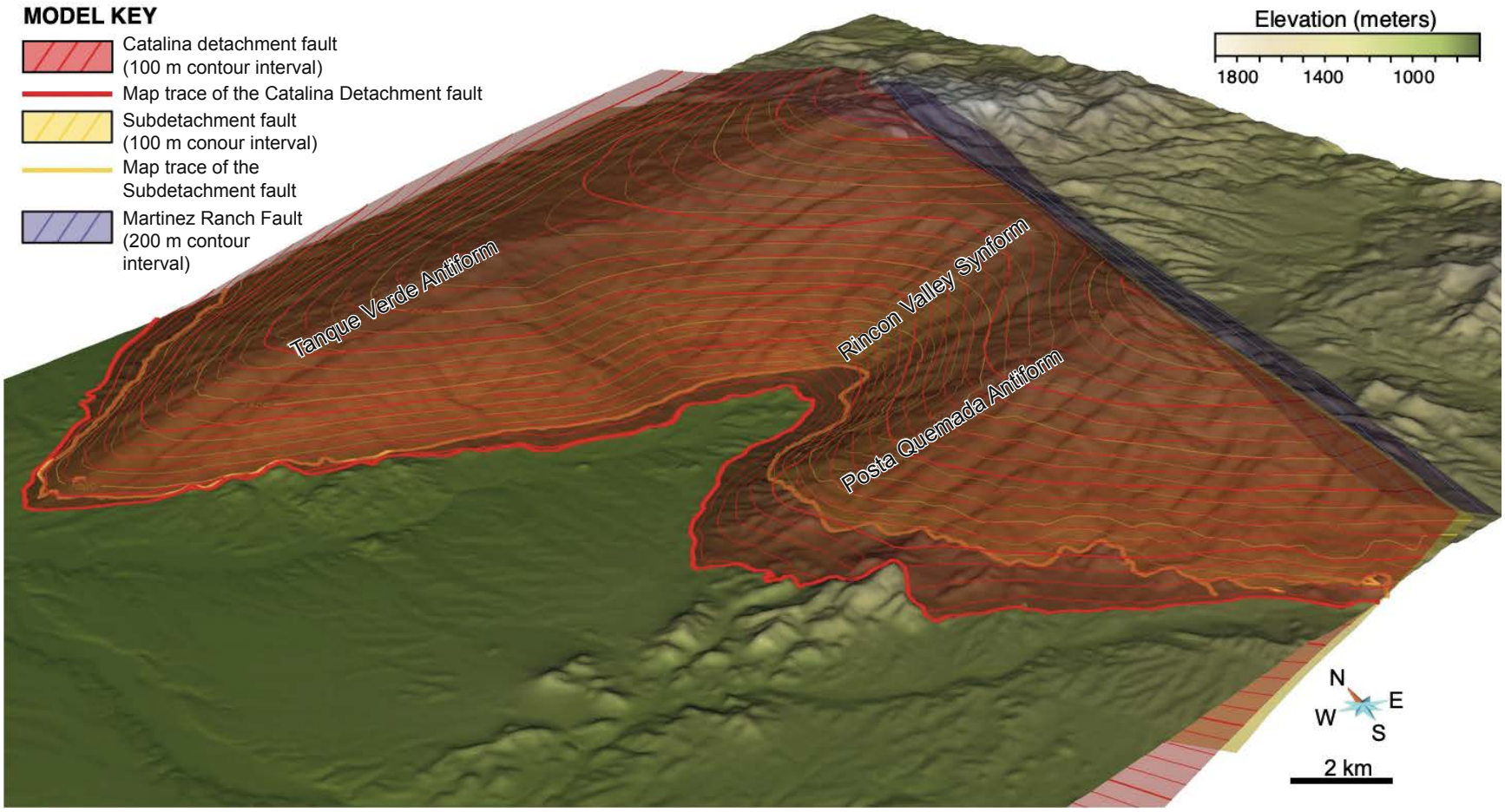


Figure 9-3. Perspective three-dimensional (3-D) view of 3-D model for the Catalina detachment fault, subdetachment fault zone, and Martinez Ranch fault with 30-m-resolution elevation data from the National Elevation Data set (USGS, 2020).

The model highlights the Posta–Quemada–Hidden Spring subarea (Fig. 3-7) and shows part of the broad, large-scale antiformal and synformal geometry that trends ~240° and plunges gently toward the SW (Fig. 9-3). As part of the broader Posta Quemada antiform, the strike and dip of the Catalina detachment fault smoothly change from an average of 113° strike, 14° SW dip (north of Charlie's Cliff, location shown on Fig. 3-7) to an average of 150° strike, 16° SW dip south of Charlie's Cliff. The subdetachment fault zone over this entire area has a strike intermediate between these values and dips slightly more steeply, with an average strike of 139° and dip of 20°.

The subdetachment fault zone is generally more variable and nonplanar in its local geometry, particularly in the Martinez-Salcido Ranch and Posta Quemada–Hidden Spring subareas (Fig. 9-3). This variability is consistent with the interpretation of the subdetachment originating from previously isolated, short-trace-length zones of ultramylonite and calc-silicate tectonite. CPC exhibits variable thicknesses as a function of local and more regional differences in strike and dip between the two bounding surfaces (Fig. 9-4). At any given location along the trace of the detachment zone, the difference in dip of the main detachment versus the subdetachment faults can be inferred by the change in thickness of CPC updip and downdip at that location.

DETACHMENT FAULT DISPLACEMENT

A complementary set of evolving models and cross sections further elucidates the character and evolution of the Catalina detachment zone. Figure 9-5A shows the Catalina detachment fault surface as projected above topography on the basis of geologic mapping constraints and into the Tucson Basin in ways consistent with subsurface data (Chapter 2). The shape of the detachment fault surface is also constrained, in part, by exposed lower-plate rocks in the high country of the Rincon Mountains. Figure 9-5B represents forward modeling of the Catalina detachment fault and exhumation of the lower plate. A minimum of 36 km of fault slip displacement is required (Spencer et al., 2019); it could be as high as 60 km (Spencer et al., 2022). The forward modeling incorporated an inferred flat paleosurface level. For simplicity, the corrugated surface of the detachment fault was modeled as part of the initial geometry and therefore does not account for progressive deformation. The corrugations decrease in amplitude downward into the subsurface. In Figure 9-5C, we represent "before-and-after" development of the detachment faulting and exhumation of the lower plate.

Total transport was distributed within five structural entities within the Catalina detachment zone: lower-plate ductile flow and later shear-induced mylonitization, creating mylonites and ultramylonites; subdetachment faulting; cataclastic deformation creating CPC, and associated minidetachment faulting; cataclastic deformation producing ultracataclasite; and Catalina detachment fault slip. Figure 9-6 shows a conceptual scheme for displacement distribution, but we remain uncertain about how the ~36 km of overall tectonic transport was partitioned among these fault rocks and structures. It is difficult to picture a practical approach to this question. To be sure, the amount of tectonic transport achieved by mylonitization and ultramylonitization can be approached through strain inventories across the full thicknesses of core complex mylonites and ultramylonites. Perhaps this is the first step, results of which will place limits on required collective contributions to the overall budget by subdetachment faulting, the transformation of mylonite to CPC, and the combination of cataclasis and ultracataclasis.

ADDRESSING THE ALTERNATIVE VIEW OF DETACHMENT FAULTS PROPOSED BY FAVORITO AND SEEDORFF (2021)

Favorito and Seedorff (2021) recently proposed an alternative hypothesis for the origin of the Catalina-Rincon metamorphic core complex. In their model, there is no complex-wide detachment system but instead a sequence of successive domino-style fault blocks that were progressively back-tilted across four principal fault generations during the Oligocene–Miocene. They emphasized, based on a sequential balanced cross section accounting for crosscutting faults and synextensional strata, that multiple generations of steeply dipping faults progressively tilted the study area by ~60°, accounting for ~59 km of total extension.

We subscribe to the interpretation offered by Favorito and Seedorff (2021) in which the eastern Rincon Mountains region was, during the Laramide orogeny, the site of the development of a NE-vergent basement-cored uplift (Fig. 9-1). However, like Spencer et al. (2022), we do not see evidence that the Catalina fault and the San Pedro fault were discrete and thus separate reverse faults during the Laramide orogeny, which were later rotated to their current positions and orientations, thereby creating a false impression that they belong to a common detachment fault. Favorito and Seedorff (2021, p. 1960) went so far as to conclude that "the detachment model, therefore, likely does not apply to the Catalina core complex and may not be applicable to other Cordilleran locales of extreme continental extension that have been interpreted as such." While geometrically admissible, the Favorito and Seedorff (2021) kinematic model does not best reconcile the observed outcrop geology. Only two large-offset (>5 km) faults within the Favorito and Seedorff (2021) model have expression in outcrop: the San Pedro fault in the northeastern Rincon Mountains and the Catalina fault at the southern edge of the Catalina Mountains and along the southwestern margin of the Rincon Mountains. Many generations of spaced domino faults with 5–10 km offsets would be necessary to accomplish rotation of the San Pedro and Catalina faults to gently dipping (<30°) attitudes. Yet, no such faults are reported. Furthermore, the large and thick syntectonic clastic basins inferred by Favorito and Seedorff (2021) at domino-block edges would exceed by a factor of greater than two the observed thicknesses in preserved Oligocene–Miocene sections surrounding the Catalina-Rincon complex (Dickinson, 1991).

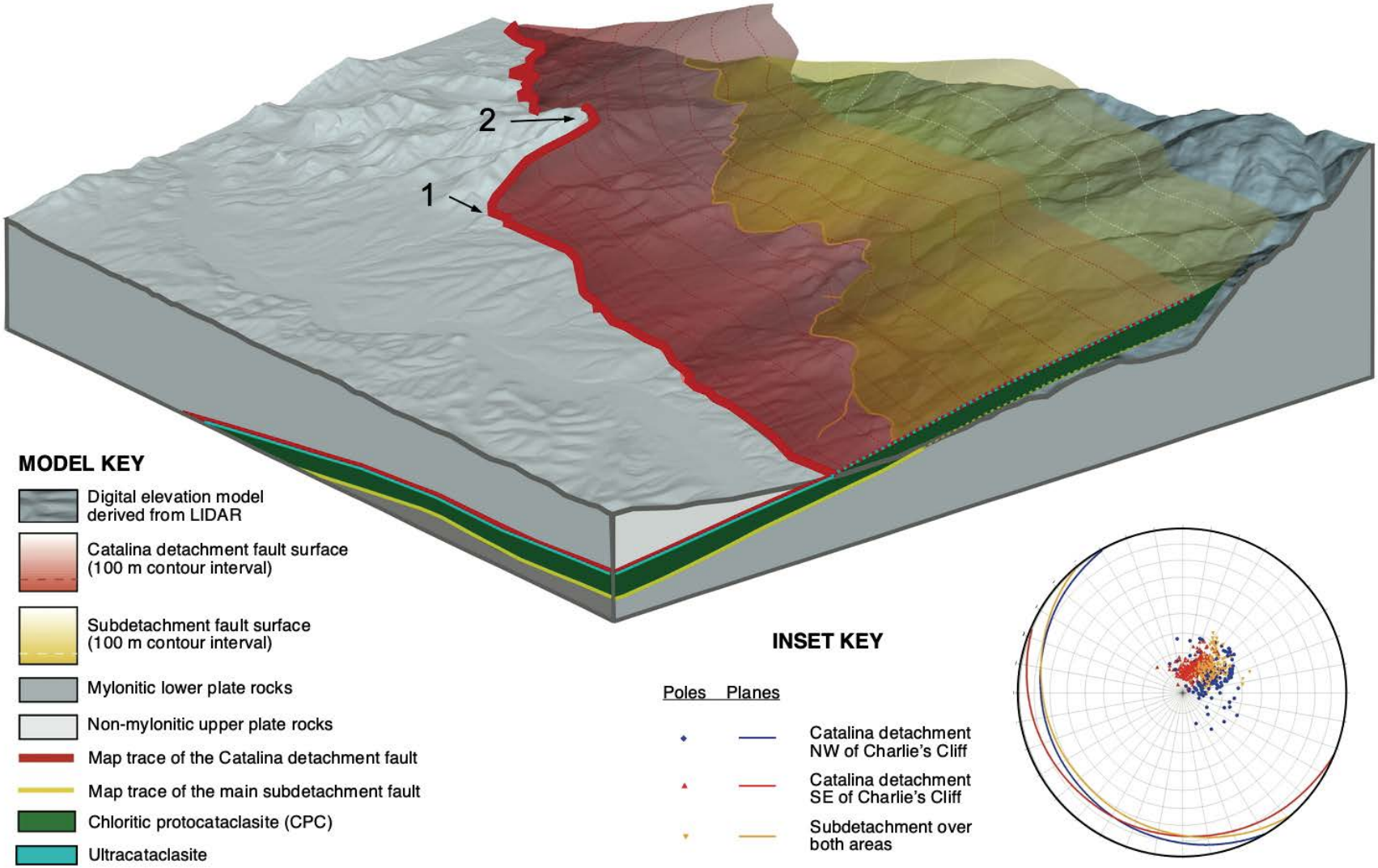


Figure 9-4. NW-directed three-dimensional (3-D) perspective view of a block model of the Posta Quemada–Hidden Spring subarea. 1—location of Charlie's Wash; 2—Charlie's Cliff (see Fig. 3-6). Inset at bottom right shows poles to planes (points) and average orientations (great circles) derived from the triangulated surface of the 3-D fault planes. LiDAR—light detection and ranging.

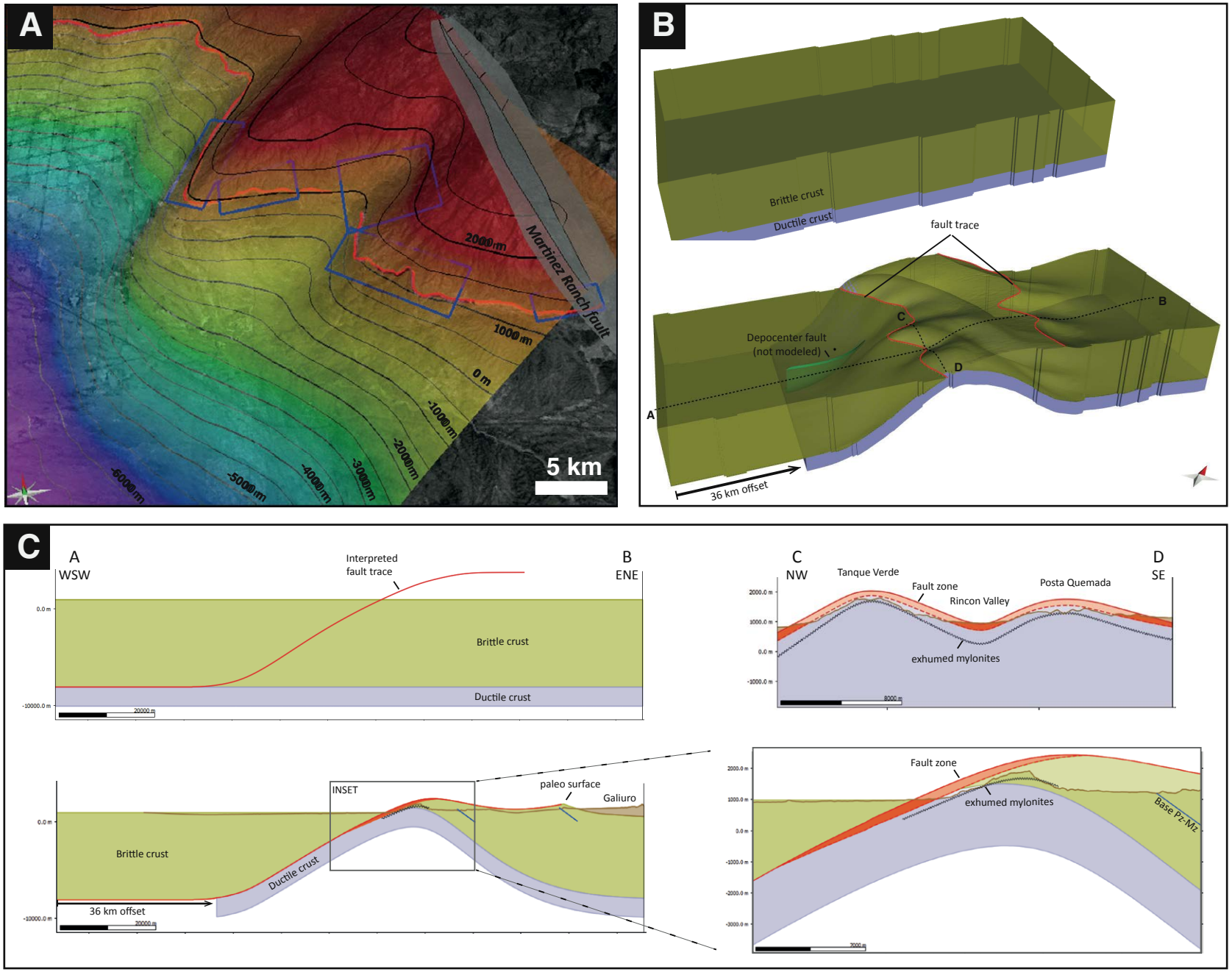

A
Martinez Ranch fault
2000 m
1000 m
0 m
-1000 m
-2000 m
-3000 m
-4000 m
-5000 m
-6000 m
5 km
B
Brittle crust
Ductile crust
fault trace
Depocenter fault
(not modeled)
A
B
C
D
36 km offset
C
A
WSW
Interpreted
fault trace
B
ENE
Brittle crust
Ductile crust
20000 m
C
NW
Tanque Verde
Fault zone
Rincon Valley
Posta Quemada
D
SE
exhumed mylonites
8000 m
INSET
paleo surface
Galiuro
Brittle crust
Ductile crust
36 km offset
20000 m
Fault zone
exhumed mylonites
Base Pz-Mz
7000 m

Figure 9-5.

Figure 9-5. Illustrative forward model of form and development of the Rincon Mountains domain of the Catalina-Rincon metamorphic core complex. (A) Catalina detachment fault (red line) as interpreted, projected upward and downward from mapped trace. Note the geometry of corrugations and the progressive reduction of amplitude toward the assumed midcrustal detachment level. (B) Three-dimensional (3-D) forward modeling of Catalina detachment fault and lower-plate exhumation, aiming to match the known late-stage geometry of the fault surface from a formerly more gently dipping structure near the brittle-ductile transition. (C) Simplified cross-sectional portrayals of Catalina detachment zone in context of "before-and-after" slip/shear and exhumation. Offset along the detachment fault was estimated by Spencer et al. (2019) as ~36 km. See text for explanation. Pz—Paleozoic; Mz—Mesozoic.

COMPARISONS WITH OTHER CALIFORNIA-ARIZONA-SONORA METAMORPHIC CORE COMPLEXES

Tectonic Significance of Regional Metamorphic Core Complexes

All of the metamorphic core complexes exposed from California through Arizona and into Sonora, Mexico, reveal profound extension accommodated on crustal-scale detachment faults. All display mylonitic fabrics resulting from ductile shearing with various degrees of brittle overprinting associated with footwall exhumation. In addition, all expose a shallow detachment fault with displaced hanging-wall fault blocks. The Catalina-Rincon metamorphic core complex, and the adjacent Picacho and Tortolita core complexes, display a top-to-SW displacement, which reverses the top-to-NE polarity across most of western and south-central Arizona. Although the local kinematics vary, the metamorphic core complexes express a consistent NE-SW extension along a continuous belt. This belt resulted from a lateral spreading of a specific domain of over-thickened crust, with tens of km of horizontal extension (Coney and Harms, 1984) (Fig. 1-3).

Regional Timing of the Metamorphic Core Complexes

The interpreted ca. 26 Ma onset of mylonitization in the Rincon Mountains domain of the Catalina-Rincon metamorphic core complex is older than that of other core complexes in the California-Arizona system (Fig. 1-4). For example, the inception of mylonitization in the Whipple Mountains metamorphic core complex was ca. 24 Ma (Foster and John, 1999; Cooper et al., 2017), and it was ca. 22–21 Ma in the Buckskin-Rawhide metamorphic core complex (Bryant and Wooden, 2008; Singleton and Mosher, 2012; Singleton et al., 2014). Our constraints of ca. 26–22 Ma for the onset of detachment faulting in the Rincon Mountains slightly predate the tight window (ca. 22 Ma to 21 Ma) of inception of detachment fault slip in other regionally proximate metamorphic core complexes, namely, the Harquahala (Prior et al., 2016), Harcuvar (Foster et al., 1993; Carter et al., 2004; Sanguinito, 2013), Buckskin-Rawhide (Scott et al., 1998; Singleton et al., 2014), Whipple (Stockli et al., 2006), and Chemehuevi (Foster and John, 1999) core complexes.

Figure 9-7 provides a comparison of the timing of initiation of detachment faulting in the Rincon Mountains with published interpretations of onset ages for the Chemehuevi, Buckskin, South Mountain, Picacho, Catalina, and Coyote metamorphic core complexes (Fig. 1-4). In southeastern California and central Arizona, core complex exhumation generally occurred between 24 and 20 Ma (Fig. 9-7) (Rehrig and Reynolds, 1980; Richard et al., 1990; Foster et al., 1990; Fitzgerald et al., 1993; Scott et al., 1998; Gottardi et al., 2018). By comparison, the onset of detachment faulting in the Catalina and Rincon Mountains occurred slightly earlier, with the exception of the Coyote Mountains metamorphic core complexes, where the onset of detachment faulting occurred at ca. 29 Ma (Gottardi et al., 2020) (Fig. 9-7). In northern Mexico, initiation of detachment faulting in the Mazatan metamorphic core complex occurred at ca. 25 Ma (Wong and Gans, 2008; Wong et al., 2010), approximately the same time as that in the Rincon Mountains. Based on the timing of initiation of detachment faulting (and thus exhumation), it would appear

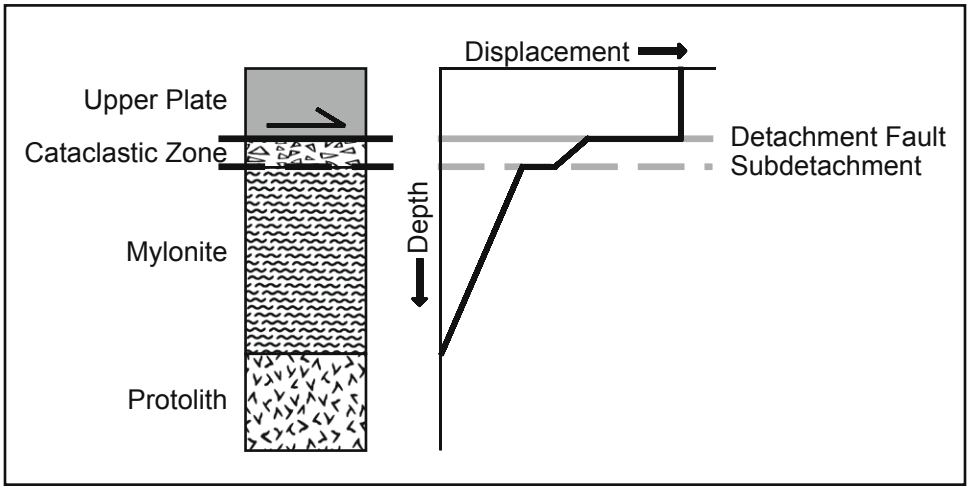


Figure 9-6. Conceptual diagram showing variation of total displacement with depth, for both discrete fault zones and zones of distributed shear. See text for explanation.

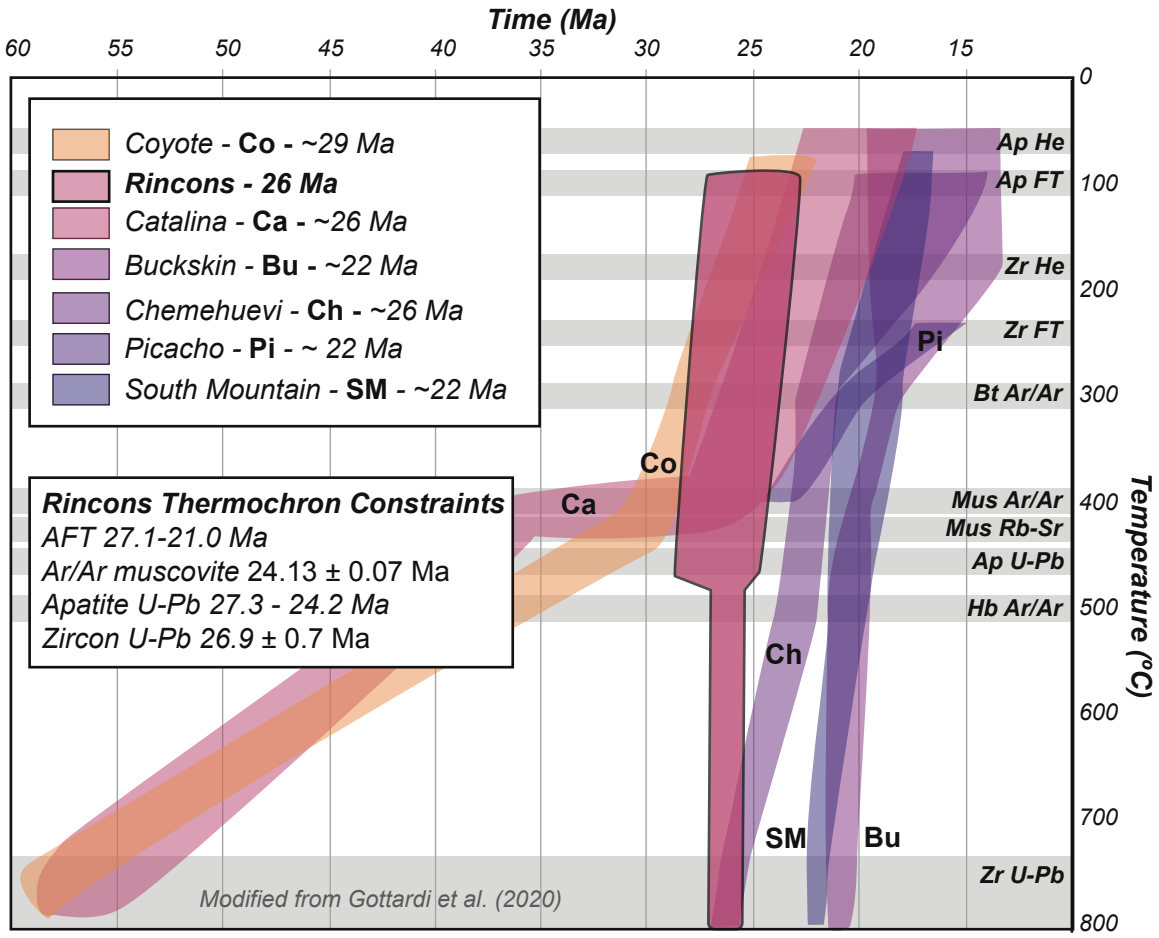


Figure 9-7. Time-temperature plot modified after Gottardi et al. (2020) to include new geochronology and thermochronology conclusions drawn from this analysis of the Rincon Mountains metamorphic core complex. Ar—argon; Ap—apatite; Zr—zircon; AFT—apatite fission track (FT); Bt—biotite; Mus—muscovite; Hb—hornblende.

that core complex–related detachment faulting overall initiated earlier in northern Sonora and southern Arizona than it did in central and western Arizona. The subregion within which the timing of initiation of detachment faulting transitions from older (ca. 29–26 Ma) to younger (ca. 24–20 Ma) occurs near the Picacho metamorphic core complex, where the shift in polarity of tectonic-transport direction also occurs.

SUMMARY

Results of our geochronology and thermochronology analyses indicate that mylonitization operated at ca. 24 Ma within the Catalina detachment zone, though initiation of mylonitization expressed now in surface exposures was earlier, perhaps ca. 27 Ma. Protolith converted to mylonite includes Oracle Suite granitoids (ca. 1450 Ma), Wilderness Suite granitoids (rims ca. 43 Ma), and Catalina Suite granitoids (ca. 27 Ma). Midtemperature (600–200 °C) thermochronology analysis reveals that the mylonitic fabrics directly beneath the Catalina detachment fault cooled between ca. 27 and 24 Ma. Muscovite porphyroclasts (i.e., mica fish) and groundmass Ar-Ar from ultramylonite and ultracataclasite document cooling to ~350 °C at ca. 24 Ma. Mylonitization ceased by ca. 22 Ma, based on Ar-Ar results from an undeformed mafic dike crosscutting mylonitic fabric and cataclastically overprinted mylonite. Chloritic protocataclasite developed in the interval ca. 24–22 Ma. Final increments of Catalina detachment faulting (mid-Miocene, from ca. 17 Ma to as young as 14 Ma), are constrained by a combination of K-Ar dating of fault gouge and zircon and apatite helium dating. Detachment zone shearing and slip was followed by or transitioned into Basin and Range extension, which is manifest in moderate- to high-angle normal faults that truncate and offset the Catalina detachment zone.

Timing conclusions based on our subsurface analysis of basin deposits and structures in the Tucson Basin are in accord with results from geochronology and thermochronology results from rocks in the lower plate of the Catalina detachment zone, and along the Catalina fault surface proper. Basin stratigraphy and structural geology is illuminated by a combination of

published well data and seismic reflection profiles. Basin accommodation space was achieved, in part, by offset on fault splays linked to the Catalina detachment fault. Most of the faulting took place 28–21 Ma.

The ca. 10 Ma period of active deformation within and along the Catalina detachment zone was marked by progressive ductile-brittle shear-zone deformation achieved through different deformation mechanisms in different rocks at different times and at different depths. Overprinting of earlier fabrics and structures by later ones are replete within the detachment zone. Throughout progressive structural development of structures and fabrics, the tectonic transport direction and sense of direction were consistently top-to-SW (~240°). Thus, structures and fabrics are now arrayed in what is a remarkably simple, coherent kinematic system. However, the discrete units of homogeneous fault rocks (i.e., cataclastic and ultracataclastic rocks, chloritic protocataclastic rocks, and mylonites) are separated not by smooth and gradual transitions but by fault discontinuities. A notable discontinuity, which we have mapped in full, is the subdetachment fault zone separating mylonite from chloritic protocataclasite. A more subtle discontinuity separates cataclasite/ultracataclasite from underlying chloritic protocataclasite. Net tectonic transport achieved by overall progressive deformation, including slip on the Catalina detachment fault, is at least 36 km. This transport contributed to overall regional core complex extension and brought deeply formed mylonites to the very surface, thereby creating the Rincon Mountains.

Deciphering Laramide tectonic heritage in the lower-plate rocks proves to be quite challenging. Prior to the discovery phase of Cordilleran metamorphic core complexes (early to mid-1970s), Laramide thrust faulting and associated "metamorphism" (i.e., mylonitization) were considered to represent the full causation of structures and fabrics within the Rincon and Catalina Mountains. The few alternative interpretations focused on a Precambrian development of the gneisses. The pendulum of interpretation swung rather swiftly to an overwhelming emphasis on an Oligocene–Miocene, post-Laramide origin of the structures and fabrics, consistent with interpretations and conclusions presented here. Presently, however, there is a resurgence of emphasis on possible contributions of Laramide tectonism in fashioning the Catalina-Rincon metamorphic core complex. A key obstacle to deciphering the nature and extent of syn-Laramide contributions within the Catalina-Rincon metamorphic core complex is absence of a consensus model on overall character and origin of Laramide tectonism in southeastern Arizona broadly. Laramide tectonism in this region is complex and understudied. One notable question of importance is how shallow-level, upper-plate, thrust-fault relations exposed from place to place in the Rincon Mountains once connected, structurally, to deeper-level Laramide shear zones mapped from place to place in southeastern Arizona. Increasingly the heart of this debate centers on the origin and significance of Wilderness Suite granitoids, whose age range in the Catalina-Rincon metamorphic core complex is ca. 57–43 Ma. We find no evidence that the Catalina detachment fault is a reactivation of a Laramide thrust fault. On the other hand, future research could productively address the exact timing and origin of the subdetachment fault zone, how it may have contributed to localizing the Catalina detachment fault, and whether any of its structural/petrologic contents (e.g., the enigmatic, mélange-like carbonate tectonites) formed during the Laramide as products of the effects of igneous intrusion and/or thrust faulting.

The essential features of the Rincon domain of the Catalina-Rincon metamorphic core complex are nearly identical to those within the overall belt of core complexes that track from southeastern California through Arizona and into Sonora. These "essential features" include geomorphology, fabrics, structures, kinematics, and timing. Timing of the progressive development of the Catalina detachment zone is closely aligned with timing determined for core complexes researched in Sonora, Mexico, but slightly older than that recorded in the part of the core complex belt from central Arizona to southeastern California. It appears that the shift in timing of these two major domains coincides, generally, with the subregion of the shift in tectonic transport direction that takes place south of Phoenix, Arizona. To the south of Phoenix, tectonic-transport direction is top-to-SW, all the way into Sonora. To the north of Phoenix, and including South Mountain, tectonic transport is top-to-NE, all the way into southeastern California. Because the belt of metamorphic core complexes is so young and geomorphically distinctive, and because Basin and Range faulting did not compromise the overall continuity of this belt, it emerges now as the most conspicuous, continuous belt of tectonic deformation in southern Arizona. Tracked and characterized regionally through intensive mapping by numerous individuals and teams, the belt of metamorphic core complexes presents itself clearly within a palimpsest of earlier-formed structure-tectonic belts of Precambrian, Jurassic, and Laramide deformations.

Conclusions

The Rincon Mountains domain of the Catalina-Rincon metamorphic core complex provides a uniquely complete lateral and vertical exposure of a crustal-scale detachment fault zone. The exceptional exposures of the Catalina detachment system in the Rincon Mountains provide insight into recognition and interpretation, in significant detail, of kinematically linked brittle through ductile, crustal-scale fault zones. Different deformation mechanisms operated at different depth levels, and different structural associations evolved as a function of factors such as depth (i.e., confining pressure), temperature, and fluid-forced alteration and overpressuring. Progressive deformation was such that lower-plate rocks, structures, and fabrics became exhumed and overprinted by more brittle mechanisms at increasingly shallow depths. Faulted and fractured hanging-wall blocks, most of which were never ever buried deeply enough to acquire metamorphic fabrics, became in contact with ductilely deformed lower-plate rocks derived from depths beneath the interval of ductile to brittle transition. Differential rheological responses over close to 9 million years created a partitioned zone of systematic and distinctive structures and fabrics. Strain localization, operating over this long-sustained time interval and marked by a uniform prevailing movement plan (i.e., shearing top-to-SW), caused the development of families of discrete faults, some of which (notably subdetachment fault zones) influenced the growth of a through-going detachment fault.

Because of the constancy of physical expression of structures, fabrics, and overall detachment zone characteristics in the SE California to Sonora belt of metamorphic core complexes, the properties and interpreted evolution of the Catalina detachment zone have broad applicability to a unified model. Fault rock stratigraphy emerged through a synchronized and progressive development of deeper ductile shear (mylonites) linked to shallow, brittle, dynamic overprint (creating chloritic protocataclasite), and ultimately to localized faulting and the evolution of the regional detachment fault. Progressive exhumation of footwall rocks changed boundary conditions and operative deformation mechanisms at both the micro- and macro-scales. Our span of geochronology and thermochronology analytical results suggests a fairly rapid evolution for the Catalina detachment zone, from ca. 26 Ma to ca. 17 Ma. This interval is slightly older than that reported in published ages for metamorphic core complexes in central Arizona, western Arizona, and southeast California.

Better understanding of fault zone behavior has been a primary goal of this research, including the influences of slip- and strain-localization. There are obvious advantages in addressing these challenges through close examination of a well-exposed extensional detachment-fault system. Such systems are marked by concentration of diverse structures, fabrics, and damage created through normal-slip shear that operated at depth levels ranging from the paleosurface that existed at the time of onset of core-complex extension, to well below the brittle-ductile transition. The concentration of ductile-to-brittle fabrics and structures is so narrow in the Rincon Mountains that a detachment zone, in this case, the Catalina detachment zone, preserves over an outcrop breadth of just 1 km an array of fault rocks created over a down-dip shear zone length on the order of 40 or 50 km. The structural components are laid out for view, providing opportunities for others to carry out additional research, utilizing applications of new and emerging tools and methods that will lead ultimately to calibration of the full physical/dynamic environment within which each component of the detachment zone was fashioned. Major structures such as the Catalina detachment zone provide time-lapse preservation of crustal-scale shearing.

Application of a diverse range of geochronology and thermochronology methods to the rocks of the Catalina detachment zone is of first-order consequence in this study, for almost all of previous such work had been carried out in the Catalina Mountains domain of the Catalina-Rincon metamorphic core complex. Noteworthy among these geochronology contributions is establishing that protolith as young as 26 Ma became overprinted by core-complex mylonitization. One of the most significant geologic contributions is characterizing what is among the best exposed chloritic protocataclasitic fault-rock units globally, mapping it in its entirety, and focusing on its strategic importance in the very transition from ductile-to-brittle deformation. Related to this is the observation that the base of chloritic protocataclasite in the Rincon Mountains is everywhere a subdetachment (proto-detachment) fault, the presence of which likely contributed to localizing the Catalina detachment fault. Finally, our analysis of the subsurface geology of the Tucson Basin secures the compatibility of the basin record of timing with the analytical results of new geochronology and thermochronology.

Again, we hope that the observations and interpretations contained herein will draw others to conduct research on the Catalina detachment zone as exposed in the Rincon Mountains. New work on the fault rocks and fabrics, carried out using new and emerging technologies, will undoubtedly further enlighten timing, conditions, and tectonic implications of the Catalina detachment

zone and precursor tectonic heritage. Moreover, the scientific discoveries benefit entities such as Saguaro National Park, Rincon Mountain District. In this study alone, we have learned that it is the fractured and slot-faulted character of CPC that has created myriad habitats for living creatures; and that numerous springs in the Rincon Mountains emanate along the trace of the subdetachment fault system, probably because the combination of ultramylonite and calc-rich mylonites creates aquicludes.

References cited

Allen, W., 2014, Pseudotachylytes of Tanque Verde Wash, Tucson, Arizona, *in* 28th Annual Student Colloquium, 6–8 March 2014: El Paso, Texas, Department of Geosciences, University of Texas at El Paso.

Arca, M.S., 2009, Investigation of Cenozoic Crustal Extension Inferred from Seismic Reflection Profiles and Field Relations, SE Arizona [Ph.D. dissertation]: Tucson, Arizona, University of Arizona, 185 p.

Arca, M.S., Kapp, P., and Johnson, R.A., 2010, Cenozoic crustal extension in southeastern Arizona and implications for models of core-complex development: Tectonophysics, v. 488, p. 174–190, https://doi.org/10.1016/j.tecto.2010.03.021.

Armstrong, R.L., 1972, Low-angle (denudation) faults, hinterland of the Sevier orogenic belt, eastern Nevada and western Utah: Geological Society of America Bulletin, v. 83, no. 6, p. 1729–1754, https://doi.org/10.1130/0016-7606(1972)83[1729:LDFHOT]2.0.CO;2.

Axen, G.J., 2020, How a strong low-angle fault formed: The Whipple detachment, southeastern California: Geological Society of America Bulletin, v. 132, no. 9–10, p. 1817–1828, https://doi.org/10.1130/B35386.1.

Axen, G.J., and Selverstone, J., 1994, Stress state and fluid pressure level along the Whipple detachment fault, California: Geology, v. 22, no. 9, p. 835–838, https://doi.org/10.1130/0091-7613(1994)022<0835:SSAFPL>2.3.CO;2.

Axen, G.J., and Wernicke, B., 1991, Comment on "Tertiary extension and contraction of lower-plate rocks in the central Mojave metamorphic core complex, Southern California," by John M. Bartley, John M. Fletcher, and Allen F. Glazner: Tectonics, v. 10, p. 1084–1086, https://doi.org/10.1029/91TC01216.

Axen, G.J., Selverstone, J., and Luther, A., 2018, A rock record of paleoseismic cycling: Unique layered cataclasites below the West Salton detachment fault, southern California: Geosphere, v. 14, no. 1, p. 187–214, https://doi.org/10.1130/GES01499.1.

Bai, T., and Pollard, D.D., 2000, Fracture spacing in layered rocks: A new explanation based on the stress transition: Journal of Structural Geology, v. 22, no. 1, p. 43–57, https://doi.org/10.1016/S0191-8141(99)00137-6.

Balcer, R.A., 1984, Stratigraphy and Depositional History of the Pantano Formation (Oligocene–early Miocene), Pima County, Arizona [M.S. thesis]: Tucson, Arizona, University of Arizona, 107 p.

Barker, S.L.L., 2005, Pseudotachylyte-generating faults in Central Otago, New Zealand: Tectonophysics, v. 397, p. 211–223, https://doi.org/10.1016/j.tecto.2004.12.005.

Behr, W.M., and Platt, J.P., 2011, A naturally constrained stress profile through the middle crust in an extensional terrane: Earth and Planetary Science Letters, v. 303, no. 3–4, p. 181–192, https://doi.org/10.1016/j.epsl.2010.11.044.

Behr, W.M., and Platt, J., 2014, Brittle faults are weak, yet the ductile middle crust is strong: Implications for lithospheric mechanics: Geophysical Research Letters, v. 41, no. 22, p. 8067–8075, https://doi.org/10.1002/2014GL061349.

Best, M.G., Christiansen, E.H., de Silva, S., and Lipman, P.W., 2016, Slab-rollback ignimbrite flareups in the southern Great Basin and other Cenozoic American arcs: A distinct style of arc volcanism: Geosphere, v. 12, no. 4, p. 1097–1135, https://doi.org/10.1130/GES01285.1.

Bird, P., 1998, Kinematic history of the Laramide orogeny in latitudes 35–49°N, western United States: Tectonics, v. 17, no. 5, p. 780–801, https://doi.org/10.1029/98TC02698.

Bjørnerud, M.G., 2010, Rethinking conditions necessary for pseudotachylyte formation: Observations from the Otago schists, South Island, New Zealand: Tectonophysics, v. 490, p. 69–80, https://doi.org/10.1016/j.tecto.2010.04.028.

Black, L.P., Williams, I.S., and Compston, W., 1986, Four zircon ages from one rock: The history of a 3930 Ma-old granulite from Mount Sones, Enderby Land, Antarctica: Contributions to Mineralogy and Petrology, v. 94, no. 4, p. 427–437, https://doi.org/10.1007/BF00376336.

Black, L.P., Kamo, S.L., Allen, C.M., Davis, D.W., Aleinikoff, J.N., Valley, J.W., Mundil, R., Campbell, I.H., Korsch, R.J., Williams, I.S., and Foudoulis, C., 2004, Improved $^{206}Pb/^{238}U$ microprobe geochronology by the monitoring of trace-element–related matrix effect: SHRIMP, ID-TIMS, ELA-ICP-MS and oxygen isotope documentation for a series of zircon standards: Chemical Geology, v. 205, no. 1–2, p. 115–140, https://doi.org/10.1016/j.chemgeo.2004.01.003.

Blackburn, T., Bowring, S.A., Schoene, B., Mahan, K., and Dudas, F., 2011, U-Pb thermochronology: Creating a temporal record of lithosphere thermal evolution: Contributions to Mineralogy and Petrology, v. 162, p. 479–500, https://doi.org/10.1007/s00410-011-0607-6.

Braun, J., Van der Beek, P., and Batt, G., 2006, Quantitative Thermochronology: Numerical Methods for the Interpretation of Thermochronological Data: New York, Cambridge University Press, 272 p., https://doi.org/10.1017/CBO9780511616433.

Broermann, J., Bennett, R.A., Kreemer, C., Blewitt, G., and Pearthree, P.A., 2021, Geodetic extension across the southern Basin and Range and Colorado Plateau: Journal of Geophysical Research–Solid Earth, v. 126, no. 6, https://doi.org/10.1029/2020JB021355.

Bryant, B., 1995, Geologic Map, Cross-Sections, Isotopic Dates, and Mineral Deposits of the Alamo Lake 30′ × 60′ Quadrangle, West-Central Arizona: U.S. Geological Survey Miscellaneous Investigations Map I-2489, 3 sheets, scale 1:100,000, https://doi.org/10.3133/i2489.

Bryant, B., and Wooden, J.L., 2008, Geology of the Northern Part of the Harcuvar Complex, West-Central Arizona: U.S. Geological Survey Professional Paper 1752, 52 p., https://doi.org/10.3133/pp1752.

Buck, W.R., 1988, Flexural rotation of normal faults: Tectonics, v. 7, no. 5, p. 959–973, https://doi.org/10.1029/TC007i005p00959.

Bykerk-Kaufman, A., 1990, Structural Evolution of the Northeastern Santa Catalina Mountains, Arizona: A Glimpse of Pre-Extension History of the Catalina Complex [Ph.D. dissertation]: Tucson, Arizona, University of Arizona, 184 p.

Bykerk-Kaufman, A., 2008, Geologic Map of the Southeastern Santa Catalina Mountains, Pima County, Arizona: Arizona Geological Survey Contributed Map CM-08-A, scale 1:24,000, 2 map sheets, http://repository.azgs.az.gov/uri_gin/azgs/dlio/767.

Bykerk-Kauffman, A., and Janecke, S.U., 1987, Late Cretaceous to early Tertiary ductile deformation: Catalina-Rincon metamorphic core complex, southeastern Arizona: Geology, v. 15, no. 5, p. 462–465, https://doi.org/10.1130/0091-7613(1987)15<462:LCTETD>2.0.CO;2.

Carter, T.J., Kohn, B.P., Foster, D.A., and Gleadow, A.J.W., 2004, How the Harcuvar Mountains metamorphic core complex became cool: Evidence from apatite (U-Th)/He thermochronometry: Geology, v. 32, no. 11, p. 985–988, https://doi.org/10.1130/G20936.1.

Chapman, J.B., Runyon, S.E., Shields, J.E., Lawler, B.L., Pridmore, C.J., Scoggin, S.H., Swaim, N.T., Trzinski, A.E., Wiley, H.N., Barth, A.P., and Haxel, G.B., 2021, The North American Cordilleran anatectic belt: Earth-Science Reviews, v. 215, https://doi.org/10.1016/j.earscirev.2021.103576.

Chew, D.M., and Donelick, R.A., 2012, Combined apatite fission track and U-Pb dating by LA-ICP-MS and its application in apatite provenance analysis, *in* Sylvester, P., ed., Quantitative Mineralogy and Microanalysis of Sediments and Sedimentary Rocks: Mineralogical Association of Canada Short Course 42, p. 219–247.

Chew, D.M., Petrus, J.A., and Kamber, B.S., 2014, U-Pb LA-ICPMS dating using accessory mineral standards with variable common Pb: Chemical Geology, v. 363, p. 185–199, https://doi.org/10.1016/j.chemgeo.2013.11.006.

Cochrane, R., Spikings, R.A., Chew, D., Wotzlaw, J.F., Chiaradia, M., Tyrrell, S., Schaltegger, U., and Van der Lelij, R., 2014, High temperature (>350 °C) thermochronology and mechanisms of Pb loss in apatite: Geochimica et Cosmochimica Acta, v. 127, p. 39–56, https://doi.org/10.1016/j.gca.2013.11.028.

Coney, P.J., 1973, Non-collision tectogenesis in western North America, *in* Tarling, D.H., and Runcorn, S.H., eds., Implications of Continental Drift to the Earth Sciences: New York, Academic Press, p. 713–727.

Coney, P.J., 1974, Structural analysis of the Snake Range 'décollement,' east-central Nevada: Geological Society of America Bulletin, v. 85, no. 6, p. 973–978, https://doi.org/10.1130/0016-7606(1974)85<973:SAOTSR>2.0.CO;2.

Coney, P.J., 1980a, Introduction, *in* Crittenden, M.D., Jr., Coney, P.J., and Davis, G.H., eds., Cordilleran Metamorphic Core Complexes: Geological Society of America Memoir 153, p. 3–6, https://doi.org/10.1130/MEM153-p3.

Coney, P.J., 1980b, Cordilleran metamorphic core complexes: An overview, *in* Crittenden, M.D., Jr., Coney, P.J., and Davis, G.H., eds., Cordilleran Metamorphic Core Complexes: Geological Society of America Memoir 153, p. 7–31, https://doi.org/10.1130/MEM153-p7.

Coney, P.J., and Harms, T.A., 1984, Cordilleran metamorphic core complexes: Cenozoic extensional relics of Mesozoic compression: Geology, v. 12, no. 9, p. 550–554, https://doi.org/10.1130/0091-7613(1984)12<550:CMCCCE>2.0.CO;2.

Coney, P.J., and Reynolds, S.J., 1977, Cordilleran Benioff zones: Nature, v. 270, p. 403–406, https://doi.org/10.1038/270403a0.

Cooper, F.J., Platt, J.P., and Behr, W.M., 2017, Rheological transition in the middle crust: Insights from Cordilleran metamorphic core complexes: Solid Earth, v. 8, p. 199–215, https://doi.org/10.5194/se-8-199-2017.

Cooper, J.R., and Silver, L.T., 1964, Geology and Ore Deposits of the Dragoon Quadrangle, Cochise County, Arizona: U.S. Geological Survey Professional Paper 416, 196 p., https://doi.org/10.3133/pp416.

Crittenden, M.D., Jr., Coney, P.J., and Davis, G.H., 1978, Penrose Conference report: Tectonic significance of metamorphic core complexes in the North American Cordillera: Geology, v. 6, no. 2, p. 79–80, https://doi.org/10.1130/0091-7613(1978)6<79:TSOMCC>2.0.CO;2.

Crittenden, M.D., Jr., Coney, P.J., and Davis, G.H., 1980, Cordilleran Metamorphic Core Complexes: Geological Society of America Memoir 153, 490 p., https://doi.org/10.1130/MEM153.

Crósta, A.P., and Moore, J.M., 1989, Enhancement of Landsat Thematic Mapper imagery for residual soil mapping in Mina Gerais State, Brazil: A prospecting case history in greenstone belt terrain, *in* Proceedings of the 7th Thematic Conference on Remote Sensing for Exploration Geology, Calgary, Alberta, Canada, 2–6 October 1989: Ann Arbor, Michigan, Environmental Research Institute of Michigan, p. 1173–1187.

Crósta, A.P., de Souza Filho, C.R., and Brodie, C., 2003, Targeting key alteration minerals in epithermal deposits in Patagonia, Argentina, using ASTER imagery and principal component analysis: International Journal of Remote Sensing, v. 24, no. 21, p. 4233–4240, https://doi.org/10.1080/0143116031000152291.

Davis, G.A., Anderson, J.L., Frost, E.G., and Shackelford, T.J., 1980, Mylonitization and detachment faulting in the Whipple–Buckskin–Rawhide Mountains terrane, southeastern California and western Arizona, *in* Crittenden, M.D., Jr., Coney, P.J., and Davis, G.H., eds., Cordilleran Metamorphic Core Complexes: Geological Society of America Memoir 153, p. 79–130, https://doi.org/10.1130/MEM153-p79.

Davis, G.A., Anderson, J.L., Martin, D.L., Krummendcher, D., Frost, E., and Armstrong, R.L., 1982, Geologic and geochronologic relationships in the lower plate of the Whipple Mountains detachment fault, Whipple Mountains, southeastern California: A progress report, *in* Frost, E.G., and Martin, D.L., eds., Mesozoic–Cenozoic Tectonic Evolution of the Colorado River Region, California, Arizona, and Nevada (Anderson-Hamilton Volume): San Diego, California, Cordilleran Publishers, p. 409–432.

Davis, G.A., Lister, G.S., and Reynolds, S.J., 1986, Structural evolution of the Whipple and South Mountains shear zones, southwestern United States: Geology, v. 14, no. 1, p. 7–10, https://doi.org/10.1130/0091-7613(1986)14<7:SEOTWA>2.0.CO;2.

Davis, G.H., 1973, Mid-Tertiary gravity-glide folding near Tucson, Arizona: Geological Society of America Abstracts with Programs, v. 5, p. 592.

Davis, G.H., 1975, Gravity-induced folding off a gneiss dome complex, Rincon Mountains, Arizona: Geological Society of America Bulletin, v. 86, p. 979–990, https://doi.org/10.1130/0016-7606(1975)86<979:GFOAGD>2.0.CO;2.

Davis, G.H., 1979, Laramide folding and faulting in southeastern Arizona: American Journal of Science, v. 279, p. 543–569, https://doi.org/10.2475/ajs.279.5.543.

Davis, G.H., 1980a, Structural characteristics of metamorphic core complexes, southern Arizona, *in* Crittenden, M.D., Jr., Coney, P.J., and Davis, G.H., eds., Cordilleran Metamorphic Core Complexes: Geological Society of America Memoir 153, p. 35–78, https://doi.org/10.1130/MEM153-p35.

Davis, G.H., 1980b, Metamorphic core complexes—Structural characteristics, kinematic expression, and relation to mid-Miocene listric faulting, *in* Coney, P.J., and Reynolds, S.J., eds., Cordilleran Metamorphic Core Complexes and Their Uranium Favorability: U.S. Department of Energy Open-File Report GJBX-258 (80), p. 119–159.

Davis, G.H., 1981, Cordilleran metamorphic core complexes—Expressions of regional ductile stretching and rotational, listric(?) faulting: Geological Society of America Abstracts with Programs, v. 13, p. 51.

Davis, G.H., 1983, Shear-zone model for the origin of metamorphic core complexes: Geology, v. 11, no. 6, p. 342–347, https://doi.org/10.1130/0091-7613(1983)11<342:SMFTOO>2.0.CO;2.

Davis, G.H., 1987a, A shear-zone model for the structural evolution of metamorphic core complexes in southeastern Arizona, *in* Coward, M.P., Dewey, J.F., and Hancock, P.L., eds., Continental Extensional Tectonics: Geological Society, London, Special Publication 28, p. 247–266, https://doi.org/10.1144/GSL.SP.1987.028.01.17.

Davis, G.H., 1987b, Saguaro National Monument Arizona: Outstanding display of the structural characteristics of metamorphic core complexes, *in* Hill, M.L., ed., Cordilleran Section of the Geological Society of America: Geological Society of America Centennial Field Guide Volume 1, p. 35–40, https://doi.org/10.1130/0-8137-5401-1.35.

Davis, G.H., 2008, Retrospective on "sense of shear" in relation to deciphering metamorphic core complexes, *in* De Paor, D., ed., Making Sense of Shear (in Honor of Carol Simpson): Journal of the Virtual Explorer, Electronic Edition, v. 30, paper 1, https://doi.org/10.3809/jvirtex.2008.00200.

Davis, G.H., 2013, Localization control for chlorite breccia deformation beneath the Catalina detachment fault, Rincon Mountains, Tucson, Arizona: Journal of Structural Geology, v. 50, p. 237–253, https://doi.org/10.1016/j.jsg.2012.12.001.

Davis, G.H., and Anderson, T.H., 1981, Metamorphic Core Complexes in Northern Sonora and Southern Arizona: Geological Society of America Cordilleran Section 1981 Annual Meeting Field Trip No. 10, 28–30 March 1981, Hermosillo, Sonora, p. 323–365.

Davis, G.H., and Coney, P.J., 1979, Geologic development of the Cordilleran metamorphic core complexes: Geology, v. 7, no. 3, p. 120–124, https://doi.org/10.1130/0091-7613(1979)7<120:GDOTCM>2.0.CO;2.

Davis, G.H., and Frost, E.G., 1976, Internal structure and mechanism of emplacement of a small gravity-glide sheet, Saguaro National Monument (East), Tucson Arizona: Arizona Geological Digest, v. 10, p. 287–304.

Davis, G.H., and Hardy, J.J., Jr., 1981, The Eagle Pass detachment, southeastern Arizona: Product of mid-Miocene listric (?) normal faulting in the southern Basin and Range: Geological Society of America Bulletin, v. 92, no. 10, p. 749–762, https://doi.org/10.1130/0016-7606(1981)92<749:TEPDSA>2.0.CO;2.

Davis, G.H., Eliopulos, G., Frost, E., Goodmundson, R.C., Knapp, R.B., Liming, R.B., Swan, M.M., and Wynn, J.C., 1974, Recumbent folds—Focus of an investigative workshop in tectonics: Journal of Geological Education, v. 22, no. 5, p. 204–208, https://doi.org/10.5408/0022-1368-22.5.204.

Davis, G.H., Cox, L.J., Ornelas, R., Constenius, K.N., Johnson, J.A., Kong, F., Bedford, J.M., Pecha, M., and Rodriguez, E.P., 1998, Protomylonite, augen mylonite, mylonite, protocataclasite, and cataclasite in granitic footwall of a detachment fault, *in* Snoke, A.W., Tullis, J.A., and Todd, V.R., eds., Fault-Related Rocks: A Photographic Atlas: Princeton, New Jersey, Princeton University Press, p. 160–163, https://doi.org/10.1515/9781400864935.160.

Davis, G.H., Constenius, K.N., Dickinson, W.R., Rodriguez, E.P., and Cox, L.J., 2004, Fault and fault-rock characteristics associated with Neogene extension in the Catalina-Rincon region of southeastern Arizona: Geological Society of America Bulletin, v. 116, no. 1–2, p. 128–141, https://doi.org/10.1130/B25260.1.

Davis, G.H., Constenius, K.N., Ornelas, E.P.R., and Cox, L.J., 2011, Structural-Geologic Map Relationships in the Salcito Ranch Area, Rincon Mountains, Southern Arizona: Arizona Geological Survey Contributed Report CR-11C, 19 p., http://repository.azgs.az.gov/uri_gin/azgs/dlio/994.

Davis, G.H., Spencer, J.E., and Gehrels, G.E., 2019, Field-trip guide to the Catalina-Rincon metamorphic core complex, Tucson, Arizona, *in*

Pearthree, P.A., ed., Geologic Excursions in Southwestern North America: Geological Society of America Field Guide 55, p. 1–38, https://doi.org/10.1130/2019.0055(01).

Dickey, D.D., Carr, W.J, and Bull, W.B., 1980, Geologic Map of the Parker NW, Parker, and Parts of the Whipple Mountains SW and Whipple Wash Quadrangles, California: U.S. Geological Survey Miscellaneous Investigations Map I-1124, scale 1:24,000, https://doi.org/10.3133/i1124.

Dickinson, W.R., 1989, Tectonic setting of Arizona through geologic time, *in* Jenney, J.P., and Reynolds, S.J., eds., Geologic Evolution of Arizona: Arizona Geological Society Digest, v. 17, p. 1–16.

Dickinson, W.R., 1991, Tectonic Setting of Faulted Tertiary Strata Associated with the Catalina Core Complex in Southern Arizona: Geological Society of America Special Paper 264, 106 p. (Includes Geologic Map of Catalina Core Complex and San Pedro Trough, 1:125,000.)

Dickinson, W.R., 1992, Geologic Map of Catalina Core Complex and San Pedro Trough, Pima, Pinal, Gila, Graham, and Cochise Counties, Arizona: Arizona Geological Survey Contributed Map CM-92-C, scale 1:125,000, 1 sheet.

DiTullio, L.D., 1983, Fault Rocks of the Tanque Verde Mountain Decollement Zone, Santa Catalina Metamorphic Core Complex, Tucson, Arizona [M.S. thesis]: Tucson, Arizona, University of Arizona, 90 p.

Döbelin, N., and Kleeberg, R., 2015, Profex: A graphical user interface for the Rietveld refinement program BGMN: Journal of Applied Crystallography, v. 48, no. 5, p. 1573–1580, https://doi.org/10.1107/S1600576715014685.

Donelick, R.A., O'Sullivan, P.B., and Ketcham, R.A., 2005, Apatite fission-track analysis: Reviews in Mineralogy and Geochemistry, v. 58, no. 1, p. 49–94, https://doi.org/10.2138/rmg.2005.58.3.

Drewes, H., 1974, Geologic Map and Sections of the Happy Valley Quadrangle, Cochise County, Arizona: U.S. Geological Survey Miscellaneous Investigations Series Map I-832, scale 1:48,000, https://doi.org/10.3133/i832.

Drewes, H., 1977, Geologic Map and Sections of the Rincon Valley Quadrangle, Pima County, Arizona: U.S. Geological Survey Miscellaneous Investigations Series Map I-997, scale 1:48,000, https://doi.org/10.3133/i997.

Drewes, H., 1981, Tectonics of Southeastern Arizona: U.S. Geological Survey Professional Paper 1144, 96 p., 10 plates, https://doi.org/10.3133/pp1144.

Drewes, H., 1991, Description and Development of the Cordilleran Orogenic Belt in the Southwestern United States and Northern Mexico: U.S. Geological Survey Professional Paper 1512, 92 p., https://doi.org/10.3133/pp1512.

Ducea, M.N., Triantafyllou, A., and Krmaric, J., 2020, New timing and depth constraints for the Catalina metamorphic core complex, southeast Arizona: Tectonics, v. 39, no. 8, https://doi.org/10.1029/2020TC006383.

Favorito, D.A., and Seedorff, E., 2017, Characterization and reconstruction of Laramide shortening and superimposed Cenozoic extension, Romero Wash–Tecolote Ranch area, southeastern Arizona: Geosphere, v. 13, p. 577–607, https://doi.org/10.1130/GES01381.1.

Favorito, D.A., and Seedorff, E., 2021, Cenozoic structural evolution of the Catalina metamorphic core complex and reassembly of Laramide reverse faults, southeastern Arizona: Geosphere, v. 17, no. 6, p. 1928–1971, https://doi.org/10.1130/GES02313.1.

Fayon, A.K., Peacock, S.M., Stump, E., and Reynolds, S.J., 2000, Fission track analysis of the footwall of the Catalina detachment fault, Arizona: Tectonic denudation, magmatism, and erosion: Journal of Geophysical Research–Solid Earth, v. 105, no. B5, p. 11,047–11,062, https://doi.org/10.1029/1999JB900421.

Ferguson, C.A., Johnson, B.J., Skotnicki, J.S., Maher, J.D., Spencer, J.E., Gibert, W.G., Richard, S.M., Youberg, A., Demsey, K.A., and House, P.K., 2003, Geologic Map of the Tortolita Mountains, Pinal and Pima Counties, Arizona: Arizona Geological Survey Digital Geologic Map DGM-26, version 2.0, map scale 1:24,000, 46 p., 2 map sheets and metadata, http://repository.azgs.az.gov/uri_gin/azgs/dlio/496.

Fitzgerald, P.G., Reynolds, S.J., Stump, E., Foster, D.A., and Gleadow, A.J.W., 1993, Thermochronologic evidence for timing of denudation and rate of crustal extension of the South Mountains metamorphic core complex and Sierra Estrella, Arizona: Nuclear Tracks and Radiation Measurements, v. 21, no. 4, p. 555–563, https://doi.org/10.1016/1359-0189(93)90196-G.

Fletcher, J.M., Bartley, J.M., Martin, M.W., Glazner, A.F., and Walker, J.D., 1995, Large-magnitude continental extension: An example from the central Mojave metamorphic core complex: Geological Society of America Bulletin, v. 107, no. 12, p. 1468–1483, https://doi.org/10.1130/0016-7606(1995)107<1468:LMCEAE>2.3.CO;2.

Force, E.R., 2002, Structural Reconnaissance of Lower-Plate Rocks along the Catalina-Rincon Range Front, Pima County, Arizona: Arizona Geological Survey Contributed Map CM-02, scale 1:24,000 and 1:48,000 (2 sheets), with 11 p. text, http://repository.azgs.az.gov/uri_gin/azgs/dlio/1516.

Fornash, K.F., Patchett, P.J., Gehrels, G.E., and Spencer, J.E., 2013, Evolution of granitoids in the Catalina metamorphic core complex, southeastern Arizona: U-Pb, Nd, and Hf isotopic constraints: Contributions to Mineralogy and Petrology, v. 165, no. 6, p. 1295–1310, https://doi.org/10.1007/s00410-013-0859-4.

Foster, D.A., and John, B.E., 1999, Quantifying tectonic exhumation in an extensional orogen with thermochronology: Examples from the southern Basin and Range Province, *in* Ring, U., Brandon, M.T., Lister, G.S., and Willett, S.D., eds., Exhumation Processes: Normal Faulting, Ductile Flow and Erosion: Geological Society, London, Special Publication 154, p. 343–364, https://doi.org/10.1144/GSL.SP.1999.154.01.16.

Foster, D.A., Harrison, T.M., Miller, C.F., and Howard, K.A., 1990, The $^{40}Ar/^{39}Ar$ thermochronology of the eastern Mojave Desert, California, and adjacent western Arizona with implications for the evolution of metamorphic core complexes: Journal of Geophysical Research–Solid Earth, v. 95, no. B12, p. 20,005–20,024, https://doi.org/10.1029/JB095iB12p20005.

Foster, D.A., Gleadow, A.J.W., Reynolds, S.J., and Fitzgerald, P.G., 1993, Denudation of metamorphic core complexes and the reconstruction of the transition zone, west-central Arizona—Constraints from apatite fission track thermochronology: Journal of Geophysical Research, v. 98, no. B2, p. 2167–2185, https://doi.org/10.1029/92JB02407.

Frost, E.G., 1981, Structural style of detachment faulting in the Whipple Mountains, California, and Buckskin Mountains, Arizona: Arizona Geological Society Digest, v. 13, p. 25–29.

Frost, E.G., and Heidrick, T.L., 1996, Three-dimensional structural geometries of the Colorado River extensional terrain and their regional exploration implications, *in* Rehrig, W.A., and Hardy, J.J., eds., Tertiary Extension and Mineral Deposits, Southwestern U.S.: Society of Economic Geologists Guidebook Series 25, p. 1–5, https://doi.org/10.5382/GB.25.

Frost, E.G., Cameron, T.E., and Martin, D.L., 1982, Comparison of Mesozoic tectonics with mid-Tertiary detachment faulting in the Colorado River area, California, Arizona, and Nevada, *in* Cooper, J.D., ed., Geologic Excursions in the California Desert: Anaheim, California, Geological Society of America, 78th Annual Meeting Field Guide, p. 113–159.

Gehrels, G.E., and Pecha, M., 2014, Detrital zircon U-Pb geochronology and Hf isotope geochemistry of Paleozoic and Triassic passive margin strata of western North America: Geosphere, v. 10, no. 1, p. 49–65, https://doi.org/10.1130/GES00889.1.

Gehrels, G.E., Valencia, V.A., and Ruiz, J., 2008, Enhanced precision, accuracy, efficiency, and spatial resolution of U-Pb ages by laser ablation–multicollector–inductively coupled plasma mass spectrometry: Geochemistry, Geophysics, Geosystems, v. 9, no. 3, https://doi.org/10.1029/2007GC001805.

Gottardi, R., Schaper, M.C., Barnes, J.D., and Heizler, M.T., 2018, Fluid-rock interaction and strain localization in the Picacho Mountains detachment shear zone, Arizona, USA: Tectonics, v. 37, no. 9, p. 3244–3260, https://doi.org/10.1029/2017TC004835.

Gottardi, R., McAleer, R., Casale, G., Borel, M., Iriondo, A., and Jepson, G., 2020, Exhumation of the Coyote Mountains metamorphic core complex (Arizona): Implications for orogenic collapse of the southern North American Cordillera: Tectonics, v. 39, no. 8, https://doi.org/10.1029/2019TC006050.

Gregorski, A., Alke, A., and Davis, G., 2019, Catalina detachment fault, Javelina detachment fault, and fault-rock relations along the southwest toe of Tanque Verde Ridge, Rincon Mountains, *in* GeoDaze Poster Session, March 29: Tucson, Arizona, University of Arizona, poster G-15.

Haines, S.H., and van der Pluijm, B.A., 2008, Clay quantification and Ar-Ar dating of synthetic and natural gouge: Application to the Miocene Sierra Mazatán detachment fault, Sonora, Mexico: Journal of Structural Geology, v. 30, no. 4, p. 525–538, https://doi.org/10.1016/j.jsg.2007.11.012.

Haines, S., Lynch, E., Mulch, A., Valley, J.W., and van der Pluijm, B., 2016, Meteoric fluid infiltration in crustal-scale normal fault systems as indicated by $\delta^{18}O$ and $\delta^{2}H$ geochemistry and $^{40}Ar/^{39}Ar$ dating of neoformed clays in brittle fault rocks: Lithosphere, v. 8, no. 6, p. 587–600, https://doi.org/10.1130/L483.1.

Halfkenny, R.D., Jr., Kerrich, R., and Rehrig, W.A., 1989, Fluid regimes and geochemical mass transport in the development of mylonites and chloritic breccias at Copper Penny, Buckskin Mountains, *in* Spencer, J.E., and Reynolds, S.J., eds., Geology and Mineral Resources of the Buckskin and Rawhide Mountains, West-Central Arizona: Arizona Geological Survey

Bulletin 198, p. 190–202, http://repository.azgs.az.gov/uri_gin/azgs/dlio/1278.

Harrison, T.M., Celerier, J., Aikman, A.B., Hermann, J., and Heizler, M.T., 2009, Diffusion of ^{40}Ar in muscovite: Geochimica et Cosmochimica Acta, v. 73, no. 4, p. 1039–1051, https://doi.org/10.1016/j.gca.2008.09.038.

Hasebe, N., Barbarand, J., Jarvis, K., Carter, A., and Hurford, A.J., 2004, Apatite fission-track chronometry using laser ablation ICP-MS: Chemical Geology, v. 207, no. 3–4, p. 135–145, https://doi.org/10.1016/j.chemgeo.2004.01.007.

Haxel, G.B., Tosdal, R.M., May, D.J., and Wright, J.E., 1984, Latest Cretaceous and early Tertiary orogenesis in south-central Arizona: Thrust faulting, regional metamorphism, and granitic plutonism: Geological Society of America Bulletin, v. 95, no. 6, p. 631–653, https://doi.org/10.1130/0016-7606(1984)95<631:LCAETO>2.0.CO;2.

Haxel, G.B., Wright, J.E., Riggs, N.R., Tosdal, R.M., and May, D.J., 2005, Middle Jurassic Topawa Group, Baboquivari Mountains, south-central Arizona: Volcanic and sedimentary record of deep basins within the Jurassic magmatic arc, *in* Anderson, T.H., Nourse, J.A., McKee, J.W., and Steiner, M.B., eds., The Mojave-Sonora Megashear Hypothesis: Development, Assessment, and Alternatives: Geological Society of America Special Paper 393, p. 329–357, https://doi.org/10.1130/0-8137-2393-0.329.

Hayes, P.T., and Raup, R.B., 1968, Geologic Map of the Huachuca and Mustang Mountains, Southeastern Arizona: U.S. Geological Society Miscellaneous Geologic Investigations Map I-509, scale 1:48,000, https://doi.org/10.3133/i509.

Henderson, L.J., Gordon, R.G., and Engebretson, D.C., 1984, Mesozoic aseismic ridges on the Farallon plate and southward migration of shallow subduction during the Laramide orogeny: Tectonics, v. 3, no. 2, p. 121–132, https://doi.org/10.1029/TC003i002p00121.

Houser, B.B., Peters, L., Esser, R.P., and Gettings, M.E., 2004, Stratigraphy and Tectonic History of the Tucson Basin, Pima County, Arizona, Based on the Exxon State (32)-1 Well: U.S. Geological Survey Scientific Investigations Report 5076, 42 p., https://pubs.usgs.gov/sir/2004/5076/.

Hoxie, D.T., 2012, Exhuming the Remains of the Inactive Mountain-Front Pirate Fault, Santa Catalina Mountains, Southeastern Arizona: Arizona Geological Survey Contributed Report CR-12-F, 18 p., http://repository.azgs.az.gov/uri_gin/azgs/dlio/1483.

Humphreys, E.D., 1995, Post-Laramide removal of the Farallon slab, western United States: Geology, v. 23, no. 11, p. 987–990, https://doi.org/10.1130/0091-7613(1995)023<0987:PLROTF>2.3.CO;2.

Humphreys, E., 2009, Relation of flat subduction to magmatism and deformation in the western United States, *in* Kay, S.M., Ramos, V.A., and Dickinson, W.R., eds., Backbone of the Americas: Shallow Subduction, Plateau Uplift, and Ridge and Terrane Collision: Geological Society of America Memoir 204, p. 85–98, https://doi.org/10.1130/2009.1204(04).

Huntington, K.W., and Klepeis, K.A., 2018, Challenges and Opportunities for Research in Tectonics: Understanding Deformation and the Processes That Link Earth Systems, from Geologic Time to Human Time: A community vision document submitted to the U.S. National Science Foundation, https://digital.lib.washington.edu/researchworks/handle/1773/40754 (accessed January 2023).

Hurford, A.J., and Green, P.F., 1983, The zeta age calibration of fission-track dating: Chemical Geology, v. 41, p. 285–317, https://doi.org/10.1016/S0009-2541(83)80026-6.

Jepson, G., Carrapa, B., George, S.W.M., Triantafyllou, A., Egan, S.M., Constenius, K.N., Gehrels, G.E., and Ducea, M.N., 2021, Resolving mid- to upper-crustal exhumation through apatite petrochronology and thermochronology: Chemical Geology, v. 565, https://doi.org/10.1016/j.chemgeo.2021.120071.

Jepson, G., Carrapa, B., George, S.W.M., Reeher, L.J., Kapp, P.A., DeCelles, P.G., Davis, G.H., Thomson, S.N., Amadori, C., Clinkscales, C., Jones, S., Gleadow, J.W., and Kohn, B.P., 2022, Where did the Arizona-plano go? Protracted thinning via upper- to lower-crustal processes: Journal of Geophysical Research–Solid Earth, v. 127, https://doi.org/10.1029/2021JB023850.

John, B.E., 1982, Geologic framework of the Chemehuevi Mountains, southeastern California, *in* Frost, E.G., and Martin, D.L., eds., Mesozoic–Cenozoic Tectonic Evolution of the Colorado River Region, California, Arizona, and Nevada (Anderson-Hamilton Volume): San Diego, California, Cordilleran Publishers, p. 317–325.

John, B.E., 1987, Geometry and evolution of a mid-crustal extensional fault system: Chemehuevi Mountains, southeastern California, *in* Coward, M.P., Dewey, J.F., and Hancock, P.L., eds., Continental Extensional Tectonics: Geological Society, London, Special Publication 28, p. 313–335, https://doi.org/10.1144/GSL.SP.1987.028.01.20.

Keith, S., and Rasmussen, J., 2018, Spring Field Trip—Petrologic and Structural Evidence for Flat Subduction Tectonics in Santa Catalina Mountains and Vicinity: Tucson, Arizona, Arizona Geological Society, 4 p.

Keith, S., and Rasmussen, J., 2019, Spring Field Trip—Petrologic and Structural Evidence for Flat Subduction Tectonics in Santa Catalina Mountains and Vicinity: Tucson, Arizona, Arizona Geological Society, 8 June 2019.

Keith, S.B., Reynolds, S.J., Damon, P.E., Shafiqullah, M., Livingston, D.E., and Pushkar, P.D., 1980, Evidence for multiple intrusion and deformation within the Santa Catalina–Rincon–Tortolita crystalline complex, southeastern Arizona, *in* Crittenden, M.D., Jr., Coney, P.J., and Davis, G.H., eds., Cordilleran Metamorphic Core Complexes: Geological Society of America Memoir 153, p. 217–267, https://doi.org/10.1130/MEM153-p217.

Kerrich, R., and Rehrig, W., 1987, Fluid motion associated with Tertiary mylonitization and detachment faulting: ^{18}O/^{16}O evidence from the Picacho metamorphic core complex, Arizona: Geology, v. 15, no. 1, p. 58–62, https://doi.org/10.1130/0091-7613(1987)15<58:FMAWTM>2.0.CO;2.

Knapp, J.H., 2018, Mid-Tertiary Detachment Tectonics at Mesquite Mountain, West-Central Arizona: Arizona Geological Survey Contributed Report CR-18-H, 58 p., http://repository.azgs.az.gov/uri_gin/azgs/dlio/1896.

Koppers, A.A.P., 2002, ArArCALC—Software for ^{40}Ar/^{39}Ar age calculations: Computers & Geosciences, v. 28, p. 605–619, https://doi.org/10.1016/S0098-3004(01)00095-4.

Koppers, A.A.P., Staudigel, H., and Wijbrans, J.R., 2000, Dating crystalline groundmass separates of altered Cretaceous seamount basalts by the ^{40}Ar/^{39}Ar incremental heating technique: Chemical Geology, v. 166, no. 1–2, p. 139–158, https://doi.org/10.1016/S0009-2541(99)00188-6.

Koppers, A.A.P., Staudigel, H., Pringle, M.S., and Wijbrans, J.R., 2003, Short-lived and discontinuous intraplate volcanism in the South Pacific: Hot spots or extensional volcanism?: Geochemistry, Geophysics, Geosystems, v. 4, no. 10, p. 1087, https://doi.org/10.1029/2003GC000533.

Krantz, R.W., 1983, Detailed Structural Analysis of Detachment Faulting near Colossal Cave, Southern Rincon Mountains, Pima County, Arizona [M.S. thesis]: Tucson, Arizona, University of Arizona, 58 p.

Kuiper, K.F., Deino, A., Hilgen, F.J., Krijgsman, W., Renne, P.R., and Wijbrans, J.R., 2008, Synchronizing rock clocks of Earth history: Science, v. 320, no. 5875, p. 500–504, https://doi.org/10.1126/science.1154339.

Lever, J., Krzywinski, M., and Altman, N., 2017, Points of significance: Principal component analysis: Nature Methods, v. 14, no. 7, p. 641–642, https://doi.org/10.1038/nmeth.4346.

Liming, R.B., 1974, Geology and Kinematic Analysis of Deformation in the Martinez Ranch Area, Pima County, Arizona [M.S. thesis]: Tucson, Arizona, University of Arizona, 86 p.

Lin, A., 1996, Injection veins of crushing-originated pseudotachylyte and fault gouge formed during seismic faulting: Engineering Geology, v. 43, no. 2, p. 213–224.

Lingrey, S.H., 1982, Structural Geology and Tectonic Evolution of the Northeastern Rincon Mountains, Cochise and Pima Counties [Ph.D. dissertation]: Tucson, Arizona, University of Arizona, 202 p.

Lister, G.S., and Davis, G.A., 1989, The origin of metamorphic core complexes and detachment faults formed during Tertiary continental extension in the northern Colorado River region, U.S.A.: Journal of Structural Geology, v. 11, no. 1–2, p. 65–94, https://doi.org/10.1016/0191-8141(89)90036-9.

Liu, L., and Gurnis, M., 2010, Dynamic subsidence and uplift of the Colorado Plateau: Geology, v. 38, no. 7, p. 663–666, https://doi.org/10.1130/G30624.1.

Loughlin, W.P., 1991, Principal component analysis for alteration mapping: Photogrammetric Engineering and Remote Sensing, v. 57, p. 1163–1169, https://www.asprs.org/wp-content/uploads/pers/1991journal/sep/1991_sep_1163-1169.pdf.

Loy, K.L., 1990, Subsurface Structure of the Southern and Central Tucson Basin, Pima County, Arizona [M.S. thesis]: Tucson, Arizona, University of Arizona, Chapter 3, p. 24–26.

Magloughlin, J.F., 1992, Microstructural and chemical changes associated with cataclasis and frictional melting at shallow crustal levels: The cataclasite-pseudotachylyte connection: Tectonophysics, v. 204, p. 243–260, https://doi.org/10.1016/0040-1951(92)90310-3.

McClelland, W.C., 1982, Structural geology of the central Sacramento Mountains, San Bernardino County, California, *in* Frost, E.G., and Martin, D.L., eds., Mesozoic–Cenozoic Tectonic Evolution of the Colorado River Region, California, Arizona, and Nevada (Anderson-Hamilton Volume): San Diego, California, Cordilleran Publishers, p. 401–407.

McDougall, I., and Harrison, T.M., 1999, Geochronology and Thermochronology by the $^{40}Ar/^{39}Ar$ Method (2nd ed.): New York, Oxford University Press, 269 p.

McDowell, F.W., McIntosh, W.C., and Farley, K.A., 2005, A precise ^{40}Ar-^{39}Ar reference age for the Durango apatite (U-Th)/He and fission-track dating standard: Chemical Geology, v. 214, no. 3–4, p. 249–263, https://doi.org/10.1016/j.chemgeo.2004.10.002.

Meijer, A., 2014, The Pinal Schist of southern Arizona: A Paleoproterozoic forearc complex with evidence of spreading ridge–trench interaction at ca. 1.65 Ga and a Proterozoic arc obduction event: Geological Society of America Bulletin, v. 126, no. 9–10, p. 1145–1163, https://doi.org/10.1130/B31002.1.

Menges, C.M., and Pearthree, P.A., 1989, Late Cenozoic tectonism in Arizona and its impact on regional landscape evolution, *in* Jenney, J.P., and Reynolds, S.J., eds., Geologic Evolution of Arizona: Arizona Geological Society Digest, v. 17, p. 649–680.

Miller, C.F., and Barton, M.D., 1990, Phanerozoic plutonism in the Cordilleran interior, USA, *in* Kay, S.M., and Rapela, C.W., eds., Plutonism from Antarctica to Alaska: Geological Society of America Special Paper 241, p. 213–231, https://doi.org/10.1130/SPE241-p213.

Min, K., Mundil, R., Renne, P.R., and Ludwig, K.R., 2000, A test for systematic errors in $^{40}Ar/^{39}Ar$ geochronology through comparison with U/Pb analysis of a 1.1-Ga rhyolite: Geochimica et Cosmochimica Acta, v. 64, no. 1, p. 73–98, https://doi.org/10.1016/S0016-7037(99)00204-5.

Misch, P., 1960, Regional structural reconnaissance in central-northeast Nevada and some adjacent areas: Observations and interpretations, *in* Boettcher, J.W., and Sloan, W.W., eds., Guidebook to the Geology of East Central Nevada, 1960, 11th Annual Field Conference held jointly with Eastern Nevada Geological Society, Intermountain Association of Petroleum Geologists: Salt Lake City, Utah, Intermountain Association of Petroleum Geologists, p. 17–42.

Morrison, J., and Anderson, J.L., 1998, Footwall refrigeration along a detachment fault: Implications for the thermal evolution of core complexes: Science, v. 279, no. 5347, p. 63–66, https://doi.org/10.1126/science.279.5347.63.

Naruk, S.J., and Bykerk-Kauffman, A., 1990, Late Cretaceous and Tertiary deformation of the Santa Catalina metamorphic core complex, Arizona, *in* Gehrels, G.E., and Spencer, J.E., eds., Geologic Excursions through the Sonoran Desert Region, Arizona and Sonora: Arizona Geological Survey Special Paper 7, p. 41–50.

Odlum, M.L., and Stockli, D.F., 2020, Geochronologic constraints on deformation and metasomatism along an exhumed mylonitic shear zone using apatite U-Pb, geochemistry, and microtextural analysis: Earth and Planetary Science Letters, v. 538, https://doi.org/10.1016/j.epsl.2020.116177.

Paces, J.B., and Miller, J.D., 1993, Precise U-Pb ages of the Duluth Complex and related mafic intrusions, northeastern Minnesota: Geochronological insights into physical, petrogenetic, paleomagnetic, and tectonomagmatic processes associated with the 1.1 Ga Midcontinent rift system: Journal of Geophysical Research, v. 98, no. B8, p. 13,997–14,013, https://doi.org/10.1029/93JB01159.

Parnell-Turner, R., Escartín, J., Olive, J.-A., Smith, D.K., and Petersen, S., 2018, Genesis of corrugated fault surfaces by strain localization recorded at oceanic detachments: Earth and Planetary Science Letters, v. 498, p. 116–128, https://doi.org/10.1016/j.epsl.2018.06.034.

Pashley, E.F., Jr., 1966, Structure and Stratigraphy of the Central, Northern, and Eastern Parts of the Tucson Basin, Arizona [Ph.D. thesis]: Tucson, Arizona, University of Arizona, 273 p.

Paton, C., Hellstrom, J., Paul, B., Woodhead, J., and Hergt, J., 2011, Iolite: Freeware for the visualisation and processing of mass spectrometric data: Journal of Analytical Atomic Spectrometry, v. 26, p. 2508–2518, https://doi.org/10.1039/c1ja10172b.

Platt, J.P., Behr, W.M., and Cooper, F.J., 2015, Metamorphic core complexes: Windows into the mechanics and rheology of the crust: Journal of the Geological Society, v. 172, no. 1, p. 9–27, https://doi.org/10.1144/jgs2014-036.

Prior, M.G., Stockli, D.F., and Singleton, J.S., 2016, Miocene slip history of the Eagle Eye detachment fault, Harquahala Mountains metamorphic core complex, west-central Arizona: Tectonics, v. 35, no. 8, p. 1913–1934, https://doi.org/10.1002/2016TC004241.

Rehrig, W.A., and Reynolds, S.J., 1980, Geologic and geochronologic reconnaissance of a northwest-trending zone of metamorphic core complexes in southern and western Arizona, *in* Crittenden, M.D., Jr., Coney, P.J., and Davis, G.H., eds., Cordilleran Metamorphic Core Complexes: Geological Society of America Memoir 153, p. 131–157, https://doi.org/10.1130/MEM153-p131.

Reiners, P.W., 2005, Zircon (U-Th)/He thermochronometry: Reviews in Mineralogy and Geochemistry, v. 58, no. 1, p. 151–179, https://doi.org/10.2138/rmg.2005.58.6.

Reynolds, S.J., 1985, Geology of the South Mountains, Central Arizona: Arizona Bureau of Geology and Mineral Technology Bulletin 195, 61 p., http://repository.azgs.az.gov/uri_gin/azgs/dlio/1655.

Reynolds, S.J., and Rehrig, W.A., 1980, Mid-Tertiary plutonism and mylonitization, South Mountains, central Arizona, *in* Crittenden, M.D., Jr., Coney, P.J., and Davis, G.H., eds., Cordilleran Metamorphic Core Complexes: Geological Society of America Memoir 153, p. 159–175, https://doi.org/10.1130/MEM153-p159.

Reynolds, S.J., Shafiqullah, M., Damon, P.E., and DeWitt, E., 1986, Early Miocene mylonitization and detachment faulting, South Mountains, central Arizona: Geology, v. 14, no. 4, p. 283–286, https://doi.org/10.1130/0091-7613(1986)14<283:EMMADF>2.0.CO;2.

Reynolds, S.J., Wood, S.E., Pearthree, P.A., and Field, J.J., 2002, Geologic Map of the White Tank Mountains, Central Arizona: Arizona Geological Survey Digital Geologic Map DGM-14, version 1.0, scale 1:24,000, 2 map sheets and metadata: http://repository.azgs.az.gov/uri_gin/azgs/dlio/552.

Richard, S.M., Fryxell, J.E., and Sutter, J.F., 1990, Tertiary structure and thermal history of the Harquahala and Buckskin Mountains, west central Arizona: Implications for denudation by a major detachment fault system: Journal of Geophysical Research–Solid Earth, v. 95, no. B12, p. 19,973–19,987, https://doi.org/10.1029/JB095iB12p19973.

Richard, S.M., Spencer, J.E., Ferguson, C.A., and Pearthree, P.A., 1999, Geologic Map of the Picacho Mountains and Picacho Peak, Pinal County, Southern Arizona: Arizona Geological Survey Open-File Report 99-18, map scale 1:24,000, 2 sheets, 43 p., http://repository.azgs.az.gov/uri_gin/azgs/dlio/377.

Richard, S.M., Spencer, J.E., Youberg, A., and Ferguson, C.A., 2005, Geologic Map of the Rincon Valley Area, Pima County, Arizona: Arizona Geological Survey Digital Geologic Map 44 (DGM-44), version 1.0, scale 1:24,000, 1 sheet, 11 p., http://repository.azgs.az.gov/uri_gin/azgs/dlio/580.

Roberts, G.P., Michetti, A.M., Cowie, P., Morewood, N.C., and Papanikolaou, I., 2002, Fault slip-rate variations during crustal-scale strain localisation, central Italy: Geophysical Research Letters, v. 29, no. 8, p. 9-1–9-4, https://doi.org/10.1029/2001GL013529.

Robertson, S., 1999, British Geological Survey (BSG) Rock Classification Scheme, Volume 2: Classification of Metamorphic Rocks: British Geological Survey Research Report RR 99–02, 24 p., https://www.bgs.ac.uk/download/bgs-rock-classification-scheme-metamorphic/#.

Rubatto, D., 2017, Zircon: The metamorphic mineral: Reviews in Mineralogy and Geochemistry, v. 83, no. 1, p. 261–295, https://doi.org/10.2138/rmg.2017.83.9.

Rutter, E.H., Holdsworth, R.E., and Knipe, R.J., 2001, The nature and tectonic significance of fault-zone weakening: An introduction, *in* Holdsworth, R.E., Strachan, R.A., Magloughlin, J.F., and Knipe, R.J., eds., The Nature and Tectonic Significance of Fault Zone Weakening: Geological Society, London, Special Publication 186, p. 1–11, https://doi.org/10.1144/GSL.SP.2001.186.01.01

Saleeby, J., 2003, Segmentation of the Laramide slab—Evidence from the southern Sierra Nevada region: Geological Society of America Bulletin, v. 115, no. 6, p. 655–668, https://doi.org/10.1130/0016-7606(2003)115<0655:SOTLSF>2.0.CO;2.

Sanguinito, S.M., 2013, Investigating the Effect of High-Angle Normal Faulting on Unroofing Histories of the Santa Catalina–Rincon and Harcuvar Metamorphic Core Complexes, Using Fission-Track and Apatite and Zircon (U-Th)/He Thermochronometry [M.S. thesis]: Austin, Texas, University of Texas at Austin, 195 p.

Schoene, B., and Bowring, S.A., 2006, U-Pb systematics of the McClue Mountain syenite: Thermochronological constraints on the age of the $^{40}Ar/^{39}Ar$ standard MMhb: Contributions to Mineralogy and Petrology, v. 151, no. 5, p. 615–630, https://doi.org/10.1007/s00410-006-0077-4.

Schoene, B., and Bowring, S.A., 2007, Determining accurate temperature-time paths from U-Pb thermochronology: An example from the Kaapvaal craton, southern Africa: Geochimica et Cosmochimica Acta, v. 71, no. 1, p. 165–185, https://doi.org/10.1016/j.gca.2006.08.029.

Scoggin, S.H., Reiners, P.W., Shuster, D.L., Davis, G.H., Ward, L.A., Worthington, J.R., Nickerson, P.A., and Evenson, N.S., 2021, (U/Th)/He and $^{4}He/^{3}He$ thermochronology of secondary oxides in faults and fractures: A regional perspective from southeastern Arizona: Geochemistry, Geophysics, Geosystems, v. 22, https://doi.org/10.1029/2021GC009905.

Scott, R.J., Foster, D.A., and Lister, G.S., 1998, Tectonic implications of rapid cooling of lower plate rocks from the Buckskin-Rawhide metamorphic core complex, west-central Arizona: Geological Society of America Bulletin, v. 110, no. 5, p. 588–614, https://doi.org/10.1130/0016-7606(1998)110<0588:TIORCO>2.3.CO;2.

Selverstone, J., Axen, G.J., and Luther, A., 2012, Fault localization controlled by fluid infiltration into mylonites: Formation and strength of low-angle faults in the midcrustal brittle-plastic transition: Journal of Geophysical Research–Solid Earth, v. 117, no. B6, B06210, https://doi.org/10.1029/2012JB009171.

Sibson, R.H., 1975, Generation of pseudotachylyte by ancient seismic faulting: Geophysical Journal International, v. 43, no. 3, p. 775–794, https://doi.org/10.1111/j.1365-246X.1975.tb06195.x.

Sibson, R.H., 1977, Fault rocks and fault mechanisms: Journal of the Geological Society, v. 133, p. 191–213, https://doi.org/10.1144/gsjgs.133.3.0191.

Sibson, R.H., 1990, Conditions for fault-valve behaviour, *in* Knipe, R.J., and Rutter, E.H., eds., Deformation Mechanisms, Rheology and Tectonics: Geological Society, London, Special Publication 54, p. 15–28, https://doi.org/10.1144/GSL.SP.1990.054.01.02.

Sibson, R.H., 1992, Implications of fault-valve behavior for rupture nucleation and recurrence, *in* Mikumo, T., Aki, K., Ohnaka, M., Ruff, L.J., and Spudich, P.K.P., eds., Earthquake Source Physics and Earthquake Precursors: Tectonophysics, v. 211, no. 1–4, p. 283–293, https://doi.org/10.1016/0040-1951(92)90065-E.

Sibson, R.H., 2020a, Dual-driven fault failure in the lower seismogenic zone: Bulletin of the Seismological Society of America, v. 110, no. 2, p. 850–862, https://doi.org/10.1785/0120190190.

Sibson, R.H., 2020b, Preparation zones for large crustal earthquakes consequent on fault-valve action: Earth, Planets, and Space, v. 72, no. 1, 31, https://doi.org/10.1186/s40623-020-01153-x.

Simpson, C., Schweitzer, J., and Howard, K.A., 1991, A reinterpretation of the timing, position, and significance of part of the Sacramento Mountains detachment fault, southeastern California: Geological Society of America Bulletin, v. 103, no. 6, p. 751–761, https://doi.org/10.1130/0016-7606(1991)103%3C0751:AROTTP%3E2.3.CO;2.

Singleton, J.S., 2013a, Development of extension-parallel corrugations in the Buckskin-Rawhide metamorphic core complex, west-central Arizona: Geological Society of America Bulletin, v. 125, no. 3–4, p. 453–472, https://doi.org/10.1130/B30672.1.

Singleton, J.S., 2013b, Geologic Map and Cross Sections of the Swansea–Clara Peak Area, Buckskin Mountains, West-Central Arizona: Geological Society of America Map and Chart MCH104, scale 1:12,000.

Singleton, J.S., 2015, The transition from large-magnitude extension to distributed dextral faulting in the Buckskin-Rawhide metamorphic core complex, west-central Arizona: Tectonics, v. 34, p. 1685–1708, https://doi.org/10.1002/2014TC003786.

Singleton, J.S., and Mosher, S., 2012, Mylonitization in the lower plate of the Buckskin-Rawhide detachment fault, west-central Arizona: Implications for the geometric evolution of metamorphic core complexes: Journal of Structural Geology, v. 39, p. 180–198, https://doi.org/10.1016/j.jsg.2012.02.013.

Singleton, J.S., Stockli, D.F., Gans, P.B., and Prior, M.G., 2014, Timing, rate, and magnitude of slip on the Buckskin-Rawhide detachment fault, west-central Arizona: Tectonics, v. 33, no. 8, p. 1596–1615, https://doi.org/10.1002/2013TC003517.

Singleton, J.S., Wong, M.S., and Johnson, S.M., 2018, The role of calcite-rich metasedimentary mylonites in localizing detachment fault strain and influencing the structural evolution of the Buckskin-Rawhide metamorphic core complex, west-central Arizona: Lithosphere, v. 10, no. 2, p. 172–193, https://doi.org/10.1130/L699.1.

Singleton, J.S., Seymour, N.M., Reynolds, S.J., Vomocil, T., and Wong, M.S., 2019, Distributed Neogene faulting across the western to central Arizona metamorphic core complex belt: Synextensional constriction and superposition of the Pacific–North America plate boundary on the southern Basin and Range: Geosphere, v. 15, no. 4, p. 1409–1435, https://doi.org/10.1130/GES02036.1.

Snoke, A.W., Tullis, J., and Todd, V.R., eds., 1998, Fault-Related Rocks: A Photographic Atlas: Princeton, New Jersey, Princeton University Press, 634 p., https://doi.org/10.1515/9781400864935.

Spencer, J.E., 1984, Role of tectonic denudation in warping and uplift of low-angle normal faults: Geology, v. 12, no. 2, p. 95–98, https://doi.org/10.1130/0091-7613(1984)12<95:ROTDIW>2.0.CO;2.

Spencer, J.E., 1985, Miocene low-angle normal faulting and dike emplacement, Homer Mountain and surrounding areas, southeastern California and southernmost Nevada: Geological Society of America Bulletin, v. 96, no. 9, p. 1140–1155, https://doi.org/10.1130/0016-7606(1985)96<1140:MLNFAD>2.0.CO;2.

Spencer, J.E., 1999, Geologic continuous casting below continental and deep-sea detachment faults and at the striated extrusion of Sacsayhuamán, Peru: Geology, v. 27, no. 4, p. 327–330, https://doi.org/10.1130/0091-7613(1999)027<0327:GCCBCA>2.3.CO;2.

Spencer, J.E., 2006, A Geologist's Guide to the Core Complex Geology along the Catalina Highway, Tucson Area, Arizona: Arizona Geological Survey Open-File Report 06-01, 38 p., http://repository.azgs.az.gov/uri_gin/azgs/dlio/360.

Spencer, J.E., and Reynolds, S.J., eds., 1989a, Geology and Mineral Resources of the Buckskin and Rawhide Mountains, West-Central Arizona: Arizona Geological Survey Bulletin 198, 272 p., http://repository.azgs.az.gov/uri_gin/azgs/dlio/1278.

Spencer, J.E., and Reynolds, S.J., 1989b, Tertiary structure, stratigraphy, and tectonics of the Buckskin Mountains, *in* Spencer, J.E., and Reynolds, S.J., eds., Geology and Mineral Resources of the Buckskin and Rawhide Mountains, West-Central Arizona: Arizona Geological Survey Bulletin 198, p. 103–167, http://repository.azgs.az.gov/uri_gin/azgs/dlio/1278.

Spencer, J.E., and Reynolds, S.J., 1991, Tectonics of mid-Tertiary extension along a transect through west-central Arizona: Tectonics, v. 10, p. 1204–1221, https://doi.org/10.1029/91TC01160.

Spencer, J.E., Ferguson, C.A., Richard, S.M., Orr, T.R., Pearthree, P.A., Gilbert, W.G., and Krantz, R.W., 2001, Geologic Map of the Narrows 7.5′ Quadrangle and the Southern Part of the Rincon Peak 7.5′ Quadrangle, Eastern Pima County, Arizona: Arizona Geological Survey Digital Geologic Map 10, scale 1:24,000, http://repository.azgs.az.gov/uri_gin/azgs/dlio/474.

Spencer, J.E., Ferguson, C.A., and Richard, S.M., 2012, Geologic Field Guides to the Southeastern Picacho Mountains and Picacho Peak, Pinal County, Arizona: Arizona Geological Survey Open-File Report 12-04, 13 p., http://repository.azgs.az.gov/uri_gin/azgs/dlio/1447.

Spencer, J.E., Cook, J.P., Lingrey, S.H., Richard, S.M., and Guynn, J.H., 2018a, Geologic Map of the Wildhorse Mountain 7.5 Quadrangle, Cochise County, Arizona: Arizona Geological Survey Digital Geologic Map DGM-62, v. 2.0, map scale 1:24,000, 18 p. and 1 map sheet, http://repository.azgs.az.gov/uri_gin/azgs/dlio/613.

Spencer, J.E., Singleton, J.S., Strickland, E., Reynolds, S.J., Love, D., Foster, D.A., and Johnson, R., 2018b, Geodynamics of Cenozoic extension along a transect across the Colorado River extensional corridor, southwestern USA: Lithosphere, v. 10, no. 6, p. 743–759, https://doi.org/10.1130/L1002.1.

Spencer, J.E., Richard, S.M., Lingrey, S.H., Johnson, B.J., Johnson, R.A., and Gehrels, G.E., 2019, Reconstruction of mid-Cenozoic extension in the Rincon Mountains area, southeastern Arizona, USA, and geodynamic implications: Tectonics, v. 38, no. 7, p. 2338–2357, https://doi.org/10.1029/2019TC005565.

Spencer, J.E., Richard, S.M., Bykerk-Kauffman, A., Constenius, K.N., and Valencia, V.A., 2022, Structure, chronology, kinematics, and geodynamics of tectonic extension in the greater Catalina metamorphic core complex, southeastern Arizona, USA: Geosphere, v. 18, no. 6, p. 1643–1678, https://doi.org/10.1130/GES02485.1.

Spray, J.G., 1992, A physical basis for the frictional melting of some rock-forming minerals: Tectonophysics, v. 204, p. 205–221, https://doi.org/10.1016/0040-1951(92)90308-S.

Steiger, R.H., and Jäger, E., 1977, Subcommission on Geochronology: Convention on the use of decay constants in geo- and cosmochronology: Earth and Planetary Science Letters, v. 36, no. 3, p. 359–362, https://doi.org/10.1016/0012-821X(77)90060-7.

Stevens, A.L., Balgord, E.A., and Carrapa, B., 2016, Revised exhumation history of the Wind River Range and implications for Laramide tectonics: Tectonics, v. 35, p. 1121–1136, https://doi.org/10.1002/2016TC004126.

Stipp, M., Stünitz, H., Heilbronner, R., and Schmid, S.M., 2002, The eastern Tonale fault zone: 'A natural laboratory' for crystal plastic deformation of quartz over a temperature range from 250 to 700 °C: Journal of Structural Geology, v. 24, v. 12, p. 1861–1884, https://doi.org/10.1016/S0191-8141(02)00035-4.

Stockli, D.F., Brichau, S., Dewane, T.J., Hager, C., and Schroeder, J., 2006, Dynamics of large-magnitude extension in the Whipple Mountains metamorphic core complex: Geochimica et Cosmochimica Acta, v. 70, p. A616, https://doi.org/10.1016/j.gca.2006.06.1143.

Strickland, E.D., Singleton, J.S., and Haxel, G.B., 2018, Orocopia Schist in the northern Plomosa Mountains, west-central Arizona: A Laramide

subduction complex exhumed in a Miocene metamorphic core complex: Lithosphere, v. 10, no. 6, p. 723–742, https://doi.org/10.1130/L742.1.

Tagami, T., 1987, Determination of zeta calibration constant for fission track dating: International Journal of Radiation Applications and Instrumentation Part D: Nuclear Tracks and Radiation Measurements, v. 13, no. 2–3, p. 127–130, https://doi.org/10.1016/1359-0189(87)90023-9.

Taylor, J.R., 1997, An Introduction to Error Analysis: The Study of Uncertainties in Physical Measurements: Mill Valley, California, University Science Books, 327 p.

Terrien, J., 2012, The Role of Magmatism in the Catalina Metamorphic Core Complex, Arizona: Insights from Integrated Thermochronology, Gravity and Aeromagnetic Data [Ph.D. dissertation]: Syracuse, New York, Syracuse University, 232 p.

Thirumalai, K., Singh, A., and Ramesh, R., 2011, A MATLABTM code to perform weighted linear regression with (correlated or uncorrelated) errors in bivariate data: Journal of the Geological Society of India, v. 77, no. 4, p. 377–380, https://doi.org/10.1007/s12594-011-0044-1.

Thomson, S.N., Gehrels, G.E., Ruiz, J., and Buchwaldt, R., 2012, Routine low-damage apatite U-Pb dating using laser ablation–multicollector–ICPMS: Geochemistry, Geophysics, Geosystems, v. 13, no. 2, Q0AA21, https://doi.org/10.1029/2011GC003928.

Titley, S.R., 1976, Evidence for a Mesozoic linear tectonic pattern in southeastern Arizona: Arizona Geological Society Digest, v. 10, p. 71–101.

U.S. Geological Survey, 2020, USGS 3D Elevation Program Digital Elevation Model: https://elevation.nationalmap.gov/arcgis/rest/services/3DEPElevation/imageServer (accessed 11 January 2020).

Vermeesch, P., 2009, RadialPlotter: A Java application for fission track, luminescence and other radial plots: Radiation Measurements, v. 44, no. 4, p. 409–410, https://doi.org/10.1016/j.radmeas.2009.05.003.

Vermeesch, P., 2018, IsoplotR: A free and open toolbox for geochronology: Geoscience Frontiers, v. 9, no. 5, p. 1479–1493, https://doi.org/10.1016/j.gsf.2018.04.001.

Vermeesch, P., Rittner, M., Petrou, E., Omma, J., Mattinson, C., and Garzanti, E., 2017, High throughput petrochronology and sedimentary provenance analysis by automated phase mapping and LA-ICP-MS: Geochemistry, Geophysics, Geosystems, v. 18, no. 11, p. 4096–4109, https://doi.org/10.1002/2017GC007109.

Wagner, F.H., III, 2005, Cenozoic Extensional Tectonics Revealed through Seismic Reflection Imaging, SE Arizona [Ph.D. dissertation]: Tucson, University of Arizona, Tucson, see p. 117–152.

Wernicke, B., 1981, Low-angle normal faults in the Basin and Range province: nappe tectonics in an extending orogen: Nature, v. 291, p. 645–648, https://doi.org/10.1038/291645a0.

Wernicke, B., and Axen, G.J., 1988, On the role of isostasy in the evolution of normal fault systems: Geology, v. 16, no. 9, p. 848–851, https://doi.org/10.1130/0091-7613(1988)016<0848:OTROII>2.3.CO;2.

Wong, M.S., and Gans, P.B., 2008, Geologic, structural, and thermochronologic constraints on the tectonic evolution of the Sierra Mazatán core complex, Sonora, Mexico: New insights into metamorphic core complex formation: Tectonics, v. 27, no. 4, TC4013, https://doi.org/10.1029/2007TC002173.

Wong, M.S., Gans, P.B., and Scheier, J., 2010, The $^{40}Ar/^{39}Ar$ thermochronology of core complexes and other basement rocks in Sonora, Mexico: Implications for Cenozoic tectonic evolution of northwestern Mexico: Journal of Geophysical Research–Solid Earth, v. 115, no. B7, B07414, https://doi.org/10.1029/2009JB007032.

Woodcock, N.H., and Mort, K., 2008, Classification of fault breccias and fault related rocks: Geological Magazine, v. 145, no. 3, p. 435–440, https://doi.org/10.1017/S0016756808004883.

Wright, C., 1978, Folds in a Mylonite Schist in the Saguaro National Monument, near Tucson, Arizona [Senior Comps Project]: Northfield, Minnesota, Carleton College, 26 p.

Wust, S.L., 1986, Regional correlation of extension directions in Cordilleran metamorphic core complexes: Geology, v. 14, no. 10, p. 828–830, https://doi.org/10.1130/0091-7613(1986)14<828:RCOEDI>2.0.CO;2.

Yin, A., and Dunn, J.F., 1992, Structural and stratigraphic development of the Whipple-Chemehuevi detachment fault system, southeastern California: Implications for the geometrical evolution of domal and basinal low-angle normal faults: Geological Society of America Bulletin, v. 104, no. 6, p. 659–674, https://doi.org/10.1130/0016-7606(1992)104<0659:SASDOT>2.3.CO;2.

York, D., 1968, Least squares fitting of a straight line with correlated errors: Earth and Planetary Science Letters, v. 5, p. 320–324, https://doi.org/10.1016/S0012-821X(68)80059-7.

Manuscript Accepted by the Society 9 November 2022
Manuscript Published Online 5 June 2023

Printed in the USA